Dynamics and Cooperativity of the Catalytic Subunit of Protein Kinase A

A Dissertation
SUBMITTED TO THE FACULTY OF THE
UNIVERSITY OF MINNESOTA

Jonggul John Kim

IN PARTIAL FULFILLMENT OF THE REQUIREMENTS FOR
THE DEGREE OF
DOCTOR OF PHILOSOPHY

Gianluigi Veglia

July 2015

Pace non trovo, e non ho da far guerra;

E temo e spero, ed ardo e son un ghiaccio;

E volo sopra 'l cielo e giaccio in terra;

E nullo stringo, e tutto il mondo abbraccio.

Tal m'ha in prigion, che non m'apre, né serra;

Né per suo mi riten, né scioglie il laccio;

E non m'ancide Amor, e non mi sferra;

Né mi vuol vivo, né mi trae d'imapaccio.

Veggio senz' occhi; e non ho lingua e grido,

E bramo di perir, e cheggio aita;

Ed ho in odio me stesso ed amo altrui:

Pascomi di dolor, piangendo rido;

Equalmente mi spiace morte e vita:

In questo stato son, Donna, per Vui.

Contents

List of Tables

List of Figures

CHAPTER 1

CHAPTER 2

CHAPTER 6

CHAPTER 7

CHAPTER 8

CHAPTER 9

CHAPTER 10

List of Abbreviations

ADP: Adenosine Diphosphate

AKAP: A kinase anchoring protein

AKIP: A kinase interacting protein

ATP: Adenosine Triphosphate

ATPγN: Adenylyl-imidodiphophate

cAMP: cyclic adenosine monophosphate

CPMG: Carr-Purcell-Meibloom-Gill

CSA: Chemical Shift Anisotropy

DCM: Dilated Cardiomyopathy

HMQC: Heteronuclear Multiple Quantum Correlation Spectroscopy

HSQC: Heteronuclear Single Quantum Correlation Spectroscopy

INEPT: Insensitive Nuclei Enhancement by Polarization Transfer

MD: Molecular Dynamics

ms: millisecond

NMR: Nuclear Magnetic Resonance

NOE: Nuclear Overhauser Effect

ps: picosecond

PDK-1: phosphoinositide-dependent kinase-1

PKA: cAMP-dependent protein kinase A

PKA-C: catalytic subunit of cAMP-dependent protein kinase A

PKI: Protein Kinase Inhibitor

PKI$_{5-24}$: 20 amino acid fragment of Protein Kinase Inhibitor

PKS$_{5-24}$: 20 amino acid substrate derived from PKI$_{5-24}$

PLN: Phospholamban

PLN$_{1-19}$: cytoplasmic domain of Phospholamban

RMSD: Root Mean Square Deviation

S^{3}CT: Spin-state-selective Coherence transfer

SERCA: Sarcoplasmic Reticulum Ca^{2+} ATPase

SH: Src-homology domain

TrHE: TROSY Hahn-Echo

TROSY: Transverse Optimized Spectroscopy

Preface

The protein kinase family is a large and diverse family of enzymes that regulate almost all facets of cellular signaling. Protein kinases function as molecular switches by attaching a phosphate group to a Ser/Thr/Tyr hydroxyl group by using ATP as a co-factor to increase or decrease the activity of their protein substrates. Over 500 kinases have been discovered, including pseudo-kinases that share the same fold but are catalytic inactive, and the kinome comprises of 2% of the human genome [1]. As such this family of enzymes has attracted much interest for understanding cellular signaling and for disease therapeutics. Of these kinases, the catalytic-subunit of cAMP-dependent Protein Kinase A (PKA-C) has been a benchmark for the study of conserved features of eukaryotic protein kinases [2-4]. This was one of the earliest kinases discovered [5], the first to have recombinant prokaryotic expression [6], the first to have its structure solved using X-ray crystallography, the one used to evaluate the kinetic mechanism of all kinases [7] and more recently extensively studied using NMR spectroscopy. Using PKA-C as a prototype for the entire kinome much has been learned about the chemical mechanism, regulation and assembly of active protein kinases.

Despite such outstanding work, there is much we still do not understand about protein kinases. The most significant issue is simply that a static structural perspective is insufficient to explain the function of not only PKA-C, but of enzymes in general. There have been many structures of PKA-C with various ligands and mutants but the structures are unable to provide a defined answer for the functional change. A novel example of this is in the work involving the Tyr204Ala mutant of PKA-C. This mutant had been found to be a mutant that was fully assembled and properly regulated but lacked catalytic activity [8, 9]. The crystal structure of this mutant was identical to the wild type

enzyme, and in this author's opinion could not explain the loss of activity [10]. Furthermore there are almost no structural studies of kinases with their substrates. The difficulty of such was explained elegantly in a recent review by the late Louise Johnson, who emphasized the weak affinity of substrates to kinases hampers the ability of study them using X-ray crystallography [11]. Much of the crystallographic work studies the regulation of protein kinases but their structural interaction with substrates is largely guessed. Cooperativity is a universal biothermodynamic phenomenon that allows for protein function that otherwise wouldn't exist. Extensive structural and spectroscopic studies have revealed the allosteric nature of protein kinases [12, 13]. What is the relationship between cooperativity and allostery in protein kinases is still largely unexplored.

The difficulties presented here have already been discussed at length by leaders in enzymology, and succinctly summarized by Hammes and Benkovic [14]. A modern view of looking at enzymes is to understand the free energy landscape and how enzyme toggles between different states along the landscape. This view contrasts with the crystallographic view which sees enzymes as toggling between a few static states much like bad 1980's animation, but rather as fluid, flexible, cooperative and almost life-like entities (similar to the stunning animation from a Miyazaki film). As such studying molecular motion and the free energy of their states is essential for a critical understanding of enzyme function. Nuclear magnetic resonance (NMR) has emerged as the most widely used experimental tool to study protein dynamics due to its ability to probe a wide range of timescale at atomic resolution. Already several outstanding works have been performed demonstrating that enzyme dynamics are correlated with function [15-17], although the relationship between protein dynamics and catalysis remains a hotly debated topic [18, 19]. However, experimental, evidence demonstrates that

enzymes exist in a series of states; the free energy landscape and dynamically toggles between different distributions of states. Understanding the role of these dynamics and the free energy landscape remains an outstanding challenge for protein kinases.

The overall goal of this thesis is to understand the conformational landscape, dynamics and cooperativity present in protein kinases by using PKA-C as a representative enzyme. I have accomplished this work by utilizing two different techniques; NMR spectroscopy and isothermal titration calorimetry (ITC). NMR spectroscopy was used to define the conformational landscape of PKA-C by using backbone and methyl side chain chemical shifts (Chapter 6, 7, 9, 10). The conformational dynamics of each of the states have been studied by using relaxation studies (Chapters 7,9). The role of binding cooperativity was studied extensively using ITC for mutants (Chapter 7, 9) as well as for different nucleotides and ATP-competitive inhibitors (Chapter 10).

In chapters 1-3 I will outline the background and theory on PKA-C, cooperativity, binding using isothermal titration calorimetry (ITC) and solution state nuclear magnetic resonance spectroscopy (NMR). The following chapters consist of reprints with permission of the following per-reviewed articles, where I was involved in:

Chaper 4: "FLAMEnGO 2.0: an Enhanced Fuzzy Logic Algorithm for Structure-Based Assignment of Methyl Group Resonances." Chao FA, **Kim J**, Xia Y, Milligan M, Rowe N, Veglia G. (2014) *Journal of Magnetic Resonance.* 245:17-23

Chapter 5: "A Semi-Automated Assignment Protocol for Methyl Group Side-Chains in Large Proteins." **Kim J**, Li G, Wang Y, Veglia G. (2015) *Methods in Enzymology* (submitted)

Chapter 6: "NMR Mapping of Protein Conformational Landscapes using Coordinated Behavior of Chemical Shifts upon Ligand Binding." Cembran A, **Kim J**, Gao J, Veglia G. (2014) *Physical Chemistry Chemical Physics*, 16(14);6508-18

Chapter 7: "Synchronous Opening and Closing Motions Are Essential for cAMP-Dependent Protein Kinase A Signalling." Srivastava AK, McDonald LR, Cembran A, **Kim J**, Masterson LR, McCLendon CL, Taylor SS, Veglia G. (2014) *Structure*, 22(12);1735-43

Chapter 8: "Mapping the Hydrogen Bond Network in the Catalytic Subunit of Protein Kinase A using H/D fractionation factors" Li G, Srivastava AK, **Kim J**, Taylor SS, Veglia G. (2015) *Biochemistry*, 54(26);4042-49

Chapter 9: "Dysfunctional conformational dynamics of protein kinase A induced by a lethal mutant of phospholamban hinder phosphorylation." **Kim J**, Masterson LR, Cembran A, Veradi R, Shi L, Gao J, Taylor SS, Veglia G. (2015) *Proc Natl Aca Sci USA*, 112(12);3716-21

Chapter 10: "Uncoupling Catalytic and Binding Functions in the cAMP-Dependent Protein Kinase A." **Kim J**, Walters MA, Taylor SS, Veglia G. (2015) (submitted)

Chapter I

Overview of the catalytic subunit of the cAMP-dependent Protein Kinase A

1.1 Architecture of PKA-C

The protein kinase family is a large and diverse family of enzymes that regulate almost all facets of cellular signaling. Over 500 kinases have been discovered, including pseudo-kinases that share the same fold but are catalytic inactive, and the kinome comprises of 2% of the human genome [1]. Despite their diversity in sequence and regulation they are all share a highly conserved catalytic core. The sequence homology has been described initially by Hanks and Hunter where they aligned all available kinase sequences available [20] totaling 65 at the time. They identified several key residues that were invariant through all kinases and several sequence "subdomains" that are conserved through the kinome. The residues Gly52, Lys72, Glu91, Asp166, Asn171, Asp184, G186, E208 and R280 of PKA-C were found to be completely conserved while residues Gly50, Val57, Phe185, Asp220, and Gly225 were highly conserved. These residues were believed to be critical for catalysis and the subdomains identified are now known as the catalytic core of the kinase.

To understand the overall architecture of the catalytic core the first crystal structure of PKA-C, and soon after other protein kinases, revealed the arrangement of the subdomains and the invariant residues [21, 22] (**Figure 1.1**). The structure is bilobal with ATP sandwiched deep within a hydrophobic core between the small and large lobes. The small N terminal lobe has largely β-sheet character with a few helices, and is responsible for the binding of nucleotide. The highly conserved glycine rich loop (Gly-X-

Gly-X-ϕ-Gly, where ϕ is an aromatic amino acid) containing Gly52 and Gly50 was identified as having a classic Rossman fold, positioning the phosphates of ATP for catalysis. Two other conserved residues, Lys72 and Glu91 were arranged in salt bridge with each other and positions the α-β phosphates in the active site. The large lobe is primarily helical, extending out to Arg280 in the primary sequence of PKA-C. These contain many important residues for substrate positioning and, later, integrated signaling within the kinase [13]. The conserved Asp184 coordinates with Mg^{2+} ions and is part of the conserved DFG loop including Phe185 and Gly186 which is now known to be highly critical in defining active and inactive states of kinases [23, 24] . A loop was also found which contains the invariant Asp166 (which orients the hydroxyl acceptor for catalysis) and Asn171 (which helps coordinate Mg^{2+} in the active site) and is now coined the catalytic loop [2]. Also one of the phosphorylation sites required for activity, T197, was found and the loop it resides in is called the activation loop. The last two conserved residues, Glu208 and Argy280, were found to form a salt bridge together, connecting the APE motif of active site to the X and XI subdomains.

Outside of the conserved catalytic core, two additional motifs were discovered in PKA-C. The first is an N-terminal helix, αA, comprising of approximately 40 amino acids that sits adjacent to αC and αE and a myristoylation group on the N-terminus. The exact role of these residues in catalysis are unknown but have been proposed to help link the N-and C-lobes together [25]. The C-terminal tail contains the last sixty amino acids and wraps around the kinase from the bottom of the C-lobe all the way up behind the C-helix. Although this C-terminal tail is not shared between all kinases, these have been found to be the hallmark of the AGC kinase family [26].These comprise of a phosphorylation site, Ser338, along a conserved motif, as well as two phenylalanines (Phe347 and Phe350) that are highly conserved within the family [27].

1.2 Substrate Specificity of PKA-C

The initial *in vitro* studies on cAMP-dependent protein kinase A (PKA) seemingly displayed a lack of substrate specificity. For example it was known that a denatured fragment of chicken egg white lysozyme was a substrate for PKA-C [28] but not the folded protein. As of 2001 there are over 100 unique substrates for PKA [29] and more still are being discovered today. For example, the phosphorylation on Serine 16 of Phospholamban was discovered by stimulating intact ventricles with Isoproterenol (a β-adrenergeic receptor agonist) and undergoing tryptic digest of the resultant protein [30]. Chemical determinants for substrate specificity of PKA were investigated by using peptide fragments of known *in vivo* substrates. The first indication of the importance of the local primary sequence was discovered in a work by Kemp and Krebs. The Michealis-Menten kinetics of peptide fragments of variants of β casein and peptide variants of chicken egg white lysozyme pointed toward the importance of arginine near the primary sequence [31, 32]. Soon, after a synthetic peptide fragment corresponding to seven amino acids in the phosphorylation site from porcine liver pyruvate kinase was found to have the identical kinetics as the full length protein [33] with an apparent K_m of 16 μM and a V_{max} of 20 μmol·min^{-1}·mg^{-1} and This peptide, Leu-Arg-Arg-Ala-Ser(P)-Leu-Gly (**Figure 1.2**), is now commonly called Kemptide. A systematic study of the amino acids in the linear sequence demonstrated that two basic residues, P-2 and P-3, from the phosphorylation site were required for optimal K_m and V_{max}. These residues could also be substituted by other basic residues, namely with Lys, but only Arg gave optimal K_m. Deletion of the Leu after the phosphorylation site resulted in negligible kinetics, indicating that a hydrophobic residue in the P+1 site gave optimal kinetics. Finally the kinetics of various peptide fragments were compared with phosphorylase kinase. Peptide fragments specific to PKA were not for phosphorylase kinase and vice versa.

These works founded idea that the linear sequence of the protein is the primary determinant of kinase substrate specificity. Furthermore, the determinant of substrate specificity was from two basic residues neighboring the phosphorylation site.

The serendipitous discovery of an inhibitor of PKA was discovered by co-purification of PKA from crude skeletal muscle extracts [34]. This protein was found to inhibit the catalytic subunit with high affinity (K_i = 2.1 nM) competitive with respect to substrates and noncompetitive with respect to ATP [35]. Furthermore this protein was found to be independent of cAMP control, and was named Protein Kinase Inhibitor (PKI). The observation of the high propensity of Arg and competitive inhibition with respect to substrates hinted at a primary sequence similar to that of native substrates. This was confirmed by the discovery of a 20 amino acid fragment that recapitulated the high affinity binding of PKI, Thr-Thr-Tyr-Ala-Asp-Phe-Ile-Ala-Ser-Gly-Arg-Arg-Asn-Ala-Ile-His-Asp (PKI$_{5-24}$, **Figure 1.2**) [36]. This fragment found that PKI has the same determinant for substrate specificity with Kemptide, Arg-Arg-X-Ala-ϕ (ϕ as a hydrophobic residues), with the same high affinity as the full length protein [37]. The contribution to inhibition by different amino acids was systematically investigated using variants of PKI$_{5-24}$ [38, 39]. Although several residues were identified as important for binding, two in particular were discovered as essential for high affinity binding. The Arg that is P-6 to the phosphorylation site is a critical residue for inhibition (K_i changed from 57 nM to 0.36 μM upon mutation of Arg15Lys for a truncated form of PKI$_{5-24}$) [38] and is also shared in other substrates. Also the Phe10 residue makes a significant contribution to affinity (K_i from 3.1 nM to 270 nM) [39]. Further investigation on this site using other hydrophobic and aromatic residues identified this region as interacting through aromatic binding to a hydrophobic cleft [40].

8

When the first crystal structure of PKA-C, complexed with ATP and PKI$_{5-24}$, was solved, the mechanism in which the critical residues for substrate specificity was uncovered [21] (**Figure 1.2**). The P-3 Arg makes electrostatic contacts with Y330, E127 of the small lobe and the hydroxyl group of ATP while the P-2 Arg makes completes the electrostatic node created by Y204, E230, and R133. The structure suggests that the two basic residues "latch" onto each lobe of the kinase and bring the active site together for catalysis. The hydrophobic residue at the P+1 position makes contacts with L205 and L198 making a small hydrophobic pocket (Section 1.4). The other two residues, the P-6 Arg from PKI$_{5-24}$ makes an electrostatic bridge with E203 and the P-11 Phe encounters aromatic π -π stacking with F239. Overall the P-2 and P-3 Arg requirement for catalysis is uniquely positioned to bring the lobes together and facilitate catalysis. The P+1, P-6 and P-11 residues are present for allow for high affinity binding to the kinase.

1.3 Chemical Mechanism of PKA-C

As one of the first kinases isolated and characterized, the kinetic mechanism of PKA-C has emerged as the model for catalysis by a protein kinase [7] and is still the most well catalytically characterized kinase. The first systematic study of the mechanism of PKA-C was first performed by Cook et. al. in 1982 [41] by using an enzyme coupled activity assay that is still widely used today. A series of initial velocity studies were performed using ATP and Kemptide as the substrates and ADP and phospho-Kemptide (Kemptide with the serine phosphorylated) as competitive inhibitors. It was concluded the products bound in a random bi-bi mechanism. After phosphorylation, the release of products was sequential, first the peptide followed by ADP. It was also found that high concentrations of Mg^{2+} was inhibitory and PKA-C possessed a secondary Mg^{2+} binding site, with an estimated K$_d$ of 2-3mM. This K$_d$ would later be confirmed by competitive fluorescence measurements [42].

Soon this mechanism was challenged by Whitehouse and Walsh who, along with competitive inhibition by ADP and phosphor-Kemptide, used two dead-end inhibitors, ATPγN (5'-adenylimidodiphosphate) and PKI [43]. The paper used characteristics of PKI; was shown to be a competitive inhibitor to Kemptide but noncompetitive with respect to ATP and required ATP, not ATPγN, for high affinity [44]. From the product inhibition pattern (with ADP being competitive with ATP varied) and dead-end inhibition (the observation of PKI with respect to ATP was found to be uncompetitive rather than noncompetitive), the authors proposed an ordered bi-bi mechanism in which ATP binds first, followed by binding of substrate (for catalysis) or PKI (for inhibition). This discrepancy between the two mechanisms existed. This was later resolved by discovering that the true pure mechanism was random bi-bi however PKA-C preferentially binds first to ATP [45] (**Figure 1.3**). This has been supported by subsequent binding experiment using NMR spectroscopy which showed that ATP has over an order of magnitude higher affinity for the apo enzyme compared to Kemptide [12].

All protein kinases require Mg^{2+} to perform catalysis. In the structure of PKA-C there are two Mg^{+2} binding sites that have been identified (**Figure 1.4**). The first, chelated between the β-γ phosphates and Asp184, is considered the primary Mg^{2+} binding site. This ion is visible under low concentrations and is believed to bind with ATP. The second site, between the α-γ phosphates and held by Asp184 and Asn171, is only visible under high concentrations. This secondary site has an estimated K_d of 2.8 mM [42]. As alluded to earlier, under high Mg^{2+} concentrations the k_{cat} decreases four fold, however, this is accompanied by a decrease of the K_m of ATP (with the K_m of Kemptide unaffected) [41, 46]. The moniker of "inhibitory" for high concentrations of Mg^{2+} is misleading as the rate under low ATP concentrations is higher due to the offsetting

lowering of the K_m. The molecular details of Mg^{2+} during the catalytic cycle were recently elucidated through using a high affinity substrate derived from PKI_{5-24}, PKS_{5-24}, (**Figure 1.2**) and ATPγN. The Michealis complex, partial phosphorylation and product complex were isolated in crystal structures [47], providing snapshots of the chemical steps. In the structures the Michealis complex and partial phosphorylated state both have Mg^{2+} present in the structure. However, with the product complex the Mg^{2+} in the first site is absent, suggesting that the removal of this Mg^{2+} is required prior to the rate limiting removal of ADP. These were predicted by a transition path ensemble study which demonstrated that Mg^{2+} acts as a linchpin for ADP, requiring to be removed first before ADP is released [48]. All of these observations would suggest that Mg^{2+} acts as a catalytic base, however QM/MM calculations demonstrate that this is not the case, rather Mg^{2+} serves to position the phosphates for transfer [49]. All of these observations conclude that Mg^{2+} plays a critical role in phosphoryl transfer and the turnover of the enzyme.

The determination of the chemical step and the rate limiting step was initially studied using viscosogens to measure the effect of viscosity on k_{cat} and k_{cat}/K_m. The principle lies in the assumption for a bimolecular event viscosity should dramatically affect the kinetic value while a unimolecular rate, such as phosphoryl transfer would be unaffected [7]. Viscosity experiments varying Kemptide concentration was analyzed using a simplified kinetic mechanism (**Figure 1.3**). It was found that the apparent second order rate, k_{cat}/K_m was relatively unaffected by viscosity while k_{cat} was full affected by viscosity [50]. These results suggest that Kemptide binds in a rapid equilibrium fashion, unaffecting the observed rate limiting step. The rate limiting step was implied to be the dissociation of ADP under high concentrations of Mg^{2+} due to the full viscosity effect. Given the low K_m for Kemptide (K_m = 31.1 µM [9]) compared to the K_d of Kemptide (K_d

~200 μM [43]). This suggests that the chemical step is very fast compared to the dissociation of ADP.

Although application of viscosity to determine the rates were very successful, the assumption that unimolecular events are unaffected by viscosity is often incorrect. Protein conformational changes are strongly dependent on solvent environment and would also be affected despite being unimolecular. Also, these measurements only give an upper limit to the chemical step. Consequently, direct measurement of the chemical step was performed by using pre-steady-state quenched flow techniques. The data is marked by a burst phase, representing the first turnover of the enzyme, followed by a linear phase which shows the steady-state rate. Application of quenched flow to PKA-C gives a value of $k_{chem} = 500 \pm 60$ s^{-1} [51] and a measured $k_{cat} = 21 \pm 1$ s^{-1}. For a low affinity substrate, such as Kemptide, these studies demonstrated that the phosphoryl transfer is extremely fast and is solely rate limiting with the release of ADP. With other higher affinity substrates this is less so. A study using a fragment of PKS$_{5-24}$ (amino acids 14-22) found that ADP release was only partially rate limiting [52]. Due to the high affinity of this substrate, it was suggested that the mechanism of release was first initiated by the release of ADP and followed by the phospho-peptide. However, most *in vivo* substrates exhibit low affinity to kinases [11], suggesting that the mechanism devised by using Kemptide reflects the native mechanism.

All the pre-steady-state kinetics that was discussed involved studying the mechanism of phosphoryl transfer under high (10 mM) Mg^{2+} concentrations. Once the Mg^{2+} concentration is lowered to more physiological conditions the kinetic picture is not as simple. At low Mg^{2+} concentrations, when PKA-C is pre-equilibrated with ATP, the burst phase is unaffected. However when the reaction is initiated using ATP, there is a marked attenuation of the burst phase that was independent of ATP concentration [53].

12

The authors interpreted this delay with a conformational change with ATP binding preceding phosphoryl transfer. The same authors, in another work, studied the effect that Mg^{2+} had on the rate determining step: ADP release [54]. Under low Mg^{2+} concentrations, the burst phase was sigmodal prior to the linear phase, which is indicative of multiple rapid steps in the burst phase. This was due to a conformational change of the protein which was partially rate limiting under these conditions [54]. These kinetic trapping experiments with nucleotides illustrate the subtle interplay between nucleotide and the Mg^{2+} ion. Under low Mg^{2+} concentration, kinetics that is not associated with a chemical step were observed, most likely from conformational changes during the enzymatic cycle These conformational changes are very likely to be present under high Mg^{2+} concentrations but likely too fast to be observed using pre-steady-state kinetics. Indeed, when NMR spectroscopy was applied to study the effect of Mg^{2+}, a marked reduction of conformational dynamics was found under high Mg^{2+} conditions [55].

Overall the steady state kinetics for PKA-C indicate that the enzyme is most likely is saturated first with ATP, especially given the high concentration of ATP *in vivo* and the low affinity of most native substrates, followed by substrate binding. The phosphoryl transfer step is very fast, allowing for a very efficient enzyme resulting in a low K_m value, and with rate limiting turnover from the dissociation of ADP. However when placed in lower Mg^{2+} concentration the picture is more muddled. The pre-steady-state results predicted that significant conformational changes accompany nucleotide binding and release in the enzyme. These would later be validated by NMR studies that highlight the flexibility of PKA-C when nucleotide is bound [56, 57].

1.4 Major Conformational States of PKA-C during the Catalytic Cycle

By identifying conformational changes that occur throughout the catalytic cycle, one would have a structural basis of catalysis and substrate specificity. Snapshots of the three main structural states of PKA-C have been identified using X-ray crystallography [2, 58] and they show that PKA-C does not undergo large significant conformational changes during its catalytic cycle. This contrasts with other kinases which have significant conformational changes upon activation by a regulatory subunit or phosphorylation [24], that assembles the kinase into an active conformation (Section 1.5). Rather the conformational changes described as an "open" to "closed" arrangement of the active site. The extent between these states is described by the distance between Ser53 of the glycine rich loop and Gly186 of the DFG loop [2]. The open state, where ATP is fully accessible for the active site cleft, has a distance between Ser53-Gly186 of 13.4 Å [59]. In the closed form the glycine rich loop folds over the phosphates in ATP and the distance between Ser53-Gly186 is at a minimum at 10.4 Å. During catalysis the enzyme toggles between these two extremes and have been captured crystallographically, the intermediate state with nucleotide binding being an example [60]. Along with the glycine-rich loop, the C-terminal tail also undergoes a large spatial shift from the *open* to *closed* transition while moving with the small lobe. For instance, Tyr330 moves from 10 Å from the active site in the open state with the apo enzyme to 3 Å in the closed state, coordinating the P-3 Arg from the substrate.

Over thirty structures of PKA-C have been solved with various inhibitors, pseudo-substrates, substrates and mutations after the initial structure, and are too numerous to discuss in detail [2, 58, 61]. Only a two of the structures and their importance for

catalysis will be discussed here. The structural consequences of important residues will be explored in section 1.5. A structure with ADP, aluminum fluoride and using PKS$_{5-24}$ as a substrate (PDB: 1L3R) provided molecular details of the transition state of phosphoryl transfer [62]. Although PKS$_{5-24}$ is not a native substrate, the high affinity allows for this substrate trapped in the crystal lattice [63, 64]. The overall conformation is nearly identical to the fully closed conformation defined by ATP and PKI$_{5-24}$ (PDB: 1ATP) with a root mean square deviation of 0.36 Å. Based on enzyme-transition state complementarity, PKI traps PKA-C in a transition state analogue. This is further supported by the requirement of ATP for high affinity binding of PKI and the same sequence specificity of native substrates. As such, after ATP and substrate binding only minor side-chain rearrangements are necessary for catalysis. The carboxylic acid of Asp166 swings and orients the hydroxyl acceptor for catalysis while the backbone of Ser53 and the amino group of Lys168 follows the γ-phosphate during catalysis. The totality of these observations implies that the active-site is pre-organized immediately prior to catalysis, but conformational changes to reach such a state.

Another structure, depicting the kinase after phosphoryl transfer has also been isolated using ADP and PKS$_{5-24}$ phosphorylated on Ser21 as the product peptide [65] (PDB: 4IAD). Interestingly this state adopts the same overall conformation as the closed form with ATP and PKI$_{5-24}$ (PDB:1ATP) with a distance of 10.7 Å between Ser53 and Gly186 (Figure 1.6). These structures show the overall architecture of the enzyme does dramatically change between just prior to phosphorylation, during phosphorylation and immediately after. However there are subtle changes in the side chain orientation with the product complex. Lys168 no longer interacts with the γ-phosphate and Asp166 is no longer positioning the acceptor hydroxyl group. Ser53 interacts with the transferred phosphate group with backbone carbonyl group, not the backbone amide in the closed

form (PDB:1ATP). From these structures we can confirm structurally there are only minimal changes, largely resulting from reorientation of critical side-chain groups in the active site.

1.5 Function of critical residues of PKA-C and insights into kinase function

After the discovery of the overall structure of the catalytic core of the kinase from the first crystal structure, significant work has been performed to ascertain the function of catalytically important regions and highly conserved motifs [20, 66]. Here we will first break the discussion down between specific important amino acids in the small and large lobe of the conserved catalytic core, then followed by a discussion of the N and C-terminus. This will be concluded by a discussion of the allosteric assembly of the hydrophobic core of the protein kinase and how assembly of this produces an active protein kinase.

1.5.1: Small Lobe

As described earlier the G-X-G-X-ϕ-G motif is nearly completely conserved amongst all known protein kinases. Structurally these position the phosphates in the active-site (**Figure 1.7**) and kinetic studies have looked at the role these have in catalysis [67]. Gly50 and Gly52 were found to be critical for the apparent affinity of ATP (K_m) with an increase of over a factor of 10 with a mutation to Ser. Although the Gly-rich loop dies not directly interact with the substrate, these mutants were also accompanied by a decrease in K_m and K_d for Kemptide. The rapid phosphoryl transfer step was also altered with mutations on the Gly residues. The Gly55Ser mutation the burst phase was attenuated with respect to the wild type enzyme and completely abolished for the Gly50Ser and Gly52Ser mutants. These observations suggest that the glycines are required for a highly flexible loop to help position the phosphates and promote the

16

hydrogen bonding with Ser53. Subsequently another study focusing on the role of Ser53 was undertaken [67]. Mutation of Ser53 to Gly or Thr did not dramatically alter the steady-state kinetics, nucleotide and inhibitor binding, indicating the side-chain of Ser53 does not have a catalytic role. Rather with substrates where Thr is the acceptor, the Ser53Gly mutant exhibited identical kinetics as with substrates with Ser as the acceptor. In all the role of the side-chain is not catalytic but demonstrates a level of substrate specificity and also must remain flexible to allow for the backbone amide to hydrogen bond with the γ-phosphate.

Lys72 is universally conserved amongst all active kinases, making a highly conserved salt bridge with Glu91 and the α-β phosphates of ATP (**Figure 1.7**). The loss of this residue is a common feature for pseudo-kinases, proteins that share the same homology as active kinases and functions but lack catalytic activity [68, 69]. Initially thought to be evolutionary dead-ends, these have found to serve critical roles in cell signaling as scaffolds to modulate kinase activity and anchor catalytic domains, direct competitors for critical substrates, and to integrate different signaling pathways. A systematic study of the role of Lys72 in PKA-C has been carried out using a Lys72His mutant that is phosphorylated in the activation loop by phosphoinositide-dependent kinase-1, PDK-1 (to be discussed more in the next section). This mutant variant of PKA-C was shown to bind to ATP, substrates and endogenous inhibitors of PKA-C once phosphorylated on the activation loop. Hence the loss of Lys72 does not significantly impact the assembly of the kinase and can act as a pseudo-kinase. Interestingly the Lys72His mutant even with phosphorylation on the activation loop is still less thermostable and more dynamic than WT enzyme. The correlation of these observations to the role of the residue is still unknown, but hints that Lys72 may do more than simply position ATP for catalysis.

1.5.2: Large Lobe

The large lobe contains several residues that were either highly conserved or hypothesized to be involved in substrate binding. Phosphorylation of protein kinases is a highly conserved mechanism for controlling kinase activity and can be found in all families of protein kinases [11]. Especially phosphorylation on the activation loop (which spans from Ala188 to Thr197 in PKA-C) is highly conserved amongst all eukaryotic protein kinases. When one glances at the positioning of phosphorylation at Thr197 in the structure of PKA-C, we can observe that phosphorylation links together the activation loop through Thr195 and Lys168, αC through His87 and the catalytic loop with Arg165 (**Figure 1.8**). Thr197 is auto-phosphorylated by PKA-C [70] or by PDK-1 [71]. The mechanism for regulation of PKA-C via activation loop phosphorylation *in vivo* is unknown. However, PDK-1 is the enzyme that phosphorylates on the activation loop for the entire AGC kinase family, with a conserved Phe-X-X-Phe motif at the C-terminus coined the hydrophobic motif [27]. This motif is required for phosphorylation by PDK-1 and has been modeled as being recruited by PDK-1 for phosphorylation of kinase substrates [72, 73]. A PKA-C variant with Arg194Ala has been produced that knocks out auto-phosphorylation but may be phosphorylated by PDK-1 [74]. Biophysical characterization only revealed that phosphorylation is required for function, which was easily predicted from studies on other kinases [24], but did not reveal much of why. However once a structure of Arg194Ala was released, the function of phosphorylation was more evident [75]. This structure revealed that loss of phosphorylation resulted in a disordered activation loop and DFG loop, explaining the loss of catalytic function. Furthermore, as will be detailed further, the R-spine was also found to be broken in the structure. The loss of catalytic function was also examined using pre-steady-state kinetics and no burst kinetics observed for the mutant. The residual phosphorylation rate

observed in the phosphorylation null mutant is from a conformational change of the enzyme moving from a DFG out (inactive) to DFG in state[24, 76].Future work with this phospholation-free variant would be to examine whether the conformationally selective inhibitors would be selective for those "DFG out" states with PKA-C, as well as with Src and other tyrosine kinases [76].

Along with examining phosphorylation on the activation loop, it was discovered that the sequence of the peptide positioning loop, or P+1 loop (Leu198-Glu208), is critical for recognition by PDK-1 [8]. As discussed earlier, Glu208 is highly conserved amongst all protein kinases. A systematic study of the role of these residues was taken by examining phosphorylation on Thr197, their activity and their ability to bind to the regulatory subunit RIIβ [8]. Gly200 and T201 were unable to auto-phosphorylate and consequently were unable to exhibit activity and regulation. Subsequent work demonstrated that, even with phosphorylation on Thr197, mutation of Gly200 and Thr201 abolishes activity [9]. Due to the consistency of these residues in the AGC kinase family and their proximity to the active site, these residues may be critical for substrate recognition for the AGC family of kinases. Indeed, mutations along this region have been recently discovered to be associated with onset of adrenal cushing's syndrome [77, 78]. However, the Tyr204Ala mutant was phosphorylated and exhibited binding to RIIβ, while was found to be an inactive kinase. This is a striking result since activation loop phosphorylation and regulatory subunit binding are hallmarks of an active protein kinase. When one observes the structure around Tyr204, there is a complex electrostatic network of interactions with Glu230, Arg133, Glu170 from the kinase and P-2 Arg from the substrate. These residues are not conserved through the kinome and may serve as a means of differentiating the substrate specificity of PKA-C from other kinases.

Due to its unique and the allosteric nature of the electrostatic node (aka not involved directly in assembly of the active site of the enzyme), Tyr204 and Glu230 has been the focus of directed investigation. The k_{cat} and K_m of ATP are not dramatically altered in the Glu230Gln mutant (only two fold lower). However the K_m for Kemptide is significnatly increased to 1.4mM and with a K_d of 4.6 mM. This is dramatically lower than the values for WT PKA-C (K_m = 31.1 μM and $K_d \approx$ 200 μM) [9], indicating that the altered kinetics are from dramatically reduced substrate binding. This hypothesis is supported by the crystal structure of Glu230Gln, which unexpectedly gave an apo structure even though it was grown in the presence of ATP and PKI$_{5-24}$ [79].

This is contrasted with Tyr204Ala mutant. Kinetically although K_m for Kemptide was increased by a factor of 10 (K_m = 341 $\pm$ 40 μM) there was dramatic decrease in k_{cat} (k_{cat} = 0.9 $\pm$ 0.5 s^{-1}), virtually making a dead kinase. This also is accompanied by a significant decrease of substrate affinity for Tyr204Ala (K_d of Kemptide was found to be 7.87 $\pm$ 0.7 mM). Unlike with the Glu230Gln mutant, it appears the dramatic decrease in turnover is not from the loss of the electrostatic contact, rather from the aromatic group from Tyr204. Mutation of Tyr204 to Phe retained k_{cat} of the WT enzyme. When the structure of Tyr204Ala bound with ATP and PKI$_{5-24}$ was solved (PDB: 1RDQ), it was evidente that the structure was identical to the WT structure (PDB: 1ATP) with RMSD of 0.4 Å^2 [10]. The NMR spectral signature for Tyr204Ala with respect to the WT enzyme in the apo, nucleotide bound and closed with PKI were also found to be virtually identical [12, 57]. Glu230 and Tyr204 appear to both affect catalysis through disruption of substrate binding (consistent with the notion that the large lobe is responsible for substrate binding), however the exact mechanism appears to be distinct. A temperature melting study of these mutants bound to ATP, PKI$_{5-24}$ only and to both ATP and PKI$_{5-24}$ was performed [80]. Glu230Gln had a similar melting temperature (T_m) to the WT

enzyme for the apo, ATP bound and PKI$_{5-24}$ bound states. However the synergistic increase in the melting temperature in the presence of both ligands was absent (T$_m$ for WT PKA-C was found to be 61.2 ± 0.5°C verses 53.5 ± 1.0°C for Glu230Gln). The melting data indicates that that Glu230 is a critical residue for modulating K-type binding cooperativity in PKA-C. For Tyr204Ala, the synergistic interaction between PKI$_{5-24}$ and ATP is maintained, however the T$_m$ is consistently lower with respect to the WT enzyme. This result pointed toward a change in dynamics for the loss of function. H/D exchange MS performed on both mutants. There was no change in dynamics for Glu230Gln mutant; however the Tyr204Ala mutant was significantly more accessible to solvent, indicating increased conformational dynamics. Consequently, Tyr204 is considered an allosteric "hot spot" for PKA-C, for modulating function through dynamics. As such this mutant has been the focus of several NMR relaxation studies to understand the link between dynamics and catalysis [12, 57].

The salt bridge between Glu208 and Arg280 is universally conserved through the kinome [81]. Structurally this connection links the active site, via the conserved APE motif at the end of the peptide positioning loop and the helical GHI subdomains through the αH-αI linker. The loss of this salt bridge results in Michealis-Menten kinetics that have 1/10th of the k$_{cat}$ and an apparent ATP affinity four times larger compared to the WT enzyme. Interestingly, substrate K$_m$ is identical to the WT. However structurally loss of this salt bridge did not significantly alter the structure, the only change were high B-factors found in the αH-αI linker [82]. The role of this conserved salt bridge is still largely unknown and more studies will be required to elucidate significance of this evolutionary conserved connection.

1.5.3: N and C-terminal Tails

The N and C-terminal tails of PKA-C are not part of the catalytic core shared amongst the kinome. It is largely believed that the presence of these two elements is what enables PKA-C to be a "constitutively active" kinase [11, 24]. The N-terminal of PKA-C largely consists of an α-helix buttressed next to αC and αE of the small and large lobe respectively and is capped by an N-myristoyl group. PKA-C from recombinant expression lacks the N-terminal myristoyl group but was shown to have identical activity and regulation as native PKA-C [6]. The only immediate biophysical impact that the N-terminal myristoyl group has is to provide thermostability. Recombinant incorporation of the myristoyl group with co-expression of N-myristoyltransferase (NMT) provided a means of expression of full mammalian enzyme to attach a eukaryotic post-translational modification in a prokaryotic system [83] and also confirmed the earlier work with regards to thermostability. The myristoyl group sits on hydrophobic pocket formed by Phe18, Phe100, Phe102, Tyr306, Trp302, Ile303 and Val15 as revealed by X-ray crystallography [22, 84] (**Figure 1.10**). Furthermore several studies have suggested that the myristoyl group plays a more subtle role in regulation of the kinase. Other proteins that are myristoylated, [85-87] demonstrate an affinity for membrane surfaces and the myristoyl group inserts into the membrane bilayer. This was first anticipated by using a peptide fragment of PKA-C with myristoylation [88] and was later confirmed with full length protein [89] using ^{2}H solid state NMR. The same study as well as a computational study [90] demonstrated the presence of interplay between Ser10 phosphorylation and myristoylation. Although Ser10 phosphorylation is not observed from tissue extracts, it is found in PKA-C from recombinant expression [70]. Using NMR it was demonstrated thatthe myristoylation group undergoes a transition from sequestered in the hydrophobic pocket ("myr-in") to solvent exposed ("myr-out"), where the myr-out state binds to membrane surfaces, allowing phosphorylation as a means to regulate membrane affinity. Similar switches have been found in other kinases as well [86]. Computational

simulations and NMR chemical shifts from the same studies also show that coupling between the αA and the active site occurs through several key residues centered on Trp30 (**Figure 1.10**). These experience correlated motions as seen through MD simulations and are suggested to be an allosteric hot spot. However, mutational studies on Trp30 gave a mixed picture compared to the computational work [91]. Trp30Tyr and Trp30Ala mutants did not exhibit altered kinetics from the WT enzyme, however had altered binding profiles with RI and RII regulatory subunits. In summary the role of the αA and myristoylation with regards to kinase function has been demonstrated to be important, but the exact functional role still remains to be elucidated.

Since the N-terminal segment of PKA-C is the most varied between different isoforms and is specific to PKA-C, a yeast two-hybrid screen using the first forty amino acids as bait was used to find novel interacting partners with PKA-C [92]. A small ~200 amino acid protein was found in a human fetal brain library and was coined as A-kinase interacting protein (AKIP). Immunoblotting results indicate that this small protein acts as a scaffold with PKA-C, interacting specifically to the N-terminal residues, and translocates PKA-C into the nucleus, independent of the regulatory subunit. Later AKIP was shown to be responsible for allowing for phosphorylation of NF-kB, the protein complex most critical for cytokine production and cell survival, on Ser 276 [93]supposedly by tethering NF-kB and PKA-C together [94]. Perhaps more interestingly, AKIP was found to be upregulated during cardiac stress, especially from oxidative stress. AKIP was found to interact with mitochondrial apoptosis inducing factor protein and together would decrease oxidative stress [95]. The discovery of this protein shows that the N-terminal helix allows for PKA-C to have distinct localization and function with respect to other kinases separate from the regulatory subunits and AKAP proteins. Especially with such scaffolding proteins, kinase function is enhanced and diversified.

23

Clearly more work has to be performed to understand the function of AKIP specifically, especially since there is no structure of this protein let alone a model with PKA-C. However these early results with AKIP indicate that scaffolding presents another coin for regulation and localization of kinases separate from their regulatory domains.

The C-terminal tail of PKA-C is comprised of approximately fifty amino acids and wraps around the kinase from the bottom of the large lobe all the way up to the back of αC. The C-terminal tail is conserved throughout the AGC kinase family [26]. There are functionally important residues along the C-terminal tail. The first is the Hydrophobic Motif with the sequence Phe-X-X-Phe. Earlier this was implicated in the importance for phosphorylation by PDK-1 and most other AGC kinases have a phosphorylation site immediately after the last Phe residue [27, 96] which is required for activity, however PKA-C does not contain this (**Figure 1.8 and 1.11**) . These residues sit on a hydrophobic pocket formed by αC, β4 and β5 of the small lobe and has been used as an allosteric druggable target for other kinases [97, 98]. Mutational studies have shown that Phe350Ala abolishes activity and Phe347Ala demonstrated significantly reduced activity, keying their role for a functional kinase [99]. Structurally these phenylalanines may help hold the significant αC in place to position critical amino acids for catalysis. Another set of aromatic residues that were unexpectedly critical for function were Tyr330 and Phe327 in a region of the C-terminal tail called the active-site tether [26]. In the *Open* conformation these residues are not attached to the kinase, and unobserved in the crystal structure. Upon nucleotide binding in the intermediate and closed state, these are found buttressed against the hydrophobic adenine ring of ATP. The hydroxyl side chain of Tyr330 makes a salt bridge with the substrate and loss of this interaction makes a slightly less active kinase (a six fold larger K_m for Kemptide) however loss of the aromatic significantly reduces activity [100]. The loss of Phe327 has a more dramatic

effect, with a fifty fold loss of activity. A structure solved with the Phe327Ala mutant confirmed that without the hydrophobic interaction the active-site tether is very dynamic (with very high B-factors) [101]. The structure also gave a few hints on the role of Phe327 in catalysis as well. The kinase was found in the open conformation and the nucleotide is not positioned properly like in other structures of PKA-C. No observation of density for two critical elements for catalysis, Mg^{2+} and the catalytically critical Lys72 suggests that these elements are either dynamic (in the case of Lys72) or not-present. The active-site tether element of the C-terminal tail actively engages in positioning of substrates in the active site, both through Tyr330 and Phe327, allowing for efficient catalysis.

A phosphorylation site also resides on Ser338 and is auto-phosphorylated during the maturation cycle in a *cis* mechanism and is required prior to Thr197 phosphorylation [102, 103] and is one of the two phosphorylation sites that have been found *in vivo* from tissue extracts. This phosphate makes electrostatic contacts with the side chains of Arg336, Asn340, and Lys342, making a small turn on the top of the small lobe called the turn motif [26]. In other kinases phosphorylation at this site is critical for association with scaffolding proteins [104, 105] Loss of this slightly reduces function and significantly reduces the thermostability (T_m reduced by approximately by 5°C) [99]. However if phosphorylation at this site is blocked during while PKA-C is maturing in the ribozyme no active kinase is produced [102], indicating that the importance of this phosphate isn't kinetic rather is a key step in the final maturation of the kinase

1.5.4: Hydrophobic Assembly of Kinase Core

Many residues and different motifs amongst all the different structural elements have been studied as discussed. Although many of these explain how kinases perform

chemistry, this does not explain the regulation of kinase activity through conformational changes. The catalytic core is highly conserved throughout the entire kinase family. Typically, kinases are usually in an "off" state where there is a conformational change from the defined catalytic core found from PKA-C. After a biochemical trigger, either by phosphorylation or by binding of another protein, the catalytic domain undergoes a conformational change and adopts a full catalytic active conformation in the "on" state with a conformation almost identical to that of PKA-C [24]. Two classic examples of this would be from the tyrosine insulin receptor kinase (IRK) [106, 107] and cyclin dependent kinase-2 (CDK2) [108, 109]. In IRK in the inactive form the activation loop slides into the active site, blocking both substrate and ATP binding, dislodges the αC helix and breaks the conserved Lys72-Glu91 salt bridge. Upon phosphorylation on three Tyr residues in the activation loop, the activation loop is pulled out, the active site is available for substrates and the conserved salt bridge is restored. In the case of CDK2 the αC is rotated outward from the kinase and is shifted away from the catalytic domain with respect to PKA-C. This breaks the conserved Lys72-Glu91 salt bridge required for activity. Cyclin binds directly on aC and pushes the helix back into a similar conformation found in PKA-C and creates an active kinase. The mutational and structural studies outlined so far does not explain why the conformation of PKA-C is that of an active kinase.

In an important bioinformatics work performed by Kornev et. al. [13, 110] looked at not the primary sequence of protein kinases, but the similarity of their spatial structure and motifs and their involvement of the motif by an algorithm called "local spatial patterns". Comparing structures from all the kinase families, they discovered many residues and motifs that were highly conserved but not appreciated before. From the analysis they authors proposed a series of hydrophobic "spines," who's assembly were

required for an active kinase (**Figure 1.12**). The regulatory spine, or R-spine, comprises of residues Leu106, Leu95, Phe185 and Tyr164 of PKA-C. Completion of the R-spine requires phosphorylation on the activation loop and assembles the R-spine by making the critical electrostatic bridge with His87 (**Figure 1.7**). Another spine, the catalytic, or C-spine, is comprised of residues Ala70, Val57, Leu172, Leu173, Ile174, Met128, Met231 and Leu227 of PKA-C. This motif is completed by the binding of the adenine ring of ATP. These two signaling elements are linked together through αF, where Asp220 tethers the R-spine to αF. These two spines traverse the two conserved lobes and mediate signaling between the nucleotide and substrate. Subsequent bioinformatics and biochemical work have expanded the spine concept and suggested the "shell" motif which surrounds the R-spine. Mutagenesis and activity assays show that these residues, with the R-spine, are required for a functional kinase [111]. As more work on the role of conserved hydrophobic core residues are performed, it is expected that more conserved motifs that expand on the hydrophobic spine will be discovered, not only in protein kinases but other signaling enzymes as well.

The proposal of the hydrophobic spines was initially proposed by a structural analysis without any biochemical data. Subsequently this has been shown to explain many aspects of inactive kinases. Two notable examples of the spines explaining kinase function can be with the mutant variant of c-Abl and c-Src kinase that exhibits resistance to imatinib (a Src kinase specific inhibitor that binds to an inactive conformation of the kinase) [112] and transformation of Raf kinases into pseudo-kinases that lacks ATP binding but perform signal cascades [113]. Imatinib is a kinase inhibitor that specifically binds to an inactive conformation of Src-kinase in the DFG out state [76]. In Src a Thr334Ile mutant, corresponding to a residue on the R-spine Shell motif, enhances the stability of the R-spine and stabilizes the active conformation of the kinase, hence

prevents imatinib binding. Mutations of this residue to glycine abolish activity and renders the kinase readily accessible to imatinib. With B-raf it was found that small molecular inhibitor paradoxically activates mitogen-activated protein kinase (MEK) and extracellular signal regulated kinase (ERK) in cells [114, 115]. It was discovered that another kinase, kinase suppressor of Ras (KSR1), using the "inhibitor" dimerizes with and activates B-raf. This effect was also accomplished by a mutation on the C-spine on C-raf kinase (Ala373Phe, the equivalent mutation is Ala70Phe in PKA-C). This mutant could not bind ATP, hence could not perform catalysis, but still functioned as a scaffold by dimerization with other kinase domains and continued to activate signaling in cells [113]. These studies both illustrate the importance of both hydrophobic spines in order to have an active protein kinase. Misregulation can be achieved by mutation in either spine and result in kinases that are constitutively active, both in terms of catalytic activity and binding. Future work will use the hydrophobic spine concept in developing targeted therapy that targets allosteric sites that disrupt the formation of an active kinase.

1.6 Dynamic nature of PKA-C

As is clear from studies on specific conserved motifs and residues, a structural perspective from crystallography alone is insufficient to explain the function of many of the functionally critical elements. Despite the static pictures provided from crystallography, it has long been recognized that proteins are flexible entities stretching as far back from then equilibrium H/D exchange studies were available [116]. Nuclear magnetic resonance (NMR) has been the experimental technique of choice to study enzyme conformational dynamics due to its ability a wide timescale from ps to the s timescale [16, 117, 118] at equilibrium and its ability to extract quantitative dynamics. NMR and other techniques have highlighted the importance of flexibility to protein function. To date only a few protein kinases have been studied using NMR: catalytic

subunit of protein kinase A [12, 55, 56], Extracellular receptor kinase 2 (ERK2) [119], p38 kinase [120], and Abl-kinase [121, 122]. The paucity of kinases studied by NMR spectroscopy is reflective on the difficult biochemical requirement for high resolution NMR studies, often requiring recombinant expression in *E. coil.*, incorporation of ^{2}H, relatively high concentration and stability for assignment and relaxation experiments.

As well as structurally, PKA-C is perhaps most well characterized kinase by NMR spectroscopy. The three major forms of PKA-C; apo, nucleotide bound and ternary complex of PKA-C have been studied [55, 56] using the TROSY Hahn-Echo experiment [123] to measure their conformational dynamics in the μs-ms timescale (**Figure 1.13**). These studies showed the apo form is dynamic but uncommitted to catalysis. Once nucleotide binds the enzyme becomes highly dynamic. There is large conformational exchange in regions directly involved in phoshoryl transfer, such as the glycine rich loop, activation loop, DFG loop and peptide positioning loop, indicating dynamics in the μs-ms timescale. With the addition of PKI_{5-24} these conformational dynamics are quenched, locking the enzyme in the closed state. As predicted with pre-steady state kinetics, there are significant conformational changes associated with the nucleotide bound state. Since this is the primary state immediately before substrate binding, these dynamics are critical for substrate recognition. PKI_{5-24} locks the enzyme in the closed state most likely resulting from the high affinity of the peptide for the kinase.

As mentioned earlier, PKA-C phosphorylates over 100 substrates *in vivo* [29]. One of the substrates is the membrane protein Phospholamban (PLN). Phospholamban is a single pass membrane protein with a cycloplasmic domain and has an L shaped structure solved from NMR spectroscopy [124]. PLN regulates magnitude of Ca^{2+} reuptake into the sarcoplasmic reticulum that defines the rate of cardiomyocyte relaxation by inhibiting the apparently Ca^{2+} of the Sarcoplasmic Reticulum Ca^{2+} ATPase

(SERCA) [125, 126]. Once phosphorylated by PKA-C at Ser16 the inhibitory function of PLN is relieved, increasing the apparent affinity of Ca^{2+} of SERCA resulting in increased muscle contraction. Although PLN is primarily membrane bound, the cytoplasmic domain undergoes a structural transition from membrane bound (T state) to a solvent exposed conformation (R state) [56, 127, 128]. It is this R state which PKA-C is able to select and perform phosphorylation on PLN [129]. By using the cytoplasmic domain of PLN, mechanism of substrate recognition by PKA-C was studied using NMR spectroscopy. Unlike with PKI_{5-24}, PKA-C in a Michaelis complex with PLN was found to be highly dynamic in the μs-ms timescale [56]. With these states of PKA-C characterized, a general model for the dynamics for kinase activation was proposed. In the apo form the kinase is dynamic, but exhibits a signature that is uncommitted for catalysis. Upon nucleotide binding the dynamics become committed toward catalysis. These dynamics are used to drive substrate binding in a conformational selection mechanism and PKA-C remains dynamic to facilitate catalysis. PKI_{5-24} quenches the productive conformational dynamics and locks the enzyme in a closed conformation. By locking the enzyme in a transition-state like conformation, the inhibitor is also able to utilize the intrinsic free energy [130] provided by conformational dynamics, i.e. conformational entropy, for high affinity binding. Building off of these works we look forward for other kinases to be characterized extensively as well as further studies on PKA-C revealing kinetics of chemical exchange at atomistic detail.

While NMR spectroscopy is the method of choice for experimental determination of molecular motion, molecular dynamic (MD) simulations have been the primary method for investigating dynamics for many groups. As such the number of simulations performed on kinases are too numerous to discuss here, only a few works will be highlighted. An early example of the utility of MD simulations for understanding the

functional role of dynamics in proteins was applied to full length Src-kinase [131]. Src-kinase kinase consists of a catalytic core, an SH2 and SH3 domain. The kinase is typically kept in an inactive form by phosphorylation on Tyr527 that locks the SH2 and SH3 domains together and creates conformational changes that inactive the kinase core. Upon dephosphorylation, the SH2 and SH3 domains are free and no longer alter the kinase core, reassembling the active core of the kinase. Short (4ns) MD simulations were undertaken to understand how these three domains work together to create this molecular switch. In the inactive form with phosphorylation on Tyr527 at the C-terminal tail the SH2 and SH3 domains, the dynamics are coupled together. Upon dephosphorylation, the SH domains exhibit uncorrelated dynamics. The interaction of the SH domains with the C-terminal tail functions as a "snap-lock" mechanism to hold the kinase in an inactive conformation and this constraint is released upon dephosphorylation.

Traditional MD simulation technologies were able to only sample dynamics in the ns time regime. With modern computers this timescale has been extended out to the μs timescale with the current Anton computers [132]. Anton has been applied to PKA-C in its apo and nucleotide bound form to study the dynamics in the μs timescale and subsequently a community map analysis was performed [25]. A community map analysis looks at proteins as if they were structurally distinct regions that move in a correlated fashion. The work divided up the kinase into nine different "community maps", and performed a tentative assignment of the function of each of the communities of PKA-C based on decades of structural and biochemical studies on PKA-C. Interesting many of the conserved hydrophobic motifs, such as the R-spine, are split between several different communities and which communities contribute to each conserved motif changes upon ligand binding. Although this reflects the correlated motions that were

found in NMR relaxation studies, the difficulty of assigning functionality to each of the communities still remains a longstanding challenge and this methodology must be further developed and supplemented with biophysical experiments to elucidate biochemical meaning for each of the communities.

Chapter II

Theory and Application of Solution NMR Spectroscopy

2.1 The Semi-classical Bloch model

All atomic nuclei, along with their translational, rotational and vibrational states, experience a quantum mechanical state that has been denoted as spin. Although analogues to orbital angular momentum (i.e. electronic orbitals for bonding), spin has no classical basis. It has been observed that all nuclei, even paramagnetic molecules have a net spin, which is now known as nuclear spin. The existence of nuclear spin was first demonstrated by the Stern-Gerlach experiment performed in the early 20th century [133]. This nuclear spin exhibits a magnetic dipole defined by the following:

$$\boldsymbol{\mu} = \gamma \boldsymbol{I} \tag{2.1}$$

Where $\boldsymbol{\mu}$ is the magnetic dipole vector, $\boldsymbol{I}$ is the spin angular momentum vector and γ is the gyromagnetic ratio. In the presence of a magnetic field the magnetic dipole interacts with the field and acquires energy by the following:

$$E = -\boldsymbol{\mu} \cdot \boldsymbol{B} \tag{2.2}$$

In NMR spectroscopy, the direction of the static field is by convention designated along in the z-axis and in equilibrium, is the only magnetic field. As a result only the z-component of the angular momentum interacts with the magnetic field (B_0) and the energy of a spin is given by the following where m is the magnetic quantum number, which describes the possible states of the nuclear spin and $\hbar$ is the reduced Planck's constant (**Figure 2.1**):

$$E = -m\gamma\hbar B_0 \tag{2.3}$$

For a particle with I = ½ (for the most commonly studied NMR nuclei) the values of m are ±½, commonly called spin up (m = ½ or α) and spin down (m = -½ β). The sample will have a magnetic moment parallel to the magnetic field governed by the Boltzmann distribution:

$$p_\alpha = \frac{\exp(-E_\alpha/k_B T)}{\exp\left(-E_\alpha/k_B T\right) + \exp(-E_\beta/k_B T)}$$

$$p_\alpha = \frac{\exp(\gamma\hbar B_0/2k_B T)}{\exp(\gamma\hbar B_0/2k_B T) + \exp(-\gamma\hbar B_0/2k_B T)}$$

$$p_\alpha \approx 1 + \frac{\gamma\hbar B_0}{2k_B T} \tag{2.4}$$

where k_B is the Boltzmann constant. Due to the small energy difference between the α and β states, there is a very small polarization of nuclear spin parallel to the magnetic field. Even in the highest magnetic field currently available at the Minnesota NMR center only an excess of one out of 10^4 protons will be aligned with the magnetic field at room temperature. Hence, the classic and most straightforward method of increasing sensitivity of NMR experiments is to increase the external magnetic field strength. Classically the evolution a magnetic dipole experiences a torque in the presence of a magnetic field which can be described as:

$$\frac{d\boldsymbol{I}(t)}{dt} = \boldsymbol{M}(t) \times \boldsymbol{B}(t) \tag{2.4}$$

Where **M** is the bulk magnetic dipole, **I** is the vector describing the angular momentum and **B**(t) is the time dependent magnetic field. Using the quantum mechanical relationship of spin the equation reduces into the following:

$$\frac{d\boldsymbol{M}}{dt} = \gamma \boldsymbol{M}(t) \times \boldsymbol{B}(t)$$

(2.4)

This equation has been coined the Bloch equation, which describes the evolution of isolated nuclear spins under a magnetic field [134]. After rotation of the magnetic field to the xy plane (transverse) using an rf pulse the magnetization must return back to equilibrium. Bloch had observed that the longitudinal magnetization returned to equilibrium with an exponential rate and had postulated that the transverse magnetization also decayed in a first order manner [134]. The relaxation of longitudinal (R_1) and transverse magnetization (R_2) is described as follows:

$$\frac{dM_z}{dt} = -R_1(M_z(t) - M_0)$$

$$\frac{dM_{x,y}}{dt} = -R_2 M_{x,y}(t)$$

With M_z representing the longitudinal magnetization and $M_{x,y}$ the magnetization on the transverse plane. With the relaxation rate of longitudinal and transverse magnetization, the Bloch equation can be decomposed into their Cartesian coordinates:

$$\frac{dM_z}{dt} = \gamma \left[M_x(t)B_y(t) - M_y(t)B_x(t) \right] - R_1(M_z(t) - M_0)$$

(2.5a)

$$\frac{dM_y}{dt} = \gamma [M_z(t)B_x(t) - M_x(t)B_z(t)] - R_2 M_y(t)$$

(2.5b)

$$\frac{dM_x}{dt} = \gamma[M_y(t)B_z(t) - M_z(t)B_y(t)] - R_2 M_x(t) \tag{2.5b}$$

The usefulness of the Bloch equations can be appreciated by observing the evolution of a nuclear spin after the application of a 90° pulse the magnetization is rotated to the transverse plane (**Figure 2A**). The magnetization around the z-axis with an angular frequency, Ω:

$$\frac{dM_z}{dt} = -R_1(M_z(t) - M_0) \tag{2.6a}$$

$$\frac{dM_y}{dt} = \Omega M_x(t) - R_2 M_y(t) \tag{2.6b}$$

$$\frac{dM_x}{dt} = \Omega M_y(t) - R_2 M_x(t) \tag{2.6c}$$

The angular frequency, as we will see later is chemical shift of the nuclei and defines the frequency of the NMR signal describing its chemical environment. NMR spectrometers only detect the in-phase element of the magnetization during acquisition. This is represented by the real part of the complex spectrum, $M^+(t)$, and the evolution of the in-phase magnetization can be described as follows:

$$M^+(t) = M_x(t) + iM_y(t) \tag{2.7a}$$

$$\frac{dM^+}{dt} = \Omega M^+(t) - R_2 M^+(t) \tag{2.7b}$$

This equation can be solved using first order differential equations to give the following:

$$M^+(t) = M_0 e^{i\Omega - R_2 t} \tag{2.8}$$

This expression describes the resultant NMR signal from a single isolated spin, often called the free induction decay (FID). Converting the FID to the frequency domain using Fourier transformation gives the mathematical description of an NMR signal.

$$S(\omega) = \int_0^\infty M^+(t)e^{(-i\omega t)}dt \tag{2.9}$$

The transformation is performed with respect to the center of the spectrum, ω (often called the offset). The absorptive part of the transformation is taken as the NMR signal and is given by the following:

$$A(\omega) = \frac{M_0 R_2}{R_2^2 + (\Omega - \omega)^2} \tag{2.10}$$

The Bloch semi-classical model correctly predicts that the line-shape of a NMR signal will be a Lorentzian with a linewidth of R_2 (**Figure 2.2**). The latter point is of utmost importance in protein NMR spectroscopy. Typically for larger systems and for those undergoing conformational dynamics, the R_2 becomes considerably large, hindering the application of NMR to macromolecules. Many clever methods have been devised, both chemically and spectroscopically, to reduce R_2 and some of those will be discussed. However the fact that R_2 is affected by conformational dynamics allows us to study protein motion spectroscopically through a wide range of timescales from the picoseconds to milliseconds [135] (discussed in Chapter 2.8)

2.2 Density Matrix Approach

In the previous section we provided a classical description of spins. This approach is useful for many applications, such as analysis of the effect of pulses and chemical exchange. However this fails when applied to coupled spin systems. Accordingly, description of phenomenon such as coherence transfer, dipolar coupling, and relaxation,

both which are instrumental to modern NMR studies, require the use of quantum mechanics. The quantum mechanical description for nuclear spins is commonly performed using the density matrix. This treatment allows for the description of states. The density matrix is defined as the following:

$$\sigma = |\varphi(t) >< \varphi(t)| = \sum_i \sum_j c_i(t)c_j^*(t)|i >< j| \tag{2.11}$$

where $\varphi(t)$ is the wavefunction describing the quantum mechanical state while $c_i(t)$ are the coefficients of the orthonormal eigenvectors |i> which make up the wavefunction. The diagonal elements can be described by the following:

$$< r|\sigma|r > = |c_r(t)|^2 = P_r$$

The diagonal elements are merely the square of the coefficients and give the the probability, hence the population, of the system in the state r. The off-diagonal elements can be described as the following:

$$< r|\sigma|s > = c_r(t)c_s^*(t)$$

This result gives rise to a coherent superposition of states. This means is the time-dependence between the two states, r and s, is correlated within the entire spin ensemble. The time evolution of the density matrix, which is what gives rise to NMR spectral lines is given by the Liouville-von-Neumann equation:

$$\frac{d\sigma}{dt} = -i(H\sigma - \sigma H) = -i[H, \sigma] \tag{2.11}$$

In which the evolution of the density matrix is governed by the commutator between the density matrix (σ) and the Hamiltonian describing the energy of the system (*H*). A

description of the most important Hamiltonians in NMR will be described later. A general solution of the equation when the Hamiltonian is time independent can be given by the following:

$$\sigma(t) = e^{-iHt}\sigma(0)e^{iHt} \qquad (2.12)$$

Where H is the Hamiltonian of the effector and $\sigma(0)$ is the initial state of the density matrix. Commonly, density matrix values are expressed in their analogues angular momentum operator forms. For a simple single spin system the most commonly used are the Pauli spin matrices and some of these are pictorially described in **Figure 2.3**:

$$\sigma_z = I_z = \begin{bmatrix} 1 & 0 \\ 0 & -1 \end{bmatrix} \qquad\qquad \sigma_x = I_x = \begin{bmatrix} 0 & 1 \\ 1 & 0 \end{bmatrix}$$

$$\sigma_y = I_y = \begin{bmatrix} 0 & -i \\ i & 0 \end{bmatrix}$$

These can be compared to equation 2.1 which relates the magnetic moment to the angular momentum of the spin. Because only detection of an oscillating magnetic moment is our means of detection I_x or I_y is often called "transverse magnetization." The expected observable of an operator from the density matrix is the trace of the product of the density matrix and the operator, O_p, is described as follows [136]:

$$\langle O_p \rangle = tr(\sigma(t)O_p) \qquad (2.13)$$

As described in Section 2.1 the detectable in-phase magnetization is M^+:

$$\langle M^+ \rangle = \gamma \langle I^+ \rangle$$

$$\langle I^+ \rangle = tr(\sigma(t)I^+)$$

I^+ and I^- are called the raising and lowering operator, respectively. They are called this because they represent the coherent raising or lower of the magnetic quantum number. Applying the expected in-phase value to σ_x we can validate I_x, and I_y to be proportional to transverse magnetization:

$$\langle M^+ \rangle = \gamma \langle I^+ \rangle = tr \begin{bmatrix} 0 & 1 \\ 1 & 0 \end{bmatrix} \begin{bmatrix} 0 & 1 \\ 0 & 0 \end{bmatrix} = \gamma$$

And using equation 2.2 we can determine the frequency of the magnetization to be the following:

$$E = -\boldsymbol{\mu} \cdot \boldsymbol{B} = -\gamma \langle I^+ \rangle B_0 = -\gamma B_0 = \Omega \tag{2.14}$$

Giving the same result as from the Bloch model for the precession of magnetization in the transverse plane.The utility of the density matrix is apparent when one is working with a coupled spin system. Here we will use the two spin weakly coupled spin system ($|\omega_I - \omega_S| \gg \pi J_{IS}$), commonly denoted as IS. This is not merely a convenience; the most commonly used probe in protein NMR spectroscopy is the ^{1}H-^{15}N groups of the backbone amides, a prototypical IS spin system. The density matrix for an IS system is given by a 4x4 matrix with four possible quantum mechanical states, $\alpha\alpha$, $\alpha\beta$, $\beta\alpha$, and $\beta\beta$.

$$\sigma = \begin{bmatrix} \sigma_{11} & \sigma_{12} & \sigma_{13} & \sigma_{14} \\ \sigma_{21} & \sigma_{22} & \sigma_{23} & \sigma_{24} \\ \sigma_{31} & \sigma_{32} & \sigma_{33} & \sigma_{34} \\ \sigma_{41} & \sigma_{42} & \sigma_{43} & \sigma_{44} \end{bmatrix} \begin{matrix} \alpha\alpha \\ \alpha\beta \\ \beta\alpha \\ \beta\beta \end{matrix}$$
$$\begin{matrix} \alpha\alpha & \alpha\beta & \beta\alpha & \beta\beta \end{matrix}$$

The density matrix describes all the possible transitions and population states that a IS spin system can undergo. The manipulation and evolution of coherences for an IS spin system will be covered more in detail in Section 2.4 after the introduction of the

Hamiltonians required for coherence transfer. However, some discussion of the density matrix in terms of product operators and their physical relevance will be done.

There are two operators for single quantum transition, or "transverse magnetization" per nuclei in an IS system, $\mathbf{S_x}$ and $\mathbf{2I_zS_x}$.

$$S_x = \begin{bmatrix} 0 & 1 & 0 & 0 \\ 1 & 0 & 0 & 0 \\ 0 & 0 & 0 & 1 \\ 0 & 0 & 1 & 0 \end{bmatrix} \quad 2I_zS_x = \begin{bmatrix} 0 & 1 & 0 & 0 \\ 1 & 0 & 0 & 0 \\ 0 & 0 & 0 & -1 \\ 0 & 0 & -1 & 0 \end{bmatrix}$$

The transitions and their respective spectroscopic results are shown in **Figure 2.4**. With the single quantum $\mathbf{S_x}$ there are two resonances that are coherently in-phase with each other, giving rise to the double. In $\mathbf{2I_zS_x}$, the two resonances are coherent, but they are out of phase by 180° of each other.

For the longitudinal operators, there are two different operators describing the state of z-magnetization, $\mathbf{S_z}$ and $\mathbf{2I_zS_z}$ (**Figure 2.5**).

$$S_z = \begin{bmatrix} 1 & 0 & 0 & 0 \\ 0 & -1 & 0 & 0 \\ 0 & 0 & 1 & 0 \\ 0 & 0 & 0 & -1 \end{bmatrix} \quad 2I_zS_z = \begin{bmatrix} 1 & 0 & 0 & 0 \\ 0 & -1 & 0 & 0 \\ 0 & 0 & -1 & 0 \\ 0 & 0 & 0 & 1 \end{bmatrix}$$

$\mathbf{S_z}$, analogues with the single spin system, corresponds to longitudinal magnetization aligned with the magnetic field. This is the state that corresponds to the equilibrium state. However, $2I_zS_z$ (longitudinal two-spin order) describes a non-equilibrium state that has no polarization along the magnetic field and is unobservable. This state has been used for its favorable relaxation properties[137], its ability to measure cross-correlation (covered in section 2.5) properties[138, 139], the fact that this state does not evolve under scalar coupling and serves as a "filter" for many COSY-type experiments [140].

The last group of operators is the multiple-quantum operators, **2I$_x$S$_x$** and **2I$_x$S$_y$** (**Figure 2.6**):

$$2I_xS_x = \begin{bmatrix} 0 & 0 & 0 & 1 \\ 0 & 0 & 1 & 0 \\ 0 & 1 & 0 & 0 \\ 1 & 0 & 0 & 0 \end{bmatrix} \qquad 2I_xS_y = \begin{bmatrix} 0 & 0 & 0 & -i \\ 0 & 0 & i & 0 \\ 0 & -i & 0 & 0 \\ i & 0 & 0 & 0 \end{bmatrix}$$

These encompass a mix of double and zero-quantum transitions, amounting to whether the two spins have a transition in the same sense (double quantum) or in the opposite sense (zero-quantum). To see the transitions each multiple-quantum operator encompasses it is commonly expressed in terms of raising and lowering operators:

$$2I_xS_x = [I^+S^+ + I^+S^- + I^-S^+ + I^-S^-]$$

$$2I_xS_y = -i[I^+S^+ - I^+S^- + I^-S^+ - I^-S^-]$$

$$I^+S^- = \begin{bmatrix} 0 & 0 & 0 & 0 \\ 0 & 0 & 1 & 0 \\ 0 & 0 & 0 & 0 \\ 0 & 0 & 0 & 0 \end{bmatrix} \qquad I^+S^+ = \begin{bmatrix} 0 & 0 & 0 & 1 \\ 0 & 0 & 0 & 0 \\ 0 & 0 & 0 & 0 \\ 0 & 0 & 0 & 0 \end{bmatrix}$$

For the 2I$_x$S$_x$ operator the double and zero quantum transitions all share the same sense while the 2I$_x$S$_y$ operator the double and zero quantum transitions the sense has inverted. Multiple quantum coherences are very useful in the design of NMR experiments. Earliest uses of multiple quantum coherences used their property the order of the multiple-quantum experiment required that spins to be coupled together (i.e. for a triple quantum coherence you need three spins coupled together) and be used to simplify NMR spectra [141, 142].

2.3 Hamiltonians of NMR

The Hamiltonians of solution NMR spectroscopy can be largely divided into two categories. One component leads to observable spectrum while the other components

are stochastically averaged to zero due to molecular tumbling. For the latter case these do not directly contribute to the spectra however are manifested in the relaxation of NMR signal. The most important of the Hamiltonians that lead to observable spectra are the rf field, the isotropic chemical shift and the scalar coupling. Of the two Hamiltonians that directly contribute to relaxation, the dipolar coupling and the anisotropic chemical shift are the two of the greatest importance.

The isotropic chemical shift can be expressed as the following:

$$H_{CS} = \gamma \sigma_{iso} \boldsymbol{I_z} B_0 \tag{2.15}$$

Where γ is the gyromagnetic ratio of the nuclei and σ_{iso} is the isotropic chemical shift. Note that the isotropic chemical shift merely scales the resonance with respect to the larmor frequency by a factor $\gamma \sigma_{iso}$. Chemical shift arises from the unique electronic shielding around the nuclei, dictated by the chemical environment. Hence, the chemical shift is often used as a reporter for the chemical environment of a state of a macromolecule[143].

Since the chemical shift is field dependent, the value measured on different spectrometers will give varying chemical shift values, complicating comparison of experimental data. In the literature the chemical shift (δ) is typically expressed in parts per million (ppm) with respect to a standard.

$$\delta = \frac{\Omega_{Signal} - \Omega_{ref}}{\omega_0} \times 10^6 \tag{2.16}$$

ω_0 is the Larmor frequency of the measured nuclei and Ω_{ref} is the frequency of the reference. For an external magnetic field strength of 9.4T, the larmor frequency of ^{1}H is 400 MHz.

Chemical shifts, since they are a universal measurable in NMR, are indicative of structure and conformational dynamics. After the systematic acquisition of backbone ^{1}H and ^{13}C chemical shifts using triple resonance experiments (Section 2.4), it was realized that the backbone chemical shifts were highly dependent on the secondary structure [144]. A systematic approach is used called the chemical shift index (CSI), in which the measured chemical shift is compared to the value measured in a random coil [145-147]. The CSI for secondary structure was defined as follows:

$$\Delta\delta_{CSI} = \delta_{Experimental} - \delta_{Random\ Coil} \tag{2.17}$$

When $\Delta\delta_{CSI}$ is greater than zero, this is an indicator of α-helical content while a $\Delta\delta_{CSI}$ value less than zero indicates a β-sheet structure. This approach has been extended to use measured backbone chemical shifts, compared to assignments of known structures, predict the backbone θ, ψ torsion angles[148-150] and also as restraints for molecular dynamics simulations[151, 152] and structure calculations[153].

The other isotropic Hamiltonian is scalar, or J, coupling between nuclei. The scalar coupling was first observed by Gutowsky and Slichter[154] as evenly spaced multiplets when the nuclei was directly bonded with another nuclei with a different chemical shift. It was deduced that this interaction was mediated by an indirect dipolar coupling mediated by the magnetic field created by the shared electrons in the chemical bonds. The general function form of isotropic scalar coupling is given by the following:

$$H_{J_{IS}} = \pi J_{IS} \boldsymbol{I} \cdot \boldsymbol{S} \tag{2.18}$$

For protein NMR spectroscopy a convenient simplification can be made. In almost all cases scalar couplings in NMR spectroscopy fall under the "weak coupling" limit, meaning the chemical shift difference between the two nuclei is much greater than the

scalar coupling between the two nuclei, $|\omega_I\text{-}\omega_S| \gg \pi J_{IS}$. With this condition the Hamiltonian for the scalar coupling reduces as follows:

$$H_{J_{IS}} = \pi J_{IS} I_z S_z \qquad (2.19)$$

As we will see later, this interaction is what allows us to perform coherence transfer in protein NMR spectroscopy, and design multi-dimensional experiments.

Of the Hamiltonians that contribute to relaxation, dipolar coupling is the most important. Although this can be reintroduced into solution NMR as residual dipolar couplings, this will not be discussed here and has been covered extensively in other reviews [155, 156]. The quantum mechanical analogue of the Hamiltonian of two spins dipolar coupled to each other is given by the following:

$$H_D = -\frac{\gamma_I \gamma_S \hbar^2}{r^6}[3(\boldsymbol{I} \cdot \boldsymbol{r})(\boldsymbol{S} \cdot \boldsymbol{r}) - \boldsymbol{I} \cdot \boldsymbol{S}] \qquad (2.20)$$

The interaction depends on the orientation between the two spins (Spins **I** and **S**) as well as the distance between them (**Figure 2.7**). The dipolar Hamiltonian is often expressed in irreducible spherical tensors. The spherical tensors have convenient transformation properties that are often utilized in NMR spectroscopy (i.e. they are rotationally invariant). The Hamiltonians are composed of a spatial orientation of the Hamiltonian (**F**) and a spin tensor operator (**A**).

$$H = \sum_{m=-l}^{l} F_l^m(t) A_l^m \qquad (2.21)$$

For all Hamiltonians in NMR, I, or the number of interacting partners, is always one or two. The spatial coordinates are similar to the molecular orbitals found describing the spatial distribution of the electron. These are commonly expressed in polar coordinates

(**Figure 2.6**) and are summarized down below for dipolar coupling and chemical shift anisotropy.

$$F_2^0 = 1 - 3\cos^2\theta \qquad\qquad F_2^{\pm 1} = \sin\theta\cos\theta\exp(\mp i\varphi) \qquad\qquad F_2^{\pm 2} =$$

$$sin^2\theta\exp(\mp 2i\varphi)$$

The description of the spin tensor operators is a little less straightforward. To obtain some insight on these spin tensors let us consider the first component:

$$A_2^0 = \frac{1}{\sqrt{6}}(3I_ZS_Z - I_+S_- + I_-S_+) \qquad\qquad (2.22)$$

The net effect of this tensor as an operator is a net zero-quantum transition; hence this tensor component reflects a zero-quantum transition caused by two spin systems. This is also reflected in the magnetic quantum number, m. The remaining four tensor components for the dipolar Hamiltonian is as follows:

$$A_2^{\pm 1} = \mp\frac{1}{2}(I_ZS_\pm + I_\pm S_Z) \qquad\qquad A_2^{\pm 2} = \frac{1}{2}I_\pm S_\pm \qquad\qquad (2.23)$$

The chemical shift, as alluded to earlier, is not isotropic but rather is better described as a shielding tensor:

$$\sigma_{CS} = \begin{bmatrix} \sigma_{xx} & \sigma_{xy} & \sigma_{xz} \\ \sigma_{xy} & \sigma_{yy} & \sigma_{yz} \\ \sigma_{xz} & \sigma_{zy} & \sigma_{zz} \end{bmatrix}$$

The chemical shift tensor is often expressed in its principle axis system, diagonalizing the tensor to its component values[157].

$$\sigma_{CS} = \begin{bmatrix} \sigma_{11} & 0 & 0 \\ 0 & \sigma_{22} & 0 \\ 0 & 0 & \sigma_{33} \end{bmatrix}$$

These values are most commonly measured using solid state NMR spectroscopy on sampled aligned with the magnetic field (**Figure 2.7**). In fact this approach has been used to determine structure and orientation of proteins in context of crystalline and lipid associated environments [158]. By convention these values are defined with the following order [157]:

$$\sigma_{33} > \sigma_{22} > \sigma_{11}$$

It can be seen from molecular tumbling that the isotropic chemical shift is given by the average of the three principle components:

$$\sigma_{iso} = \frac{\sigma_{11} + \sigma_{22} + \sigma_{33}}{3} \tag{2.24}$$

The anisotropy of the overall chemical shift tensor, the chemical shift anisotropy, (CSA) is defined as the following [159]:

$$\Delta\sigma = \sigma_{11} - \frac{1}{2}(\sigma_{22} + \sigma_{33}) \tag{2.25}$$

The CSA describes the overall width of chemical shift distribution that the nuclei can undergo. The CSA parameter will become very important later (Section 2.5) for the discussion of ^{15}N relaxation in backbone nuclei and for cross-correlation effects in IS spin systems. The corresponding complete Hamiltonian for the chemical shift is given as:

$$H_{CS} = \boldsymbol{I} \cdot \boldsymbol{\sigma_{CS}} \cdot \boldsymbol{B} \tag{2.26}$$

The Hamiltonian can also be deconstructed into their spin operators similarly to the dipolar Hamiltonian as follows:

$$A_2^0 = \frac{1}{\sqrt{6}}(3I_z B_0) \qquad\qquad A_2^{\pm 1} = \mp\frac{1}{2}I_\pm B_0 \qquad\qquad\qquad \text{(2.27)}$$

There is no $A_2^{\pm 2}$ component for the chemical shift as there is no second spin to make a double quantum transition with. The final Hamiltonian that is of importance to NMR is the quadrupolar interaction. Nuclei with I > ½ interact with the quadrupolar electric field gradient of the nuclei. Direct detection of quadrupolar nuclei is typically not performed because of poor sensitivity and rapid relaxation of the signal and is only performed in specialized cases [89, 160, 161]. The components of the spherical spin tensors are provided by the following:

$$A_2^0 = \frac{1}{\sqrt{6}}(3I_z^2 - I(I+1)) \qquad\qquad\qquad \text{(2.28a)}$$

$$A_2^{\pm 1} = \mp\frac{1}{2}(I_z I_\pm + I_\pm I_z) \qquad\qquad\qquad \text{(2.28b)}$$

$$A_2^{\pm 2} = \frac{1}{2}I_\pm I_\pm \qquad\qquad\qquad \text{(2.28c)}$$

In solution NMR the most commonly used quadrupolar nuclei is deuterium, especially in the study of dynamics in side chains. Theory and application for deuterium relaxation will be described more in detail in Section 2.5.

2.4 Coherence Transfer and Multi-dimensional NMR

With descriptions of the density matrix and the Hamiltonians of interest we can now describe one of the important facets of NMR spectroscopy, coherence transfer. This is what enables us to correlate different nuclei together, transfer polarization from an abundant spin to another less sensitive nucleus, and to generate the increased resolution provided by multi-dimensional NMR. In solution NMR spectroscopy, the

observable Hamiltonians are the isotropic chemical shift and weak scalar coupling (Section 2.3). Although a full description using the density matrix to evaluate the effect of rf pulses, chemical shift and scalar coupling evolution can be carried out this is often unnecessary. It has been noted that under evolution under these affects only a subset of density matrix elements evolve and can be described by the operators of choice. This approach to understanding NMR experiments, now coined the product operator formalism, was first championed by Sorensen and Ernst [162] and is now the preferred approach to analyze NMR pulse sequences. Its strength is the relative simplicity of use and the intuitive results that the experimenter can correlate with spectroscopic results. However, this approach often fails under strong coupling conditions and often obscures the effect of relaxation. The product operator formalism divides up the density matrix in a linear set of operators:

$$\sigma(t) = \sum b(t)\mathbf{B} \tag{2.29}$$

And these operators evolve analogously to the evolution of the density matrix under a Hamiltonian. As such an operator, **A**, will evolve under another operator, **C**, as the following:

$$e^{-i\theta C}\mathbf{A}e^{i\theta C} = \mathbf{A}\cos\theta + \mathbf{B}\sin\theta \tag{2.30}$$

And the three operators, A, B, and C must be related by the following:

$$[\mathbf{A}, \mathbf{B}] = i\mathbf{C} \tag{2.31}$$

Geometrically this can be seen as rotating around the axis, **C**, between **A** and **B** (**Figure 2.8**). This is identical to the non-commutivity of angular momentum operators and the same relationship holds here. The two commutator relationships that are of importance for the evolution of product operators are:

$$[I_x, I_y] = iI_z \qquad\qquad [I_x, 2I_yS_z] = i2I_zS_z \qquad\qquad (2.32)$$

The permutations of these commutators can be performed to confirm they hold for other Cartesian operators as well. Here we will briefly describe the effect of rf pulses, free precession with chemical shift and scalar coupling. Then we will describe two important NMR "building" blocks using the product operator formalism and discuss their importance.

The effect of rf pulses are described by the Hamiltonians:

$$H_{rf} = \alpha \boldsymbol{I_x} \qquad\qquad H_{rf} = \alpha \boldsymbol{I_y}$$

This describes the rotation of the nuclear spin around the x-axis (x-pulse) or the y-axis. This is schematically described in **Figure 2.9**. The most common pulses in NMR spectroscopy are 90° and 180° pulses and their effects on different spin operators are described as follows:

$$
\begin{array}{llll}
I_x \xrightarrow{\;90°_x\;} I_x & \qquad & I_x \xrightarrow{\;180°_x\;} I_x & \qquad (2.33)\\[4pt]
I_y \xrightarrow{\qquad} I_z & \qquad & I_y \xrightarrow{\qquad} -I_y \\[4pt]
I_z \xrightarrow{\qquad} -I_y & \qquad & I_z \xrightarrow{\qquad} -I_z
\end{array}
$$

$$
\begin{array}{llll}
I_x \xrightarrow{\;90°_y\;} -I_z & \qquad & I_x \xrightarrow{\;180°_y\;} -I_x \\[4pt]
I_y \xrightarrow{\qquad} I_y & \qquad & I_y \xrightarrow{\qquad} I_y \\[4pt]
I_z \xrightarrow{\qquad} I_x & \qquad & I_z \xrightarrow{\qquad} -I_z
\end{array}
$$

The chemical shift evolution can be described with a frequency Ω, being the offset of the chemical shift, around the $\boldsymbol{I_z}$ operator and is described for all three Cartesian operators as follows:

$$I_x \xrightarrow{\quad \Omega_I I_z t \quad} I_x \cos(\Omega_I t) + I_y \sin(\Omega_I t) \qquad\qquad (2.34)$$

$$I_y \xrightarrow{\hspace{2cm}} I_y \cos(\Omega_I t) - I_x \sin(\Omega_I t)$$

$$I_z \xrightarrow{\hspace{2cm}} I_z$$

This is also consistent with the Bloch model where longitudinal magnetization does not precess. Since we are considering a weakly coupled system ($|w_I\text{-}w_S| \gg \pi J_{IS}$) the operator describing evolution under scalar coupling is $\mathbf{2I_zS_z}$. Since the operator is bilinear with respect to both spins, this Hamiltonian evolves single spin operators into two-spin operators and vise versa This allows, as we will see later, allow for the transfer of coherence between coupled spins.

$$I_x \xrightarrow{\quad \pi J_{IS} I_z S_z t \quad} I_x \cos(\pi J_{IS} t) + 2I_y S_z \sin(\pi J_{IS} t) \qquad\qquad (2.34)$$

$$I_y \xrightarrow{\hspace{2cm}} I_y \cos(\pi J_{IS} t) - 2I_x S_z \sin(\pi J_{IS} t)$$

$$I_z \xrightarrow{\hspace{2cm}} I_z$$

$$2I_x S_z \xrightarrow{\quad \pi J_{IS} I_z S_z t \quad} 2I_x S_z \cos(\pi J_{IS} t) + I_y \sin(\pi J_{IS} t)$$

$$2I_y S_z \xrightarrow{\hspace{2cm}} 2I_y S_z \cos(\pi J_{IS} t) - I_x \sin(\pi J_{IS} t)$$

$$2I_z S_z \xrightarrow{\hspace{2cm}} 2I_z S_z$$

Multiple quantum coherence does not evolve under the effect of scalar coupling because these operators commute with the $\mathbf{2I_zS_z}$ operator:

$$\left[2I_y S_x, 2I_z S_z\right] = 0 \qquad\qquad [2I_x S_x, 2I_z S_z] = 0$$

We will use the product operator to investigate two pulse sequence motifs used widely in solution NMR. The most common and powerful motif used to transfer magnetization from I to S (^{1}H to ^{15}N for amide groups) is the INEPT (Insensitive Nuclei Enhanced by Polarization Transfer) sequence (**Figure 2.10**) [163, 164]. This sequence performs a full

transfer of magnetization from I to S spin with the only loss coming from T_2 relaxation during coherence transfer. By using the product operator notation starting from equilibrium ^{1}H magnetization we can analyze the effect of the sequence:

$$I_z \xrightarrow{\quad 90°_{x,I} \quad} -I_y \qquad (2.35)$$

$$\xrightarrow{\quad \pi J_{IS} I_z S_z t \quad} -I_y \cos(\pi J_{IS} t) + 2I_x S_z \sin(\pi J_{IS} t)$$

$$\xrightarrow[\quad 180°_{x,S} \quad]{\quad 180°_{x,I} \quad} I_y \cos(\pi J_{IS} t) - 2I_x S_z \sin(\pi J_{IS} t)$$

$$\xrightarrow{\quad \pi J_{IS} I_z S_z t \quad} I_y \cos(2\pi J_{IS} t) - 2I_x S_z \sin(2\pi J_{IS} t)$$

$$t = \Delta = 1/4 J_{NH}$$

$$\xrightarrow{\qquad\qquad} -2I_x S_z$$

$$\xrightarrow[\quad 90°_{x,S} \quad]{\quad 90°_{y,I} \quad} 2I_z S_y$$

The chemical shift evolution is suppressed by the simultaneous 180° pulses leaving only scalar coupling active. If we set Δ to 1/4J_{IS}, evolution under scalar coupling converts the coherence anti-phase with respect to ^{1}H (**-2I$_x$S$_z$**) and the subsequent 90° pulses convert this coherence to anti-phase with respect to ^{15}N. The INEPT sequence has *completely* converted all the I (^{1}H) magnetization to S (^{15}N) but also the S signal has been scaled by the I spin. The effect of this is enormous for insensitive nuclei such as ^{15}N which has a gyromagnetic ratio 1:10 of ^{1}H. Of all the methods to perform coherence transfer in NMR, this is the only method available to perform complete, or adiabatic, coherence transfer.

The INEPT sequence has become the core building block for multi-dimensional experiments. The heteronuclear single-quantum coherence (HSQC) is the simplest two-dimensional experiment that has been constructed around the INEPT sequence [165-167]. The experiment uses an INEPT sequence to transfer the magnetization to the heteronuclei (most commonly 15N), records the chemical shift and then back transfers

the magnetization with a reverse INEPT sequence to ^{1}H (**Figure 2.11**). The spin system at the end can be described as:

$$\sigma = I_x \cos(\Omega_S t_1) \qquad (2.36)$$

This produces a correlation map of ^{1}H and -N chemical shift on two axes. In protein NMR spectroscopy the [^{1}H-^{15}N], HSQC is the basic building block for many experiments and has found almost uniform application due to straightforward incorporation of ^{15}N through prokaryotic expression in minimal media. This experiment allows for the simultaneous mapping of the chemical shifts of all the backbone amides in a protein at atomic resolution and this spectral pattern has been dubbed the "protein fingerprint." Two examples of [^{1}H,^{15}N],-HSQC spectra are shown in **Figure 2.11**, one for a 21kDa phosphatidylethanolamine binding protein and another for ubiquitin (8.6 kDa). of The [^{1}H,^{15}N],-HSQC experiment is the basis for chemical shift perturbation experiments used to determine location and affinity of ligand binding[143], and structural calculations[168].

The most straightforward extension of the [^{1}H,^{15}N]-HSQC is to use the INEPT type transfer to extend the correlation to a 3rd dimension. The polymeric protein backbone generates distinct one and two bond scalar coupling values between the atoms in the backbone (**Figure 2.12**) but the scalar coupling between characteristic atoms is homogenous throughout the protein. This allows for the design of experiments to correlate the ^{1}H-^{15}N resonances to the backbone ^{13}C chemical shifts, allowing for a sequential walk through the protein backbone using cleverly designed triple resonance experiments that select out specific correlations along the backbone ^{13}C chemical shifts. This approach was pioneered by Ikura, Kay and Ad Bax and demonstrated its applicability to Ca^{2+} bound calmodulin [169, 170]. A typical scheme is to record one experiment with ^{13}C correlations with the current and preceding residue (i and i-1) and

another with just the preceding residue (i -1, **Figure 2.12**), allowing the spectroscopist to perform the "backbone walk." Higher dimension variants of these experiments have been devised and performed [171-173], however the 3D version remains the most common because of the deleterious length required for 4D/5D experiments.

The second motif, the spin-state selective transfer (S^3CT) will be briefly described. In traditional solution NMR spectroscopy specific transitions were manipulated by selective inversion of the resolved multiplet (**Figure 2.13**). However these sorts of operations are not feasible for macromolecules and sequences, such as S^3CT and spin-state excitation (S^3E) have been developed [174]. This motif has been used to measure three bond scalar couplings [174, 175] and to manipulate cross-correlation effects (Section 2.6) in ^{1}H-^{15}N groups [139, 176, 177]. For simplicity, analysis of the pulse sequence will be performed starting on equilibrium $\mathbf{S_z}$:

$$S_z \xrightarrow{\quad 90°_{x,S} \quad} -S_y \tag{2.37}$$

$$\xrightarrow{\quad \pi J_{IS} I_z S_z t \quad} -S_y \cos(\pi J_{IS} t) + 2 I_z S_x \sin(\pi J_{IS} t)$$

$$\xrightarrow[\quad 180°_{x,I} \quad]{\quad 180°_{x,S} \quad} S_y \cos(\pi J_{IS} t) - 2 I_z S_x \sin(\pi J_{IS} t)$$

$$\xrightarrow{\quad \pi J_{IS} I_z S_z t \quad} S_y \cos(2\pi J_{IS} t) - 2 I_z S_x \sin(2\pi J_{IS} t)$$

$$\xrightarrow{\qquad\qquad} -2 I_z S_x \qquad t = \Delta = 1/4 J_{NH}$$

$$\xrightarrow[\quad 180°_{x,I} \quad]{\quad 90°_{y,S} \quad} -2 I_z S_z$$

The effect of the sequence is to selectively invert one of the S spins, the one with the I spin at the α state. This is more easily seen when the I spin is decomposed into the follows:

$$S_z \xrightarrow{\hspace{3cm}} -2I_z S_z \tag{2.38}$$

$$(I^\alpha + I^\beta)S_z \xrightarrow{\hspace{3cm}} (-I^\alpha + I^\beta)S_z$$

The ability to manipulate specific transitions has allowed for TROSY-based (section 2.6) experiments to expand from traditional triple resonance experiments [178, 179],allowed for relaxation optimized relaxation experiments and for chemical exchange experiments [180-182], and for directly measuring cross-correlation effects [139].

2.5 Nuclear Spin Relaxation

As discussed in Section 2.1, the energy levels of nuclear transitions are small and result in low sensitivity, requiring a number of technical advances to improve sensitivity. The small nuclear energies also mean that we can selectively manipulate Hamiltonians in NMR spectroscopy (discussed in part in Section 2.4) but also this leads to relatively long living quantum states. This can be seen from a classic expression relating the lifetime and the energy of a transition derived from time-dependent perturbation theory [183]:

$$\Delta t \Delta E \sim \hbar \tag{2.38}$$

One of the features in the creation of coherent quantum states by use of rf pulses is the slow relaxation of NMR signal compared to other fields of spectroscopy. The study of nuclear spin relaxation is critical for NMR spectroscopy for two reasons. Understanding of the relaxation processes enables the researcher to design experiments to maximize the precious signal available. Secondly, is that nuclear spin relaxation directly provides information on molecular motion and intramolecular distances. The latter is of direct importance for studies of macromolecules, as it is one of the best experimental techniques that provide atomic resolution of molecular motion in the ps-ns timescale.

Unlike other fields of spectroscopy, relaxation is not caused by spontaneous or stimulated emission of a photon. Rather, due to the small nuclear energy levels, relaxation is caused by coupling of the spin system to the environment. For example let us examine the effect of a nuclear spin with a neighboring spin. Along with the external magnetic field from the spectrometer, the spin also experiences an external local field from the neighboring spin (**Figure 2.14**). As the external spin rotates, the effective magnetic field is altered based on the orientation of the second spin. This causes the energy levels to fluctuate and induces a transition if this fluctuation is near the Larmor frequency. This mechanism is the primary driver for longitudinal relaxation, or T_1. If a neighboring spin is parallel and on resonance to the spin system then another phenomenon can occur in which the magnetization between the two spins are exchanged (**Figure 2.14**) This mechanism is the one primarily responsible for transverse relaxation, or T_2.

The Hamiltonians that contribute to relaxation randomly fluctuate and average to zero. This can be mathematically expressed as the following:

$$\langle H(t) \rangle = 0 \tag{2.39}$$

The angular brackets represent the time averaged value. However the Liouville-von-Neumann equation can be expanded to first order to take into account the time-dependence of the fluctuating Hamiltonians:

$$id\sigma(t) = [H, \sigma(t)]dt$$

$$i \int_{t_0}^{t} d\sigma = i\hbar\big(\sigma(t) - \sigma(t_0)\big) = \int_{0}^{t} [H(t'), \sigma(t')] \, dt'$$

$$\sigma(t) = \sigma(t_0) - i \int_0^t [H(t'), \sigma(t')]\, dt'$$

To evaluate the evolution of the evolution of the density matrix including the effects of relaxation, the time-dependence of the above term is evaluated to give the following:

$$\frac{d\sigma(t)}{dt} = -i[H(t), \sigma(t)] - \int_0^\tau [Ht), [H(t-\tau), \sigma(t-\tau)]]\, d\tau \qquad (2.40)$$

where τ is the correlation time of the time-dependent Hamiltonian. A couple assumptions are made of the system. First is that ensemble time average of the Hamiltonians is zero, save the observable isotropic chemical shift and scalar coupling. Second is that the time-dependency of the Hamiltonians (τ) is uncorrelated and is much shorter than the evolution of the density matrix (t), allows us to transform $\sigma(t-\tau)$ to $\sigma(t)$. Third is that the correlation time of the Hamiltonians are much shorter than the relaxation time. This allows us to extend the integral to infinity. Lastly an *ad hoc* correction is made to allow the magnetization return to equilibrium. These assumptions are made to make the problem tractable and are reasonable for the system in interest. Discussions of the validity of these assumptions are made by Abragam [184]. With these substitutions in mind the expression of the time evolution of the density matrix becomes the following:

$$\frac{d\sigma(t)}{dt} = -i[H_0, \sigma(t)] - \int_0^\infty [H(t), [H(t-\tau), \sigma(t) - \sigma_0]]\, d\tau \qquad (2.41)$$

The motion most responsible for nuclear spin relaxation is molecular rotation. As such it is most convenient to express the time-dependent Hamiltonian using irreducible spherical tensors as described in Section 2.3:

$$H(t) = \sum_{l=0}^{2} \sum_{m=-1}^{l} F_l^m(t) A_l^m \qquad (2.42)$$

Where F(t) describes the random time-dependent spatial fluctuations of the Hamiltonian and $\mathbf{A}_l$ are the spin operators acting on the density matrix. With some substitution the evolution of the density matrix can be expressed as the following:

$$\frac{d\sigma(t)}{dt} = -i[H_0, \sigma(t)] - \frac{1}{2} \sum_{l=0}^{2} \sum_{m=-1}^{l} \left[A_l^{-m}, [A_l^m, \sigma(t) - \sigma_0] \right] J(\omega_m) \qquad (2.43)$$

The random spatial fluctuations are imbedded in the function, $J(\omega_m)$, called the spectral density function. This function describes the distribution of states in at each frequency of motion. More precisely, it is the Fourier transform of the auto-correlation function of the spatial variables of the Hamiltonian

$$J(\omega_m) = \int_0^\infty \langle F_l^{-m}(t) F_l^m(t-\tau) \rangle e^{i\omega t} d\tau \qquad (2.44)$$

The expression above for the evolution of the density matrix has often been called the master equation [184, 185]. This is often expressed in a convenient form:

$$\frac{d\sigma(t)}{dt} = -i[H_0, \sigma(t)] - \boldsymbol{\Gamma}[\sigma(t) - \sigma_0] \qquad (2.44)$$

$\boldsymbol{\Gamma}$ is often called the relaxation superoperator [185]. As discussed earlier it is more convenient to express the density matrix in terms of operators, which have spectroscopic observables. As such the relaxation term is expressed as the following:

$$\frac{d\langle \boldsymbol{O_p} \rangle}{dt} = -\frac{1}{2} \sum_{l=0}^{2} \sum_{m=-1}^{l} \left[A_l^{-m}, [A_l^m, \boldsymbol{O_p}] \right] J(\omega_m) \qquad (2.45)$$

Inspection of the master equation reveals a few insights on the mechanism of relaxation. First is that the double commutator must be non-zero for a Hamiltonian to contribute to relaxation. This states that the time-dependent magnetic fluctuations from the Hamiltonians must be able to induce a transition in the density matrix. Secondly is that the frequency of the random spatial variations (in macromolecules is typically molecular rotation) must have significant contributions of in the frequency of the spin transitions. This contribution is embedded in the spectral density functions. The stochastic fluctuations from molecular tumbling must be on resonance with the spin transitions to promote relaxation. As will be discussed, transitions that involve no exchange of energy dominate relaxation in protein NMR spectroscopy.

Spectral Density Function

Before describing the relaxation rates expressed in spectral density function, a brief description of the auto-correlation function and the various expressions of spectral density functions will be given. Although the spectral density function in itself is exact, parlaying the function into a physical system requires a model. In particular two models will be discussed in detail. The first is that of an *isotropic rigid rotor* (**Figure 2.15**). This situation can be likened to that of a rigid bond rotating within an isotropic protein. The auto-correlation function (expressed as $G(\tau)$) is described as follows:

$$G(\tau) = \langle F_l^{-m}(t)F_l^m(t-\tau) \rangle = \frac{1}{5}\exp(|\tau|/\tau_c) \tag{2.46}$$

τ_c is a constant called the rotational correlation time, which is the average time required for a full rotation. The corresponding spectral density function is given as the following[186]:

$$J(\omega) = \frac{2}{5}\frac{\tau_c}{1 + \omega^2\tau_c^2} \tag{2.47}$$

Where ω is the frequency of the transition associated with the relaxation phenomenon. Although this is a simplistic model, the characteristic behavior of spectral density functions at different motional regimes can be evaluated with this model. The first extreme, where $(\omega\tau_c)^2 \ll 1$, is denoted in the literature as the *extreme narrowing limit* (**Figure 2.16**) experienced with small molecules. In this motional scale all spectral density functions contribute equally [186, 187]:

$$J(0) = J(\omega) = J(2\omega) = \frac{2}{5}\tau_c \tag{2.48}$$

In the other extreme, called the *macromolecular* or *spin diffusion limit*, is where $(\omega\tau_c)^2 \gg 1$ (**Figure 2.16**). This is the motional regime that all macromolecules, including proteins, reside at. If $(\omega\tau_c)^2 \gg 1$ the denominator approaches infinity resulting in the following [186, 187]:

$$J(0) = \frac{2}{5}\tau_c \tag{2.49a}$$

$$J(\omega) = J(2\omega) = 0 \tag{2.49b}$$

This states that there are no motions that are near single and double quantum transition frequency, and only transitions that produce no net change in quantum states are involved in relaxation. Furthermore this effect scales as the molecular weight increases with τ_c.

The description of a rigid bond vector is not reflective of the physical phenomenon because stochastic modulation of bond vectors also contributes to relaxation. Although specific motional models had been considered previously [188, 189], the most widely

60

used approach is the so called "model-free" Lipari-Szabo formalism [190, 191]. The only explicit assumption of the model is that the extremely rapid motion of the bond vector is uncorrelated with macromolecular tumbling [190] and does not formally assume a motional model. For proteins with well folded structure this assumption holds well. For spectral density function is expressed as the following:

$$J(\omega) = \frac{2}{5}\left(\frac{S^2\tau_c}{1+\omega^2\tau_c^2} + \frac{(1-S^2)}{1+\omega^2\tau^2}\right) \tag{2.50a}$$

$$\frac{1}{\tau} = \frac{1}{\tau_c} + \frac{1}{\tau_e} \tag{2.50b}$$

In the model-free formalism τ_e is the lifetime of the fast internal motion and S^2 is the generalized order parameter describing the amplitude of motion. Several studies have suggested the τ_e derived from least-squares fitting is physically unreasonable [192, 193], however S^2, describing the amplitude of the motion, has found widespread acceptance in the field [186].

Although the model-free formalism is not directly tied to a motional model, widespread interpretation of the motion has been done within the framework of the diffusion in a cone model[186]. In this model the bond vector is assumed to move stochastically within a cone in an angle, θ, around its symmetry axis (**Figure 2.15**). The relationship between S^2 and angle of motion in the diffusion in a cone model is as follows:

$$S^2 = \left[\frac{1}{2}\cos\theta\,(1+\cos\theta)\right]^2 \tag{2.51}$$

Where S^2 = 1 describes a perfectly rigid bond vector and S^2 = 0 undergoes free diffusion around a hemisphere. It can be seen that when S^2 = 1 and τ_e approaches infinity, the model free approach reduces back to the *isotropic rigid rotor*.

Relaxation Rates of NMR Observables

The most common relaxation experiments performed on proteins are on the ^{15}N backbone amide groups [186, 194]. These groups predominantly rely on the [1]H-^{15}N dipolar coupling and ^{15}N chemical shift anisotropy for relaxation. The three experiments performed are to measure the lifetime of the longitudinal (T_1), transverse (T_2) elements and steady-state NOE (**Figure 2.17**). The calculations of using the master equation for relaxation have been covered extensively in the literature [184, 194-196] and only the results will be reported here. The longitudinal relaxation for ^{15}N in an amide group is given by the following:

$$\frac{1}{T_1} = \frac{d}{4}[J(\omega_H - \omega_N) + 3J(\omega_N) + 6J(\omega_H + \omega_N)] + cJ(\omega_N) \tag{2.52a}$$

$$d = \left(\frac{\mu_0}{4\pi}\right)^2 \left(\frac{\gamma_N^2 \gamma_H^2 \hbar^2}{r_{NH}^6}\right) \tag{2.52b}$$

$$c = \frac{\Delta\sigma^2 \omega_N^2}{3} \tag{2.52c}$$

μ_0 is the permeability of free space, ω_N is the Larmor frequency of ^{15}N, γ_N and γ_H are the gyromagnetic ratio of nitrogen and proton respectively, $\hbar$ is the reduced planck's constant, r_{NH} is the length of the NH bond vector[197] ($<r_{NH}>$ = 1.02 Å) and $\Delta\sigma$ is the chemical shift anisotropy of [15]N (value is determined to be ~-160 ppm from solid state NMR[198] and -170ppm from relaxation measurements[199]).

Since the longitudinal magnetization does not evolve under evolution, this stays invariant over time. However with transverse magnetization for a scalar coupled system the magnetization evolves between the in-phase (I_x) and anti-phase ($2I_yS_z$) state and the relaxation rate are different between the two operators, with the anti-phase operator relaxing faster. To measure the relaxation of the in-phase transverse operator a series of 180° pulses are applied (Carr-Purcell-Meiboom-Gill, CPMG sequence[200, 201]) with the period between 180° pulses (2δ) set to less than $1/4J_{NH}$ to prevent the magnetization from evolving into the anti-phase operator. The transverse relaxation for the in-phase (I_x) operator is:

$$\frac{1}{T_2} = \frac{d}{8}[4J(0) + J(\omega_H - \omega_N) + 3J(\omega_N) + 6J(\omega_H) + 6J(\omega_H + \omega_N)] \quad (2.53)$$

$$+ \frac{c}{6}[4J(0) + 3J(\omega_N)]$$

The constants are defined the same as with T_1. It should be noted that for small molecules that are under the extreme narrowing limit $T_1 = T_2$ while for the spin diffusion limit $T_2 \ll T_1$. This is due to the fact that T_2 possess a *J(0)* spectral density function which increases in contribution with molecular weight while the other components decrease in their contribution.

The last fast relaxation experiment performed on backbone amides is the steady state nuclear overhauser effect (NOE) [202] experiment. The NOE predicts that the longitudinal magnetization of two dipolar coupled spins are coupled together, hence they relax biexponentially. In the steady state NOE experiment two sets of experiments are performed, first applies a weak rf field on the ^{1}H spins prior to ^{15}N evolution and another without the weak rf field (**Figure 2.17**). The ratio of the two spectra is called the NOE enhancement (σ_{NH}) and is related to the spectral density function by the following:

$$\sigma_{NH} = \frac{I_{sat}}{I_{ref}} \qquad (2.54a)$$

$$\sigma_{NH} = 1 + \left(\frac{\gamma_H}{\gamma_N}\right)\frac{d^2}{4}[6J(\omega_H + \omega_N) - J(\omega_H - \omega_N)]T_1 \qquad (2.54b)$$

For a ^{1}H-^{15}N amide group the maximum theoretical value is one (in the spin diffusion limit) and the minimal value (at the extreme narrowing limit) is -4. These measurements are frequently used to determine the degree of secondary structural character in a polypeptide chain [127, 203], which has found germane use in the study of intrinsically disordered proteins [204, 205].

Until now the description of relaxation experiments has largely been tied to backbone amide groups. The study of side-chain dynamics has typically been performed using methyl-bearing side chain groups and predominately using relaxation of quadrupolar nuclei because the relaxation rate is at least an order of magnitude larger than the dipolar coupling [184]. This considerably simplifies the analysis of the relaxation data. However experiments are currently being developed to circumvent this limitation [206-208]. Using recombinant expression at 40-60% D_2O[209] or deuterium labeled metabolic precursors [210] methyl isotopomers of deuterium can be incorporated by CH_2D and CHD_2 isotopomers. Experiments have been devised to measure the quadrupolar relaxation rate (R^Q) of all five spin tensors [211, 212] :

$$R^Q(D_z) = \frac{3}{40}Q^2[J(\omega_D) + 4J(2\omega_D)] \qquad (2.55a)$$

$$R^Q(3D_z{}^2 - 2) = \frac{3}{40}Q^2[3J(\omega_D)] \qquad (2.55b)$$

$$R^Q(D_+) = \frac{1}{80}Q^2[9J(0) + 15J(\omega_D) + 6(2\omega_D)] \qquad (2.55c)$$

$$R^Q(D_+D_z + D_zD_+) = \frac{1}{80}Q^2[9J(0) + 3J(\omega_D) + 6(2\omega_D)] \qquad (2.55d)$$

$$R^Q(D_+{}^2) = \frac{3}{40}Q^2[J(\omega_D) + 2(2\omega_D)] \qquad (2.55e)$$

$$Q = \left(\frac{e^2qQ}{\hbar}\right)^2 \qquad (2.55f)$$

The value e^2qQ/h is called the quadrupolar coupling constant and has been found to be 167 ±1 kHz for deuterium [213]. The In the limit of large proteins in the macromolecular limit, both transverse relaxation operators (D_+ and $D_+D_z + D_zD_+$) are identical. Assuming a physical model in which the methyl group rotates extremely quickly with respect to molecular rotation (τ_c) the deuterium transverse rates reduce to the following (see also Section 2.7):

$$R_2 \approx R^Q(D_+D_z + D_zD_+) \approx R^Q(D_+) = \frac{1}{80}Q^2S^2\tau_c \qquad (2.56)$$

This approximation is used primarily for $^{13}CHD_2$ probes. For $^{13}CHD_2$ probes only a state with a single quantum relaxation rate can be generated unlike with $^{13}CH_2D$ probes [210]. Although longitudinal relaxation can be used, it has been shown that transverse relaxation (T_2) is a more direct probe of the magnitude of the order parameter while the longitudinal relaxation is a better reporter for the fast internal motion (τ_e) [193, 214].

2.6 Cross-correlation and TROSY

All the relaxation rates that have been described earlier are derived from a single Hamiltonian affecting a spin system. The derivations were made under the assumption that each of the Hamiltonians effected relaxation independently, or are auto-correlated. However there is a relaxation phenomenon called cross-correlation where the relaxation of a spin is dependent on another spin. This can arise from one of two ways. The first is

where the fixed symmetry of a molecular group can give rise to either constructive or destructive dipolar interactions that affect the environment around a nuclear spin. As a result whether the other nuclei in the molecular group are in the spin up or spin down state will affect the relaxation rate. This factors into the relaxation of methyl groups considerably and is discussed in Section 2.7. The second instance when this can happen is when two different Hamiltonians on the same spin system interact together. In this instance the nuclear spin can either interact constructively or destructively with another Hamiltonian contributing to relaxation, resulting in differential relaxation rates for different transitions. This was first observed in tRNA[Met] with a series of studies which observed that an isolated ^{15}N imino doublet with different linewidths. A series of elegant experiments[215] and theoretical treatment using the master equation[216] determined the differential linewidth for a ^{1}H-^{15}N (IS) system was due to cross-correlation between the ^{1}H-^{15}N dipolar coupling and the chemical shift anisotropy. The cross-correlation term (η) in terms of their spectral density functions was found to be the following:

$$\eta_z = \sqrt{3}cd[3cos^2\theta - 1]J(\omega_I) \qquad (2.57a)$$

$$\eta_{xy} = \frac{\sqrt{3}}{6}cd[3cos^2\theta - 1]\{4J(0) + 3J(\omega_I)\} \qquad (2.57b)$$

The constants, c and d, are identical from the T_1 T_2 measurements and θ is the angle between the ^{1}H-^{15}N bond vector and the CSA tensor. θ was found experimentally to be approximately 20° [217]. Spectroscopically the cross-correlated relaxation is manifested in the transverse relaxation rates of each of the doublet resonances (**Figure 2.17**):

$$\frac{d(I^{\alpha}S^+)}{dt} = -(R_2 + \eta_{xy})I^{\alpha}S^+ = -R_2^{\alpha}I^{\alpha}S^+ \qquad (2.58a)$$

$$\frac{d(I^\beta S^+)}{dt} = -(R_2 - \eta_{xy})I^\beta S^+ = -R_2^\alpha I^\alpha S^+$$

<div align="right">(2.58b)</div>

The resonance in which the passive spin (I in this case) is in the β (or spin down state), the cross-correlated relaxation adds destructively with the intrinsic transverse relaxation rate, resulting in an increase of resolution and sensitivity for this transition. It is also noted here that an analogous effect is observed for longitudinal magnetization, converting the **I$_z$** operator to **2I$_z$S$_z$** [218]. This can be seen graphically (**Figure 2.17**), when the neighboring spin is at the α state (spin up) the dipole is co-linear with the CSA, and these two interactions work together. However when the spin is spin down (β), the dipolar interaction counteracts the CSA, resulting in relaxation interference and a slower relaxation of the transition. As the cross-correlation rate scales with magnetic field (through the CSA term) and the molecular weight (from the increase of τ_c) the cross-correlation term starts completing with the auto-relaxation term (R$_2$) and exploitation of this effect has been dubbed the TROSY-effect (transverse-relaxation optimized spectroscopy) [176]. Theoretical calculations demonstrate that at a magnetic field strength of 1000 MHz (using a CSA value of -155 ppm) achieves complete cancelation of the auto-relaxation term via cross-correlation [219].

Although we treat the ¹H-¹⁵N backbone amides as isolated spin systems, this is not a reasonable situation. A network of neighboring protons within the protein is dipolar coupled with the ¹H of the backbone amide and may exchange magnetization (**Figure 2.17**). When this happens the sign of ¹H flips back to α (spin up) and the neighboring proton is in the β state. The presence of external protons attenuates the effectiveness of the TROSY-effect. This can be eliminated by incorporating ²H in place of ¹H for all the non-exchangeable protons during recombinant expression [219].

In the "early" days of protein NMR spectroscopy the cross-correlation rate was either seen as a nuisance that hindered measurements of accurate relaxation rates [220, 221] or as a mechanism to transfer coherence between two spins [222]. The systematic use of relaxation interference to increase sensitivity and resolution in spectroscopy was first performed by Wüthrich and co-workers [176]. To obtain "relaxation optimized" 2D spectra by correlating the two transitions that experience relaxation interference and filtering the other transitions [223]:

$$I^\beta S^\pm \rightarrow I^\pm S^\beta \qquad\qquad (2.58)$$

This is achieved by first encoding coupled ^{15}N single quantum coherence during the t_1 period, followed up a two spin-state selective transfers; the first inverting the $\alpha\alpha$ and $\beta\alpha$ states and the second inverting the $\alpha\beta$ and $\alpha\alpha$ states. This results in two correlations:

$$I^\beta S^\pm \rightarrow I^\pm S^\beta \ (TROSY) \qquad\qquad I^\alpha S^\pm \rightarrow I^\pm S^\alpha \ (anti-TROSY)$$

Where the TROSY resonance the cross-correlation adds destructively and the anti-TROSY the relaxation adds constructively. To separate out these two signals the key was to recognize that the transfer of ^{15}N to ^{1}H for the TROSY resonance is through a double quantum intermediate (**Figure 2.19**) while the anti-TROSY resonance is transferred through a zero-quantum state[175]. As a result the anti-TROSY resonance can be actively suppressed by phase cycling or gradients. Other transfer schemes have been developed to increase the sensitivity of the experiment [224-226] but the double spin-state selective transfer scheme is still widely used. The improvement in spectral quality can be seen for a section of the [^{1}H,^{15}N]-HSQC and [^{1}H,^{15}N]-TROSY-HSQC spectrum of apo PKA-C (**Figure 2.19**). The dramatic increase in sensitivity and resolution from TROSY allows for structural studies of macromolecules over 30 kDa, including PKA-C.

Successful application of TROSY to backbone amides have allowed for systematic structural and dynamic studies of macromolecules up to 100 kDa in weight [227]. This author would also like to point out the impressive application of TROSY-NMR to the full backbone assignment of the monomeric Malate Synthase G, a 723 residue metabolic enzyme [172]. However the efficiency of TROSY-based approaches fails considerably at higher molecular weights, even with theoretical perfect cancelation of transverse relaxation. This occurs because during the coherence transfer from ^{1}H to ^{15}N and then back to ^{1}H there is no TROSY effect and for very large systems after coherence transfer using INEPT (duration is approximately 5.4 ms for an INEPT element for backbone ^{1}H-^{15}N groups) the magnetization has completely relaxed. Pulse sequences have been used to exploit the cross-correlation to transfer magnetization [228, 229]; however, these have found limited applicability due to their inherent transfer inefficiency. Subsequently the application of NMR to larger molecular systems necessitated the development of novel labeling and pulse sequence techniques.

2.7 Cross-Correlation in Methyl Groups

After the initial success of TROSY spectroscopy on ^{1}H-^{15}N based spin systems, other groups explored whether other spin systems would be amenable to TROSY-based approaches. This has led to the development of the methyl-TROSY which now allows for structural and dynamic studies on large supramolecular systems several hundred kilodaltons in size [230] using specifically side-chain labeled methyl groups. The development of specifically labeled metabolic a-ketobutyrate and a-ketovalerate allows for specific labeling of Ile, Leu and Val side chains at will, creating isolated ^{13}CH$_3$ groups in a highly deuterated background [231-233]. Approaches to labeling will be discussed at length in Chapter V.

For this discussion we will be making the following assumptions with regards to the form of the relaxation. First is that we are at the macromolecular limit, meaning ($\omega\tau_c$) >> 1. This is readily achieved in our system and most other protein systems in aqueous buffer. Second is the methyl groups rotates extremely quickly around its rotational axis, meaning ($\omega\tau_e$) >> 1. This is a valid assumption considering that methyl groups experience rotation even at -77°C [234, 235]. This will enable us to write the spectral density functions in a compact form expressed in terms of the model-free order parameter. The last assumption we will make is that the methyl group is an isolated spin system and the predominant contributions to relaxation are the intra-methyl ^{1}H-^{1}H dipolar and ^{1}H-^{1}C dipolar interactions. Experiments have shown this is a reasonable assumption [236] and other relaxation contributions can be added ad hoc to the final rates.

The energy levels of a ^{13}CH$_3$ methyl groups is shown in **Figure 2.20**. Since the protons within a methyl groups are strongly coupled (Δw_H = 0 in this case), we cannot use the weakly coupled basis set to calculate the resonances. Instead we express the ^{1}H spins using a set of eigenfunctions that describe the total angular momentum (S^2, not to be confused with the order parameter) of the three ^{1}H spin states. We express the ^{13}CH$_3$ spin system in terms of the total ^{1}H spins and ^{13}C in terms of the weakly coupled basis (since ^{13}C is weakly coupled to the protons) using the following eigenfunctions:

$$\varphi_1 = \alpha(\alpha\alpha\alpha) \qquad \varphi_5 = \beta(\alpha\alpha\alpha) \tag{2.59}$$

$$\varphi_2 = \alpha(\alpha\alpha\beta+\alpha\beta\alpha+\beta\alpha\alpha)/\sqrt{3} \qquad \varphi_6 = \beta(\alpha\alpha\beta+\alpha\beta\alpha+\beta\alpha\alpha)/\sqrt{3}$$

$$\varphi_3 = \alpha(\alpha\beta\beta+\beta\beta\alpha+\beta\alpha\beta)/\sqrt{3} \qquad \varphi_7 = \beta(\alpha\beta\beta+\beta\beta\alpha+\beta\alpha\beta)/\sqrt{3}$$

$$\varphi_4 = \alpha(\beta\beta\beta) \qquad \varphi_8 = \beta(\beta\beta\beta)$$

$$\varphi_9 = \alpha(\alpha\alpha\beta-\alpha\beta\alpha)/\sqrt{6} \qquad \varphi_{11} = \beta(\alpha\alpha\beta-\alpha\beta\alpha)/\sqrt{6}$$

$$\varphi_{10} = \alpha(\beta\alpha\beta-\beta\beta\alpha)/\sqrt{6} \qquad \varphi_{12} = \beta(\beta\alpha\beta-\beta\beta\alpha)/\sqrt{6}$$

$$\varphi_{13} = \alpha(\alpha\alpha\beta+\alpha\beta\alpha-2\beta\alpha\alpha)/\sqrt{6} \qquad \varphi_{15} = \beta(\alpha\alpha\beta+\alpha\beta\alpha+2\beta\alpha\alpha)/\sqrt{6}$$

$$\varphi_{14} = \alpha(-2\alpha\beta\beta+\beta\beta\alpha+\beta\alpha\beta)/\sqrt{6} \qquad \varphi_{16} = \beta(-2\alpha\beta\beta+\beta\beta\alpha+\beta\alpha\beta)/\sqrt{6}$$

The spectroscopic meaning of these transitions can be appreciated by looking at the uncoupled ^{13}C and ^{1}H 1D spectra of a methyl group (**Figure 2.20**). For an uncoupled 1D ^{13}C spectrum we would expect a quartet pattern from the three coupled protons and for the 1D ^{1}H spectra we expect a doublet from the one bond scalar coupling with ^{13}C. The carbon transitions all contribute to the quartet splitting of a ^{13}C resonance, where the most upfield resonance is given by the (1,5) transition and the lowest field is given by the (4.8) transition. Since there are three times as many transitions for the other two energy levels (**Figure 2.20**), this gives rise to the characteristic 1:3:3:1 intensity. For the ^{1}H spins there are only two possible states, $\omega_H-\pi J_{CH}$ or $\omega_H+\pi J_{CH}$, and these each contain five of the ^{1}H transitions given in **Figure 2.20**.

For the design of TROSY based experiments, the relaxation of all the quantum transitions must be considered in designing experiments to optimize the relaxation properties of the spin system. Work from the literature, particularly from Kay[237-239] and Ernst[240], has demonstrated for macromolecules the relaxation of the ^{1}H transitions shown in **Figure 2.20** are given by the following:

$$R_{2,H}^{f} = \frac{81}{4}q_{HH}J_{HH}(0) + q_{CH}J_{CH}(0) \tag{2.60a}$$

$$R_{2,H}^{s} = q_{CH}J_{CH}(0) \tag{2.60b}$$

$$q_{HH} = \frac{1}{5}\left(\frac{\mu_0}{4\pi}\right)^2 \frac{\gamma_H^4 \hbar^2}{r_{HH}^6} \tag{2.60c}$$

$$q_{CH} = \frac{1}{5}\left(\frac{\mu_0}{4\pi}\right)^2 \frac{\gamma_C^2 \gamma_H^2 \hbar^2}{r_{CH}^6} \tag{2.60d}$$

q_{HH} and q_{CH} are the dipolar coupling constants between ^{1}H-^{1}H and ^{1}H-^{13}C respectively. The first term, $J_{HH}(0)$ is from the sum of the auto and cross-relaxation terms of the intra-methyl protons and the $J_{CH}(0)$ is the contribution from the ^{1}H-^{13}C dipolar interaction. For the central transition the auto and cross-relaxation terms from the ^{1}H-^{1}H interaction cancel out the $J(0)$ contribution to relaxation, making the ^{1}H-^{13}C interaction the only contributor to relaxation. A reasonable physical picture is from the fixed geometry of the methyl group and the possible spin orientations. When one 1H has transverse magnetization on one spin and the other spins are either spin up or two down then two possible arrangements of the two other 1H spins can occur (**Figure 2.21**). Either the spins can align parallel to each other, i.e. the dipolar fields add constructively, or they are anti-parallel to each other, cancelling their dipolar field. Hence when they are anti-parallel to one another then the cross-correlation term adds destructively and reduces the relaxation rate.

The transverse relaxation of the ^{13}C transitions are contributed by the ^{1}H-^{13}C dipolar interaction and have been calculated previously by Kay and Werbelow[241].

$$R_{2,C}^{f} = 9q_{CH}J_{CH}(0) \tag{2.61a}$$

$$R_{2,C}^s = q_{CH} J_{CH}(0) \qquad\qquad (2.61b)$$

$$q_{CH} = \frac{1}{5}\left(\frac{\mu_0}{4\pi}\right)^2 \frac{\gamma_C^2 \gamma_H^2 \hbar^2}{r_{CH}^6} \qquad\qquad (2.61c)$$

Again the manifestation of a slower relaxation rate for the central transition is from the destructive interference between the auto-correlation (caused by the libration of the [1]H-^{13}C bond) and the cross-correlation (influence from a neighboring [1]H-^{13}C bond).

The spectral density functions for methyl groups are frequently expressed in terms of the Lipari-Szabo order parameter [190, 191]. For methyl groups, assuming standard tetrahedral geometry, describes the amplitude of motion of the group around its C-C bond (3-fold symmetrical axis). With the assumption that the rotation of the methyl group is extremely rapid ($\omega\tau_e \gg 1$), we can make the following simplification to the Lipari-Szabo formalism (Equations 2.50) [190, 191]:

$$J(\omega) = \frac{1}{9}\left[\frac{S^2 \tau_c}{1 + (\omega\tau_c)^2} + \frac{(1 - S^2)\tau}{1 + (\omega\tau)^2}\right] \approx \frac{2}{5}\left[\frac{S^2 \tau_c}{1 + (\omega\tau_c)^2}\right] \qquad (2.62a)$$

$$J(0) \approx \frac{2}{5}[S^2 \tau_c] \qquad\qquad (2.62b)$$

The factor of 1/9 used for methyl groups instead of 2/5 is because of the three-fold symmetry of the methyl group [212]. We can place this in the relaxation rates described earlier for all the ^{1}H and ^{13}C transitions to obtain the following in terms of the model-free order parameter.

$$R_{2,H}^f = \frac{9}{20}\left(\frac{\mu_0}{4\pi}\right)^2 \frac{S^2 \gamma_H^4 \hbar^2 \tau_c}{r_{HH}^6} + \frac{1}{45}\left(\frac{\mu_0}{4\pi}\right)^2 \frac{S^2 \gamma_C^2 \gamma_H^2 \hbar^2 \tau_c}{r_{CH}^6} \qquad (2.63a)$$

$$R_{2,H}^{s} = \frac{1}{45}\left(\frac{\mu_0}{4\pi}\right)^2 \frac{S^2 \gamma_C^2 \gamma_H^2 \hbar^2 \tau_c}{r_{CH}^6} \qquad (2.63b)$$

$$R_{2,C}^{f} = \frac{1}{5}\left(\frac{\mu_0}{4\pi}\right)^2 \frac{S^2 \gamma_C^2 \gamma_H^2 \hbar^2 \tau_c}{r_{CH}^6} \qquad (2.63c)$$

$$R_{2,C}^{s} = \frac{1}{45}\left(\frac{\mu_0}{4\pi}\right)^2 \frac{S^2 \gamma_C^2 \gamma_H^2 \hbar^2 \tau_c}{r_{CH}^6} \qquad (2.63d)$$

To accomplish a relaxation optimized ^{1}H-^{13}C heteronuclear experiment, the pulse sequence must be designed to select out slowly relaxation quantum transitions from the remaining transitions. Kay and coworkers discovered that the standard heteronuclear multiple quantum correlation (HMQC) pulse sequence achieved all of these aims. From analyzing the fate of all the spin density matrix elements of a methyl group it was theoretically determined that in the HMQC experiment the slowly and rapidly relaxing components are not mixed, leading to sensitivity gains without the use of selection as in ^{1}H-^{15}N based TROSY experiments [176, 178].

A brief overview of the HMQC and its features for relaxation optimized experiments will be discussed. The detailed calculations of the density matrix components have been extensively described elsewhere [242, 243]. To facilitate discussion we will mark the slowly relaxing components as **A** and the rapid relaxing components as **B**. In **Figure 2.22** a general pulse scheme for a ^{1}H-^{13}C HMQC experiment is shown. After a 90° pulse on ^{1}H the magnetization can be described as follows:

$$\sigma_a = -I_y^A - I_y^B \qquad (2.64)$$

After evolution under scalar coupling for a period, Δ, is taken for a duration of $1/2J_{CH}$ (Δ ~3.5 ms for $^1J_{CH}$ = 140 Hz for methyl groups). After the 90° pulse on ^{13}C the magnetization can be described as follows:

$$\sigma_b = -2I_x^A S_y \exp(-\Delta R_{2,H}^s) - 2I_x^B S_y \exp(-\Delta R_{2,H}^f) \qquad (2.65)$$

The relaxation of each component, **A** and **B**, has been explicitly taken into account. To understand the relaxation of the multiple-quantum system we will first decompose the operator, to first approximation, to the contribution from each of the proton spins:

$$-2I_x S_y = -2I_x^1 S_y - 2I_x^2 S_y - 2I_x^3 S_y \qquad (2.66)$$

For purposes of discussion we will explore what proton **1** experience from the other two protons (only considering the $2I_x{}^1S_y$ of the $2I_xS_y$ manifold). The evolution of the magnetization under multiple-quantum period results in a 1:2:1 triplet pattern from scalar coupling with the neighboring protons (**Figure 2.22**). The central ^1H 180° pulse interconverts the two outer lines and leaves the central resonance unaffected. To understand the dipolar coupling of the neighboring protons we will decompose the $2I_x{}^1S_y$ operator:

$$-2I_x^1 S_y = -2I_x^1 S_y \{|\beta\beta><\beta\beta| + |\beta\alpha><\beta\alpha| + |\alpha\beta><\alpha\beta| + |\alpha\alpha> \qquad (2.67)$$
$$<\alpha\alpha|\}$$

Note that the sum of the proton spin states is equal to one. The first and last terms of the expanded operator gives rise to L1 and L3, respectively, while the two central terms gives rise to L2 (**Figure 2.22**). On **Figure 2.22** one can observe that for the central line the orientations of the dipoles are opposite of each other cancel the dipolar field from each other. The dipolar field for the outer transitions are additive [243, 244]. A more quantitative description of the dipolar cancellation has been presented elsewhere [245]. Using the model-free formalism described earlier the relaxation rates of these two lines can be described as the following [243, 245]:

$$R_{2,CH}^{f}(L1, L3) = \frac{9}{20}\left(\frac{\mu_0}{4\pi}\right)^2 \frac{S^2\gamma_H^4\hbar^2\tau_c}{r_{HH}^6} + \frac{4}{45}\left(\frac{\mu_0}{4\pi}\right)^2 \frac{S^2\gamma_C^2\gamma_H^2\hbar^2\tau_c}{r_{CH}^6} \qquad (2.68a)$$

$$R_{2,CH}^{S}(L2) = 0 \qquad (2.68b)$$

Incredibly the central line does not relax at all due to ^{1}H-^{1}H and ^{1}H-^{13}C dipolar coupling. This is because the auto-correlation and cross-correlation terms of the relaxation completely cancel each other out while for the outer lines these are additive. This characteristic slow relaxation for the central transition was also realized for methylene (^{13}CH$_2$) groups in macromolecules by Prestegard and Grant[246]. In essence the multiple-quantum experiment has performed a spectroscopic conversion of a methyl group into a methylene.

After chemical shift evolution in ^{13}C and subsequent 90° pulse on ^{13}C the density matrix can be described as follows, retaining only the observable terms:

$$\sigma_c = -2I_x^A S_z \exp(-(\Delta R_{2,H}^S + R_{2,CH}^S t_1))\cos(\Omega_c t_1) \qquad (2.69)$$

$$- 2I_x^B S_z \exp(-(\Delta R_{2,H}^f + R_{2,CH}^f t_1))\cos(\Omega_c t_1)$$

The relaxation rates are described in **Figure 2.20** and Ω_C is the chemical shift of ^{13}C. After refocusing under scalar coupling, immediately prior to detection the density matrix can be described as follows:

$$\sigma_d = -I_y^A \exp(-(2\Delta R_{2,H}^S + R_{2,CH}^S t_1))\cos(\Omega_c t_1) - I_y^B \exp(-(2\Delta R_{2,H}^f \qquad (2.69)$$

$$+ R_{2,CH}^f t_1))\cos(\Omega_c t_1)$$

It can be seen that magnetization arising from the slowly relaxing coherences decay through the experiment by the term $\exp(2\Delta R_{2,H}^s + R_{2,CH}^s t_1)$ while the rapidly relaxing coherences decay through a rate of $\exp(2\Delta R_{2,H}^f + R_{2,CH}^f t_1)$. The rapid and slowly relaxing

components are completely separate in the HMQC experiment. Slowly relaxing ^{1}H coherences generated by the initial 90° 1H pulse are transformed into slowly relaxing multiple quantum coherence during the t_1 period. This magnetization is converted back to slowly relaxing ^{1}H coherence for detection. The HMQC sequence attains transverse relaxation optimization without sacrificing sensitivity as is performed using the ^{1}H-^{15}N based TROSY experiments[176], allowing it to retain much more sensitivity. Furthermore unlike with ^{1}H-^{15}N TROSY experiments, the entirety of the experiment is relaxation optimized. This facet is what has allowed the methyl-TROSY effect to be utilized for molecular systems an order of magnitude larger than for ^{1}H-^{15}N TROSY approaches. The methyl-TROSY approach however can only be retained if the only 90° ^{1}H pulse is at the start of the experiment [242, 243]. It has been shown that additional 90° pulses on the ^{1}H break the complete separation of the two classes of relaxation, breaking the TROSY effect from the HMQC. This has resulted in some limitation of the number of possible experiments using the methyl-TROSY effect.

2.8 Chemical Exchange: Study of molecular dynamics in the μs-s timescale

Studies of motions of macromolecules along the μs-ms timescale are all based on the phenomenon of chemical exchange. Chemical exchange, often called conformational exchange, occurs where a nucleus is rapidly undergoing a reversible conformational or chemical transformation [135] at equilibrium. NMR has emerged as the most powerful technique to study chemical exchange due to its ability to perturb the nuclear spins without altering the chemical environment; consequently much of what we understand through chemical exchange comes from NMR. An early example was the determination that the rearrangement of heptamethyl-benzenonium ion occurs through an 1-2 alkyl shift that makes all the methyl groups spectroscopically identical at sufficiently high temperature [247]. Common examples of these can be proton transfer

with solvent, bond rotation, movement of a catalytic loop and domain rearrangements. This leads to magnetization transfer between the two resonances and dephasing, or additional relaxation, or transverse magnetization. These are the foundation for a series of experiments that probe molecular motion along a wide timescale of motions. Most critically the timescale of these motions are able to probe motions that are most interesting for enzyme function, including protein folding, domain movement and allostery (**Figure 2.23**).

The most straightforward analysis of chemical exchange is performed using a two-site exchange model without any scalar couplings using a modified set of the Bloch equations [248]. Although approaches using the modified form of the Master equation have been developed [249, 250], the classical model has found the most universal application due to its simplicity and its application to powerful biological models related to cooperativity and allostery (Chapter 3):

$$\mathbf{A_1} \underset{k_{-1}}{\overset{k_1}{\rightleftharpoons}} \mathbf{A_2} \tag{2.70}$$

Where A and B are the two states, k_1 is the forward rate and k_{-1} is the reverse rate. Using this one can construct a matrix describing the kinetics as the following:

$$\begin{bmatrix} \dfrac{dA_1(t)}{dt} \\ \dfrac{dA_2(t)}{dt} \end{bmatrix} = \begin{bmatrix} -k_1 & k_{-1} \\ k_1 & -k_{-1} \end{bmatrix} \begin{bmatrix} A_1(t) \\ A_2(t) \end{bmatrix} = \boldsymbol{KA} \tag{2.71a}$$

$$k_{ex} = k_1 + k_{-1} \tag{2.71b}$$

$$k_1 p_A = k_{-1} p_B \tag{2.71c}$$

Where **K** is called the kinetic matrix, where all the kinetic relationships between all the states are located. The total exchange, k_{ex}, is the sum of all the kinetic rates and the populations, p_A and p_B, are directly proportional to the rates due to microscopic reversibility (Equation 2.71c). If we consider the states to be proportional to their magnetization then the chemical exchange can be included into the Bloch equations as demonstrated by McConnell [248].

$$\frac{dM_x^A}{dt} = \gamma(1-\sigma)[\boldsymbol{M}_A(t) \times \boldsymbol{B}(t)]_x - R_2^A M_x^A(t) - k_1 M_x^A(t) + k_{-1} M_x^B(t) \tag{2.72a}$$

$$\frac{dM_x^B}{dt} = \gamma(1-\sigma)[\boldsymbol{M}_B(t) \times \boldsymbol{B}(t)]_x - R_2^B M_x^B(t) + k_1 M_x^A(t) - k_{-1} M_x^B(t) \tag{2.72b}$$

$$\frac{dM_y^A}{dt} = \gamma(1-\sigma)[\boldsymbol{M}_A(t) \times \boldsymbol{B}(t)]_y - R_2^A M_y^A(t) - k_1 M_y^A(t) + k_{-1} M_y^B(t) \tag{2.72c}$$

$$\frac{dM_y^B}{dt} = \gamma(1-\sigma)[\boldsymbol{M}_B(t) \times \boldsymbol{B}(t)]_y - R_2^B M_y^B(t) + k_1 M_y^A(t) - k_{-1} M_y^B(t) \tag{2.72d}$$

$$\frac{dM_z^A}{dt} = \gamma(1-\sigma)[\boldsymbol{M}_A(t) \times \boldsymbol{B}(t)]_z - R_1^A \Delta M_z^A(t) - k_1 \Delta M_z^A(t) + k_{-1} \Delta M_z^B(t) \tag{2.72e}$$

$$\frac{dM_z^B}{dt} = \gamma(1-\sigma)[\boldsymbol{M}_B(t) \times \boldsymbol{B}(t)]_z - R_1^B \Delta M_z^B(t) + k_1 \Delta M_z^A(t) - k_{-1} \Delta M_z^B(t) \tag{2.72f}$$

$$\Delta M_z(t) = M_z(t) - M_0 \tag{2.72g}$$

The superscripts A and B denote the different states in chemical exchange. We will first examine the effect of chemical exchange on longitudinal magnetization. Using the simplifications from Section 2.1 (Equations 2.5-2.7) the longitudinal magnetization can be recast as

$$\frac{dM_z^A}{dt} = -R_1^A \Delta M_z^A(t) - k_1 \Delta M_z^A(t) + k_{-1} \Delta M_z^B(t) \qquad (2.73a)$$

$$\frac{dM_z^B}{dt} = -R_1^B \Delta M_z^B(t) + k_1 \Delta M_z^A(t) - k_{-1} \Delta M_z^B(t) \qquad (2.73b)$$

Recast in matrix form in the following:

$$\frac{d}{dt}\begin{bmatrix} \Delta M_z^A(t) \\ \Delta M_z^B(t) \end{bmatrix} = \begin{bmatrix} -R_1^A - k_1 & k_{-1} \\ k_1 & -R_1^B - k_{-1} \end{bmatrix} \begin{bmatrix} \Delta M_z^A(t) \\ \Delta M_z^B(t) \end{bmatrix} \qquad (2.74)$$

In a more general form [185]:

$$\frac{d}{dt}\Delta \boldsymbol{M_z} = (-\boldsymbol{R} + \boldsymbol{K})\Delta \boldsymbol{M_z} \qquad (2.75)$$

$$\Delta \boldsymbol{M_z} = \begin{bmatrix} \Delta M_z^A(t) \\ \Delta M_z^B(t) \\ \vdots \end{bmatrix} \qquad \boldsymbol{R} = \begin{bmatrix} R_1^A & 0 & ... \\ 0 & R_1^B & ... \\ \vdots & \vdots & \ddots \end{bmatrix} \qquad \boldsymbol{K} = \begin{bmatrix} -k_1 & k_{-1} & ... \\ k_1 & -k_{-1} & ... \\ \vdots & \vdots & \ddots \end{bmatrix}$$

$\Delta \boldsymbol{M_z}$ is a column matrix describing the longitudinal magnetization of all the state, $\boldsymbol{R}$ is a diagonal matrix describing the longitudinal relaxation of all the states and $\boldsymbol{K}$ is the matrix describing the entire kinetic process. The solution consists of solving a set of coupled differential equations using standard matrix algebra techniques. The functional form of longitudinal chemical exchange is identical to cross-relaxation through the NOE effect [187]. In fact these effects are spectroscopically indistinguishable, and studies of dynamics using longitudinal relaxation were not widespread until the application of heteronuclear 2D experiments [251, 252]. The general solution is given by the following [135, 253]:

$$\Delta M_z^A(t) = a_{AA}(t)M_z^A(0) + a_{AB}M_z^B(0) \qquad (2.76a)$$

$$\Delta M_z^B(t) = a_{BA}(t)M_z^A(0) + a_{BB}M_z^B(0) \qquad (2.76b)$$

$$a_{AA}(t) = \frac{1}{2}\left[\left(1 - \frac{R_1^A - R_1^B + k_1 - k_{-1}}{\lambda_+ - \lambda_-}\right)\exp(-\lambda_- t)\right. \tag{2.76c}$$

$$\left. + \left(1 + \frac{R_1^A - R_1^B + k_1 - k_{-1}}{\lambda_+ - \lambda_-}\right)\exp(-\lambda_+ t)\right]$$

$$a_{BB}(t) = \frac{1}{2}\left[\left(1 + \frac{R_1^A - R_1^B + k_1 - k_{-1}}{\lambda_+ - \lambda_-}\right)\exp(-\lambda_- t)\right. \tag{2.76d}$$

$$\left. + \left(1 - \frac{R_1^A - R_1^B + k_1 - k_{-1}}{\lambda_+ - \lambda_-}\right)\exp(-\lambda_+ t)\right]$$

$$a_{AB}(t) = \frac{k_{-1}}{\lambda_+ - \lambda_-}[\exp(-\lambda_- t) - \exp(-\lambda_+ t)] \tag{2.76e}$$

$$a_{BA}(t) = \frac{k_1}{\lambda_+ - \lambda_-}[\exp(-\lambda_- t) - \exp(-\lambda_+ t)] \tag{2.76f}$$

$$\lambda_{\pm} = \frac{1}{2}\left[R_1^A + R_1^B + k_{ex}[(R_1^A - R_1^B + k_{ex}(p_B - p_A)^2 + 4p_A p_B k_{ex}^2]\right] \tag{2.76g}$$

$\Delta M_z{}^A$ and $\Delta M_z{}^B$ are the intensities of state A and B respectively. The coefficients of the exchange matrix (a_{AA}, a_{AB}, a_{BA}, a_{BB}) can be observed directly through the zz-exchange experiment (**Figure 2.24**). By inspection of the equations it can be seen that only visible exchange crosspeaks occurs under slow chemical exchange. To simplify the equation, we will assume that $R_1{}^A = R_1{}^B$. Doing so simplifies the coefficients into the following:

$$a_{AA}(t) = [p_A + p_B \exp(-k_{ex}t)]\exp(-R_1 t) \tag{2.77a}$$

$$a_{BB}(t) = [p_B + p_A \exp(-k_{ex}t)]\exp(-R_1 t) \tag{2.77b}$$

$$a_{AB}(t) = p_A[1 + \exp(-k_{ex}t)]\exp(-R_1 t) \tag{2.77c}$$

$$a_{BA}(t) = p_B[1 + \exp(-k_{ex}t)]\exp(-R_1 t) \tag{2.77d}$$

In case of even populations, a_{AA} and a_{BB} relax evenly and also the exchange resonances, a_{AB} and a_{BA}, relax equally as well (**Figure 2.24**). However as the populations become unequal (p_A= 0.75 in **Figure 2.24**) the build-up and the relaxation of the four resonances are different. The a_{AB} resonance builds up significantly more than a_{BA} due to the increased population of state A and also the relaxation of a_{AA} and a_{AB} is much slower. Studies on chemical exchange using longitudinal relaxation not only provide the exchange rate between two states (k_{ex}) but also the relative populations of each of the states and these are directly manifested in the intensity of the resonances.

Studies of chemical exchange using longitudinal magnetization are limited to slow processes. However, faster processes can be studied observing the effect of exchange on transverse magnetization. First the M_x and M_y components will be combined in terms of complex notation, M^+ (Equation 2.7):

$$\frac{dM^{+,A}}{dt} = -\delta_A M^{+,A}(t) - R_2^A \Delta M_z^A(t) - k_1 \Delta M_z^A(t) + k_{-1} \Delta M_z^B(t) \qquad (2.78a)$$

$$\frac{dM^{+,B}}{dt} = -\delta_B M^{+,B}(t) - R_2^B \Delta M_z^B(t) + k_1 \Delta M_z^A(t) - k_{-1} \Delta M_z^B(t) \qquad (2.78b)$$

The evolution of the transverse magnetization is due to the chemical shift (δ), transverse relaxation (R) as well as the exchange between the two states (k_1 and k_{-1}). The evolution of the two states ($M^{+,A}$ and $M^{+,B}$) is linked together through chemical exchange. By observing the relaxation and chemical shift of one resonance, one can observe the presence of the second state because these are coupled together through chemical exchange. This is important for bio-macromolecules, as the second state are often called "excited" states due to their low population. In fact, a state that is $2k_bT$ higher in energy (1.2 kcal/mol at room temperature) will only be populated 13% [254].

The transverse magnetization can be cast in a general matrix form similar to that with longitudinal magnetization [157, 185, 255]:

$$\frac{d}{dt}\boldsymbol{M}^+ = (i\boldsymbol{\Omega} - \boldsymbol{\Lambda} + \boldsymbol{K})\boldsymbol{M}^+ \tag{2.79}$$

Where:

$$\boldsymbol{M}^+ = \begin{bmatrix} M_A^+(t) \\ M_B^+(t) \\ \vdots \end{bmatrix} \qquad \boldsymbol{\Omega} = \begin{bmatrix} -\delta_A & 0 & \cdots \\ 0 & -\delta_B & \cdots \\ \vdots & \vdots & \ddots \end{bmatrix}$$

$$\boldsymbol{\Lambda} = \begin{bmatrix} R_2^A & 0 & \cdots \\ 0 & R_2^B & \cdots \\ \vdots & \vdots & \ddots \end{bmatrix} \qquad \boldsymbol{K} = \begin{bmatrix} -k_1 & k_{-1} & \cdots \\ k_1 & -k_{-1} & \cdots \\ \vdots & \vdots & \ddots \end{bmatrix}$$

$\boldsymbol{M}^+$ is a column vector describing the transverse magnetization for all the states, $\boldsymbol{\Omega}$ is a diagonal matrix containing the chemical shift, in units of frequency, of all the states, $\boldsymbol{\Lambda}$ is a diagonal matrix with the transverse relaxation rate (R_2) of all the states and $\boldsymbol{K}$ is the kinetic matrix as described previously. The precession is described by:

$$\boldsymbol{M}^+ = \mathbf{1}\exp(i\boldsymbol{\Omega} - \boldsymbol{\Lambda} + \boldsymbol{K})\boldsymbol{M}^+(0) = \boldsymbol{A}\boldsymbol{M}^+(0) \tag{2.80}$$

The NMR spectrum is given by the real part of the Fourier transformation of $\boldsymbol{M}^+$. The solution has been solved for the basic two-site exchange in the literature [135, 253]:

$$\boldsymbol{A} = \begin{bmatrix} a_{11} & a_{12} \\ a_{21} & a_{22} \end{bmatrix} \tag{2.81a}$$

$$a_{11}(t) = \frac{1}{2}\left[\left(1 - \frac{-i\Delta\omega + R_2^A - R_2^B + k_1 - k_{-1}}{\lambda_+ - \lambda_-}\right)\exp(-\lambda_- t)\right. \tag{2.81b}$$

$$\left. + \left(1 + \frac{-i\Delta\omega + R_2^A - R_2^B + k_1 - k_{-1}}{\lambda_+ - \lambda_-}\right)\exp(-\lambda_+ t)\right]$$

$$a_{22}(t) = \frac{1}{2}\left[\left(1 + \frac{-i\Delta\omega + R_2^A - R_2^B + k_1 - k_{-1}}{\lambda_+ - \lambda_-}\right)\exp(-\lambda_- t)\right.$$

$$\left. + \left(1 - \frac{-i\Delta\omega + R_2^A - R_2^B + k_1 - k_{-1}}{\lambda_+ - \lambda_-}\right)\exp(-\lambda_+ t)\right] \tag{2.81c}$$

$$a_{12}(t) = \frac{k_{-1}}{\lambda_+ - \lambda_-}[\exp(-\lambda_- t) - \exp(-\lambda_+ t)] \tag{2.81d}$$

$$a_{21}(t) = \frac{k_1}{\lambda_+ - \lambda_-}[\exp(-\lambda_- t) - \exp(-\lambda_+ t)] \tag{2.81e}$$

$$\Delta\omega = \delta_A - \delta_B \tag{2.81f}$$

$$\lambda_\pm = \frac{1}{2}\left[\left(-i\delta_A - i\delta_A + R_2^A + R_2^B + k_{ex}\right)\right. \tag{2.81g}$$

$$\left. \pm \left[\left(-i\Delta\omega + R_2^A - R_2^B + k_1 - k_{-1}\right)^2 + 4p_A p_B k_{ex}^2\right]^{1/2}\right]$$

Where $\Delta\omega$ is the chemical shift difference between the two states. The NMR spectrum is given by the Fourier transform of the signals:

$$S(\omega) = Re\left|\int_0^\infty M^+(t)e^{(-i\omega t)}dt\right| \tag{2.80}$$

Although the resultant mathematics is complex, under limiting conditions some physical insight can be drawn. Typically for macromolecules the observation and quantification of chemical exchange is typically done by quantifying the contribution to transverse magnetization. The transverse magnetization can be decomposed into the component from nuclear spin relaxation (previously denoted as R_2^A and R_2^B, now denoted as $R_{2,0}$) and from chemical exchange (R_{ex}):

$$R_2(total) = R_{2,0} + R_{ex} \tag{2.81}$$

Under the condition of slow exchange ($\Delta\omega \ll k_{ex}$) there corresponds two resonances (δ_A and δ_B), with their intensity proportional to their population and the transverse relaxation from chemical exchange is given by:

$$R_{ex}^A = k_1 = p_B k_{ex} \qquad\qquad R_{ex}^B = k_{-1} = p_A k_{ex} \qquad\qquad (2.82)$$

Under conditions of fast exchange ($\Delta\omega \ll k_{ex}$) there is one resonance corresponding to the weighted average of the two states (both $R_{2,0}$ and δ). The exchange contribution to transverse relaxation is given by:

$$R_{ex} = \frac{p_A p_B \Delta\omega^2}{k_{ex}} \qquad\qquad (2.83)$$

The last limiting case is intermediate exchange ($k_{ex} \approx \Delta\omega$), in which chemical exchange provides the most contribution to transverse relaxation. These have low sensitivity and often unobservable in protein NMR spectroscopy. As a result these residues are often unobservable and are often coined as "exchange broadened." Simulation of exchange for a resonance in two states **(Figure 2.25)** shows many of the features involved in chemical exchange. For systems when the populations are highly asymmetric, which is very common for proteins, the minor population will experience a significantly larger degree of relaxation from the exchange (esp. for slow exchange as the populations become more asymmetric) and often is unobservable (note **Figure 2.25B**). In fact it has well noted in the literature that a single resonance should be taken as an indication of fast exchange [256].

Additional transverse relaxation due to chemical exchange arises from stochastic fluctuations of the chemical shift; R_{ex} is also dependent on the external magnetic field strength. From inspection of the dependence of R_{ex} on the slow and fast exchange timescale, it is evident that there is no field dependence in the slow exchange regime. In

the fast regime R_{ex} has a quadratic dependence with the magnetic field (from the $\Delta\omega^2$ term). For highly asymmetric cases of exchange ($p_A > 0.7$) and equivalent $R_{2,0}$ for both states, Millet and Palmer [257] estimated R_{ex} as the following:

$$R_{ex} \approx \frac{p_A p_B k_{ex}}{1 + (k_{ex}/\Delta\omega)^2}$$

(2.84)

Since for skewed populations the observation of one resonance cannot determine the timescale of exchange a constant of proportionality, α, which indicates the timescale of exchange was defined [257]:

$$\alpha = \frac{d \ln R_{ex}}{d \ln \Delta\omega}$$

(2.85)

As long as $p_A > 0.7$ for two-state exchange then the timescale of chemical exchange is defined as follows:

$$0 \leq \alpha < 1 \; (slow \; exchange)$$

$$\alpha = 1 \; (intermediate \; exchange)$$

$$1 < \alpha \leq 1 \; (fast \; exchange)$$

For $p_A = p_B = 0.5$ the transition between slow to intermediate to fast exchange can be easily recognized by inspection (**Figure 2.25**). However for the asymmetric case, where $p_A = 0.75$ the transition is not as obvious. It can be observed that a situation in slow exchange, the minor population is not observable and is more dramatically affected by the exchange phenomenon (**Figure 2.25**). In both cases when the dynamics are in the intermediate timescale there is a severe reduction in intensity compared to either the slow or fast exchange timescales. This, combined with low sensitivity from large systems due to nuclear spin relaxation, makes for dynamic systems, like PKA-C, difficulty to

study using NMR spectroscopy. However, the mere presence of exchange on the intermediate scale indicates exchange on the μs-ms timescale which alone is informative on the dynamics of the system.

To extract out kinetics, rates and populations, from chemical exchange the experimenter must induce a perturbation in the system and measure the change in transverse relaxation from the system. Several methods have been developed over the years, including inducing an rf field to tilt the magnetic field ($R_{1\rho}$ experiments)[258-261] to shaped pulses to manipulate the magnetization[262, 263]. The most widely used method is the Carr-Purcell-Meiboom-Gill (CPMG) spin echo method [200, 201]. In this approach (**Figure 2.26**) the magnetization is brought to the transverse plane with a 90° pulse along the x-axis and then a series of 180° pulses are applied along the y-axis in a fixed time interval. The 180° pulse will invert the direction of evolution of nuclear spins, including chemical exchange. If the time between 180° is equivalent this will refocus the evolution of chemical shift, scalar coupling and chemical exchange, but not nuclear spin relaxation coming from dynamics in the ps-ns timescale. When the pulsing rate is increased the degree in which R_{ex} is refocused is increased, leading to a smaller measured R_2 and increase in signal intensity (**Figure 2.26**). Measuring the systematic change in observed R_2 with respect to the pulsing rate allows for the spectroscopist to determine the kinetics and population of the chemical exchange phenomenon.

The inversion of procession by a 180° pulse can be mathematically written as the following:

$$M^+\left(\tau_{cp}\right) = AA^\dagger M^+(0) \tag{2.86}$$

A is the same matrix as defined earlier and $\textbf{A}^\dagger$ is the complex conjugate of **A** (inverted around the diagonal with all complex numbers multiplied by -1). After a general n number of 180° pulses the magnetization is expressed as the following:

$$M^+(T) = \left(AA^\dagger\right)^n M^+(0) \tag{2.87}$$

Where T is the total time of the CPMG duration and is τ_{cp} = T/2n. Note that the total time of procession for each **A** element is τ_{cp}/2. For the case for two-site exchange an analytical solution has been solved, first by Allerhand and Gutowsky [264, 265] subsequently recast in a more general form by Carver and Richards [266] (often called the Carver-Richards equation):

$$R_2\left(\frac{1}{\tau_c}\right) = R_{2,0} + \frac{1}{2}\left(k_{ex} - \frac{1}{\tau_c}cosh^{-1}[D_+ \cosh(\eta_+) - D_- \cosh(\eta_-)]\right) \tag{2.88a}$$

$$D_\pm = \frac{1}{2}\left(\pm 1 + \frac{\psi + 2\Delta\omega^2}{(\psi^2 + \xi^2)^{1/2}}\right) \tag{2.88b}$$

$$\eta_\pm = \frac{\tau_{cp}}{\sqrt{2}}\left((\psi^2 + \xi^2)^{1/2}\right)^{1/2} \tag{2.88c}$$

$$\psi = k_{ex}^2 - \Delta\omega^2, \xi = -2\Delta\omega(p_A - p_B) \tag{2.88d}$$

The analytical solution is a non-linear fit of the observed R_2 with respect to different pulsing rates (1/τ_{cp}). The equation is extremely non-linear, creating highly degenerate solutions. Several investigations have been performed regarding the robustness of the "fitting" of the Carver-Richards equation to extract accurate kinetic parameters. Ishima and Torchia [267] had both demonstrated that explicit fitting of the $R_{2,0}$ of both states are required to extract accurate population and kinetics. To address the highly degenerate nature of the solution to the Carver-Richards equation it is standard to carry out

experiments in different magnetic fields, as many fields as there are states (for a two-state exchange at least two magnetic fields) [268]. The kinetic parameters are all interdependent on each other; however a change in magnetic field alters $\Delta\omega$ but not the rate or the populations, allowing for an accurate evaluation of the chemical exchange using CPMG experiments.

The constant time CPMG experiment for ^{15}N edited experiments is shown in **Figure 2.27**. The experiment transfers transverse magnetization via INEPT to ^{15}N and performs a CPMG sequence on [15]N. As described earlier in section 2.4 and 2.5, the transverse magnetization for a coupled spin system will evolve between an in-phase (**S_x/S_z**) and anti-phase (**$2I_zI_x$/$2I_zS_y$**) operator and the relaxation of the in-phase and anti-phase operators are different (Equation 2.53). This will create a situation in which the observed nuclear spin relaxation will vary not because of the modulation of the R_{ex} but the differential relaxation of the in-phase and anti-phase operators during the CPMG period. The effective relaxation during the period is given by the following [220, 221, 269]:

$$R_{2,0} = \frac{1}{2}\left(1 + \frac{\sin \pi J_{NH}\tau_{cp}}{\pi J_{NH}\tau_{cp}}\right)R_{2,IS} + \frac{1}{2}\left(1 - \frac{\sin \pi J_{NH}\tau_{cp}}{\pi J_{NH}\tau_{cp}}\right)R_{2,S} \qquad (2.89)$$

$R_{2,0}$ is the observed transverse relaxation rate in the absence of chemical exchange, $R_{2,IS}$ is the relaxation of the anti-phase operator and $R_{2,S}$ is the relaxation of the in-phase operator. The relative contribution to relaxation of each operator in the CPMG element is plotted on **Figure 2.27B**. It can be observed for very fast pulsing rates (τ_{cp} <1/2J_{NH}) the scalar coupling evolution is effectively eliminated and the transverse magnetization will only relax with $R_{2,IS}$ (or with $R_{2,S}$, if a refocused INEPT is used instead of an INEPT), restricting the use of CPMG to studies of faster timescale dynamics. It is noted that when τ_{cp} = N/J_{NH}, where N is an integer, the observed transverse relaxation rate is equally weighed by the in-phase and anti-phase components. To overcome this limitation, Loria

and Palmer devised the U element in the middle of the CPMG pulse train [270]. This element converts the **$2I_zS_y$** magnetization into **I_x** magnetization in the middle of the CPMG pulse sequence, averaging the relaxation contribution from the in-phase and anti-phase operators. The final $R_{2,0}$ in a constant time CPMG is the average between $R_{2,IS}$ and $R_{2,S}$. This eliminates the dependence on the CPMG pulsing rate on the relaxation and allows for straightforward extraction of chemical exchange values using the Carver-Richards equation. This U element is now nearly universally applied to all heteronuclear CPMG experiments and has been shown to be universally applicable for various coupled spin systems [271-273].

As can be observed in **Figure 2.23**, the CPMG experiment does not cover a wide range of timescales, but does cover many of the biologically important functions within its range. Consequently the CPMG experiment has been the workhorse for applying chemical exchange to protein dynamics. Several enzymes have already been extensively studied using the CPMG pulse sequences, such as Dihydrofolate Reductase [118, 274], Protein Tyrosine Phosphatase I [16], and the 20S Proteosome [275]. Another approach to measure R_{ex} is to measure the total transverse relaxation and the nuclear spin relaxation rates and measure the difference between the two. Although, in theory, a traditional T_2 experiment (section 2.5, Equation 2.53) would allow for measurement of the "intrinsic" transverse relaxation rate, a traditional T_2 does not alter the CPMG frequency, hence the effect of R_{ex} is also included in the final measurement. Another approach is to recognize in macromolecules the *J(0)* term dominates relaxation and the intrinsic transverse relaxation is proportional to the cross-correlation term between dipolar coupling and CSA:

$$R_{2,0} = \kappa \eta_{xy} \tag{2.90}$$

κ is a proportionality constant that can be calculated [276, 277] or extracted from the trimmed mean of residues that do not experience chemical exchange [278]. This approach does not take into account the variability of the CSA between residues. This approach is useful because η_{xy} is not affected by chemical exchange and provides an unbiased reporter for transverse nuclear spin relaxation in the absence of chemical exchange. Each of the multiplets a ^{1}H-^{15}N single quantum transition is modified differently by the cross-correlation rate (**Figure 2.18**). The total transverse relaxation of each of the single quantum ^{15}N transitions is then given as the following:

$$R_2^\alpha = R_{2,0} + \eta_{xy} + R_1^H/2 + R_{ex} \tag{2.91a}$$

$$R_2^\beta = R_{2,0} - \eta_{xy} + R_1^H/2 + R_{ex} \tag{2.91b}$$

$R_1{}^H$ is the longitudinal relaxation of the scalar coupled ^{1}H spin caused by neighboring protons. An approximation for the measurement of $R_1{}^H$ is used as the following:

$$R_1^H \approx R_1^{2HzN} - R_1^N \tag{2.92}$$

$R_1{}^{2HzNz}$ is the longitudinal relaxation of the two-spin order state of the amide group and $R_1{}^N$ is the longitudinal relaxation of ^{15}N. For large proteins (>30 kDa) $R_1{}^N$ is negligible and is often ignored. Making the substitutions for $R_{2,0}$ and $R_1{}^H$ the R_{ex} can be expressed as the following:

$$R_{ex} \approx R_2^\beta - R_1^{2IzSz}/2 - \eta_{xy}(\kappa - 1) \tag{2.93}$$

This expression shows that if one can measure the $R_2{}^\beta$, $R_2{}^\alpha$ and $R_1{}^{2HzNz}$ relaxation rates then the chemical exchange contribution to transverse relaxation can be determined. These rates are measured by the TROSY Hahn-Echo experiment developed by Palmer and co-workers. Using the TROSY Hahn-Echo Experiment (**Figure 2.28**) the relaxation

rate of R2a and R2b is measured during the time T. T = N/J_{NH} where N is an integer to prevent the cross-relaxation between the two multiplets during the relaxation period (see also equation 2.89). The cross-correlation rate can be measured by the following:

$$\eta_{xy} = \frac{1}{2T}\ln\left[\langle S^+ I^\beta\rangle(T)/\langle S^+ I^\alpha\rangle(T)\right]$$

(2.94)

where, $\langle S^+ I^\beta\rangle$ is the intensity from the TROSY transition and $\langle S^+ I^\alpha\rangle$ is the intensity from the anti-TROSY transition. To find $R_1^{2HzNz}/2$ a modification to the pulse sequence (**Figure 2.28B**) is placed in the relaxation period. Using three experiments, the TROSY Hahn-Echo can measure R_{ex} by the following:

$$R_{ex} \approx \frac{1}{T}\ln\left[\frac{\langle 2I_z S_z\rangle(T/2)}{\langle S^+ I^\beta\rangle(T)}\right] - \frac{(\kappa-1)}{2T}\ln\left[\frac{\langle S^+ I^\beta\rangle(T)}{\langle S^+ I^\alpha\rangle(T)}\right]$$

(2.95)

where $\langle 2I_z S_z\rangle$ is the intensity of the resonance from R_1^{2IzSz} relaxation experiment. Measurement of R_{ex} using TROSY Hahn-echo does not take into account the variability of the CSA, and fluctuations are to be expected. As a result only large values of R_{ex} are used from the TROSY Hahn-echo. Secondly, since we are measuring R_{ex} the only closed relationship with k_{ex} and population exists in the fast or slow exchange regime (Equations 2.82 and 2.83). Consequently if kinetic information is to be extract using the TROSY Hahn-Echo then other experiments will have to be performed to determine the exchange timescale and the chemical shift difference between the two states.

Chapter III

Isothermal Titration Calorimetry and Binding Cooperativity

3.1 Isothermal Titration Calorimetry

Molecular recognition underlies the basis for all biological activity from signal transduction to enzyme catalysis. In particular the development of new pharmaceuticals is soundly rooted in the principles of specific disruption of molecular recognition processes. The free energy, ΔG, provides the thermodynamic driving force for all macromolecular complexes. Although there are many tools available to measure binding isotherms, such as NMR spectroscopy, fluorescence, and surface plasmon resonance, Isothermal titration calorimetry (ITC) is the only technique currently available to simultaneously measure ΔG and ΔH for a binding event, allowing for the full thermodynamic characterization of binding. For any chemical reaction, a change of heat accompanies the event, allowing one to trace the progression of the binding event by the measurement of heat with a known ligand concentration. As a result ITC requires no external tag and is currently the only true label free technique in measuring binding constants. As such it is also an ideal tool for measuring binding of small molecules to macromolecules and has been used extensively in studying mechanisms of drug binding [279]. The rate of heat change upon ligand binding is provided by the following:

$$dQ = d[MX]\Delta H°V \qquad (3.1)$$

Where dQ is the differential heat, d[MX] is the change in the concentration of the complex, $\Delta H°$ is the enthalpy of binding and V is the volume of the titration cell. The

modern ITC works by having two chambers, one filled with buffer, named the reference cell, and one filled with the macromolecule, the sample cell. The cell is composed of an inert conductive metal encased in an adiabatic shell. A small electrical current is used to maintain isothermal condition and the reference cell is used to measure the differential heat required to keep the sample cell at isothermal conditions. A computerized titration syringe adds a ligand of a known volume and concentration to the sample cell (**Figure 3.1**). The heat released through the event is measured by the change in the differential heat between the two cells to maintain the isothermal condition. The heat of a titration of ligand is measured by integrating the differential power required to maintain isothermal condition per titration point. As the titration progresses further there is less un-ligated macromolecule available and heat released per titration point decrease until the macromolecule is fully saturated. In very basic terms, the magnitude of the signal determines the ΔH of the binding event, while the shape of the curve determines the ΔG. The simplest case, and the most common binding event is one to one binding

$$M + nX \leftrightarrow MX^n \tag{3.2}$$

where M is the macromolecule, X is the ligand and n is the stoichiometry of the binding. The Wiseman Isotherm[280], which relates the change of heat with respect to total titrated ligand, is given by the following:

$$\frac{dQ}{d[X_{tot}]} = n\Delta H° V_0 \left[\frac{1}{2} + \frac{1 - (1+r)/2 - R_m/2}{(R_m^2 - 2R_m(1-r) + (1+r)^2)^{1/2}} \right] \tag{3.3a}$$

$$r = \frac{K_d}{[M_{tot}]} \tag{3.3b}$$

$$R_m = \frac{[X_{tot}]}{[M_{tot}]} \tag{3.3c}$$

In which $[X_{tot}]$ is the total ligand concentration inside the cell, $[M_{tot}]$ is the total macromolecule concentration and K_d is the dissociation constant. The value n is sometime used if there are multiple identical binding sites, but is often used as a scaling factor in the fitting procedure to compensate for concentration errors. The term "r" defines the shape of the titration curve and R_m is the molar extent the experiment is performed (**Figure 3.2**). To note, in ITC the experimenter is measuring the differential response to ligand binding during a titration. This is in direct contrast to other binding techniques, such as NMR and fluorescence anisotropy, which measure the direct response to ligand binding. As a result the binding profile need not look like a rectangular hyperbola like in other isotherms As such, ITC often has a characteristic sigmodial shape for non-cooperative single site binding and is confused as being cooperative. This feature of ITC has been used to determine multi-site binding and cooperativity using various differential binding models [281, 282].

ITC is also flexible in the sense that this has a very wide range of affinities can be measured, extending from K_d of 10^3 to 10^9 and even tighter binding can be accessed using competition binding assays [283]. This is in contrast to other techniques, such as NMR spectroscopy where only weak affinities may be measured accurately due to the high sample concentrations required. The extension to lower affinity binding using ITC was first described by Turnbull et. al. [284] and later expanded [285, 286]. These authors demonstrated that the characteristic sigmodial shape is not required for extracting accurate affinities using ITC. By extending the ligand concentration past two-fold excess and fixing n to one, accurate values for low affinity systems can be obtained. In this analysis n must be fixed to one, as there is not enough information in the data to allow

for the stoichiometry correction and consequently it is imperative for low affinity binding to measure accurate concentrations of ligand and protein prior to experiment.

3.2 Cooperativity

Cooperativity is a phenomenon in which the binding event of one ligand affects the binding or kinetics for another ligand. This allows for very specific processes to occur in an accelerated fashion, amplifies biomolecular signals, and allows for molecular adaptation. Chemically this is classically exhibited by the chelating effect of ethylenediaminetetraacetic acid (ETDA). The binding of one carboxylic acid to a divalent metal reduces the entropic penalty of binding, allowing for the subsequent carboxylic acids to bind with higher affinity. This approach is commonly utilized in fragment based drug screening in which small molecules which bind to different pockets of proteins are strung together, leading to a single higher affinity molecule [287, 288]. However, the binding energies of the two fragments are not simply additive as commonly described in the literature. This point has been reviewed extensively by Jencks [289]. Additivity of free energy of binding does not take into account the loss of translational and rotational entropy of the molecule upon binding and these elements. Ultimately the interpretation of ΔH and $T\Delta S$ terms, which can be very accurately measured using ITC, is very ambiguous despite the recent advances in spectroscopy [290, 291]and computation [292-294]. A primary factor in this is due to the dominating solvent effect in these reactions. For instance the ΔH of a binding event in ITC is scaled by the heat of protonation that is buffer dependent [295].

The coupling, or cooperativity, of two events can be described using a closed thermodynamic cycle. For the binding of two ligands, the procedure can be described as

shown in **Figure 3.3**. For such a cycle going from E to E·A·B is path independent, as such:

$$\frac{K_A}{K'_A} = \frac{K_B}{K'_B}$$

(3.4)

This ratio can be defined by a factor σ here the affinity of the second ligand is influenced by the first. This scalar factor can be linked to cooperativity in the following way:

$$\sigma > 1 \ (Positive\ Cooperativity)$$

$$\sigma < 1 \ (Negative\ Cooperativity)$$

$$\sigma = 1 \ (non-cooperative)$$

Since this a thermodynamic cycle the cooperativity is reciprocated each way, as in if the presence of ligand A increases the affinity of ligand B, then the opposite is also true. This method allows one to quantitate the degree of cooperativity between two ligands. In the literature this has also been called the coupling free energy , and thermodynamic linkage [296]. σ can be converted to a free energy by the following:

$$\Delta\Delta G_{int} = -RT \ln\frac{K_A}{K'_A} = -RT ln\ \sigma$$

(3.5)

$\Delta\Delta G_{int}$ is the free energy between the two ligands and R is the universal gas constant. This approach is a very general approach to measuring cooperativity between any two systems for any thermodynamic event (such as binding or unfolding). For example to measure the thermodynamic contribution of an amino acid to protein stability one can measure the free energy of unfolding (using either thermal or chemical denaturation) and define the following [297]:

$$\Delta\Delta G_A = \Delta G_U^A - \Delta G_U \tag{3.6}$$

$\Delta G_U{}^A$ is the free energy of stability for the wild type protein (E^A in **Figure 3.3**) and ΔG_U is the free energy of stability for the mutant (E in **Figure 3.3**). It should be noted that the $\Delta\Delta G_A$ for denaturation only represents the relative change of the folded state with respect to the unfolded state, hence is not extremely informative. However the measurement of the thermodynamic coupling between two amino acids within a protein [298, 299] has proven to be more fruitful. The interaction energy of the two amino acids, like with two ligands, maybe linked and the coupling energy between the two residues can be defined as the following:

$$\Delta\Delta G_{int} = \left(\Delta G_{AB}^U - \Delta G_A^U\right) - \left(\Delta G_B^U - \Delta G^U\right) \tag{3.7}$$

Where $\Delta G^U{}_{AB}$ is the free energy of unfolding of the WT protein, $\Delta G^U{}_A$ and $\Delta G^U{}_B$ is the free energy of unfolding of the mutant protein and ΔG^U is the unfolding free energy of the double mutant. This interaction energy presumes that there are no interactions between the two amino acids in the unfolded state, which is usually a safe assumption. Although originally devised to map out critical interactions for protein stability [300], this approach is being increasingly used to understand protein networks and how allostery is propagated through protein structure[301, 302].

Biology uses cooperativity to carry out functions it normally would be unable to. Hemoglobin, often taught in introductory biochemistry classes, is a classic example of cooperativity in biology. Cooperativity allows hemoglobin to efficiently bind O_2 to all four hemes when the concentration of O_2 is high, reuptaking oxygen from the lungs when available, and release all bound oxygen in tissues where the concentration is low. Two models were devised to account for cooperativity in hemoglobin (**Figure 3.4**). The first proposed was from J. Monod, J. Wyman, and J.P. Changeux [303] who showed that

cooperativity could be explained by assuming that each subunit had two conformational states, a T state which had low affinity for O_2 and a R state which has high affinity (MWC model). Even without the presence of ligand this dynamic two-state equilibrium was assumed to exist. Upon O_2 binding, the population of the R state of the other subunits increases explaining the resultant increased affinity of O_2 upon higher partial pressure. Since the MWC model explicitly considers the presence of two states, T and R, this has often been called a "two-state" model or "conformation selection."

Shortly after another work by D. Koshland, G. Nemethy and D. Filmer [304] proposed a second model (KNF model). In this model they also proposed two states T, which has low affinity for O_2, and R, with high O_2 affinity. In this model upon binding of O_2 to a subunit transforms into a high affinity state. The next O_2 binds subsequently as well until all four subunits are filled. In this model each binding event is sequential. Binding of O_2 increases the affinity of subsequent O_2 molecules.. As such this is also often called the "induced fit" model. As described both models were demonstrated to adequately describe the cooperative binding of O_2 to hemoglobin. Over the years the MWC model has gained in popularity in explaining allosteric cooperativity due to its mathematical and physical simplicity. The founding principles of the MWC model are the existence of two states and the presence of a conformational equilibrium. The MWC model only requires three variables to describe the cooperative binding phenomenon, the K_d of the R state, the K_d of the T state and allosteric constant:

$$L = \frac{P_T}{P_R} \tag{3.8}$$

P_T is the probability the state will be in the T state and P_R is the probability being in the R state. Despite the rough unreasonable assumption of having two states and containing a pre-existing equilibrium, this approach has been widely successful in explaining

allosteric cooperativity. This is largely because it has been found that many biological events function as two-state events and concepts from statistical mechanics can be applied to predict results [305, 306]. The probability of a state, i, is given by the Boltzmann distribution:

$$p_i = \frac{e^{-\beta E_i}}{Z} \tag{3.9}$$

where $\beta = 1/k_B T$ and E_i is the energy of the state i. Z is the partition function of all the available states and their energies. For a two-state system this turns into:

$$p_A = \frac{e^{-\beta E_A}}{e^{-\beta E_A} + e^{-\beta E_B}} = \frac{1}{1 + e^{-\beta \Delta E}} \tag{3.10}$$

where $\Delta E = E_B - E_A$. The last form of the equation is the one that is most useful because experimentally we cannot measure absolute energy (or of any state function), only changes. We can see that the functional form of the population of a two state system is a rectangular hyperbola. This is significant because many biological phenomenon, such a steady-state kinetics and binding, occur with the same functional form. If there are more than two states, then the partition function can be expanded to reflect additional states. These concepts have been utilized to understand allostery in intrinsically disordered proteins (IDPs) where the folding of a domain by binding alters its population and this enhances or decreases the stability of a neighboring binding site [307]. Such a two-state conformational ensemble approach to cooperativity compliments very well with NMR relaxation studies. As discussed in Chapter 2, chemical exchange allows one observe structural states that have a low population and techniques such as CPMG allows quantitative estimation of the population, structure and kinetics of these lowly populated states along the conformational landscape. These concepts and techniques have been utilized to detect and model a misfolding intermediate in amyloid formation [308] and to

detect drug binding in a lowly populated state [309]. Combining a statistical ensemble perspective of cooperativity with NMR spectroscopy allows for the direct study of conformational ensembles, both their flexibility and cooperativity.

Chapter IV

FLAMEnGO 2.0: an Enhanced Fuzzy Logic Algorithm for Structure-Based Assignment of Methyl Group Resonances

Fa-An Chao[1], Jonggul Kim[2], Youlin Xia[1], Michael Milligan[3], Nancy Rowe[3], Gianluigi Veglia[1,2*]

[1]*Department of Biochemistry, Molecular Biology, & Biophysics, and [2]Department of Chemistry, [3]Minnesota Supercomputing Institute - University of Minnesota, Minneapolis, Minnesota 55445*

4.1: Introduction

Recent development of methyl-TROSY based methodology on selectively protonated methyl groups in a highly deuterated background has significantly expanded the molecular weight range in which high-resolution NMR studies can be performed [275, 310, 311]. However, such studies require methyl group resonance assignments to provide site-specific probes to analyze structure, conformational dynamics, and molecular interactions. For small and medium size proteins, through-bond assignment strategies have been developed to correlate backbone carbon chemical shifts with methyl chemical shifts, either via TOCSY- or COSY-type transfer schemes [312-314]. For large proteins, however, these experiments are often insensitive. To assign the methyl groups in these cases, one can utilize extensive site-specific mutagenesis[315, 316]. Alternatively, it is possible to apply a "divide and conquer" approach, where protein domains are expressed individually, making it more amenable to current assignment procedures [317]. The above methods, however, are cumbersome and time consuming.

To address this problem, we developed a new methodology based on a previous algorithm proposed by the Matthews laboratory, MAP-XS[318, 319]. MAP-XS utilizes a pre-existing protein X-ray structure and exploits methyl-methyl NOESY networks to assign the methyl group resonances. Building on this approach, we previously developed a new and more efficient algorithm based on fuzzy logic and Monte Carlo sampling (FLAMEnGO or Fuzzy Logic Assignment of Methyl Group) that dramatically improved the accuracy (correctness) of the resonance assignment [320].

Here, we report version 2.0 of FLAMEnGO (version 2.0) with new and improved modules that incorporate methyl-methyl NOESY, paramagnetic relaxation enhancement (PRE), and methine-methyl TOCSY data, as well as partial assignments obtained from mutagenesis or through-bond experiments. FLAMEnGO 2.0 was tested on maltose

binding protein (MBP) and then applied to the more challenging C subunit of the cAMP-dependent protein kinase A (PKA-C). For the kinase, the application of FLAMEnGO 2.0 resulted in 100% assignment of Ile, 95% of Leu, and 100% of Val residue methyl groups. Overall, 98% of total methyl groups were assigned and ~80% of these were found to be correct when compared to traditional scalar-coupled experiments. The assignments obtained with FLAMEnGO 2.0 and sparse data are validated using methyl resonance assignments through-bond correlation experiments.

4.2: Material and Methods

Protein Expression and Sample Preparation. Expression and purification of PKA-C and RIIα (R213K) subunit were carried out as described previously [84, 321] (13, 14). Briefly, cell pellets of catalytic subunit and RIIα(R213K) were combined and lysed in buffer A (30mM Mops, 200µM ATP, 15mM $MgCl_2$, 5mM 2-mercaptoethanol, pH 8). After removing cell debris by centrifugation, the supernatant was incubated overnight with HIS-Select Ni^{2+} affinity gel (SIGMA, 1ml resin/1L culture) at $4^{o}C$. After incubation, the flow-through was collected and buffer B (buffer A containing 25mM KCl) was used to wash the Ni^{2+} resin. Finally, PKA-C was eluted using elution buffer A (buffer B containing 1mM cAMP), and the RIIα subunit was eluted using buffer B (buffer A containing 250mM imidazole). The three isoforms of PKA-C were further separated by HiTrap SP column (GE) chromatography, with a gradient from buffer A (20 mM KH_2PO_4, pH 6.5) to 30% buffer B (20 mM KH_2PO_4, 1.0 M KCl, pH 6.5) and a flow rate of 2.0 mL/min. The ternary complex PKA-C/AMPPNP/PKI_{5-24} was prepared using 12mM of AMP-PNP in NMR buffer (20mM KH_2PO_4, 90mM KCl, 60mM $MgCl_2$, 10mM DTT, pH 6.5). The final concentration of PKA-C was about 0.5 mM.

NMR spectroscopy. All NMR experiments were carried out on Bruker Avance III spectrometers operating at 850 or 900 MHz ^{1}H frequencies. The temperature was held

constant at 27°C. To map the methyl group fingerprint, we used constant-time (CT) [^{1}H, ^{13}C]-HMQC with wild-type PKA-C selectively labeled with [^{15}N,^{13}C]-Leu or [^{15}N,^{13}C]-Val. To obtain the PRE restraints, PKA-C mutants (K16C and I244C) were expressed in ^{15}N labeled M9 medium supplemented with 70mg/L of ^{13}C$_{me}$ α-ketobutyrate and 90 mg/L of ^{13}C$_{me}$ α-ketoisovalerate. Approximately 200 μM sample solutions were reacted with (1-Oxyl-2,2,5,5-tetramethylpyrroline-3-methyl) methanethiosulfonate, MTSSL, (10 times the protein concentration) and incubated for 3 hours at 4 ^{0}C. The MTSSL excess was removed by filtration. To quantify the PREs, two separate experiments were performed with both oxidized and reduced kinase as described previously [320].

To obtain the NOESY restraints, wild-type PKA-C was expressed in ^{15}N labeled deuterated M9 medium (80% ^{2}H$_2$O and 100% ^{2}H-glucose) supplemented with 70 mg/L of 2-ketobutyric acid-4-^{13}C,3,3-d$_2$ and 90mg/L of 2-keto-3-(methyl-d$_3$)-butyric acid-4-^{13}C. The final concentration of the enzyme was ~0.5 mM and experiments were performed at 27°C. The optimal mixing time (0.25 seconds) was chosen after analyzing the 2D NOESY build-up at different mixing times ranging from 0.1- 0.5 seconds. The 3D ^{13}C-^{13}C-^{1}H HMQC-NOESY-HMQC was collected with 32 scans using 2048 (proton), 80 (carbon), and 120 (carbon) complex points. For the methine-methyl TOCSY restraints, we used the same sample and carried out a 3D TOCSY-HMQC experiment to correlates intra-residue methine proton resonances with the methyl groups. The 3D TOCSY-HMQC spectrum was carried out using a 50 ms mixing time and 16 scans, with 2048 (proton), 90 (carbon), and 136 (proton) complex points.

For the backbone triple resonance and HMCM(CG)CBCA experiments, the kinase was expressed in ^{15}N labeled deuterated M9 medium (80% ^{2}H$_2$O and 100% ^{2}H$_7$,^{13}C$_6$-glucose) supplemented with 70 mg/L of 2-ketobutyric acid-^{13}C$_4$,3,3-d$_2$ and 90 mg/L of 2-keto-3-methyl-d$_3$-3-d$_1$-^{13}C-butyric acid. The final sample concentration was

~0.8 mM. TROSY-based HNCA and HN(CO)CA experiments were collected with 24 scans, using 2048 (proton), 70 (nitrogen), and 80 (carbon) complex points; while TROSY-based HN(CA)CB and HN(CO)CACB spectra were collected with 40 scans, using 2048 (proton), 70 (nitrogen), and 100 (carbon) complex points. The 3D methyl "out-and-back" HMCM(CG)CBCA experiment was performed with 32 scans, and 2048 (proton), 80 (methyl carbon) and 100 (C_β and C_α) complex points.

Theoretical basis of the fuzzy logic algorithm. In the first version of FLAMEnGO, we started from a random assignment for the methyl-TROSY spectra, using a 3D NOESY peak list generated from the methyl-methyl distances obtained from the crystal structure and fixing the NOE cutoff distance [320]. The peak list was then compared to the corresponding list obtained from experimental 3D NOESY. The congruence between simulated and experimental lists was established using a global scoring function:

$$G(x) = \max_{a \in A}[Match_{total}]$$

(4.1)

where the global score, G(*x*), is the maximum of the total matching function with an assignment, *a*, among all possible assignments, *A,* at a fixed NOE cutoff distance, *x* . This maximum of G(*x*) was calculated using a Monte Carlo algorithm sampling over all of the possible assignments. The total matching function includes the individual matching functions for the different restraints:

$$Match_{Total} = Match_{NOE} + Match_{CS} + Match_{PRE} + Match_{TOCSY}$$

(4.2)

Note that all of the restraints (NOE, chemical shift, PRE, and TOCSY) are scored for each NOE cutoff distance and assignment. All of the original matching functions are reported in our previous work[320]. The new implementations for FLAMEnGO 2.0 are summarized in the following synopsis.

1. *Higher tolerance for sparse and ambiguous data.* For large proteins undergoing intermediate conformational exchange, some methyl group resonances may be missing in the methyl-TROSY spectrum. In addition, severe peak overlap may prevent the unambiguous determination of the PRE restraints. In the old version of FLAMEnGO, those resonances were treated as unambiguous information. In contrast, here the missing information is assigned arbitrarily and introduced after the calculation. This logic is implemented in the new total matching function:

$$\text{Match}_{\text{total}} = \sum_{m \in M; \, r \in B} \text{Match}_{m,r}$$

(4.3)

where m indicates each single detectable methyl resonance, M indicates all of methyl resonances, r indicates the restraint associated to m, and B represents the total possible restraints. These states that contribute to the matching function will only arise from observable resonances with experimental restraints. Therefore, unobserved resonances are not taken into account and the algorithm does not try to find an assignment for these resonances.

2. *Improved assignment of Val and Leu resonances using methine-methyl TOCSY correlations.* In this new version, *methine-methyl* TOCSY correlations are used to assign methyl groups that belong to the same Val or Leu residues. For the methine-methyl TOCSY experiments on PKA-C, we utilized a sample containing a protonated methine group for all Val and Leu residues in a highly deuterated background. Therefore, a pair of methyl resonances originating from the same residue will share the same methine resonance. These restraints are quite powerful since they are independent of the structural models, reducing the sampling space and speeding up the assignment protocol. The matching function for the TOCSY restraints is formulated as it follows:

$$Match_{TOCSY} = \sum_{(m_1,m_2)\in C} e^{-4ln2\cdot|f(m_1)-f(m_2)/LW|}$$ (4.4)

where C represents all pairs of methyl resonances, m_1 and m_2, assigned to the same residues, f(*m*) is a function that associates an *m* methyl group with the corresponding methine proton,, and LW is the linewidth of the methine resonance in the ^{1}H dimension. The matching function calculates the agreement between the frequencies of methine resonances associated to an assigned pair of methyl groups.

3. *Improved version of the fuzzy logic step for NOE matching function.* Due to errors in phasing the 3D spectra or lack of resolution in the 3D spectra, NOE cross peaks between two methyl groups can have proton and carbon chemical shifts that differ slightly from those of the methyl groups. In the previous version of the algorithm (12), these differences in chemical shifts affected the score, even if these peaks were unambiguously assigned and located in well-resolved regions of the spectrum. To avoid this problem, we assigned scores for cross peaks located in a well-resolved region higher than those for cross peaks located in crowded regions. To take this into account, we modified the matching function:

$$Match_{NOE} = \sum_{p_1\in E} \begin{cases} 1; if\ |\{p_2 \in S | D(p_1,p_2) \le 1\}| = 1 \\ max_{p_2\in S}e^{-4ln2\cdot D^2(p_1,p_2)}; otherwise \end{cases}$$ (4.5)

where p_1 is the peak position of the experimental NOE, E, and p_2 is the peak position of the synthetic NOE, S,

$$D(p_1,p_2) = \left[\left(\frac{(x_1-x_2)}{LW_x}\right)^2 + \left(\frac{(y_1-y_2)}{LW_y}\right)^2 + \left(\frac{(z_1-z_2)}{LW_z}\right)^2\right]^{\frac{1}{2}}$$ (4.6)

where $p_i = (x_i, y_i, z_i)$ is the coordinate of the peak and LW_j is the linewidth in the j dimension. In the NOE matching function, the first conditional statement indicates a perfect match is considered. The second statement, gives a % confidence on the assignment.

4.3: Results

For ease of use, a GUI FLAMEnGO interface was built to allow users to incorporate several different types of NMR restraints and adjust parameters during the calculation (**Figure 4.1**). In the initial window, the user enters the input files consisting of the structural coordinates, the assigned chemical shifts, predicted chemical shifts, and the assignment swap file. The optional NMR restraints include NOE data (methyl-methyl or amide-methyl NOE data), PRE data (qualitative or quantitative data), TOCSY data (spin systems), and assigned amide shifts (only required for incorporation of amide-methyl NOE data). Moreover, a partial assignment can also be included in the list of arbitrarily assigned resonances. In the pop-out tab, one may set the number of steps in the Monte Carlo search, the range and interval for NOE distance cutoffs, as well as the amino acid types. At the end of the first run, the program plots the global score as a function of the NOE cutoff distance (**Figure 4.1**). In this auto-assignment algorithm, several calculations need to be performed to maximize the global score curve and provide a probability-based assignment. Since the global score function is non-decreasing, a negative slope may originate when insufficient sampling steps are carried out. The latter is a more likely scenario when the calculations are carried out with large proteins, where the conformational space to be sampled is larger. In this case, multiple calculations are needed to prevent the search algorithm from being trapped in local minima and to maximize the global score function. Using the mouse, the user can pick the maximum of the global score function, setting the optimal NOE distance cutoff. At this point, a small window appears to set the number of calculations to be performed

toward reaching the final probability-based assignment, which is then saved in a separate file (**Figure 4.1**).

The new version of the algorithm was first tested with synthetic data obtained from MBP. The purpose of this test was to: a) assess the accuracy of the new algorithm with sparse and ambiguous NOE data, b) establish how the search algorithm handles multiple experimental restraints, and c) test the tolerance for deviations of the X-ray structure from the solution structure. To generate the list of synthetic restraints (NOESY peak list), we used the crystal structure of MBP (1DMB) as an input. Chemical shift assignments and 3D methine-methyl TOCSY data were obtained from BMRB (access #7114). The NOE distance cutoff was chosen to be 7 Å. Sparse NOE data sets were generated by removing 70% of the cross peaks randomly. The effects of spin labels at positions S145C and S306C were back-calculated assuming that methyl groups within 15 Å of the spin label were completely quenched, those between 15 and 35 Å were partially quenched, and that the rest were not affected. Different combinations of data sets were input into versions 1.0 and 2.0 of FLAMEnGO and the results were compared. During the Monte Carlo sampling, we found that the new modules allow the algorithm to converge faster than the old version. To test the tolerance of FLAMEnGO 2.0 for structural deviations, different conformers from the solution NMR structural ensemble of MBP (2H25) were used as inputs. Indeed, we found that structural deviations lower the accuracy of the assignment when only NOE restraints are used. However, this problem can be solved by supplementing additional restraints such as PRE and TOCSY data.

Once validated with MBP, we applied FLAMEnGO 2.0 to the assignments of the methyl groups of PKA-C. This enzyme is quite challenging for through-bond NMR techniques, since in addition to its relatively large size (~41 kDa), it shows prominent conformational dynamics in the intermediate time scale [12, 56, 129] As an input structure, we utilized

the coordinates of the structure 1ATP, rebuilding the hydrogen atoms using CHARMM19 [322]. To predict the ^{1}H and ^{13}C chemical shifts of the methyl groups, we used CH3Shift [323]. The deviations from the experimental and the calculated methyl chemical shifts were minimized using the chemical shift matching function described previously (**Figure 4.2A**) [320]. Residue-type assignments were performed using selective amino acid labeling and mapped with CT-HMQC experiments.

Three sets of experimental restraints (PRE, methyl-methyl NOESY, and methine-methyl TOCSY) were utilized to determine the most probable assignment. Long-range distance PRE restraints were obtained by engineering MTSSL spin labels at two PKA-C sites, K16C and I244C. The intensity ratios of resonances from oxidized samples to those from reduced samples provide distance restraints for the methyl groups with respect to the positions of two spins labels. The average positions of these two spin labels in the crystal structure were calculated using XPLOR-NIH [324]. Short-range distance restraints were obtained from the 3D HMQC-NOESY-HMQC data on methyl groups. The 3D TOCSY-HMQC intra-residue correlations between methine and two methyl groups were used to assign pairs of methyl resonances belonging to the same spin system. Finally, two site-specific assignments were obtained using mutagenesis (I244 and I315) and enforced during the calculations.

In the first iteration, the probabilistic assignment of methyl group resonances was generated using each group of experimental restraints separately to evaluate their individual performance. In the second iteration, all of the restraints were combined into a single run. Once the optimum NOE cutoff distance was found, the calculation was repeated to provide a probabilistic confidence value for each residue. We found that the PRE data alone are not sufficient to generate an assignment with high confidence (**Figure 4.2B**). In contrast, when only NOE restraints are included, the confidence is

significantly higher, although the assignment thus generated does not independently satisfy the experimental PRE restraints (92% percent of the assignment). Once both PRE and NOE data are combined, the overall confidence slightly decreases (**Figure 4.2B**), but most of the experimental PRE restraints are well satisfied (99% of the assignment). The latter does not mean that the assignment is less accurate; rather the increased number of restraints may converge to the correct assignment. The incorporation of TOCSY restraints with PRE and NOE data boosts the confidence value dramatically (**Figure 4.2C**). To calculate the final statistics and assignment, 100 randomized calculations using all the experimental data were performed at the optimized NOE cutoff value (10.2 Å). The ten sets of assignments with the highest scores were used to determine the final assignment. The preliminary result shows that 92% of methyl groups are assigned and 80% of the assignments have above 90% confidence.

Site-directed mutagenesis on V191 and L82 was also performed to assess the overall accuracy of the assignment. Both V191 methyl groups are assigned with 100% confidence, but both methyl groups of L82 resulted unassigned. Although site-specific labeling (V191C) is consistent with the assignment, the identification of L82 methyl groups was ambiguous and these methyl groups were erroneously assigned to L27 with 70% confidence level. Upon closer inspection, we found that the mis-assignment was due to the lack of experimental restraints for L27. We then repeated the calculations, fixing the assignments for both V191 and L82. Imposing these restrains did not change the general outcome and we obtained a global score with a confidence level greater than 90%, confirming that the L82 assignment via mutagenesis is consistent with the entire experimental data set. The same scenario was observed for the other mutagenesis data. Their inclusion in the calculations resulted in 100% assignments for Ile, 100% for Val,

and 95% for Leu methyl groups (**Figure 4.3**). Overall, FLAMEnGO 2.0 calculations resulted in ~98% of total methyl group assignments.

Finally, to validate the accuracy of the assignment provided by FLAMEnGO 2.0 for PKA-C, we carried out several through-bond experiments to correlate the α and β carbon resonances (assigned with HNCA, HN(CO)CA, HN(CO)CACB, and HNCACB) with the methyl groups (HMCM(CG)CBCA) (**Figure 4.4**) (4,18,19). These experiments resulted in a total of 109 out of a possible 121 correlations established between the methyl groups and the corresponding α and β carbon resonances from the backbone based experiments: 37/40 for Val, 51/60 for Leu, 21/21 for Ile. The through-bond correlation experiments confirmed the assignment of 80% of the available residues from FLAMEnGO 2.0 and identified 16% as incorrect. (**Table 4.1**). Most of these mis-assigned resonances (~73%) are due to spatially close methyl groups (**Figure 4.5**), where the correct assignments were obtained by simply swapping their assignments. Other mis-assigned resonances are related to methyl groups positioned at the surface of the protein, which do not have inter-methyl NOE restraints.

To compare the performance of FLAMEnGO with the MAP-XS auto-assignment software, we used identical input data and constraints. Since MAP_XS does not utilize qualitative PRE restraints, the PRE data was not used in the calculations. Twenty-five iterations of the auto-assignment were carried out and the assignments with the top ten scores were used. When compared to the through-bond experiments only 59% of the available resides were assigned with 1.6% of the residues assigned incorrectly. In contrast, FLAMEnGO 2.0 gives 80% assignments with an additional 15% residues, whose assignments are swapped. The latter is due to residues that are spatially close in the crystal structures and impossible to discriminate based on our approach.

4.4: Discussion

FLAMEnGO 2.0 presents several improvements over the original version, providing better handling of missing resonances, including TOCSY-based restraints, and with an improved fuzzy logic algorithm. Incorporation of PRE restraints [325] was implemented so that the intensity reduction pattern was considered for the calculations. In addition, the new implementation takes into account that many resonances are not detectable in the methyl-TROSY spectra due to exchange broadening. In this case, missing resonances are excluded from the calculations, randomly assigned to methyl groups with zero probability and excluded from the unambiguous list. The latter will not interfere with the assignment of the other resonances. Another significant aspect is the implementation of the methine-methyl TOCSY data, which improve the assignment procedure for Leu and Val residues by linking them to the shared methine proton. Finally, the new version of the fuzzy logic algorithm takes into account the resolution of the methyl-resonances in the TROSY spectrum, with higher confidence attributed to well-resolved regions.

For the assignment of PKA-C, a combination of 3D NOESY, PRE, and methine-methyl TOCSY restraints were utilized, each with their own experimental challenges. In the case of PKA-C, the NOESY experiment was the least sensitive, which may be due to conformational dynamics of the enzyme and incomplete deuteration of the sample. In fact, only 26% of the predicted NOE cross peaks were detectable in a NOESY at 250 ms mixing time. The optimized NOE cutoff distance for the global score function was determined to be ~10 Å, which is unlikely to reflect the experimental distance. A possible explanation is the existence of a deviation between the crystal structure and the solution-state structure. However, our tests show that FLAMEnGO 2.0 has high tolerance for these structural deviations. For long-distance restraints, PRE data are the most sensitive

experiments. The total PRE restraints contain 78% of the simulated data, assuming no peak overlapping ambiguity. With the assignment of PKA-C, we have selected a structural form that has been previously shown to be be relatively rigid to reduce the ambiguities on the methyl group position in the structure. Finally, it should be noted that the methine-methyl TOCSY experiment is a quite sensitive experiment, less ambiguous than the NOESY cross peaks for crowded regions. For PKA-C, 97% of the expected TOCSY cross peaks were detected with only a 4 day experiment.

The assignment from FLAMEnGO 2.0 was validated using the through-bond approach. Mis-assignments were mapped onto the crystal structure (**Figure 4.5**), and it was found that these incongruences originate from spatially close methyl groups whose assignments are swapped. In the case of the kinase, this was expected since only 26% of the theoretical NOE contacts were observed. Other mis-assignments were found on the surface of the protein, due to the lack of NOE cross peaks. This result also highlights the quality of the NOE cross peaks, which, however sparse, are essential for an accurate assignment. FLAMEnGO was also compared with MAP-XS (Supp Fig.5). We found that FLAMEnGO provides a higher percentage of assignment with respect to MAP-XS. Note that FLAMEnGO also provides ~15% of incorrect assignments due to the proximity of residues in the crystal structure. In this case, site-specific labeling can be utilized to further reduced the ambiguity and increase the number of methyl group assigned. Overall, the logic used to assign the NOE connectivity pattern is different in the two algorithms. While MAP-XS utilizes a strict binary logic, FLAMEnGO's fuzzy logic is more flexible and enables a more exhaustive search. Due to the varied nature of the logic used in both programs there were a significant number of correct assignments that were not degenerate between the two programs, and one would benefit from using both during the assignment process.

Overall, the computational approach with sparse and ambiguous data proved to be as accurate as the through-bond approach, with a significant reduction of experimental time. For the kinase, the total experimental time necessary to generate meaningful inputs for FLAMEnGO 2.0 was approximately 12 days. In contrast, the through-bond approach requiring the Cα and Cβ chemical shifts from the backbone and methyl groups required approximately 26 days by using the TROSY-based HNCA, HN(CO)CA, HNCACB, HN(CO)CACB and the HMCM(CG)CBCA (4) experiments. Most importantly, FLAMEnGO has been shown to work with comparable accuracy as the through-bond approach, but will be successful in situations where sensitivity is lacking in the latter, especially with increasing molecular weight, as one can utilize the full methyl-TROSY effect throughout the data acquisition. A near complete assignment of ~95% complete assignment with high accuracy was obtained only when all the data sets and approaches were combined for a self-consistent assignment. We demonstrate here that FLAMEnGO in the future can serve as an essential piece for such multi-faceted assignment approaches that are becoming more routine as higher molecular weight systems are being studied.

4.5: Conclusion

In conclusion, the enhanced version of the FLAMEnGO algorithm has higher tolerance for sparse and ambiguous data and can incorporate multiple data sets from different spectroscopic techniques, making it more flexible and efficient. FLAMEnGO 2.0 can be used to assist the resonance assignment when incomplete through-bond correlations are available or it can be used as a standalone method for larger macromolecular systems, where through-bond correlations experiments fail.

4.6: Footnotes

Chapter V

A Semi-Automated Assignment Protocol for Methyl Group Side-Chains in Large Proteins

Jonggul Kim[1], Yingjie Wang[1], Geoffrey Li[1], and Gianluigi Veglia[1,2]*

[1]Department of Chemistry- University of Minnesota, Minneapolis, MN 55455; [2]Department of Biochemistry, Molecular Biology, and Biophysics– University of Minnesota, Minneapolis, MN 55455.

5.1: Introduction

Isotopic labeling is at the heart of NMR spectroscopy. After the pioneering work in the early '60s by several research groups [326-329], more complex labeling schemes have been used to attenuate transverse relaxation and push the boundaries of NMR analysis of large macromolecular complexes [330-332]. A significant step forward was made when non-labile protons in proteins were substituted by deuterons, ameliorating the relaxation from ^{1}H-^{13}C and ^{1}H-^{1}H dipole interactions, increasing sensitivity and resolution, thereby rendering proteins larger than 20 kDa amenable to structural NMR studies [333, 334]. Although complete deuteration has been used for backbone assignments in conjunction with transverse relaxation optimized spectroscopy (TROSY), NOESY-based experiments benefit of incomplete (or fractional) deuteration, which preserves some protons for distance measurements [334]. Another quantum leap in the NMR structure determination of large complexes was made by Kay and co-workers, who developed a biosynthetic strategy in which metabolic precursors were protonated, resulting in specific methyl group protonation in a highly deuterated background [231, 232]. Since then, this labeling strategy has expanded to include selective methyl group labeling on isoleucine, valine, leucine, methionine [335], threonine [336], and alanine [337]. Although selective labeling schemes for aromatic side chains will certainly have an impact both in structure determination and dynamic characterization of large proteins [332], in this paper we will focus on the use of methyl groups for the spectroscopy of large systems [243] akin to the TROSY method developed for backbone amides [176]. Following these methyl labeling schemes, quantitative studies on binding, structure, and conformational dynamics of proteins that are several hundred kDa are emerging, such as large molecular machinery [275, 310, 338], allosteric enzymes [339], chaperones [340], and protein thermodynamics [341].

5.2: Labeling of side chain methyl groups for large proteins

The first methyl labeling schemes was published in 1997 by Gardner and Kay[231], who obtained a selective protonation of amino acids in which the direct biosynthetic precursor to isoleucine, 2-ketobutyrate, was enzymatically and chemically prepared with selective $^{13}CH_3$ labeling in a highly deuterated background. Exploiting the Escherichia coli (*E. coli)* biosynthetic pathway, this protocol enables the specific $^{13}CH_3$ labeling of the Cδ of Ile, while the remaining non-labile protons are replaced by deuterons. The incorporation of 2-ketoisovalerate, in a similar fashion, leads to selective labeling on the Cδ and Cγ of leucine and valine, respectively [232], resulting in the so-called "ILV labeling" scheme (**Figure 5.1**). Nowadays, these biosynthetic precursors are commercially available in a variety of labeling schemes for assignment, structure determination, and dynamics studies. Selective labeling of the Cγ methyl of isoleucine has also been devised [233], but is uncommon due to the superior spectral qualities of the Cδ methyl group. Usually, selective labeling of other amino acids is achieved through direct addition of the amino acid to the growth medium during cell growth. For alanine and methionine, this is most commonly accomplished by directly incorporating the amino acid prior to induction (30 minutes to 1 hour) at final concentrations of 100-250 mg/L [340, 341] for Met and from 100-800 mg/L for alanine [337, 341]. An alternate approach is to engineer cysteine and react with ^{13}C-methyl-methanethiosulfonate (^{13}C-MMTS) to produce a methionine mimic [342]. Kay and coworkers have also developed an *in vitro* biosynthetic method to produce U-[^2H],Thr-γ2[$^{13}CH_3$] ($^{13}CH_3$ labeled threonine in a deuterated background) [336]. Threonine is a direct biosynthetic precursor to 2-ketobutyrate, leading to isoleucine methyl (Cδ) labeling. Since threonine is converted to glycine either from threonine aldolase or threonine dehydrogenase/2-amino-3-ketobutyrate ligase, the authors used 100 mg/L of d_5-glycine along with 50 mg/L of U-

[^{2}H] Thr-γ2[^{13}CH$_3$] and 50 mg/L of 2-ketobutyrate for specific threonine and isoleucine labeling (**Figure 5.1**).

5.3: Methyl labeling protocol for the cAMP-dependent Protein Kinase A (PKA-C)

In this outline, we highlight a method to label the ^{13}C isoleucine (Cδ), leucine, and valine methyl groups for the catalytic subunit of cAMP-dependent Protein Kinase A (PKA-C) (**Figure 5.2**). Specific labeling of side-chain methyl groups is achieved using the M9 minimal medium typically used for ^{15}N labeling of proteins with the addition of appropriate amounts of methyl labeling precursors. As the protocols for overexpression and purification of PKA-C have been described extensively [321, 343, 344], we will report only the most crucial steps (**Figure 5.3**). Note that for binding titrations studies we mostly used 2D NMR experiments and the favorable relaxation properties of PKA-C methyl resonances make it possible to use fully protonated kinase samples. However, for the 3D ^{13}C-^{13}C methyl NOESY experiments we utilized 80% D$_2$O for the expression protocol. In our hands, the utilization of a fully perdeuterated medium resulted in a scarce overexpression of the kinase. Nonetheless, for larger proteins with molecular weights greater than 100 kDa, high levels of deuteration are often necessary. In the latter case, over-expression of proteins in 100% D$_2$O is highly strain-, vector-, and protein-dependent and requires optimization for each of these variables. Several tips for the optimization of perdeuterated growths have been provided by Gardner *et al.* [345].

Materials

Note: All stocks should be sterile before usage.

LB Media (1L)

      10.0 g Tryptone

      5.0 g Bacto-Yeast

10.0 g NaCl

M9 Media (1L)

3.0 g KH_2PO_4

12.8 g $Na_2HPO_4 \cdot 7H_2O$

1.0 g NH_4Cl (for ^{15}N labeling use [15]NH_4Cl)

0.5 g NaCl

Vitamins (50mL)

5.0 mg Ca D(+)-panthothenate

5.0 mg Biotin

5.0 mg Folic Acid

5.0 mg Niacinamide USP

5.0 mg Pyridoxal 5-phosphate monohydrate

1000 mg Thiamin

Trace Metals (1x, 100mL)

50 mM $FeCl_3$

20 mM $CaCl_2$

10 mM $MnCl_2$

10 mM $ZnSO_4$

2 mM $CoCl_2$

2 mM $CuCl_2$

2 mM $NiCl_2$

2 mM Na_2MoO_4

2 mM Na_2SeO_3

2 mM H_3BO_3

Note: More details in the preparation of Trace Metal solution is provided at Studier et. al.[346]

Keto-acid Stock (10 mL, water)

2-ketobutyric acid-4-^{13}C sodium salt (70mg/L of media)

2-keto-3-(methyl-^{13}C)-butyric acid-4-^{13}C sodium salt (90mg/L of media)

Calcium Chloride

Magnesium Sulfate

D-glucose

Ampicillin

Isopropyl β-D-1-thiogalactopyranoside (IPTG)

1. Place 500 mL of M9 media into baffled flasks and autoclave.
2. Grow BL21 (DE3) cells containing the pRSET plasmid with PKA-C overnight in LB media (with Ampicillin).
3. In the morning the culture should be in log phase growth. Then pellet the BL21 (DE3) cells under 2200xg for 10 minutes. During this time prepare add the following per 500 mL flask containing M9 media:
   a. 10 ml of 20% w/v glucose
   b. 5 mL of Vitamin stock
   c. 1 mL of 1 M MgSO$_4$.
   d. 1 mL of 50 mM CaCl$_2$
   e. 500 μL of 1000x Trace Metals
   f. 500 μL of 10% w/v Ampicillin stock
4. Resuspend the cell pellet in M9 media and allow to growth for at least an hour to allow for the culture to adapt to the adjusted metabolism. We usually have an initial OD$_{600}$ of ~0.8.
5. Once the cells reach log phase growth, lower the temperature to 24°C and add in the appropriate concentration of keto-acids into each flask (70 mg/L of 2-ketobutyric acid-4-^{13}C sodium salt and 90 mg/L of 2-keto-3-(methyl-^{13}C)-butyric acid-4-^{13}C sodium salt).
6. After one hour, induce with 0.4 mM IPTG for at least 5 hours. Harvest under 8000xg for 25 minutes at 4°C.

Purification of PKA-C

<div align="center">Buffer A (1L)</div>

- 30 mM MOPS (3-(N-morpholino)propanesulfonic acid)   (6.28g)
- 15 mM MgCl$_2$ (3.05g)
- 5 mM β-mercaptoethanol   (352μl/L of buffer)
- pH 8.0

- 30 mM MOPS   (6.28g)
- 15 mM $MgCl_2$
      (3.05g)
- 25 mM KCl   (1.86g)
- 5 mM β-mercaptoethanol   (352µl/L of
  buffer)
- pH 8.0

Elution Buffer (100mL)

- 30 mM MOPS   (628 mg)
- 15 mM $MgCl_2$ (305 mg)
- 25 mM KCl   (186 mg)
- 1 mM cAMP   (33 mg)
- 5 mM β-mercaptoethanol   (35.2µl/100 mL of
  buffer)
- pH 8.0

Cell Lysis

1) Re-suspend PKA and the His_6-RIIβ(R213K) overexpressed cells Buffer A. Make sure the pellet containing RIIα was grown at least 1/3 of the volume of your PKA.
2) Grind the cells in ice for approximately 10 minutes then lyse using a French press using 1000 psi of pressure.
3) Spin down the solution at 20,000 rpm for 40 minutes at 4°C. Mix with 10 mL of NiNTA slurry and batch bind at 4°C for a minimum of 3 hours.

Elution

1) Run the slurry through the column (make sure the resin does not dry).
2) Wash with Buffer B (~200 mL). If preferred the wash buffer can also include 20 mM Imidazole to remove some non-specific binding proteins. This will not affect the PKA:RIIα interaction.
3) Elute PKA-C using 150 mL of elution buffer.
4) To remove RIIα wash with ~50 mL of Buffer B with 250 mM imidazole.

Although mass spectrometry is a viable method to assess the labeling of proteins with stable isotopes, the most straightforward way to determine the correct isotopic incorporation is to acquire the [^{1}H,^{13}C]-HMQC spectra of the system of interest. The

characteristic chemical shift patterns allow one to easily identify isoleucine (Cδ), leucine, and valine methyl groups as they resonate in distinct regions of the ^{1}H/^{13}C correlated spectra. Due to the high sensitivity of methyl groups, 2D spectra of large proteins (~40 kDa) with reasonable sensitivity can be measured with modern spectrometers with relatively modest concentrations (~200 μM). A [^{1}H,^{13}C]-HMQC spectrum of apo PKA-C shows the labeling and spectral quality of ILV-methyl groups labeling (**Figure 5.4**). Below, we outline the NMR sample preparation that we use for *apo* form of PKA-C:

Materials

Potassium Phosphate Monobasic

Potassium Chloride

Dithiothreitol

Magnesium Chloride

Sodium Azide

10kDa Centrifugal Concentrator

99+% Deuterium Oxide

Long-tip Pipet, 13-1/4"

5 mm Shigemi Tube

1. Dialyze purified PKA-C under NMR buffer (20 mM KH$_2$PO$_4$, 90 mM KCl, 10 mM DTT, 10 mM MgCl$_2$, 1mM NaN$_3$ at pH 6.5) overnight at 4°C. Initial concentration of PKA-C should < 5 μM.
2. Concentrate PKA-C at 2400xg using a 10kDa cutoff centrifugal concentrator at 4°C until the enzyme is concentrated to ~200 μM. The protein concentration can reliably be measured by absorbance measurement at 280 nm using an extinction coefficient of 52060 M^{-1}cm^{-1}.
3. Pipette 250 μL (for Agilent spectrometers) or 300 μL (for Bruker spectrometers) and add 12.5 or 15 mL of D$_2$O (~5% v/v), respectively. Transfer the protein solution into a shigemi tube using a long-tip pipet. Place the plunger inside the tube until the plunger is evenly covered with no visible bubbles in the solution.

4. After spectrometer set up (spectrometer details are dependent on model and spectrometer) acquire a ^{13}C-HMQC spectrum.

5.4: Semi-Automated Methyl Group Resonance Assignment Strategies

The Achilles' heel for methyl group NMR studies is site specific assignments of the resonances. For backbone studies, the assignment is carried out by *walking* through the peptide backbone through a series of triple resonance NMR experiments [170, 171, 178, 179]. For the assignment of methyl groups resonances, the classical approach requires TOCSY-based spectroscopy with the magnetization starting on the methyl groups and transferred *via* ^{13}C-^{13}C couplings to the protein backbone [347]. This approach, however, is not applicable to methyl group side-chains of large proteins, such as the 82 kDa malate synthase G with a correlation time of ~46 ns [348]. In the latter case, the branched amino acids present a bifurcation of the magnetization pathways with a significant loss of transfer. Although several experiments have been tailored to correlate backbone Cα, Cβ and C' chemical shifts to methyl groups [312, 314, 349], the relatively fast transverse relaxation rates of these nuclei for larger proteins or conformational exchange phenomena (see the case of PKA-C [57]) do not allow to carry out sequential backbone assignments. A possible solution is to use a *divide and conquer* approach in which proteins are dissected into several smaller domains and the assignments are pieced together [317, 340]. However, there are many large monomeric proteins that are unamenable to this approach. An alternative strategy is to use site-specific mutations to exchange amino acids with methylated side chains for glycine or other amino acids. The latter method, however, is very cumbersome and time-consuming, particularly for very large systems. In response to this need, Matthews and co-workers proposed an automatic method that uses both NMR and X-ray structural

data to back calculate methyl side chain assignments [318]. This automated procedure was designed to rapidly assign methyl groups using full-length proteins and without mutagenesis [318]. This approach requires a crystal structure as a starting point to calculate methyl group chemical shifts and synthetic NOEs. An algorithm is then used to rank the scores of the initial (seed) assignment against the experimental NMR data. The latest version of this method features an improved algorithm with no manual intervention in NOESY spectra peak picking.

Inspired by this work, we developed an approach that uses a similar philosophy, but utilizes a probabilistic method to tackle assignment problem. Specifically, we improved the efficiency of the phase space search using *fuzzy logic* coupled with Monte Carlo sampling. This approach, named FLAMEnGO (Fuzzy Logic Assignment of Methyl Groups), utilizes NOESY data as the primary input in concert with other data sets, such as methine-methyl TOCSY data, as well as paramagnetic relaxation enhancements (PREs). In our newer version of this software, FLAMEnGO 2.0 [350], we introduced a graphic interface that enables the interactive assignment of the methyl group resonances with the option of including secondary constraints, such as mutagenesis or supplemental NMR data.

In the following synopsis, we describe the construction and usage of FLAMEnGO 2.0, as well as its application to the side-chain methyl groups of PKA-C.

5.5: Semi-Automated Assignment Protocol using FLAMEnGO 2.0

All of the available methyl auto-assignment algorithms share the same philosophy: searching for the best assignments by comparing experimental NOE connectivities and chemical shifts to back-calculated data from the X-ray coordinates [318-320, 325, 350]. Starting from the available crystal structure or NMR structural

bundle, FLAMEnGO 2.0 back-calculates a 3D/4D NOESY spectrum from the internuclear methyl-methyl distances and compares synthetic data to an experimental NOESY spectrum (**Figure 5.5**). The algorithm iteratively swaps the resonance assignments until the scoring function is maximized. This process is repeated iteratively for an array of different simulated NOE distances until no further improvement is found. Given the probabilistic nature of this algorithm, multiple runs are performed in parallel to provide a statistical weight to the resonance assignments. Although FLAMEnGO is designed to handle sparse NOE data sets, sufficient coverage of the NOE network and other restraints (i.e., methine-methyl TOCSY or methyl-HN COSY, PREs or site-directed mutagenesis) are required for a confident assignment. The outline of the procedure for using FLAMEnGO GUI is shown in **Figure 5.6**.

Below, we detail the experimental data and data formatting, as well as brief instructions on usage of FLAMEnGO 2.0.

Materials

- 3D C,C,H ^{13}C-HMQC NOESY ^{13}C-HMQC data set (These pulse sequences are part of the TOPSPIN release for Bruker spectrometers, and are downloadable from the NMRFAM website http://pine.nmrfam.wisc.edu/download_pulseprogs.html for Agilent spectrometers).
- 2D ^{13}C-HMQC data set (required)
- Predicted chemical shift table (required, sources listed below)
- Paramagnetic Relaxation enhancement data (optional)
- Methine-methyl TOCSY data (optional)
- Assigned amide chemical shifts (optional, if amide-methyl NOESY data are incorporated)
- PDB file for protein. Note that hydrogen atoms need to be added to the PDB. Molprobity (http://molprobity.biochem.duke.edu/) is a resource to perform this function.

System Requirements and Specifications

The python-based FLAMEnGO 2.0 program includes two main components: 1) the frontend GUI program flame.py, and 2) the backend engine FLAMEnGO.py. The former provides a convenient interface for configuring the setup and displaying the results, while the latter is the driver for a Monte-Carlo search. The software is ready to run under Python 2.7, and requires wxPython and matplotlib modules for GUI and plotting. An integrated scientific python package, such as Enthought Canopy (https://www.enthought.com/products/canopy/) or Anaconda Python (https://store.continuum.io/cshop/anaconda/) are needed for full functionality.

Input File Formats

FLAMEnGO 2.0 uses a Monte Carlo search algorithm to swap resonance assignments from given input data and computes the *fitness* of the resonance assignments based on a score function. The details of the scoring function are discussed in Chao *et al.* [320, 350].

Initial Random Assignment

The algorithm needs an *arbitrary* initial assignment to start the swapping process associated with the Monte Carlo algorithm. This *seed* assignment must be consistent with PDB numbering and included in all input data. The data are formatted in a series of columns by <assignment #> <amino acid type> <resonance atom ID> -> <assignment #> <amino acid type> <resonance atom ID>. Note that there is no change in residue, rather this indicates to the program which residues to assign. To constrain a specific resonance assignment (*e.g.*, found using site-directed mutagenesis), the user should place an asterisk at the beginning of the line:

```
296 VAL HG2 -> 296 VAL HG2
* 301 ILE HD1 -> 301 ILE HD1
321 ILE HD1 -> 321 ILE HD1
```

```
323 VAL HG1 -> 323 VAL HG1
323 VAL HG2 -> 323 VAL HG2
325 ILE HD1 -> 325 ILE HD1
```

3D C,C,H ^{13}C-HMQC-NOESY-^{13}C-HMQC

The 3D C,C,H ^{13}C-HMQC-NOESY-^{13}C-HMQC data need to be formatted in a series of columns in the following order: <^{13}C (ω2) chemical shift> <^{1}H (ω3) chemical shift> <^{13}C (ω1) chemical shift> <^{13}C (ω2) linewidth> <^{1}H (ω3) linewidth> <^{13}C (ω1) linewidth>

```
18.32 1.28  27.41 0.4   0.025 0.4
22.76 0.88  19.53 0.4   0.025 0.4
22.76 0.88  15.69 0.4   0.025 0.4
22.76 0.88  21.55 0.4   0.025 0.4
22.76 0.88  18.66 0.4   0.025 0.4
20.97 0.78  17.77 0.4   0.025 0.4
25.05 0.68  23.33 0.4   0.025 0.4
```

^{13}C-HMQC/^{15}N Amide

The data is formatted in a series of columns by <assignment #> <amino acid type> <resonance atom ID> <chemical shift value>. Note that the assignment reported in this file at the beginning of the calculation is arbitrary for the ^{13}C-HMQC. The amide chemical shifts are optional and only required if one is using amide to methyl NOE data. The amide chemical shifts must be assigned based on previous experiments.

```
 7 LEU HD1     0.34
 7 LEU HD2     0.56
 7 LEU CD1    25.39
 7 LEU CD2    24.56
20 LEU HD1     0.88
20 LEU HD2     0.64
20 LEU CD1    25.10
20 LEU CD2    27.22
```

Paramagnetic Relaxation Enhancement Data (PREs)

Although the PRE data are listed as an option, we demonstrated that the inclusion of these constraints in the computation dramatically increases both the speed and accuracy of the resonance assignments [320, 350]. In particular, PRE data are crucial to

solve the ambiguities caused by partial peak overlap (**Figure 5.7**). PRE data are included as distances using the semi-quantitative approach described by Battiste and Wagner [351], in which the ratios of the peak intensities in the presence of the oxidized versus the reduced spin label are converted into three different categories: weakly affected (< 20% of signal is lost through the PRE effect), moderately affected (20-80% of the signal is lost) or strongly effected (<20% of the signal is lost). These categories are flagged as W, M, and S in the input file. If a resonance is unobserved regardless of the PRE effect, then a flag of 999 is used in the 4th column of the input file. The data are formatted in four columns, including <assignment #> <amino acid type> <resonance atom ID> <Flag (W, M, S, 999)>:

```
 89   HD1   LEU    999
 92   HD2   LEU    999
102   HD1   LEU    M
102   HD2   LEU    M
 71   HD1   ILE    S
 92   HD1   LEU    S
138   HD1   LEU    W
 13   HD1   LEU    W
```

Prediction of Methyl group chemical shifts from the PDB file

Various algorithms are used to predict the side chain chemical shift values. Output from any commonly used program, such as CH3SHIFT[323] (http://www-sidechain.ch.cam.ac.uk/CH3Shift/), SHIFTX2 [352], (http://www.shiftx2.ca/) and PPM [353] (http://spin.ccic.ohio-state.edu/index.php/ppm) can be implemented in FLAMEnGO 2.0. Since the output is not uniform between programs, data must be reformatted as follows: <residue #> <amino acid type> resonance atom ID> <predicted chemical shift value> <error of prediction>

```
1 VAL CG2 19.992 1.128
1 VAL HG2 0.828 0.173
5 LEU CD1 25.747 1.412
```

```
5 LEU HD1 0.969 0.176
```

Residue Type

Amino acid-type assignments can be included as constraints in the search algorithm.

The data format is identical to that of the initial assignment file.

Instructions to run FLAMEnGO 2.0 GUI

1. Open FLAMEnGO

   "`python flame.py`"

2. Specify the location of each input file on the main window..
3. To set up FLAMEnGO go under **File** > **SetUp** (**Figure 5.8A**). Set the NOE range between 5.0-10.0 with step size of 0.5. The sampling number is the number of Monte Carlo calculations run at each point and should be over 100k (**Figure 5.8B**).
4. Select the **Run** button. Please note that calculations take a considerable amount of time.
5. Once the runs are finished a plot of the score with respect to the NOE distance will appear (**Figure 5.8C**). To minimize the uncertainty of the assignment, click on the point where the NOE value where the maximum score is first reached (**Figure 5.8D**)
6. Select the number of calculations you wish to run (≥10). The final output will give the assignment and the statistical weight of each assignment.

Output Files

FLAMEnGO provides two types of output files. The first is the assignment file, which provides the calculated assignment at each given calculation at a specified NOE cutoff distance. Once the aggregate calculations are performed at a cutoff distance, the probability of each assignment is calculated. The probability of each assignment from the calculations is what is used to determine the *fitness* of the assignment.

Score and Assignment

The output file provides the user with the percent of the residues assigned, the assignment score and the assignment from the single calculation. The assignment is provided as the following <initial assignment> -> <calculated assignment. On the first line the first two columns provide the <final scoring value> <% of residues assigned>.

```
     (205.2936878260806, 93.079554272662747, 193,
17.844744345905379)
     ############################
     158    LEU    HD1 ->     148    LEU    HD1
     237    VAL    HG1 ->      90    VAL    HG2
     321    ILE    HD1 ->     196    ILE    HD1
     259    LEU    HD2 ->     191    LEU    HD2
     197    LEU    HD1 ->      75    LEU    HD1
```

Summary

The summary file will provide the assignment, as well as the number of times the particular assignment was made across all the calculations. A confident assignment is defined in this case as one that is consistent through all calculations at least 80% of the time; a reliable statistic for this assessment requires ≥10 calculations.   For each assignment the output is as follows: <initial assignment> -> <calculated assignment> <number of times the assignment was calculated>.

```
    105    VAL    HG1 ->    137    VAL    HG1    10
    254    LEU    HD1 ->     68    LEU    HD1    10
     75    LEU    HD2 ->    263    LEU    HD2     6
    143    LEU    HD2 ->     45    LEU    HD2     7
     13    LEU    HD1 ->    259    LEU    HD1    10
    241    VAL    HG2 ->    137    VAL    HG2    10
```

5.6: Conclusions and Perspectives

Selective labeling of the methyl group side-chains has extended the application of NMR methods to the analysis of both structure and dynamics of proteins up to 1 MDa. However, as the systems become larger, classical methods for resonance assignments fail. In this chapter, we reported a semi-empirical approach that enables the assignment

of methyl group resonances in large proteins. The structure-based approach requires the X-ray or the NMR ensemble of structures to generate a probability-based assignment. Inclusion of NOEs, PRE, site-specific mutagenesis data, methine-methyl TOCSY, and partial assignment from methyl-HN COSY data dramatically improves both the accuracy and the speed of the assignment procedure. This method promises to extend biomolecular NMR studies beyond the MDa limit.

5.7: Footnotes

Chapter VI: NMR Mapping of Protein Conformational Landscapes using Coordinated Behavior of Chemical Shifts upon Ligand Binding

Alessandro Cembran, [1,2] Jonggul Kim,[2] Jiali Gao, [2] and Gianluigi Veglia[1,2]*

[1]Department of Biochemistry, Biophysics & Molecular Biology; [2]Department of Chemistry – University of Minnesota 55455.

6.1: Introduction

To perform their functions, proteins undergo conformational transitions among different states that are distributed in funnel-like free energy landscapes similar to the classical folding funnels [354, 355]. Allosteric effectors, such as co-factors, drugs, and other binding partners, modulate the conformational equilibrium by shifting the population of these conformers among different energy basins [356-358]. Understanding how the equilibrium between these states is altered upon ligand binding is of critical importance for elucidating allosteric signaling and regulation of proteins [359].

NMR spectroscopy is emerging as the technique of choice to map allosteric phenomena at the atomic level [360-362]. Heteronuclear correlation experiments [363] provide NMR amide "fingerprints" of proteins and protein complexes. For amide groups, the [^{1}H,^{15}N]-HSQC experiment correlates the ^{1}H and ^{15}N frequencies (chemical shifts); amide chemical shifts are sensitive probes for structural changes and are used to assess folded state and monitor the effects of ligand binding on protein structures[364-367]. Resonance chemical shifts reflect the weighted average of different conformer populations within the sample and are affected by the exchange regime between the different conformational states. Under a slow exchange regime in the NMR time scale ($k_{ex} \ll \Delta\omega$), the amide resonances display distinct peaks. Under intermediate exchange ($k_{ex} \sim \Delta\omega$), the resonances broaden out, while for a fast exchange regime ($k_{ex} \gg \Delta\omega$), the resonances display narrow lines, reflecting the weighted average of the populations present in the sample. For ligand binding studies, it is customary to carry out titration experiments. If a protein exists in fast equilibrium between different states, and ligand binding shifts the equilibrium toward a single state, the trends of the chemical shifts upon ligand titration follow linear paths that reflect ligand dissociation constants (reviewed in

[143]). Similarly, if a protein exists in equilibrium between different states in a fast exchange regime and one were to promote the population of other states by mutations or posttranslational modifications, the trajectories of the chemical shifts follow linear trends [12, 55, 56, 143, 341, 368-370].

These linear trends can be used to quantitate both the stability and functional states of proteins [371]. Amide chemical shift linear trends provide the basis for a quantitative method recently proposed by Melacini's group to correlate long-range chemical shift changes to allosteric regulation, as well as to differentiate between active and inactive states of the regulatory subunit of cAMP dependent Protein Kinase A [372-375]. More recently, the Forman-Kay group used a similar approach to analyze the allosteric coupling in the cystic fibrosis transmembrane conductance regulator [376] and quantify the differential engagement of peptide complexes [377]. Finally, chemical shift trajectories have been utilized to determine the affinities and the number of binding sites in protein ligand interactions [378].

Inspired by this body of work, we developed a complementary analysis method (CONCISE, COordiNated ChemIcal Shifts bEhavior) that estimates the density of the states of a protein in different bound forms, providing a degree of collective response, or cooperativity, of the protein residues upon ligand binding. When combined with thermocalorimetric data, the density of populations obtained by this analysis defines a free energy landscape of the protein's ligated states. We tested this method for the conformational transitions of the C-subunit of the cAMP-dependent protein kinase A (PKA-C) upon nucleotide and pseudo-substrate binding, and constructed the free energy landscape along the enzymatic reaction coordinates.

PKA-C is a ubiquitous enzyme involved in many signaling pathways, playing a fundamental role in the pathophysiology of several different cellular events. PKA-C has a bilobal fold, with a small lobe (N-lobe), comprising mostly β-sheets that harbor the nucleotide binding pocket, and a large lobe (C-lobe), including mostly helical segments that host the substrate binding groove[379, 380]. During turnover, PKA-C is thought to interconvert between three major conformational states: *open* (apo), *intermediate* (nucleotide-bound), and *closed* (nucleotide and substrate bound) [379, 380]. While the *apo* form explores mainly an open conformation, with the two lobes disengaged and conformational dynamics uncommitted to catalysis, nucleotide binding shifts the enzyme conformational ensemble toward a dynamically committed state that is able to bind the substrate with enhanced affinity (positive cooperativity)[12, 55, 56]. Finally, substrate binding shifts the equilibrium toward a new basin, where the conformational dynamics are redistributed throughout the entire protein, priming it for phosphoryl transfer [55]. Binding of an inhibitor peptide (PKI$_{5-25}$), however, traps the kinase in a fully closed state, quenching the conformational dynamics throughout the enzyme and restricting the opening and closing motions required for product release [55]. To map these equilibria, we utilized previously measured chemical shifts of the PKA-C fingerprints of the apo, ATP-γ-N (AMP-PNP)-bound, ATP-bound, and AMP-PNP/PKI-bound forms, and applied both CONCISE and the chemical shifts covariance analysis (CHESCA)[372]. We found that our method is able to distinguish between the multiple states and quantitate the density of each state, and, when combined with binding free energy data, define the free energy landscape of the kinase. While site-specific correlations among the residues are attainable through the CHESCA analysis[372], CONCISE is able to estimate the collective response of the enzyme.

6.2: Methods

Calculation of the Population Density

In order to validate our method, we generated synthetic [^{1}H,^{15}N]-HSQC spectra corresponding to four virtual states (A, B, C, and D) similar to those obtained experimentally for PKA-C, with an identical number of peaks, positions, and range of chemical shift perturbations. Then, we simulated four different cases. In the first case (*ideal*, **Figure 6.1A**), we placed the chemical shifts of the resonances in four virtual states according to perfect linear trajectories, with equilibrium positions: 0 (state A), 1/3 (state B), 2/3 (state C), and 1 (state D), going from A to the D state. For the second case (*ideal+noise*, **Figure 6.1B**), we added random noise to both the nitrogen (standard deviation, SD = 0.20 ppm) and proton (SD = 0.03 ppm) dimensions of the ideal spectrum in **Figure 6.1A**. In the third case (*random*, **Figure 6.1C)**, the positions of the resonances were completely randomized, and in the fourth case (*mixed random+ideal*, **Figure 6.1D**), we set half of the peaks following linear trajectories with added random noise (with nitrogen and proton SD of 0.10 and 0.02 ppm, respectively), while the other half of the peaks represented a random distribution of the states, as in **Figure 6.1C**.

In order to analyze the chemical shift trajectories, we utilized principal component analysis (PCA). This approach is similar to the one proposed by Sakurai and Goto [371, 381] and allows one to filter out nearest-neighbor effects and perturbations that do not reflect the shifts in the conformational equilibrium upon ligand binding (see also Melacini [373] and Forman-Kay[377]). In **Figure 6.2**, we report a typical example of the PCA analysis filtering procedure for two selected resonances in the *ideal+noise* case (**Figure 6.1B**). To give equal weight to both proton and nitrogen chemical shift perturbations, ^{15}N chemical shifts were scaled by a factor of 0.154. PCA is applied separately to each residue, and rotates the residue's resonances from the ^{1}H, ^{15}N plane to a new coordinate system, defined by PC1 and PC2, which is a linear combination of the original axes. The

new axes (PC1/PC2) maximize the variance along PC1 and minimize it along PC2. As a result, a perfectly linear correlation would perfectly align along PC1 and show no spread along PC2, and thus we consider the PC1 projection as a measure of the equilibrium position as reported by each individual residue. The ratio between the SD along PC1 and that of PC2 defines the degree of linearity for each residue, which is used to filter out those resonances whose chemical shift changes do not report on the conformational equilibrium.

After linearizing the trajectories for each residue, the per-residue information is averaged together into a global descriptor – the average PC score – that reports on the position of each state along the equilibrium. To average the PC1 projections, all PCs must be oriented in the same direction. Since the PCA analysis orients the trajectories of the peaks either toward the positive, or rotated by 180° toward negative values (**Figures 6.2B and 6.2E),** we imposed a common orientation for all of the trajectories, applying a 180° rotation for those trajectories in the opposite direction (**Figures 6.2E** and **6.2F**). The two states that define the directionality correspond to the extremes (initial, A, and final, D, states) of the conformational equilibrium. The scores of different residues along PC1 are then normalized, dividing by the standard deviations of PC1 (see scale on top of **Figures 6.2B, 6. 2C, 6.2E, and 6.2F**). Once oriented and normalized, the PC1 projections of the selected subset of residues are averaged and the standard deviations computed (**Figure 6.3**). The average PC1 score indicates the position of each state along the equilibrium, while the spread reported by the standard deviation bars is a measure of the collective response of the selected subset of residues to ligand binding. In this context, narrow distributions are indicative of a collective behavior of the protein residues reaching the ligated state, while broad distributions indicate the presence of uncoordinated behavior. To filter out resonances not reporting on conformational

equilibrium, the average is performed on a reduced set of residues with the highest degree of linearity. We found that a SD_{PC1}/SD_{PC2} ratio ≥ 3 gives a reasonable threshold for linearity, while at the same time ensuring a sufficient number of residues for a statistically significant sampling. The experimental error was taken into account by discarding all of the residues with a PC1 range below 0.05 ppm, which is analogous to the range used in the projection analysis method [372].

Covariance Analysis (CHESCA)

The CHESCA analysis of the chemical shift covariance was carried out in agreement with the protocol proposed by Melacini and co-workers [372]. While the original CHESCA method uses the ^{15}N and ^{1}H chemical shifts weighted sum $(\delta = w^N \delta^N + w^H \delta^H$, with $w^N = 0.2$ and $w^H = 1)$ to calculate the covariance matrix, we used instead the PC1 scores, which more directly report on the conformational equilibrium.. While our approach gives a concise view of the conformational transitions, CHESCA gives a residue-specific view of the correlations among the residues in different protein domains [372]. Therefore, we calculated the correlation coefficients between the PC1 scores of the different residues using the following relationship:

$$(6.1)$$

$$c_{ij} = \frac{\left\langle \left(s_i - \langle s_i \rangle\right)\left(s_j - \langle s_j \rangle\right)\right\rangle}{\sqrt{\left(\langle s_i^2 \rangle - \langle s_i \rangle^2\right)\left(\langle s_j^2 \rangle - \langle s_j \rangle^2\right)}}$$

where *s* indicates the normalized PC1 scores for residues *i* and *j*, and the brackets indicate the mean over all of the states. The correlation coefficients between residues are plotted in a matrix format to identify the residues with highly correlated chemical shift changes. Furthermore, we clustered the residues using a hierarchical clustering step as described by Selvaratnam *et al*. [372]. The largest cluster of correlated residues was identified using a correlation coefficient of 0.99 as threshold for the clustering trees.

Experimental HSQC titration data of PKA-C

The HSQC data used in our analysis were taken from the previous published work by Masterson *et al.* [55], and all the samples were obtained under the same buffer, pH, and temperature conditions. A crucial element for the successful application of this method is the correct referencing of the resonances in the $[^1H,^{15}N]$-HSQC spectra, since the chemical shifts are highly sensitive, even to small structural perturbations. Therefore, the corrections to the chemical shifts ($\Delta\delta^{15}N^j$, $\Delta\delta^1H^j$) for a state j were calculated minimizing a distance function, D^j, defined as:

$$D^j = \sum_{i=1}^{Nres} \left| \left(\delta^{15}N_i^j + \Delta\delta^{15}N^j - \delta^{15}N_i^{ref} \right) \right| + \left| \left(\delta^1H_i^j + \Delta\delta^1H^j - \delta^1H_i^{ref} \right) \right|$$

(6.2)

where the superscript *ref* indicates the reference state (in our case the apo form), the subscript *i* runs over all of the *N* residues, and *j* is the state to be re-referenced.

6.3: Results

CONCISE analysis of synthetic data

The CONCISE calculations carried out on the synthetic data are shown in **Figure 6.3**, where the average position and spread of the PC1 scores for each state are displayed as bar plots and normal distributions. For the ideal case illustrated in the first panel of **Figure 6.3A-B** (perfect linear correlation), the equilibrium values for the four states were -1.34, -0.45, 0.44, and 1.35 standard units, which correspond to the equilibrium positions of 0, 1/3, 2/3, and 1. Since no random noise was added to the spectrum, there is no spread in the equilibrium positions. In contrast, the introduction of random noise (**Figure 6.3A-B**, second panel) causes a slight shift of the average PC score, broadening the distribution by approximately one standard deviation. When a random distribution of the chemical shifts is used (**Figure 6.3A-B**, third panel), the B and C states are indistinguishable (SD -0.04 and -0.01), while states A and D are still

distinguishable (SD -0.63 and 0.68). The latter originates from the rotation of the principal components, which requires a specific peak order and the assignment of the two reference states. Therefore, if the average values of the two reference states differ by ~1.3 standard deviations and the broadening is greater than 2 standard deviations, the analysis cannot be applied. Finally, the fourth panel in **Figure 6.3A-B** illustrates the results obtained for the mixed case, where the first half of the peaks (1-175) are ordered along the linear trajectory, while the second half (176-350) are randomly distributed. As expected, the random data introduce a broadening of the distributions, which can be eliminated using the filtering method described above (**Figure 6.3C-D**). While the filtering improves the accuracy of the average position and reduces the broadening of the distribution reported in the fourth panel of **Figure 6.3**, it produces no effect in the case of random chemical shift distribution reported in the third panel of **Figure 6.3**.

CHESCA analysis of synthetic data

Figure 6.4 shows the calculated correlation matrices of PC1 scores for the synthetic data, with a threshold for displaying correlation coefficients higher than 0.9. For the ideal case, the changes in chemical shifts are all strongly correlated, since the residues follow perfect linear trajectories. Upon addition of random noise (**Figure 6.4B**), the values of the correlation coefficients throughout the protein sequence lower substantially. Nonetheless, it is still possible to observe that several residues throughout the proteins are highly correlated. For the random case (**Figure 6.4C**), the degree of correlations among the different residues is much lower. However, some of the residues still show correlation coefficients greater than 0.9. The latter is due to a limited number of samples (4 states). If more states are included, these correlations will become much weaker or filtered out. When only half of the protein resonances have linear changes in the chemical shifts, (mixed case, **Figure 6.4D**) it is possible to see a higher density of correlations in the map for the first part of the protein, while weaker correlations are

observed for the remaining residues. To identify the large correlation clusters, we applied a hierarchical clustering analysis to the data. The largest clusters obtained from these calculations are shown in the correlation matrices of **Figure 6.5**. To select the clusters, we used a threshold of 0.99. For the ideal case (**Figure 6.5A**), there is only one cluster, which includes all of the protein's residues. Addition of noise reduces the size of the largest cluster (**Figure 6.5B**), while in the random case (**Figure 6.5C**), the correlations among the residues through the protein are sparse, with only a handful of residues contributing to the largest correlated cluster. In the mixed case (**Figure 6.5D**), the method shows more dense correlations for the linear trajectories of the residues, while the fictitious correlations are rather sparse.

Mapping Protein kinase A Intramolecular Allostery using CONCISE and CHESCA

We applied CONCISE to the conformational transitions of PKA-C as mapped by $[^1H,^{15}N]$-HSQC spectra for four different states of the enzyme: apo, binary (AMP-PNP bound), binary (ATP-bound), and ternary (AMP-PNP and PKI_{5-25} bound). Peak positions for the four experimental data sets are shown in **Figure 6.6A**. The distributions of the residue positions in the different states are reported in **Figure 6.6B**. The two limits of the linear trajectories are represented by the apo and the ternary complex, corresponding to the open and closed conformations, respectively [380]. The average PC scores obtained using the full set of residues (dashed lines in **Figure 6.6B**) are within reliable thresholds, with the two extremes of the linear relationship separated by 2.22 standard units and with a spread of about one standard deviation. After filtering out the residues characterized by low linearity and small perturbations, the results obtained with the reduced set (solid lines in **Figure 6.6B**) improved significantly, *i.e.*, the distance between the two extremes increases and the spread is reduced to less than one standard deviation. Overall, the positions of the four states (-1.11, -0.50, 0.28, and 1.33) correspond to equilibrium positions of 0, 0.25, 0.57, and 1, defining the fractional

144

populations of the different states. The binding of the two different nucleotides induces two intermediate conformations: one (AMP-PNP bound) slightly shifted toward the open state and the second (ATP-bound) shifted toward the closed state. The spread of the distribution indicates the collective behavior of the residues, since it measures the extent to which each residue approaches a defined state. Since the distributions of the chemical shifts are directly related to the populations of the different states, it is possible to combine this information with thermocalorimetric measurements and define a conformational energy landscape for PKA-C. To construct the free energy basins for the open, intermediate, and closed states of the kinase along the open to close reaction coordinate, we used a harmonic potential underlying the Boltzmann distribution for each state:

$$E(s) = \left(\frac{RT}{2\sigma^2}\right)(s-\mu)^2$$

(6.3)

where s is the position along the average PC score in standard deviation units, and μ and σ are the mean and standard deviation for each distribution. The transition from apo to ATPγN-bound was mapped using the dissociation constant K_d (39 μM) and the k_{on} (0.7 10^6 to 2.8 10^6 $M^{-1}s^{-1}$) from ATPγN binding [12], which resulted in an energy barrier ranging from 8.7 to 9.5 kcal mol^{-1}, and a free energy difference between the two minima of -6.0 kcal mol^{-1}. In addition, using the K_d for PKI binding to the ADP:PKA binary form (0.03 to 0.06 μM)[12], we determined an upper limit (-9.9 to -10.3 kcal mol^{-1}) for the free energy associated to the transition from the binary to the ternary complex. For the transition state between the binary and ternary forms, we were able to set an upper limit of about 7 kcal mol^{-1} based on the following considerations: first, the transition state barrier for PKI and PLN binding should be comparable (Hammond's postulate); second,

the rate limiting step is associated with ADP release, which sets an upper limit of about 15 kcal mol^{-1} to S16p-PLN dissociation; and third, the K_d for PLN binding to ADP:PKA (10±4 μM) brackets its binding free energy between -6.7 and -7.2 kcal mol^{-1}. Based on these considerations, we modeled the transition state (TS) to be about 3 kcal mol^{-1}. **Figure 6.7** shows the free energy surface with three energy basins, corresponding to the apo, intermediate and closed state. The shapes of the minima correspond to the density of the populations calculated from the chemical shifts. These results are in qualitative agreement with the molecular dynamics calculations [55].

To analyze the extent of the chemical shift correlations between residues in the different part of the kinase, we mapped the largest cluster of correlated residues on the correlation matrix (**Figure 6.8A**). We found that a large number of residues report on the open-to-close transitions of the enzyme. Interestingly, these correlations span the entire enzyme structure (**Figure 6.8B**), indicating a collective response of the protein to the binding events. Several residues with large chemical shift changes ($\Delta\delta$ > 0.15 ppm, red spheres in **Figure 6.8C**) do not follow linear paths and are mostly localized near the ligand binding sites. For these residues it is not possible to discern the perturbations associated with the opening and closing equilibrium from the electrostatic and structural changes induced locally by ligand binding. Within the largest correlated cluster, we identified six groups of residues that were spatially connected (**Figure 9**), suggestive of a structure-based allostery. The largest group indicated in red encompasses eighteen residues in the small lobe of the kinase that are not in direct contact with the nucleotide binding pocket. Another significant group (displayed in yellow) involves residues that connect the C-helix with the magnesium-positioning, the activation, and peptide-positioning loops. The yellow cluster of residues is also in close proximity with other residues indicated in purple, although no physical contact exists in the X-ray structure

[379]. Interestingly, there are residues that trace the inner core of the enzyme, connecting Ala-40 involved in the C-spine [382], Val-104, and Phe-100 of the C-helix-$\beta4$ loop (peripheral to the C-spine) with both the E- and F-helices. These residues form a long conduit from the small to the large lobe. Finally, residues in the $\beta6$-$\beta8$ connecting loop form a cluster of 8 residues with the C-terminal loop indicated in green. However, we identified several pairs and isolated residues, whose correlated behavior could not be traced along contiguous paths. The latter may reveal non-structure-based allosteric phenomena as described by Hilser et al. [383].

6.4: Discussion

Proteins exert their function via binding of ligands or other partners. Binding of a ligand to rigid protein scaffolds follows a mechanism reminiscent of the classical lock-and-key [384] or induced-fit mechanisms [385]. However, many proteins undergo conformational interconversions involving domains or loops, and in more extreme cases, the entire protein. For instance, signaling proteins such as protein kinases are notoriously dynamic molecules [24, 386], with conformational isomers distributed among high and low energy states resembling classical folding funnels [354, 355, 357]. The extent of conformational dynamics manifested by a protein defines the shape of these free energy basins as well as the heights of the energy barriers between the different basins [387]. Dynamic proteins display broad basins and low energy barriers between them, whereas more rigid proteins populate low energy basins and possess high energy barriers between the different states [388]. A revised view of allostery suggests that binding events are interpretable as conformational shifts of proteins among the different energy basins [389], with ligands *selecting* those conformers that are complementary to their structural and dynamic features, shifting the population of the biomacromolecules from the unligated to the more stable ligated state [390-392].

NMR chemical shifts are atomic reporters of the conformational equilibria that the proteins undergo upon ligand binding. Although the extent of the chemical shift perturbations has been routinely used to identify binding hotspots and estimate the populations of the conformers, more recent analyses of the chemical shift trajectories for two-state equilibria suggest that statistical correlations can give a more complete view of the conformational transitions of proteins and identify possible allosteric networks [372, 373]. The latter is particularly important to rationalize the conformational transitions of PKA-C [4, 393], where we observed chemical shift changes interspersed throughout the entire enzyme. When analyzed using the compounded ^{1}H/^{15}N chemical shifts of the enzyme fingerprint, we were able to identify contiguous paths localized in the proximity of the nucleotide and ligand binding sites [12]. However, in several instances we were not able to interpret the long-range chemical shift perturbation sparsely distributed across the entire enzyme. Nonetheless, many of these changes followed linear trajectories upon ligand binding [55, 56].

The CONCISE approach presented here enables us to filter out chemical shift changes occurring in the immediate proximity of the ligand binding crevices from those that report on the conformational transitions, identifying the progressive conformational transitions of the enzyme from the apo (open), intermediate (partially closed) to the ternary complex (fully closed state) upon nucleotide and substrate binding. Importantly, our analysis shows that the residues involved in the opening and closing transitions act collectively, i.e., with a coordinated behavior upon ligand binding (**Figure 6.6C**). Interestingly, CONCISE discriminates between the positions of the equilibrium reached upon binding two nucleotides, ATP and ATPγN (AMP-PNP). ATPγN has been considered a non-hydrolyzable nucleotide, which mimics the effects of ATP binding. Our analysis reveals that ATPγN induces a conformational state slightly more open than the

corresponding ATP-bound enzyme. The density distribution of the amide resonances upon addition of ATPγN is shifted toward the apo state of the enzyme, with an average position for the ATPγN-bound of ~27%; whereas the corresponding distribution of the population of the ATP-bound kinase is shifted toward the closed state with an average value of ~62%. A possible explanation is that the geometry around the β- and γ-phosphates is crucial to define the intermediate state, and small changes in the geometry of the γ-phosphate may cause the enzyme to adopt a more open conformation. The latter suggests that ATPγN is not a perfect mimic for ATP.

How does the kinase reach a defined conformational state? Are there preferential paths activated by ligand binding that modulate allosteric response (networks)? Are the perturbations localized or does the protein respond collectively?

For PKA-C, we found that the major cluster of residues reporting on the opening and closing of the enzyme is not localized in a specific area; rather it is distributed throughout the enzyme across the small and large lobes. Although some contiguous paths of correlated residues can be identified (**Figure 6.9**), especially in the small lobe and across the enzyme's core, it is not possible to explain all the observed correlations in terms of spatial proximity. Perhaps, the best explanation for allosteric behavior in PKA-C is a combination of well-defined pathways [394, 395] together with non-structure-based allosteric phenomena, reflecting thermal fluctuation (local folding and unfolding) in agreement with ensemble-based model [383], where allostery is formulated as thermodynamic coupling between protein domains in the absence of physical couplings. It should be noticed that the chemical shift analysis provided here gives only a partial view of signal propagation throughout the enzyme. A definite answer will require analysis

of further isotopic probes, including those of methyl side chain groups, that can trace the changes in the hydrophobic residues populating the core of the kinase [61].

6.5: Conclusions

In conclusion, we presented a statistical interpretation of the linear trajectories of the chemical shifts that gives a quantitative and concise view of the transitions associated with ligand binding. In the case of PKA-C, our method describes the collective behavior of the resonances through the structural transitions upon ligand binding, and shows that it is possible to discern between different nucleotides, nucleotide analogs, and competitive inhibitors in the conformational transitions of the enzyme. This method is also applicable to other structural perturbations, such as post-translational modifications or mutations, to identify the average conformational state of a protein. The combination of the population densities derived from the chemical shifts with thermocalorimetric and kinetic data enables the description of the free energy landscape of proteins. Therefore, this method gives a concise view of the way in which different ligands, such as drugs and peptides, can affect the conformational equilibrium and will be instrumental in the design of positive or negative allosteric effectors.

6.6: Footnotes

Chapter VII

Synchronous Opening and Closing Motions are Essential for cAMP-Dependent Protein Kinase A Signaling

Atul K. Srivastava[1], Leanna R. McDonald[1], Alessandro Cembran[2], Jonggul Kim[2], Larry R. Masterson[2], Christopher L. McClendon[3], Susan S. Taylor[3], and Gianluigi Veglia[1,2]

[1]Department of Biochemistry, Molecular Biology and Biophysics, University of Minnesota, MN, 55455 United States.

[2]Department of Chemistry, University of Minnesota, Minnesota, 55455 United States.

[3]Department of Chemistry and Biochemistry, University of California at San Diego, La Jolla, CA 92093, USA

7.1: Introduction

Protein kinase A (PKA) is a ubiquitous phosphoryltransferase involved in a myriad of cellular events. PKA was one of the first kinases to be discovered and characterized [396], and represents a benchmark for understanding the structure-function relationship and catalytic mechanism for the entire kinase superfamily [61, 81]. Unlike metabolic enzymes optimized for fast turnover rates, PKA has evolved to orchestrate cell signaling events, mediating the transfer of external stimuli inside the cell [81]. Although it targets several hundred substrates [1], this kinase is highly specific, due to a tight spatio-temporal control that ensures physiological levels of phosphorylation of its specific cellular targets [397]. β-adrenergic stimulation activates the PKA holoenzyme (two catalytic and two regulatory subunits, C- and R- subunits) [398], which unleashes the active C-subunits (PKA-C), a catalytic core that PKA shares with other serine/threonine- and tyrosine-specific protein kinases. PKA-C has a bilobate structure, comprised of a small β-strand-rich lobe with a short α-helix (C-helix), which harbors the nucleotide binding pocket, and a large, mostly helical lobe containing the substrate binding site [379]. PKA-C's catalytic cycle is a multistep process that involves nucleotide binding, substrate recognition and positioning, phosphoryl transfer and product release (ADP and phosphorylated substrate) [399]. Crystal structures have captured this enzyme in the major conformational states along the reaction coordinates: apo, intermediate (nucleotide-bound), and closed (ternary complex with nucleotide and pseudo-substrate) [111, 380]. More recently the peptide substrate and product complexes have been trapped in crystals [47]. However, these structures offers static images that do not fully describe the conformational changes and the role of motions occurring during allosteric regulation and catalysis [24]. The prominent role of conformational fluctuations for PKA-C's catalytic cycle was inferred from the analysis of mutants aimed at disrupting the

152

proposed allosteric network [400-405]. These studies, coupled with kinetic assays, suggest that the rate-determining step of the turnover is the ADP release following a fast phosphoryl transfer (~500 s^{-1}), with the conformational transition from closed to open state being rate-limiting [406]. Among these mutants, Y204A (PKA-C^{Y204A}), located in the large lobe of the enzyme and distant from the active site (**Figure 7.1**), has been shown to substantially affect both k$_{cat}$/K_m and k_{cat} [400, 404]. Interestingly, the X-ray structure of PKA-C^{Y204A} is virtually superimposable to that of the wild-type in the presence of PKI and ATP-Mg$_2$, with an overall rmsd of ~0.5 Å [403]. From the comparison of the two X-ray structures, it emerges that Y204 couples the P+1 loop in the activation segment to both E230 and the hydrophobic core. Interestingly, Y204 does not have any direct contact with the peptide substrate, and yet this alanine substitution reduces dramatically the enzyme's catalytic efficiency. Because the mutation induces no significant structural changes in the enzyme, let alone the active site, PKA-C^{Y204A} represents an ideal benchmark to test the relevance of the rates of motions in the PKA-C catalytic cycle.

To analyze the effects of the Y204A mutation on the conformational dynamics of the enzyme, we carried out NMR spin relaxation measurements both in fast (ps-ns) and slow (μs-ms) timescales [407-409], focusing on the nucleotide-bound, dynamically-activated and substrate-primed forms of PKA-C^{WT} and PKA-C^{Y204A}. We found that by disrupting the electrostatic network at the fringe of the small and large lobes, the enzyme responds with global dynamical changes; structural fluctuations in the ps-ns timescale show regions with both enhanced and reduced mobility. Importantly, relaxation dispersion measurements for quantifying chemical exchange in the μs-ms timescale range show synchronous motions in the wild-type protein that are obliterated by the mutation. These effects are particularly evident for the Gly-rich loop and hinge region, those that mediate nucleotide binding, substrate recognition, and the rate-determining-

step of the catalysis, i.e., ADP release. We conclude that synchronous (i.e., concerted) conformational fluctuations are essential for catalytic efficiency.

7.2: Experimental Procedures

ITC. Both PKA-C^{WT} and PKA-C^{Y204A} were dialyzed into 20 mM MOPS, 90 mM KCl, 10 mM DTT, 10 mM MgCl$_2$, 1 mM NaN$_3$ at pH 6.5. PKA-C concentrations for ITC measurements were between 11.8 - 32 μM. ATPγN was added to reach a final concentration of 2 mM. All ITC measurements were performed with a Microcal VP-ITC instrument at 27°C. Approximately 1.7 mL of PKA-C was used for each experiment and 280 μL of 2-4 mM of ATPγN or 140-210μM of PKI$_{5-24}$ in the titrant syringe. All experiments were performed in triplicate. The heat of dilution of the ligand to the buffer was taken into account by measuring the heat of dilution of the ligand to the buffer and was subtracted from the experiment accordingly. The binding curves were analyzed with the NanoAnalyze software (TA Instruments) assuming 1:1 stoichiometry and using the Wiseman Isotherm:

$$\frac{d[MX]}{d[X_{tot}]} = \Delta H° V_0 \left[\frac{1}{2} + \frac{1 - (1+r)/2 - R_m/2}{(R_m^2 - 2R_m(1-r) + (1+r)^2)^{1/2}} \right]$$

where the change of the total complex, d[MX] with respect to the change of the ligand concentration, d[X$_{tot}$] is dependent on r, the ratio of the K_d with respect to the total protein concentration, and R$_m$, the ratio between the total ligand and total protein concentration. The free energy of binding was determined using the following:

$$\Delta G = RT \ln K_d$$

where R is the universal gas constant and T is the temperature at measurement (300K). The entropic contribution to binding was calculated using the following:

$$T\Delta S = \Delta H - \Delta G$$

154

NMR Spectroscopy. Uniformly ^{15}N-labeded perdeuterated wild-type PKA-C and its Y204A mutant were overexpressed and purified as described elsewhere (Masterson et al., 2008). The NMR samples contained 90 mM KCl, 20 mM KH_2PO_4, 10 mM MEGA-8 (Octanoyl-N-methylglucamide), 5% glycerol, 12 mM ATPγN, 10 mM $MgCl_2$, 20 mM DTT, 1 mM NaN_3 in a mixed solvent of 5% D_2O in water, pH 6.5. The protein concentrations for PKA-C^{WT} and PKA-C^{Y204A} were ~400 µM, as determined from A_{280} measurements. Experiments were performed at 27 °C on Varian Inova spectrometers operating at ^{1}H frequency of 800 MHz and 900 MHz. The [^{1}H,^{15}N] TROSY-HSQC spectra of PKA-C^{WT} and PKA-C^{Y204A} in the apo, nucleotide bound (ATPγN), and inhibitor bound (ATPγN and PKI) forms were re-referenced to remove any shifting artifacts. To improve our statistics we carried out the CONCISE analysis using a total of six states [410]. The ^{15}N shifts were then scaled by 0.154 to balance the weight of perturbations along the nitrogen and proton dimensions, and principal component analysis (PCA) was applied independently to each residue to identify the direction of largest variance across the six states defined above. The ratio between the standard deviations along PC1 and PC2 constitutes a measure of how well the different states follow a linear pattern for a given residue. Residues characterized by poor linearity (σ-PC1/σ-PC2) < 3.0) were discarded from our analysis, together with residues with small perturbations (range of chemical shift along PC1 < 0.05 ppm) and thus more heavily affected by experimental error. These thresholds reduced the number of residues available for all states from 155 to 94. Nuclear spin (^{15}N) relaxation experiments performed with TROSY detected T_1, $T_1\rho$ and [15]N[^{1}H]-NOE, TROSY-Hahn-echo, and TROSY-CPMG experiments for the PKA-C^{WT} and PKA-C^{Y204A} samples were carried out using 50x1600 points and spectral widths of 2403x10504 Hz in the indirect and direct dimensions. The ^{1}H and ^{15}N carrier frequencies were set on water resonance and 120.5 ppm, respectively.

Molecular Dynamics Simulations. The details of the systems simulated are described in the Supporting Information. The systems were prepared using AMBER12 [411, 412]. Production simulations (wild-type, 5.7 μs, and Y204A, 5.1 μs) were run on a 512-node Anton supercomputer, and the trajectories were analyzed using mutual information values to capture correlated motions involving semi-rigid regions [413].

Community Analysis. For our community analysis, we computed Cartesian mutual information values instead of dihedral mutual information values, as the former better capture correlated motions involving semi-rigid regions [414], while the latter are more suitable for analyzing couplings between surface sites [415, 416]. We calculated the Cartesian mutual information for backbone Cα atoms, as well as for an additional representative terminal atom for each residue. The matrix of mutual information among these atoms was calculated with the MutInf software package [415, 417], splitting each trajectory into six blocks of equal size and using uniformly binned histograms with 24 bins per degree of freedom. We used 20 sets of scrambled data to estimate the distribution of mutual information under the null hypothesis of independence, and calculated the excess mutual information with the previously-described under sampling correction [415].

7.3: Results

PKA-C^{Y204A} displays lower binding cooperativity. Kinetic data reported in the literature show the Y204A mutation affects both k_{cat}/K_m and k_{cat} [403]. To dissect the thermodynamics of nucleotide and substrate binding from the kinetics data, we monitored the binding of the nucleotide ATPγN and the pseudo-substrate PKI$_{5-24}$ using Isothermal Titration Calorimetry (ITC) for both PKA-C^{WT} and PKA-C^{Y204A} (**Figure 7.7, Table 7.2**). We found that Y204A exhibits a slightly higher affinity for ATPγN ($K_d \sim 23$ μM) compared to that of the wild-type ($K_d \sim 58$ μM), with a higher enthalpy of binding

($\Delta H \approx$ -4.2 versus -2.7 kcal/mol). However, the affinity for PKI$_{5-24}$ binding to the ATPγN-saturated enzymes is substantially different. While for PKA-C^{WT} we observed K_d ~ 120 nM consistent with previous literature data [418], for PKA-C^{Y204A} K_d is ~14 µM, corresponding to a loss of affinity of nearly 100 fold and a reduction of binding enthalpy of 10 kcal/mol. Since the k_{cat}/K_M and substrate affinities for the Y204A mutant is different from the wild-type enzyme, we chose to focus on the analysis of the dynamics for the nucleotide bound state.

Nucleotide-bound PKA-C^{WT} is dynamically activated. To monitor the structure and dynamics of PKA-C^{WT} and PKA-C^{Y204A}, we collected [^{1}H,^{15}N]-TROSY-HSQC spectra of the apo, nucleotide-bound (ATPγN), and ternary (ATPγN and PKI) forms. Saturating the apo forms of both wild-type and mutant PKA-C with ATPγN resulted in significant broadening of numerous amide resonances, several of which broadened beyond detection, indicating the presence of conformational heterogeneity (**Figure 7.2**). Importantly, we detected substantial resonance broadening in the Gly-rich, DFG, and activation loops, which play major roles in the catalytic cycle [380]. Residues in the C-terminal loop flanking the Gly-rich loop and the C-helix also display notable amide resonance broadenings. Some regions with significant line broadening coincide with several loops displaying high B-factors in the crystal structure 1BKX.

Chemical shifts report only minimal structural effects for Y204A. Overall, the chemical shift differences incurred by mutation at Y204A in all three states are minimal (**Figure 7.3A**), with the most prominent changes close to the mutation site, indicating that the average solution structures of PKA-C^{WT} and PKA-C^{Y204A} are nearly identical (**Figure 7.3B**). However, tracing these subtle chemical shift changes offers useful information regarding local and global allosteric phenomena [372]. Building on the chemical shift covariance analysis [372], we developed CONCISE (COordiNated ChemIcal Shifts bEhavior) that defines the probability density of each state and traces

changes in the conformational equilibria upon ligand titration or mutation [410]. For both

PKA-C^{WT} and PKA-C^{Y204A}, CONCISE identified 94 residues interspersed throughout the

whole structure that follow linear paths of the amide resonances upon titration with both

the nucleotide and PKI$_{5-24}$.This indicates that the entire enzyme is involved in the open to

closed transition. The probability density curves of the apo, intermediate, and closed

states for the mutant are similar to those of the wild-type, with only slight differences for

the apo and nucleotide-bound forms, which appear slightly more closed in the mutant.

For the ternary complexes, however, the average conformations are essentially the

same, with a complete overlay of the probability density curves (**Figure 7.3C**). This

indicate that PKI$_{5-24}$ (although with reduced binding affinity) traps for Y204A in a

inhibited, dynamically quenched state [55].

  Fast timescale dynamics are redistributed throughout Y204A. In PKA-C^{WT},

nucleotide binding drives the enzyme conformation toward a state committed to catalysis

(i.e., dynamically committed state) [55, 56]. The adenine ring binds in a deep cleft

located underneath the Gly-rich loop, completing the C-spine, engaging both lobes, and

promoting backbone fluctuations in the ps-ns time scale [55, 56]. The total entropy

changes dramatically upon binding the substrate peptide or PKI$_{5-24}$. At the same time,

the conformational fluctuations of the ternary complexes with the substrate and inhibitor

are radically different, with the substrate binding re-distributing the motions throughout

the enzyme and the pseudo-substrate quenching the conformational dynamics both in

the slow and fast time scale. Based on these data, we hypothesized that the motions in

the intermediate (nucleotide-bound) state of the kinase may be responsible for substrate

binding cooperativity [55]. To test this hypothesis, we probed the conformational

dynamics for the PKA-C^{Y204A} mutant in complex with ATPγN over a range of timescales

(Summarized in **Table 7.1**). Specifically, we measured the ^{15}N relaxation parameters R_1

(longitudinal relaxation rate constant), R_2 (longitudinal relaxation rate constant), and ^{1}H-

[15]N heteronuclear steady-state NOE (HX-NOE) [407]. From the R_1 and R_2 relaxation rates, we estimated an overall rotational correlation time of approximately 24 and 23 ns for the wild-type and Y204A mutant, respectively, values that are indicative of a monomeric enzyme. The average NOE values for wild-type PKA-C and the mutant Y204A were found to be 0.79 ± 0.13 and 0.81 ± 0.12, respectively, indicating that on average the overall fluctuations in the fast time scale are very similar in both enzymes. However, we identified local differences in the HX-NOEs between the two proteins. Overall, no clear patterns emerged from the data, suggesting that the conformational freedom gained by disrupting the electrostatic node impinged on Y204 is redistributed across the entire enzyme. This reorganization of fast timescale dynamics may contribute to the drastically reduced binding affinity for PKI_{5-24} as measured by ITC.

Slow conformational dynamics are no longer synchronized in Y204A. According to our proposed model [56], the nucleotide-bound enzyme still undergoes opening and closing transitions, although with a smaller amplitude. We hypothesize that these motions are necessary for organizing the active site for substrate binding and phosphoryl transfer to occur, but also for product release. To test this hypothesis, we measured the rates of conformational exchange for those residues manifesting fast/intermediate exchange in both the wild-type and the mutant. To quantify the rates of these motions, we measured the exchange contribution to the total transverse relaxation rate constant (R_{ex}) with two different NMR techniques: [15]N Carr-Purcell-Meiboom-Gill (CPMG) relaxation dispersion measurements [419] and TROSY-Hahn echo [420]. The rates obtained from the CPMG relaxation dispersion experiments depend on the equilibrium populations (p_{closed} and p_{open}), the chemical shift difference between the two interconverting species ($\Delta\omega$), and the kinetics of exchange ($k_{ex}=k_f +k_r$, where the *f* and *r* subscripts indicate the forward and reverse rates) [421]. From the individual fitting of the dispersion curves, we clustered fifteen residues manifesting similar exchange rates

(**Figure 7.4**). These residues are distributed mainly in the small lobe, comprising G55 in the Gly-rich loop, M58 and L59 in β-sheet 2, L77 and K78 in the B-helix, E91 and Q96 in the C-helix, A124 and F318 in the hinge region between the two lobes, and E332 and E446 located in the C-terminal that wraps around the enzyme. Also included from the large lobe are I163, in the catalytic loop, and Y306. The clustering of the relaxation rates for these residues distributed among several regions indicates that in the wild-type in the nucleotide-bound state the small lobe undergoes concerted motions between the open and closed conformations present. Fitting the dispersion profiles using the full Richard-Carver equation (see Supplementary Information) resulted in populations of 94 and 6% for the closed and open states, respectively, with an exchange constant of ~1020±150 s^{-1} (k_f ~ 66 and k_r ~ 953 s^{-1}). While the broadened resonances for both the wild-type and mutated enzymes are identical, the dispersion curves for the fast/intermediate exchange residues are quite different (**Figure 7.5**). Remarkably, the individual fitting carried out on the resonances did not result in similar k_{ex} values, and the cluster of residues identified for the wild-type as responsible for the synchronous motions is no longer present. As a result, a global fit is not possible for multiple residues, and only sparse pairs of residues in the small lobe can be coupled. Therefore, mutation of Y204A induces a dramatic change in the dynamics of PKA-C on the μs-ms timescale in which a large region of the protein involved in active site motions is no longer synchronized. Moreover, several residues of the mutant enzyme show faster exchange dynamics as detected from the individual fits and uncorrelated motions in the small lobe, suggesting that there is a shift in the motional regime. To support the latter, we used the ^{15}N TROSY Hahn-echo (TrHE) experiment [420] for both PKA-C^{WT} and PKA-C^{Y204A}. The window of observation of the chemical exchange for CPMG and TrHE is different, with the TrHE more sensitive to faster conformational dynamics [420, 422]. For the wild-type, we found a good

agreement between the R_{ex} values measured by CPMG experiments and the corresponding values measured using the TrHE experiments (**Figure 7.6**). In sharp contrast, R_{ex} values measured with these two techniques are markedly different for the mutant, as the R_{ex} values measured with the TrHE are systematically higher than the corresponding values measured by CPMG experiments. Overall, these data suggest that the mutation increases the rates of motions throughout the enzyme with the most prominent effects localized in the small lobe (β_2- and β_3-sheet as well as B- and C-helix) and between the activation and positioning loop. Therefore, the disruption of the electrostatic node shifts the range of the conformational dynamics to a faster timescale that affects both substrate binding and product release.

Molecular dynamics simulations highlight loss of correlated motions in Y204A. To interpret the motions highlighted by the nuclear spin relaxation measurements and visualize how the Y204A mutation alters inter-residue contacts and correlated motions at a global level, we performed multiple-microsecond timescale molecular dynamics simulations for both the wild-type (5.7 μs) and Y204A (5.1 μs) kinases. The MD trajectories were analyzed using the community analysis [423-425], which identifies structurally-contiguous regions exhibiting correlated motions. The community analysis views motions in the protein as a dynamical network and highlights correlated motions in proteins as semi-rigid, semi-flexible units of three-dimensional sub-structures that are grouped together and connected to other units by physical contacts and correlated motions. Community analysis of PKA^{WT} clusters the kinase residues in eight major communities (**Figure 7.6**). A prominent feature of the wild-type enzyme is the regulatory ComC, which acts as a hub and is strongly connected to the rest of the community (thick lines in **Figure 7.6**). In the mutated enzyme, these correlations are completely rearranged, with ComC splitting into two different sub-communities (ComC and ComC1), losing the role of central communication hub. As a result, the αC-β4 linker,

DFG-motif, and several R-spine residues pull away from ComC that contains the αC-helix, a critical domain for catalysis. The loss of correlations within and between the communities parallels the effects of the mutation on the slow time scale motion as probed by NMR and is consistent with the loss of concerted motion in Y204A. Overall the changes in the distribution of motions and the reduced couplings within and between communities throughout the entire enzyme upon mutation support the conclusions reached by the NMR analysis and identify subtle but important changes that reduce the binding affinity and catalytic efficiency for the enzyme

7.4: Discussion

There is a passionate debate about the role of conformational fluctuations in enzymatic catalysis [426-430]. Recent studies have inferred that motions in the NMR-detectable timescale might affect the chemical step of catalysis [16, 431, 432]. On the other hand, theoretical calculations seem to dismiss this argument [426]. Nonetheless, enzyme motions are implicated in several steps of catalysis, including allosteric activation [309, 389, 433-435], active site optimization [432, 436, 437], co-factors or substrate binding, as well as product release [56]. An intriguing hypothesis is that enzyme structure and conformational dynamics may have co-evolved [438-441]. Indeed, the importance of conformational flexibility in protein kinases is emerging in several different instances. In particular, motions in the intermediate-exchange timescale (μs-to-ms) have been detected by NMR in several different kinases, *e.g.*, p38a mitogen-activated protein kinase [442], Abelson kinase [122], the CheA histidine kinase [443], and extracellular signal-regulated kinase 2 (ERK2) [119]. In past years, we have used nuclear spin relaxation measurements to trace the conformational changes as well as structural fluctuations of kinase A, mimicking major states along the reaction coordinates [55, 56]. We found that the apo state is malleable and water accessible, but does not

display conformational fluctuations that are synchronous to the enzymatic turnover. Nucleotide binding shifts the population of the enzyme toward an intermediate state, providing the phosphoryl group for the reaction and connecting the small lobe to the large lobe via the hydrophobic C-spine. Upon substrate binding, the conformational fluctuations of the enzyme are redistributed, allowing the enzyme to adopt a dynamically competent state [56]. In sharp contrast, binding of a pseudo substrate peptide inhibitor such as PKI obliterates the conformational fluctuations, trapping the enzyme in a dynamically quenched state [55].

Although these studies have advanced our understanding of the role of motions on enzymatic turnover, they did not clearly demonstrate the importance of the rates and the correlations of the conformational fluctuations with respect to the structural changes. The X-ray structures of the different states [444] as well as molecular dynamics simulations [55] suggest that motion is a driving force in the catalytic cycle [445]. Fluctuations in kinase A involve a mechanical hinge-bending motion of the two lobes, featuring an asymmetric twist that brings the glycine-rich loop close to the triphosphate moiety, thus causing the complete closure of the active cleft over the substrate [446]. The kinetics of exchange for these large amplitude motions occurring during the turnover were estimated at a k_{ex} of ~200 s^{-1} [56], a value remarkably similar to that of ERK2 [119]. However, the importance of the faster rates of motions that we measured in the nucleotide bound form (i.e., $k_{ex} \sim 1020$ s^{-1}) has not been fully appreciated. The Y204A mutant offers a unique opportunity to test the role of conformational dynamics as the structures of the PKA-C^{WT} and PKA-C^{Y204A} are virtually superimposable [403]. Yet, the mutation causes a 400-fold decrease of the catalytic efficiency [404] and approximately a 100-fold reduction in the affinity for the pseudo-substrate, two phenomena essentially inexplicable from the structural data alone. Thermocalorimetric studies and deuterium exchange mass spectrometry data showed an overall reduction of the PKA-C^{Y204A}

163

stability, inferring an increase of conformational dynamics [400]. Indeed, our data show that the key to understanding the anomalous behavior of the mutant is the nucleotide binding event. In contrast to ERK2 [119], where the nucleotide binding seems to have a marginal role in modulating the conformational fluctuations, our data emphasize the central role of the nucleotide in orchestrating phosphoryl transfer in PKA-C. Binding of the nucleotide first links the two hydrophobic spines so that all of the catalytic machinery is integrated. In addition, the nucleotide provides the phosphoryl group necessary for chemistry to take place; however it also pre-organizes the substrate binding site, enhancing its binding affinity, shifting the range of the dynamics in a regime that is competent for catalysis. Importantly, the changes in the rates of the opening and closing motions detected for the nucleotide-bound form of PKA-C^{Y204A} by the relaxation dispersion measurements are probably responsible for both the decreased affinity for the substrate and the decrease in k_{cat}, affecting product release. In the wild-type enzyme, the opening and closing motions of the nucleotide-bound form are synchronous for several residues in the small lobe and in the hinge regions. For the Y204A mutant, these conformational fluctuations are no longer synchronous, reducing the enzyme's catalytic efficiency. These dysfunctional conformational fluctuations of PKA-C^{Y204A} are too fast to be captured by the CPMG experiments, but are detectable by TrHE experiments. Since the chemical step of the catalysis is too fast to be determined by NMR experiments, a logical explanation for the reduced catalytic turnover in PKA-C^{Y204A} is that these dysfunctional dynamics reduce the probability of the enzyme reaching a conformation competent for phosphoryl transfer [437, 447]. While our previous studies have shown that absence of motion renders the kinase inactive, relaxation dispersion data show that the presence of asynchronous motions affects the opening and closing of the enzyme, reducing the enzyme catalytic turnover.

Using a mutation of PKA-C that removes a crucial electrostatic node far from the active site, we demonstrated the relevance of both exchange rates and coordination of the conformational fluctuations for the kinase A catalytic turnover. When the fluctuations of the small lobes are synchronous, the enzyme functions with proper turnover rates. Upon removal of the electrostatic node, the rates of opening and closing are no longer synchronous and the enzyme becomes sluggish. Since different kinases display a wide range of catalytic efficiencies while maintaining the same fold, modulation of the conformational fluctuations across the entire kinome are probably responsible for tuning the signaling efficiency of these enzymes.

7.5 Footnotes

Chapter VIII

Mapping the Hydrogen Bond Networks in the Catalytic Subunit of Protein Kinase A using H/D Fractionation Factors

Geoffrey C. Li[1], Atul K. Srivastava[2], Jonggul Kim[1], Susan S. Taylor[3] and Gianluigi Veglia[1,2]*

[1]Department of Chemistry– University of Minnesota, Minneapolis, MN 55455.

[2]Department of Biochemistry, Molecular Biology, and Biophysics- University of Minnesota, Minneapolis, MN 55455;

[3]Howard Hughes Medical Institute, Department of Chemistry and Biochemistry, University of California at San Diego, CA 92093

8.1: Introduction

Cyclic AMP-dependent protein kinase A (PKA) is a ubiquitous signaling enzyme that catalyzes the phosphoryl transfer from ATP to the serine or threonine residues of their protein substrates. First crystallized in 1991,[379, 448] it served as a prototype for the kinase family. The catalytic subunit of PKA (PKA-C) is a 350-residue protein consisting of a conserved bilobal core flanked by an N-terminus helical segment, known as the A-helix, and a 50-residue C-terminal tail that wraps around the kinase.[379] The small lobe of the kinase is rich in β-strands with only two short helical segments, while the large lobe is mostly helical. The active site cleft is positioned at the interface of the two lobes and harbors the nucleotide binding site. A glycine-rich loop acts as a lid, protecting the nucleotide's phosphates that protrude from the binding cleft toward the substrate from hydrolysis. A short helix (C-helix) positioned by the activation loop contributes to the organization of the active site. The peptide positioning loop registers the substrate with respect to the nucleotide, aligning the P-site toward the γ-phosphate, with two Mg^{2+} ions participating in the active site organization for phosphoryl transfer. While the catalytic regions of PKA-C are responsible for the chemistry at the active site, signaling involves the core of the protein, [110] with two hydrophobic spines (C- and R-spines) that contribute to the definition of active and inactive states of the enzyme. The C-spine is assembled upon nucleotide binding, while the R-spine is assembled upon phosphorylation of the activation loop.[13, 111] Structural studies on other protein kinases suggest that the spines are responsible for both allosteric signaling [25] and regulation. [112, 449]

During the catalytic cycle, the kinase is thought to undergo extensive structural rearrangements. High-resolution crystal structures revealed at least three main conformational states: apo, intermediate (nucleotide-bound), and closed (ternary

complex).[2] NMR relaxation experiments have shown that the conformational dynamics of the enzyme drive the structural transitions from the open to closed conformation and play a key role in substrate recognition and turnover.[55, 56] The nucleotide acts as an allosteric effector, completing the catalytic spines [12, 13, 56] and shifting the kinase toward a structurally and dynamically committed state.[55] Reaching the committed state may require the rearrangement of the internal forces that stabilize each conformational state, such as hydrophobic, electrostatic, van der Waals, and hydrogen bonding interactions. Although to a lesser extent, hydrogen bonds are thought to play an important role in protein stability and in fine-tuning their tertiary structure. [450]

In this paper, we studied the changes in the kinase hydrogen bond strengths across the three major conformational states. To obtain residue-specific information in the hydrogen-bond strengths, we measured the hydrogen/deuterium (H/D) fractionation factors (φ) using solution NMR spectroscopy. [451, 452] The φ values report on the preference of each amide site to take up deuterium over protium from a mixed H_2O/D_2O solution. Initially developed to probe hydrogen bond strengths in dicarboxylic acids,[453] φ values have been widely utilized to investigate low-barrier hydrogen bonds in enzymes[454] and in evaluating the contribution of hydrogen bonds to protein stability.[455, 456] Recently, Cao and Bowie revisited issue of hydrogen/deuterium fractionation providing a revised energetic scale for the φ values and underscoring the importance of analyzing φ values to determine the changes in hydrogen bond strength for ligand binding to proteins.[457]

Generally, a φ value of unity indicates equal distribution of deuterium and protium between protein and bulk solvent. The amide sites involved in strong hydrogen bonds prefer protium over deuterium with $\varphi < 1$; whereas amides involved in weak hydrogen bonds have $\varphi > 1$.[455] In proteins, amide hydrogens have φ values ranging from 0.3 to

2.0, with the latter measured for very weak hydrogen bonds.[455] We measured the φ values for the backbone amides of PKA-C in three different forms: apo, ADP-bound (binary complex), and ADP-PKI peptide bound (ternary complex). Our results show that the overall φ values decrease as the kinase binds ADP and a pseudo-substrate peptide (PKI_{5-24}), indicating that the strength of hydrogen bonds gradually increases from the free to the ternary forms. Importantly, the changes in hydrogen bond strengths are not localized to the binding site but are pervasive throughout the entire protein. Whereas the majority of the hydrogen bonds increase their strengths, several other hydrogen bonds away from the ligand binding sites become weaker, suggesting a redistribution of the protein free energy. From this study, φ measurements emerge as an important complement to other NMR parameters such as chemical shifts,[90, 372, 373, 375] H/D protection factors,[458, 459] residual dipolar couplings,[308, 460] and nuclear spin relaxation measurements[16, 309, 341, 433, 461] to characterize protein conformational dynamics and to identify long-range allosteric changes upon ligand binding or mutations.

8.2: Experimental Procedures

NMR sample preparation. Uniformly ^{15}N-labeled PKA-C was expressed in *E. coli* bacteria and purified as reported previously.[6] A single protein stock solution was used for each set of the experiments for each form of the kinase. Each NMR sample contained ~200 μM PKA, 20 mM KH_2PO_4, 90 mM KCl, 10 mM $MgCl_2$, 10 mM MEGA-8 (Octanoyl-N-methylglucamide), 5% Glycerol, 20 mM dithiothreitol (DTT), 1 mM NaN_3. The pH of the buffer solutions in both protonated and deuterated water was adjusted to 6.5 (without correction for the isotope effect). For the nucleotide-bound form, PKA-C was saturated with 12 mM ADP, while for the ternary complex, the enzyme was saturated with 12 mM ADP and 350 μM of a peptide corresponding to the recognition sequence of

the protein kinase inhibitor (PKI$_{5-24}$), and 60 mM MgCl$_2$ was used. The samples containing varying concentrations of D$_2$O (5%, 20%, 40%, and 60% by volume for the apo and ternary forms; 5%, 20%, 40%, 50%, and 60% by volume for the binary form) were prepared by mixing buffer solutions of protonated and deuterated water. A 60% maximum deuteration fraction was chosen in the study due to the increase in T$_1$ as deuteration level increases, which will introduce external factors that will alter the apparent value of φ.

Determination of H/D fractionation factors. The H/D equilibrium fractionation factor (φ) is defined as the equilibrium constant of the following reaction:

$$NH:B+\frac{1}{2}D_2O \Leftrightarrow ND:B+\frac{1}{2}H_2O \tag{8.1}$$

$$\varphi = \frac{([D]/[H])_{protein}}{([D]/[H])_{water}} \tag{8.2}$$

where NH represents the weak acid and B the weak base.

To determine the fractionation factors, a series of [^{1}H,^{15}N]-TROSY-HSQC[176] spectra using a modified version of the original pulse sequence [462] were recorded on all of the forms of the kinase for all of the D$_2$O concentrations. The spectra were acquired on an 850 MHz Bruker spectrometer equipped with a triple resonance probe at 27°C with either 128 scans (for both the binary and ternary forms) or 64 scans (for the apo form) and 60 increments and a recycle delay of 1.5 seconds. The spectra were processed using NMRPipe.[463] The peak intensities were determined using Sparky [464] with assignments previously determined for PKA-C.[465] Fractionation factors are obtained by the linear least-squares analysis of

$$\frac{1}{y} = C\left[\varphi\frac{1-x}{x} + 1\right]$$

(8.3)

where *y* is the peak intensity, x is the mole fraction of water and C is the normalization parameter, which is the inverse peak intensity at 100% H_2O.

8.3: Results

H/D fractionation factors and structural transitions of PKA-C. Fractionation factors (φ) were measured by incubating PKA-C in aqueous solutions with D_2O concentrations ranging from 5 to 60% (**Figure 8.1**). Under these conditions, the intensities of the amide resonances in the [^{1}H,^{15}N]-TROSY-HSQC spectrum decrease according to their relative propensity to incorporate deuterium, reflecting the strength of the hydrogen bonds in which they are involved.[451, 455] To ensure that the exchange reached equilibrium, we incubated the samples and kept them at 25 ^{o}C for 24 hours prior to acquiring the [^{1}H,^{15}N]-TROSY-HSQC spectra. [176] Indeed, we found that the amide resonance intensities were unchanged after a 7 day incubation period. To calculate the φ values, we fit the trend of the amide peak intensities as a function of the mole ratio of D_2O. To mimic the three major conformational states of PKA-C, we performed our experiments on the apo, ADP-bound, and ADP/PKI$_{5-24}$-bound kinase. ADP was used in place of the common ATP mimic, ATPγN, because of the very slow hydrolysis on the timescale of weeks that was observed with ATPγN. [47] The [^{1}H,^{15}N]-TROSY-HSQC spectra of PKA-C saturated with either ADP or ATPγN are almost superimposable, indicating that the average conformations of the kinase are very similar. As for the binary complexes, the spectra of the ternary complexes formed with either ADP/PKI$_{5-24}$ or ATPγN/PKI$_{5-24}$-bound are similar. Only small chemical shift perturbations are observed nearby the active site, reflecting the effect of the γ-phosphate group. Upon ligand binding, PKA-C undergoes

linear chemical shift changes between the apo and closed form of the enzyme, [57, 410, 465] indicating that ligand binding shifts a pre-existing conformational equilibrium from *open* and *closed* state in the fast exchange regime on the chemical shift time scale. [410] To estimate the average conformational state of the kinase free and bound undergoing fast exchange equilibrium, we used CONCISE (COordiNated ChemIcal Shifts beHavior). [410] As reported in **Figure 8.2**, the probability densities of the complexes with ADP and ATPγN are essentially overlapped. A small but significant difference is observed for the probability densities for the ternary complexes, which reflect the differences in the observed chemical shifts (**Figure 8.2A**). Nonetheless, the average positions of the distributions on the average principal component (PC) score indicate that these complexes recapitulate both the intermediate and the closed states (**Figure 8.2C**).

When ADP is bound, the enzyme's resonances undergoes significant line broadening originating from conformational dynamics on the μs-ms timescale similar to those experienced with ATPγN or ATP. [56, 57] Therefore, several resonances in the intermediate states are not available for analysis. Overall, 211, 201, and 243 resonances for the apo, binary, and ternary forms of PKA-C, respectively, were available for the calculations of the φ values. Of the calculated φ values, we eliminated those exceeding the value of 2.0, which are affected by rapid exchange and T_1 values[455] as well as those residues showing poor correlation coefficients ($R^2 < 0.70$). Note that in a few instances we measured φ values slightly lower than 0.20. Although included in the plots, those residues are considered not exchanging with the solvent in the time scale we analyzed. Although it is possible that highly buried residues may not reach full exchange, there are specific regions in PKA-C, particularly the hydrophobic core, that are resistant to deuterium exchange. Taylor and coworkers found similar observations for the

residues in the hydrophobic core of PKA-C through deuterium exchange mass spectrometry (DXMS).[466] The overall mean fractionation factor values for the apo, binary, and ternary complexes were 1.06 ± 0.52, 1.04 ± 0.52 and 0.96 ± 0.55, respectively.

Although the overall strength of the hydrogen bonds increases in agreement with the thermostability of the protein,[2] there is variability of the φ values across the enzyme, reflecting local changes in hydrogen bond strength upon ligand binding (**Figure 8.3**). In fact, the plots describing the number of occurrences versus φ values for all three forms of PKA-C show broad distributions of φ values (**Figure 8.4**). This contrasts with the tight bell-shaped distribution of φ in staphylococcal nuclease that was centered at 0.85.[455] The variability of φ is apparent in all of the structural motifs for all of the states (**Table 8.1**). In the apo state, high φ values ($<\varphi>$ greater than 1.2) were measured for the N-terminus (αA and β1) and C-terminal tail; while the helices in the large lobe, namely along αE and αF, display very low φ values ($<\varphi>$ less than 0.5, **Table 8.1**). These results, in qualitative agreement with the DXMS experiments, suggest that these hydrogen bonds make a significant contribution to the stability of the large lobe.[466] Unlike previous fractionation studies,[455, 467-469] there is no correlation between φ values and secondary structure in PKA-C. For instance, W30 and I228, both located in α-helices, exhibit rather different hydrogen bond strengths (**Figures 8.1**). We also observed that most residues that show unusually high φ values ($\varphi > 2.0$) in the apo form are located in the solvent-exposed, unstructured region of the enzyme. Due to exchange broadening on the μs-ms timescale upon ADP binding, we were unable to measure φ in the active site, including the Gly-rich, DFG, activation, and peptide positioning loops. However we observed several changes in φ values radiating away from the nucleotide

binding pocket to more peripheral domains of the enzyme (**Figures 8.4 and 8.5**). In the

small lobe these changes include β strands 1, 4-5 ($<\Delta\varphi^{binary-apo}>$ = -0.27), the αA-β linker

($<\Delta\varphi^{binary-apo}>$ = -0.23), and αA ($<\Delta\varphi^{binary-apo}>$ = -0.16) (**Figure 8.5**). Interestingly, the

loops connecting the αE, αF, and αH helices in the large lobe display lower φ values

than in the apo state ($<\Delta\varphi^{binary-apo}>$= -0.25, **Table 8.1**). Previous research has shown that

the nucleotide in PKA-C functions as an allosteric effector. [12, 56] These results

suggest that nucleotide binding may affect short- and long-range intermolecular forces

through altering in part the hydrogen bonding network.

Binding of PKI$_{5-24}$ increases the compactness of the enzyme as it adopts a

closed, solvent-protected conformation, [2] with 54 out of 231 resonances displaying φ

values around 0.3 (**Figure 8.4**), including residues in β strands 2 and 3, C-helix, αC-β4

loop, hinge, αD, αE, the segment from the P+1 loop until the F helix, αF, αH, and the

αH-αI loop. Most of these residues are buried in the interior of the kinase. Overall, we

observed a decrease of the average φ values ($<\Delta\varphi^{ternary-binary}>$ = -0.10 $\pm$ 0.38),

particularly for residues localized in the large lobe and C-terminal tail (**Figure 8.5**),

except for a few residues in the αA helix ($<\Delta\varphi^{ternary-binary}>$ = -0.09 $\pm$ 0.21) and the small

lobe ($<\Delta\varphi^{ternary-binary}>$ = -0.09 $\pm$ 0.24) (**Figure 8.5**). In contrast, the hinge region shows a

positive change of $<\Delta\varphi>$ (0.35 $\pm$ 0.30, **Figure 8.5 and Table 8.1**), which may result from

a reorientation of the hinge region that enables the active site cleft to close. Additionally,

PKI$_{5-24}$ binding increases the hydrogen bond strength in the inner core of the kinase for

helices αE, αF and αH (**Table 8.1**) as well as for several residues in the C-terminal tail

(**Figure 8.5**)**,** consistent with the crystallographic data[2, 22, 470]. Specifically, the acidic

patch (residues 330-334) has been hypothesized to recruit the basic substrate into the

active site cleft, where Y330 is poised to interact with the substrate's P-3 arginine

residue.[100, 465] Substrate binding primarily strengthens the hydrogen bonds in the large lobe of the enzyme, and also those in the C-terminal tail, recruited to assemble the active site for catalysis.

To account for the changes in catalytically important motifs (i.e. Gly-rich, DFG loop, peptide positioning loops, etc.), we considered only the φ values for the apo and ternary forms (**Figure 8.6**). The majority of the catalytic motifs experienced strengthening of hydrogen bonds, including the Gly-rich loop ($<\Delta\varphi^{ternary-apo}>$ = -0.61 $\pm$ 0.28), αC ($<\Delta\varphi^{ternary-apo}>$ = -0.43 $\pm$ 0.27), and the peptide positioning loop ($<\Delta\varphi^{ternary-apo}>$ = -0.39 $\pm$ 0.24). In contrast, the only reporter of the DFG loop (Phe185) shows a higher φ value for the ternary complex ($\Delta\varphi^{ternary-apo}$ = 0.50). Its propensity to incorporate deuterium could result from the increased conformational fluctuations caused by nucleotide binding. Taken together, these results show that nucleotide and pseudo-substrate binding assembles the active site, strengthening the hydrogen bonds in the active site and coordinating catalysis in PKA-C.

8.4: Discussion

In recent years, PKA-C has emerged as a model system to understand both kinase function as well as intramolecular allosteric signaling.[2, 13] The transitions of PKA-C between different states involve both conformational and dynamic (protein flexibility) changes that propagate from the ligand binding sites to remote parts of the molecule.[12, 56] Therefore, a complete understanding of this allosteric signaling necessitates the analysis of intra- and inter-molecular interactions that hold the protein together.[471] Among those, hydrogen bonds play a key role in allosteric regulation[472] and recent reports have demonstrated their importance in enzymatic catalysis and inhibition.[473, 474] DXMS techniques have been used to analyze hydrogen bond

networks of proteins to identify domains that might be involved in allosteric transitions.[466, 475] Unlike DXMS, NMR spectroscopy monitors H/D exchange in a site-specific manner, making it possible to track hydrogen bonds throughout the protein at the atomic level. On the other hand, the NMR H/D exchange technique reports on the kinetic protection factors, monitoring the decay of the amide signals versus time.[458, 459] However, this technique, with a few exceptions for selected systems,[476-478] usually requires the lyophilization of the protein under examination. In contrast, the equilibrium φ measurements can be accomplished by incubating the proteins in H_2O/D_2O solutions without lyophilization and report directly on the strength of the hydrogen bonds. These measurements are carried out under equilibrium conditions, which avoid the freezing-drying procedures required for the H/D protection factor measurements. This is crucial for PKA-C, an enzyme that is partially or completely inactivated upon lyophilization. Previous studies using H/D fractionation factors focused on the enzyme's active sites [456, 479] and did not fully exploit the potential of this approach for identifying local and long-range changes in the hydrogen bond network and allosteric communication. In fact, only marginal changes were detected for the φ values upon ligand binding to the proteins analyzed.[451, 455, 469, 479] These proteins, however, possess relatively rigid and compact structures with uniform values of φ. In contrast, the structure of PKA-C is highly dynamic, undergoing substantial conformational changes upon ligand binding.[4, 393] As a result, the φ values we measured for PKA-C have a much broader distribution than those measured for staphylococcal nuclease,[455] ubiquitin,[467] histidine-containing proteins,[468] and immunoglobulin G binding domain of protein G.[468] As PKA-C transitions from the open to closed conformations upon binding the nucleotide and the pseudo-substrate inhibitor, the average φ values decrease, suggesting that the intramolecular hydrogen bonds

become stronger. Globally, these results correlate well with X-ray crystallography,[2] NMR spectroscopy,[12] florescence studies,[480, 481] thermodynamic[482] as well as DXMS analysis[466, 475] that show PKA-C's structure becoming more compact and thermostable in the closed conformation. Structurally, nucleotide binding allosterically couples the two lobes of the kinase, causing positive binding cooperativity between the nucleotide and the pseudo-substrate.[12, 465] Binding of the pseudo-substrate further stabilizes the complex, as is also evident in the increased strengths of hydrogen bonds in the large lobe as measured by the fractionation factors. Overall, nucleotide binding affects the strength of hydrogen bonds both in the small and large lobes, while pseudosubstrate binding affects mostly the residues in the large lobe. This is consistent with the view that the nucleotide is an allosteric effector, organizing the active site, while the large lobe provides a docking surface for the substrate to bind.[2, 12] These detailed effects of the nucleotide binding went undetected in the previous DXMS measurements *[475]* either for lack of data points or intrinsic limitations of the technique. Recent community maps analysis of molecular dynamics simulations [25] predicted that the motions of the different secondary structural elements of the small lobe are highly correlated. The $\beta 1$, $\beta 4$, $\beta 5$ and the αA-β linker were attributed to community A (responsible for nucleotide binding), while the A-helix, portion of αA-β linker, and αC-$\beta 4$ linker were ascribed to community C, a central hub that controls the functions of the other communities.[25] The increase in the strength of the hydrogen bond networks in the small lobe upon nucleotide binding supports the communication between these communities that may act in concert for the enzyme's closure. [25] Moreover, the φ values show that, from the apo to the ternary complex, the hydrogen bonds in the αC helix become stronger, indicating that perhaps strengthening these interactions is essential for proper organization of the active site. From the X-ray structure, the side

chains in each turn of the αC helix interact with the different domains of the enzyme. Specifically, Arg93 forms a cation-π interaction with the aromatic side chains of Trp30 and Phe26 of the αA helix. Glu91 forms a conserved dyad with Lys72 of β-strand 3, while His87 forms an ion pair with the phosphate group of Thr197 in the closed conformation.[2] The H/D fractionation factors also show an extensive rigidification of the hydrophobic core in the enzyme upon ligand binding as previously highlighted by DXMS studies, with the αE, αF, and αH helices involved in the intra-molecular communication are more resistant to deuterium exchange.[466]

Nucleotide binding also increases the hydrogen bond strengths of residues in the region that caps the bottom of the large lobe. The allosteric coupling between the catalytic loop and the large lobe was also observed using DXMS experiments.[466] In particular, the interactions between the conserved residues Glu208 of the APE motif and Arg280 are evident in our data, where these residues show lower φ values upon PKI binding to the binary form of the enzyme. This ion pair connects the P+1 loop and the loop between the G and H helices. The C-terminal tail undergoes significant domain movement when the enzyme transitions from open to closed conformation, as observed in the crystal structure.[22] While DXMS data suggest that the nucleotide binding increase the amide protection factors for the entire C-terminal tail,[475] our data show that residues 315-345, which contains the gate controlling the nucleotide access, display hydrogen bonds weaker than in the apo form. These weak hydrogen bonds concur to the increased flexibility of the intermediate state, but eventually become stronger upon formation of the ternary complex, with the interactions between the acidic cluster and the basic residues of the pseudo-substrate.[100]

Overall, this study demonstrates that the changes in the allosteric network of the kinase are manifested through variations in hydrogen bond strengths. These changes

are not unidirectional: while several hydrogen bonds become stronger upon ligand binding, other interactions become weaker, underscoring a redistribution of the free energy of binding occurring throughout the whole enzyme. As NMR methodology progresses toward understanding the mechanisms of allosteric transmission at the atomic level, the measurement of equilibrium H/D fractionation factors emerges as a complementary method to other NMR techniques to trace allosteric communications within proteins and enzymes.

8.5 Footnotes

Chapter IX

Dysfunctional Conformational Dynamics of Protein Kinase A Induced by a Lethal Mutant of Phospholamban Hinder Phosphorylation

Jonggul Kim[1], Larry R. Masterson[2], Alessandro Cembran[1,2,3], Raffaello Verardi[2], Lei Shi[1], Jiali Gao[1], Susan S. Taylor[4]* and Gianluigi Veglia[1,2]*

[1]Department of Chemistry– University of Minnesota, Minneapolis, MN 55455.

[2]Department of Biochemistry, Molecular Biology, and Biophysics- University of Minnesota, Minneapolis, MN 55455;

[3]Present address: Department of Chemistry and Biochemistry, University of Minnesota Duluth, Duluth, MN 55812

[4]Howard Hughes Medical Institute, Department of Chemistry and Biochemistry, University of California at San Diego, CA 92093

9.1: Introduction

Phosphorylation by cAMP-dependent protein kinase A (PKA) is a central signaling pathway in cardiomyocytes, where it modulates the activity of several Ca^{2+} handling proteins[483, 484]. In particular, PKA targets phospholamban (PLN), a small membrane protein embedded in the sarcoplasmic reticulum that binds and regulates the activity of the Ca^{2+}-ATPase (SERCA). The SERCA/PLN complex plays a critical role in cardiac contractility, since it is responsible for Ca^{2+} reuptake in the sarcoplasmic reticulum, thereby controlling muscle relaxation, or diastole [483]. PLN regulation of SERCA keeps Ca^{2+} flux within a physiological window [485]. Unphosphorylated PLN reduces SERCA's apparent affinity for Ca^{2+}, while phosphorylation at Ser16 reverses PLN's inhibitory effect, increasing Ca^{2+} flux and enhancing cardiac muscle relaxation[486]. PKA phosphorylation of PLN is a primary response to β-adrenergic stimulation in the heart, affecting cardiac output directly[487]. Altered levels of PLN phosphorylation (i.e., hypo- or hyper-phosphorylation) cause SERCA's function to be outside this physiological window. Specifically, aberrant PLN phosphorylation depresses Ca^{2+} cycling, with an attenuation of Ca^{2+} transients in both amplitude and frequency, resulting in cardiac disease[125, 488]. Six naturally occurring mutations of PLN have been linked to early and/or late onset dilated cardiomyopathy (DCM), a leading cause of morbidity and mortality worldwide[489, 490]. First reported by Kranias *et al.* [491, 492] the R14del mutation of PLN (PLN^{R14del}) was found in several DCM patients[491], and more recently identified in 14% of a cohort of 354 patients diagnosed with either DCM or arrhythmogenic right ventricular cardiomyopathy[493]. It has been proposed that the dysfunctional effects of PLN^{R14del} are due to chronic suppression of SERCA activity, with a synergistic inhibition by the mutant and the wild-type PLN (PLN^{WT})[491, 494]. Recent

studies, however, show that PLN phosphorylation by PKA-C is significantly hindered in R14del transgenic mice (approximately 7% of wild-type levels), causing Ca^{2+} mishandling and progression of DCM[494]. While the phenotype and genotype of the R14 deletion have been identified, the molecular mechanisms for its aberrant phosphorylation are still unknown.

The R14 deletion is located at the recognition sequence for the catalytic subunit of PKA (PKA-C) (**Figure 9.1**)[491]. From the X-ray structure of the PKA-C/ATPγN/PLN^{WT} complex (PDB:3O7L), the PLN consensus sequence for PKA-C ($R-R-X_1-S-X_2$, where X denotes a variable amino acid) adopts an extended conformation within the binding groove[56, 129]. The side chain of R14 (P-2 site) points toward the large lobe and interacts with Y204, E230, and E203, while the side chain of R13 (P-3 site) interacts with S51, the ribose ring, and hydroxyl group of Y330, clamping on the small lobe (**Figures 9.1**)[56]. Based on these structural features, we hypothesized that the R14 deletion disrupts intermolecular interactions between enzyme and substrate, affecting the motions responsible for opening and closing the active cleft and ultimately enzyme turnover. To test this hypothesis, we compared the kinetics of phosphorylation, thermodynamics of binding, and enzyme structural dynamics of the PKA-C/PLN^{R14del} complex to PKA-C/PLN^{WT} using steady-state kinetic measurements, isothermal titration calorimetry (ITC), nuclear magnetic resonance (NMR) spectroscopy, and molecular dynamic (MD) simulations. We found that, thermodynamically and kinetically, PLN^{R14del} exhibits characteristics of a poor substrate compared to PLN^{WT}. More importantly, deletion of R14 prevents the formation of a catalytically committed Michaelis complex, causing dysfunctional conformational dynamics that concur with the reduction of catalytic

182

efficiency. These findings explain the molecular mechanisms for the sluggish phosphorylation kinetics, leading to the Ca^{2+} mishandling associated with DCM. Overall, our study emphasizes the importance of well-tuned dynamic interplay between enzyme and substrate to achieve optimal catalysis.

9.2: Materials and Methods

Sample Preparation. Recombinant catalytic subunit of PKA was expressed in BL21 DE3 cells by the method described by Studier at 24°C[346] and $^2H/^{13}C/^{15}N$ and $^2H/^{15}N$ PKA-C was expressed as previously described[12]. Purification of PKA-C was performed as previously described using the His_6-RIIα(R213K) subunit[321] and a second purification step was performed by using the HiTrap SP cation exchange column. Peptides (PLN_{1-19}^{WT}/PLN_{1-19}^{R14del}/PKI$_{5-24}$) were synthesized using standard Fmoc chemistry on a CEM Liberty microwave synthesizer, cleaved with Reagent K (TFA/thioanisole/water/phenol/2-2'-(ethylenedioxy)diethanethiol, 82.5:5:5:5:2.5 v/v) for 3 hours and purified using a semi-preparative Supelco C18 reverse-phase HPLC column at 3 ml/min. Molecular weight and the quantity of the peptides were verified by amino acid analysis (Texas Tech, College Station, TX).

ITC measurements. All ITC data was acquired on a VP-ITC microcalorimeter (Malvern, Inc.). PKA-C, PLN_{1-19}^{WT}, and PLN_{1-19}^{R14del} was prepared in 20 mM MOPS, 90 mM KCl, 10 mM DTT, 10 mM MgCl$_2$, 1 mM NaN3 at pH 6.5. For nucleotide saturation 2 mM of ATPγN was added. All experiments were performed in 300K. Data was fit to the Wiseman Isotherm[280] assuming one-site binding using the NanoAnalyze (TA instruments, New Castle, DE) software.

Enzyme Assays. The steady state activity assays of PLN$_{1-19}$ and R14del$_{1-19}$ under saturating ATP concentrations were performed spectrophotometrically at 298K as

described by Cook et. al[41]. The values of V_{max} and K_m were obtained from a non-linear fit of the initial velocities to the Michaelis-Menten equation. The extent of phosphorylation for full-length PLN analogs was monitored by gel-shift assays using 10 μM of substrate (assessed by densitometry), 1000 U/mg PKA-C in 0.1% octyl-glucoside, 20 mM MOPS (pH 7.25), 0.05 mM PMSF, 0.02 % NaN_3, 1 mM $MgCl_2$. The reaction was initiated by adding 1 mM ATP and incubated for 12 hours at 30 ^{o}C. The phosphorylation reaction was then stopped by addition of 1% SDS. Tris-Tricine polyacrylamide gels (12%) were run with 2 μg of PLN (~5 μL reaction mixture) and stained with Coomassie brilliant blue.

NMR measurements. Standard Trosy-select triple resonance, steady-state NOE and HSQC experiments were carried out on a 850 MHz Bruker Advance III spectrometer equipped with a TCI cryoprobe. Concentrations of samples for triple resonance experiments were ~0.4- 0.7 mM and samples for relaxation experiments were 0.25-0.4 mM. 12mM of ATPγN was added for the nucleotide bound form and 1.0-2.0 mM of peptide (PLN_{1-19}^{WT}/PLN_{1-19}^{R14del}) for the ternary complex. Spectra were collected at 300K and processed using NMRPipe[495] and visualized using Sparky. R_{ex} values were measured using the Trosy Hahn-Echo pulse sequence[123] and analyzed as described previously[55, 278]. Qualitative verification of R_{ex} was done by measuring inverse peak heights as previously described[278].

MD Simulations. MD simulations were set up using CHARMMc36 and run with NAMD using an initial docked structure. All Structures were solvated in a TIP3 water box with K+ and Cl- added as counter ions to reach an ionic strength of approximately 150 mM. Following an initial equilibration, 80 ns of MD simulations of PKA-C/PLN_{1-19}^{R14del} was performed at constant temperature and pressure. PCA and RMSF analysis was performed as previously described[55].

9.3: Results

R14del causes a reduction of binding affinity and kinetics. The binding thermodynamics of $\mathrm{PLN^{WT}}$ and $\mathrm{PLN^{R14del}}$ to the apo and nucleotide-bound protein kinase (PKA-C/ATPγN complex) were measured using isothermal titration calorimetry (ITC) with the synthetic peptides, $\mathrm{PLN_{1-19}^{WT}}$ and $\mathrm{PLN_{1-19}^{R14del}}$, corresponding to the first 19 residues of the cytoplasmic domain of $\mathrm{PLN^{WT}}$ and $\mathrm{PLN^{R14del}}$, respectively, which include the recognition sequence for the kinase. From the ITC measurements carried out in the presence of the nucleotide analog (ATPγN), we derived the binding enthalpy, entropy, dissociation constants (K_d) as well as substrate binding cooperativity for $\mathrm{PLN^{WT}}$ [12, 55, 56]. We found that PKA-C exhibits high substrate affinity for $\mathrm{PLN_{1-19}^{WT}}$ in the presence of ATPγN (K_d = 28 μM) with a slightly unfavorable entropic contribution to binding (TΔS = -0.37 kcal/mol, **Figure 9.2A**). In contrast, binding titrations of $\mathrm{PLN_{1-19}^{R14del}}$ under identical experimental conditions resulted in a K_d ~200 μM, with the entropic change TΔS ≈ 4 kcal/mol as the dominating contribution to binding (**Figure 9.2A**). Interestingly, for $\mathrm{PLN_{1-19}^{R14del}}$ binding in the absence of ATPγN, we were unable to measure the binding cooperativity observed for $\mathrm{PLN_{1-19}^{WT}}$ and typical of other substrates [12, 56]. These thermodynamic measurements indicate that the affinity and the nature of the interactions are affected by the R14 deletion. To evaluate the efficiency of phosphorylation by PKA-C, we carried out steady-state phosphorylation kinetics using a coupled enzyme assay with $\mathrm{PLN_{1-19}^{WT}}$ and $\mathrm{PLN_{1-19}^{R14del}}$ (**Figure 9.2B**). Kinetically, $\mathrm{PLN_{1-19}^{WT}}$ behaves similarly to the standard substrate Kemptide (k_{cat} = 23 ± 1 s^{-1}) [50]. In contrast, we did not detect any significant phosphorylation for $\mathrm{PLN_{1-19}^{R14del}}$. Upon a four-fold increase in PKA-C

concentration (from 64 to 256 nM total enzyme) and an increase in substrate from 100 to 900 μM, we observed only marginal phosphorylation. Under these experimental conditions, the k_{cat} is approximately 6 times smaller and the catalytic efficiency is approximately 300 times lower for PLN_{1-19}^{R14del} than that of PLN_{1-19}^{WT}. Moreover, we repeated phosphorylation assays using full-length PLN^{WT} and PLN^{R14del}. Upon incubation with PKA-C, we detected complete phosphorylation of PLN^{WT} (5 phosphates per pentamer, **Figure 9.2C**). In contrast, PLN^{R14del} was only partially phosphorylated, as shown by the slight band shift in the SDS-PAGE (**Figure 9.2C**). These phosphorylation assays exclude any effect of the transmembrane domains and confirm the sluggish phosphorylation kinetics measured for PLN_{1-19}^{R14del}. These data are in agreement with phosphorylation kinetics carried out with model peptides missing the P-3 site [496] and PLN .[497, 498].

NMR mapping of substrate binding to PKA-C. To analyze the structural changes that PKA-C undergoes upon binding PLN_{1-19}^{WT} and PLN_{1-19}^{R14del}, we mapped the amide backbone fingerprint of the enzyme using [^{1}H,^{15}N]-TROSY-HSQC experiments[176]. To further validate the assignment of the major conformational equilibria, we performed a full triple resonance assignment on the apo, binary and closed states. The combined ^{1}H and ^{15}N chemical shift perturbations ($\Delta\delta$) at each amide site of PKA-C report the changes in the local chemical environment (structure, electrostatics, dynamics, *etc.*) upon substrate binding (**Figure 9.3**). Binding of the PLN_{1-19}^{WT} and PLN_{1-19}^{R14del} peptides to PKA-C results in different chemical shift patterns. Binding of PLN_{1-19}^{R14del} to the binary form of the enzyme (PKA-C/ATPγN complex) retains significant line broadening in many resonances, similar

to the nucleotide-bound enzyme [12] primarily along catalytically important motifs. In contrast, binding of PLN_{1-19}^{WT} to the binary complex renders observable several residues that were previously broadened upon nucleotide binding (**Figure 9.3B**). Residues belonging to the Gly-rich loop, peptide positioning loop, the hinge region and the DFG loop, which play critical roles in catalysis, are observed only with the wild-type substrate, but absent in the complex formed with the deletion mutant. Since these spectra were compared at saturating conditions, this phenomenon indicates that the conformational dynamics of the ternary complexes are different. To evaluate the structural transition of PKA-C with the addition of the substrates, we used CONCISE (COordiNated Chemical Shifts bEhavior)[410]. This method performs a statistical analysis on linear chemical shift trajectories of each amide resonance to identify the position of each state along the conformational equilibrium. Following ligand binding (*i.e.*, nucleotide and substrate), the PKA-C amide resonances display linear chemical shift, with the resonances corresponding to the *apo* enzyme populating one extreme and those of the closed state (ternary complex with the inhibitor, PKI_{5-24}) populating the opposite extreme of the linear correlations (**Figure 9.3a,c**). This behavior exemplifies a conformational equilibrium among the three major conformational states of the kinase (open, intermediate, and closed), whose relative populations are modulated by ligand binding [56, 58, 410]. The nucleotide shifts the open state population toward the intermediate state*,* and the substrate shifts the population toward the closed state [55, 56]. We found that PLN_{1-19}^{WT}, as well as Kemptide, is able to shift the conformational equilibrium of PKA-C toward a catalytically committed state, while PLN_{1-19}^{R14del} is unable to cause a significant conformational change, remaining in an intermediate state (**Figures 9.3B,C**). Dynamic light scattering experiments also demonstrate that the enzyme in complex with PLN_{1-19}^{WT}

exhibits a rotational correlation time shorter than the corresponding $\text{PLN}_{1-19}^{R14del}$ bound complex, adopting a more open conformation with $\text{PLN}_{1-19}^{R14del}$. Based on this analysis, we conclude that $\text{PLN}_{1-19}^{R14del}$ binding shifts the population of the enzyme towards a conformation that is both structurally and dynamically different from the PKA-C/PLN_{1-19}^{WT} complex, forming a partially closed state.

R14del mutant binding causes dysfunctional conformational dynamics of PKA-C.

The crystal structure of the PKA-C/PLN_{1-19}^{WT} complex[56] shows that the arginine residue in P-2 position of PLN forms an electrostatic network with E127, Y330, and the ribose moiety of ATP (**Figure 9.1B**); while the P-3 arginine interacts with R133, E230, and Y204. This dense network of interactions positions the substrate in a catalytically committed conformation. We reasoned that the removal of one of the two arginine residues in the recognition sequence may alter the enzyme conformation and motions. To test this hypothesis, we analyzed the conformational dynamics of the complexes using solution NMR spectroscopy. Specifically, we used the [^{1}H,^{15}N] heteronuclear steady-state NOE experiment (HX-NOE)[196] as a proxy for motions on the ps/ns timescale. The average trimmed HX-NOE values for PKA-C bound to PLN_{1-19}^{WT} and $\text{PLN}_{1-19}^{R14del}$ are 0.84 ± 0.09 and 0.83 ± 0.10, respectively, indicating that the overall conformational dynamics of the complexes on the fast timescale are similar. However, significant local variations of HX-NOE values were found between the two complexes. Residues in neighboring the Mg^{2+} positioning, catalytic loop, the αF-αG loop and the αG-αH loop (D161, R190, V191, D241, Q242, G253, K254, and R256), linked to be involved in substrate binding and regulation[2], are more flexible when PKA-C is bound to

PLN_{1-19}^{R14del}; while several residues flanking the C-helix, the αA-β1 linker and the C-terminus (S34, Q35, T37, K83, Q96, A97, F347, T348, E349, F350) appear to be more rigid. These changes in the fast dynamic time scale might be related to the changes in the overall binding entropy as measured by ITC[290].

Moreover, we investigated conformational dynamics in the μs/ms timescale by quantifying the contribution of chemical exchange to the transverse relaxation rate (R_{ex}) using the TROSY Hahn-Echo experiment[123]. We found striking differences in the R_{ex} values for the two complexes . In agreement with the previously reported data, the binary form of the enzyme with ATPγN experiences considerable conformational dynamics[56], especially along catalytic structural elements such as the glycine rich loop, C-helix, peptide positioning loop, and DFG loop[2]. When PLN_{1-19}^{WT} is bound to PKA-C/ATPγN, these structural elements remain considerably dynamic; however, substrate binding decreases the R_{ex} values. Residues along catalytically important motifs such as G55 and M58 in the glycine-rich loop, D166 in the catalytic loop, R190 and V191 near the Mg^{+2} positioning loop, and E208 belonging to the APE motif all experience a substantial decrease in R_{ex} values. These results indicate that the ternary complex with PLN_{1-19}^{WT} is still dynamic, although the motions are attenuated with respect to the binary form; in contrast, the PKA-C/ATPγN/PLN_{1-19}^{R14del} complex displays enhanced conformational dynamics in regions important for catalysis. For instance, residues in the Glycine-rich loop (G55, M58, and L59), near the Mg^{2+} positioning (R190 and V191), and the APE motif (such as E208) all experience R_{ex} values similar to those found in the PKA-C/ATPγN comple. In addition, we observed a substantial increase in conformational dynamics in the μs-ms time scale in several other regions. Specifically, due to the loss of the P-2 arginine the acidic patch region positioned along the C-terminal tail (residues

330-334) is no longer electrostatically connected to the active site and experiences an increase in conformational dynamics (**Figure 9.4**). Increased motions occur for residues around D220, which is the conduit for allosteric signaling from the F-helix to the regulatory spine (R-spine, **Figure 9.4**)[12].

Molecular dynamics (MD) simulation of the ternary complexes with PLN_{1-19}^{WT} ***and***

PLN_{1-19}^{R14del}. To interpret the dynamic effects of the deletion of P-3 arginine in the substrate, we performed atomistic MD simulations in explicit environments on both PKA-C/PLN_{1-19}^{WT} and PLN_{1-19}^{R14del} complexes. Starting from the crystal structure of PKA-C (PDB:3O7L), we used the HADDOCK package [168] to dock the substrates (PLN_{1-19}^{WT} or PLN_{1-19}^{R14del}) to the enzyme's binding groove according to the canonical consensus sequence in the PKA-C/PKI$_{5-24}$ X-ray structure [2]. In general, MD simulations show that the interactions in the proximity of the active site are similar to those observed in the PKA-C/PKI$_{5-24}$ and PKA-C/PLN_{1-19}^{WT} crystal structures (**Figure 9.1B**)[2, 56]. In particular, the acidic cluster surrounding Y330 latches on the small lobe, clamping the glycine-rich loop down into the active site. Also, E127 in the linker region connects the small and large lobes. In contrast, the P-2 arginine points toward the large lobe, interacting with E203, Y204, and E230. These electrostatic interactions are part of an allosteric network that ensures structural and dynamic communication within the enzyme[9, 12, 58] (**Figure 9.5A**). During ~100 ns of MD simulations of the PKA-C/PLN_{1-19}^{WT} complex, we found that the P-2 arginine residue (R14) does not change its side chain conformation, thus preserving the inter-residue interactions present in the crystal structure (**Figures 9.5A**). In contrast, the electrostatic interaction between the R13 guanidino group (P-3 site) and the hydroxyl group of Y330 breaks apart, with an approximately 90° rotation of the Arg

side chain torsion angles (**Figure 9.5A**). The latter causes the formation of new, transient interactions between the guanidino group and the α and β phosphates of ATP [55], with the P-3 Arg (R13) acting as a three-way switch between the small lobe, large lobe, and the ATP molecule. With the PKA-C/$\text{PLN}_{1-19}^{R14del}$ complex the transient interactions between the guanidine group, Y330 and the phosphates of ATP are lost, pushing the P-3 side chain away from the active site (**Figure 9.5B**). The opening and closing motions of the enzyme upon binding the wild-type and mutated substrate were analyzed using principle component analysis (PCA) (**Figure 9.5C**). The first principal component (PC1) reports on the opening and closing motion of the two lobes. When monitored with the C^{α} distance between S53 and G186 ($d_{S53\text{-}G186}$), PC1 describes the open, intermediate, and closed conformational states of the kinase[55]. The PKA-C/PLN_{1-19}^{WT} complex samples an ensemble of conformations situated between the open and closed states. In contrast, the ensemble of conformations accessible to the PKA-C/$\text{PLN}_{1-19}^{R14del}$ complex is closer to the open/intermediate basin. The slightly more open state found with the mutated substrate is supported by both the hydrodynamic radii from dynamic light scattering, indicating a less compact conformation of the PKA-C/$\text{PLN}_{1-19}^{R14del}$ complex as well as the chemical shift trajectories (**Figure 9.3C**). Root mean square fluctuation analysis (RMSF) was performed to see the largest change in dynamics upon R14 deletion. The analysis demonstrates that the glycine rich loop, αF-αG loop and the αG-αF loop, become more dynamic with the mutation while the αA-β1 linker and the C-terminus becomes more rigid. This analysis corroborates the HX-NOE data and, taken together, these results suggest that the missing P-3 guanidino group changes the interactions in the vicinity of the active site, affecting the opening and closing of the kinase.

9.4: Discussion

The R14 deletion mutant of PLN provides a unique opportunity to study the effects of dysfunctional substrates on kinase structural dynamics using NMR spectroscopy. In fact, structural studies on complexes between kinases and their substrates are rather sparse, since the low binding affinity prevents crystallization. As a result, most X-ray structures are obtained in the presence of small drugs or pseudo-substrate inhibitors[11]. The R14 deletion is located within the kinase recognition site and eliminates the P-3 site. The P-3 site is crucial for efficient kinetics as assessed in model peptide substrates[496]. In fact, the missing electrostatic interactions at the P-3 arginine changes the register of the recognition sequence, with Arg 9 shifted to the P-6 position (**Figure 9.1**). These structural changes hinder $\text{PLN}_{1-19}^{R14del}$ binding to PKA-C. However a reduction in affinity alone is insufficient to explain the sluggish kinetics as most kinase/substrate interactions are weak in nature[11]. For instance, the standard PKA-C substrate Kemptide has a K_d of approximately 200 µM, yet it displays kinetic parameters common to other PKA-C substrates[7, 9, 12]. Although the R14 does not actively participate in the phosphorylation reaction[49], the removal of R14 in PLN has a dramatic effect on the enzyme. Not only does it reduce PLN's binding affinity, it also affects the organization of the active site. In fact, in the complex with the wild-type R13 and R14 act as a bridgehead between the small lobe (through R13/Y330) and large lobe (R13/E127 and R14/E203/Y204). The guanidino group of R13 interacts with the γ-phosphate of ATP, likely facilitating the opening and closing of the active site. While the guanidino group of the R14 arginine residue is firmly anchored to the large lobe (**Figure 5A**), the R13 arginine is more dynamic and establishes transient interactions with the acidic cluster of PKA-C (328-334), a key region for determining opening and closing of the active cleft[2]. The role of these interactions in catalysis is also supported by steady-

state phosphorylation kinetic measurements, which show that the PKA-C[Y330F] mutant decreased k_{cat} by approximately sixty percent and increased K_M for Kemptide approximately five-fold[100]. The dramatic loss of catalytic efficiency $\text{PLN}_{1-19}^{R14del}$ compared to Y330F indicates the loss of P-3 site in PLN is more disruptive than simply the loss of an electrostatic bridge. In addition to a perturbation of the structural and electrostatic preorganization at the active site, the deletion of R14 disrupts the anchoring of the substrate with the small lobe, enhancing the conformational dynamics across the enzyme backbone (**Figures 9.4**). With completion of the backbone resonance assignment on the three major structural forms of PKA-C (apo, binary, and closed), we were able to identify several resonances that were previously unassigned and were observable with the addition of PLN_{1-19}^{WT}. This allowed us to identify that PKA-C bound to substrate remains dynamic, but attenuated with respect to the nucleotide bound form, reflecting an opening and closing of the enzyme (committed conformational dynamics)[55, 56]. In contrast, the elimination of the interactions at the P-3 site in the PKA-C/$\text{PLN}_{1-19}^{R14del}$ complex prevents the assembly of the small and large lobes, and the complex adopts a partially closed conformation with dysfunctional dynamics (**Figure 9.6**).

Recently, we showed that the allosteric mutant of PKA-C, Y204A[499] disrupts the hydrophobic core adjacent to the active site and removes electrostatic interactions with the P-2 arginine, desynchronizing the opening and closing motions globally. The deletion of the P-3 arginine increases the conformational dynamics extending throughout the N terminus (αC-β1-linker), the C-terminal tail (acid patch)[2], and the F-helix, which constitute the central signaling conduit of the kinase connecting the R-spine with the F-helix [13] (**Figure 9.4**). While the lack of allosteric transmission from the active site to

the C-terminal tail could be anticipated by the loss of the P-3 electrostatic interaction in the active site, the behavior of the conformational dynamics displayed by the central signaling conduit was unexpected. Therefore, this lethal mutation along with a partial closing of the active cleft and dysfunctional motions, alters the allosteric network with concomitant decrease of the catalytic efficiency [55, 56].

Case studies on dihydrofolate reductase using artificial mutations have predicted that dysfunctional dynamics[437] or a dynamic knockout [15, 500] dramatically reduce enzymatic activity and have been exemplified in other systems as well[16, 117, 309, 338, 374, 478]. These studies have overlooked the contribution that substrates have on promoting productive motions. The natural occurring R14 deletion in the PKA-C recognition sequence of PLN is a unique example that advocates for a central role of the substrate in the organization of the active site and to promote productive conformational fluctuations. While these motions might not play a direct role in the chemical step[18] (i.e., phosphoryl transfer), they dictate the opening and closing of the active cleft for phosphoryl transfer.

Absent or reduced PLN phosphorylation levels cause SERCA to be constitutively down-regulated, leading to reduced Ca^{2+} uptake in the SR lumen and, ultimately, heart disease[125, 488]. Recent *in vitro* studies demonstrated that several hereditary mutants of PLN constitute a poor substrate for PKA-C[497, 501]. Specifically, hypo-phosphorylation of PLN has been detected for the PLN^{R9C} mutant, where a cysteine substitution occurs at the P-7 site [501] as well as for PLN^{R14del}. However, the molecular etiologies for these mutants' lack of phosphorylation are dissimilar[498, 502]. While reduced phosphorylation of PLN^{R9C} has been attributed to disulfide bond formation between adjacent monomers in the pentamers, rendering the phosphorylation site

inaccessible to PKA-C[501], R14 deletion prevents the formation of the catalytically committed conformation. Nonetheless, in both cases slow phosphorylation kinetics reduce calcium uptake with concomitant decline of cardiac output, leading to heart failure. Importantly, the *fight or flight* mechanism, which results in increased PKA-C activity and decreased SERCA inhibition, is severely impaired by the slow phosphorylation of $\text{PLN}_{1-19}^{R14del}$, affecting Ca^{2+} transients and leading to DCM[491, 494]. Our findings emphasize the importance of functional dynamics between the enzyme and substrate to achieve physiological phosphorylation levels for normal cardiac function. These results elucidate a pathway by which dysfunctional conformational dynamics of proteins may result in pathological phenotypes, giving new and exciting evidence of a structural basis of DCM linked to this specific pathway.

9.5: Footnotes

Chapter X

Uncoupling Catalytic and Binding Functions in the cAMP-Dependent Protein Kinase A

Jonggul Kim[1], Michael A. Walters[3], Susan S. Taylor[4] and Gianluigi Veglia[1,2]*

[1] *Department of Chemistry, University of Minnesota, Minnesota, 55455 United States.*

[2] *Department of Biochemistry, Molecular Biology and Biophysics, University of Minnesota, MN, 55455 United States.*

[3] *Department of Medicinal Chemistry and Institute for Therapeutics Discovery and Development, University of Minnesota, MN, 55455 United States.*

[4] *Department of Chemistry and Biochemistry, University of California at San Diego, La Jolla, CA 92093, USA*

Submitted for publication

10.1: Introduction

Protein kinases are ubiquitous phosphoryl transferases that regulate many cellular signaling processes [503]. Due to their primary role in cell physiology and pathology, protein kinases have become major drug targets to counteract human diseases, such as heart failure and cancer [504, 505]. Kinases canonical function is to transfer the γ-phosphate of ATP to Ser/Thr/Tyr residues of substrates, thereby activating or deactivating various signaling pathways [1, 27, 505, 506]. About a decade ago, Manning and co-workers identified a non-canonical function for protein kinases that, in several instances, do not carry out any catalytic function; rather they provide binding scaffolds to modulate, integrate, or compete in signaling cascades, the so-called pseudo-kinases [1]. While kinases are capable to perform this dual function in signaling, pseudo-kinase function is independent from catalysis [68, 69]. To date, approximately 10% of the 518 members of the mammalian kinases are defined as pseudo-kinases, with reduced or completely obliterated ability to catalyze phoshoryl transfer [69, 507].

A modern conundrum is to uncouple canonical and non-canonical functions in kinases. This would enable one to achieve a higher level of functional control in kinase-mediated signaling pathways [507]. Site-directed mutagenesis studies have shown that this functional uncoupling is possible [113, 449, 508]. In addition, it was found that small molecules, which inhibit kinase *in vitro,* can paradoxically activate other kinase pathways in cell [114, 115, 509]. The latter suggests that inhibited kinases (i.e., scaffolds) can still modulate signaling events.

Although substantial progress has been made for the development of allosteric inhibitors [510-512], the most common kinase inhibitors target the kinases' nucleotide binding pockets, abolishing kinase catalytic activity [513]. However, these molecules have not been engineered to produce pseudo-kinases (devoid of catalytic activity) or

dead kinases (non-catalytic and non-scaffolding). So, how can we uncouple kinase functions?

A hallmark of kinases is the allosteric cooperativity (*K-type* cooperativity) [4, 12]: *nucleotide binding affects substrate affinity*. Therefore, we hypothesize that by modulating the chemical moieties of nucleotides and nucleotide-analogs it is possible to control the allosteric binding cooperativity and steer kinase function toward pseudo-kinases or dead kinases. As a model system, we chose the catalytic subunit of the cAMP-dependent protein kinase A (PKA-C). This enzyme is one of the most studied and has represented the benchmark for the entire kinase family [2]. PKA-C is organized into two lobes, an N-terminal small lobe with 5 β-strands and one helix (αC helix), and a C-terminal large lobe mostly helical that harbors the substrate binding cleft [448] (**Figure 10.1A**). The nucleotide (ATP) binds at a critical junction of the kinase core, which is embedded between the small and large lobe [448]. Through coordination of two Mg^{2+} ions, the nucleotide positions several amino acids from various catalytic motifs such as the DFG loop, glycine-rich loop, and catalytic loop for phosphoryl transfer (**Figure 10.1C**) [25]. Structurally, the nucleotide's adenine ring completes the architecture of the catalytic spine (C-spine), an array of hydrophobic residues that play a key role in intramolecular allosteric signaling and kinase activation [13]. The substrate binds the C-lobe, laying on the peptide positioning loop, which provides high-binding affinity for registering the recognition sequence. It has been hypothesized that ATP acts as an allosteric effector priming the kinase structure for substrate binding [13, 43, 55]. The dynamic apo enzyme toggles between three major conformational states (open, intermediate, and closed, **Figure 1.01B**). ATP binding shifts the enzyme conformational ensemble from an open to an intermediate state, increasing substrate affinity through a *K*-type binding cooperativity [58, 514, 515]. In spite a plethora of structural [2] and biophysical data [516], it is still

unclear how the different chemical moieties of ATP confer positive K-type cooperativity for substrates.

Here, we combined isothermal titration calorimetry (ITC) measurements with solution NMR spectroscopy to study how chemically different nucleotides modulate the degree of the binding cooperativity for the pseudo-substrate peptide inhibitor PKI$_{5-24}$. Importantly, we found a linear correlation between the degree of cooperativity and the population of the closed state of the enzyme. The adenine ring, ribose and β-γ phosphates all contribute to allosteric cooperativity. The highest degree of cooperativity is reached with ATP, where the phosphate groups pre-organize the active site for phosphoryl transfer and primes the substrate binding site for high affinity (catalytically competent state). A common ATP analog, ATPγN, shows substantially reduced cooperativity, which is completely abrogated with ATPγC. In fact, the substitution of the oxygen in the phosphoester with methylene group disrupts the coordination geometry around the second Mg^{2+} ion in the active site, resulting in a dramatic loss of cooperativity. Remarkably, the binary complex PKA-C/ATPγC does not have detectable binding affinity for phospholamban, a substrate of PKA-C in the cardiac muscle. Lastly, we tested substrate binding cooperativity with two ATP-competitive inhibitors of PKA-C, H89 and balanol. While both molecules block catalysis, H89 and balanol display negative and positive binding cooperativity, respectively. Our results show that it is possible to uncouple the high affinity of inhibitors for the nucleotide binding cleft and substrate binding cooperativity by changing the chemical nature in the active site, especially around the phosphoester bond, opening new directions for manipulating protein kinases functions in a specific manner.

9.2: Experimental Procedures

Adenosine 5'-triphosphate (ATP), adenosine 5'-monophosphate (AMP), γ-β-methyleneadenosine 5'-triphosphate (ATPγC), and adenine were purchased from Sigma Aldrich (St. Louis, MO, USA). Adenosine 5'-diphosphate (ADP) and adenosine were purchased from Research Products International (Mt. Prospect, IL, USA). Adenosine 5'-(β,γ-imido)triphosphate (ATPγN) was purchased from Roche Diagnostics (Indianapolis, IN, USA)

Sample Preparation. Recombinant catalytic subunit of PKA was expressed in BL21 DE3 cells as previously described by Studier[346] at 24 °C. Purification of PKA-C was performed as previously described using the His_6-RIIα(R213K)[321] subunit and a second purification step was performed using the HiTrap SP cation exchange column as previously described[350]. The most abundant isoform, corresponding to phosphorylation at S338, T197 and S10, was used for all experiments. Peptide synthesis was performed on a CEM Liberty microwave synthesizer as described previously[55]. Kinase activity was tested with a gel shift assay and quantified using A_{280} = 52060 $M^{-1}cm^{-1}$.

ITC measurements. All ITC measurements were performed with a Microcal VP-ITC instrument or TA NanoITC instrument at 300K. Samples were buffer exchanged into 20 mM MOPS, 90 mM KCl, 10 mM DTT, 10 mM $MgCl_2$, 1 mM NaN_3, pH 6.5. Approximately 1.7 mL of 11.4-32μM of PKA-C was used for each experiment and 280 μL of 140-350μM of PKI_{5-24} in the titrant syringe. For the AMP binding experiment 300 μL of 238μM of PKA-C was used with 50 μL of 3.3mM of AMP. Final concentration of 2mM of nucleotide was used for nucleotide saturated experiments and a concentration of 50 μM for the inhibitor saturated experiments. All experiments were performed in triplicate. The heat of dilution of the ligand to the buffer was taken into account by measuring the heat of dilution of the ligand to the buffer and was subtracted from the experiment accordingly.

Binding was assumed to be 1:1 and was analyzed using the NanoAnalyze software (TA instruments New Castle, DE, USA), with the Wiseman Isotherm[280]:

$$\frac{d[MX]}{d[X_{tot}]} = \Delta H^\circ V_0 \left[\frac{1}{2} + \frac{1 - (1+r)/2 - R_m/2}{(R_m^2 - 2R_m(1-r) + (1+r)^2)^{1/2}} \right]$$

where the change of the total complex, d[MX] with respect to the change of the ligand concentration, d[X_{tot}] is dependent on r, the ratio of the K_d with respect to the total protein concentration, and R_m, the ratio between the total ligand and total protein concentration. The free energy of binding was determined using the following:

$$\Delta G = RT \ln K_d$$

where R is the universal gas constant and T is the temperature at measurement (300 K). The entropic contribution to binding was calculated using the following:

$$T\Delta S = \Delta H - \Delta G$$

Calculations for the cooperativity constant (σ) were calculated as follows:

$$\sigma = \frac{K_{d,Apo}}{K_{d,nucleotide}}$$

where $K_{d,Apo}$ is the K_d of PKI$_{5\text{-}24}$ to the apo enzyme and $K_{d,nucleotide}$ is the K_d of PKI$_{5\text{-}24}$ to the nucleotide bound enzyme.

NMR Experiments. Samples for ^{13}C IVL ^{15}N labeled PKA-C were expressed and purified as previously described[12, 350]. Effective final sample concentrations were 0.2-0.25 mM in 20 mM KH$_2$PO$_4$, 90 mM KCl, 10 mM DTT, 10 mM MgCl$_2$ 1 mM NaN$_3$ at pH 6.5 with 12 mM of nucleotide. Adenosine and adenine lack solubility in aqueous solution and concentrations of 10 mM and 6mM respectively were used. Samples with ATP and ATPγN were performed with 60 mM MgCl$_2$ for MgATP. Additions of 4, 8, 12, 18, 24, and

32 μL of 4.0 mM of PKI$_{5-24}$ were used for a minimum final two fold molar excess of ligand. NMR assignments on the apo, nucleotide bound (ATPγN) and ternary (ATPγN and PKI$_{5-24}$) were carried out on an 850 MHz Bruker Advance III spectrometer and described elsewhere [517]. All ^{1}H-^{15}N TROSY-HSQC experiments and ^{1}H-^{13}C HMQC experiments were carried out on a Varian Inova 600 MHz spectrometer equipped with a Cold HCN probe operating at 300 K.

9.3: Results

Different nucleotides provide varying degree of binding cooperativity. To measure substrate binding cooperativity of PKA-C, we utilized ITC and measure the binding affinities of PKA-C for a 20 amino acid inhibitory peptide from the heat stable protein kinase A inhibitor (PKI$_{5-24}$). Since PKI$_{5-24}$ contains the substrate recognition motif for PKA-C (with Arg residues on the P-2 and P-3 positions) and an Ala instead of a Ser at the P-site, it is considered a pseudo-substrate[2], recapitulating the high binding affinity of the R-subunits[38, 55, 379, 448]. The binding cooperativity between PKI$_{5-24}$ and the nucleotide was assessed by saturating the kinase with a series of nucleotide analogs: adenine, adenosine, AMP, ADP, ATPγN, ATPγC, and ATP (**Figure 10.2**). Under the time scale of our experiments, there is no hydrolysis of ATPγN, which was detected in the crystallized PKA-C/ ATPγN/SP20, a substrate peptide derived from PKI$_{5-24}$ with Asn20Ala and Ala21Ser mutations, complex after several days [47]. The different nucleotides were chosen to dissect the contribution of each chemical moiety (*i.e.*, adenine ring, ribose, and phosphates). All of these nucleotides display very similar binding affinities for the enzyme [42, 57, 518], with K_d values between 20-50 μM. Note that under our experimental conditions, two Mg^{2+} ions occupy the binding site, which are required for the high binding affinity of PKI$_{5-24}$ [519]. To quantify the extent of cooperativity, the binding thermodynamics were interpreted using a classical

heterotropic linkage model (**Figure 10.2A**), where the binding of one ligand enhances or reduces the affinity of the second ligand. The degree of cooperativity (σ), which is independent of the order of ligand binding, quantifies the extent of *K*-type cooperativity [12, 281]. Saturation with most nucleotides increases the binding affinity toward PKI$_{5-24}$. The highest affinity and degree of cooperativity ($\sigma = 400$) was measured for ATP. Specifically, we found a gradual increase of cooperativity for the following series: adenine < adenosine < ADP < ATPγN << ATP (**Figure 10.2B**). These data indicate that the adenine ring, the ribose as well as the three phosphates contribute incrementally to the enzyme's binding affinity for PKI$_{5-24}$. As previously observed [42], the adenine moiety (**Figures 2** and **Table 1**) is especially important for the binding affinity, since its ring, sandwiched between residues Val57 in the N-Lobe and Leu173 in the C-Lobe, is stabilized by hydrophobic interactions. The ribose moiety and phosphate groups further increase PKI$_{5-24}$ binding affinity, with a significant increase in cooperativity correlated with the number of phosphate groups. Notice that the affinity of the pseudo-substrate peptide is much greater when the enzyme is bound to ATP than ADP, suggesting that ADP facilitates the exit of the enzymatic product. An anomalous behavior is observed for AMP, which has been shown to have a lower binding affinity for PKA compared to other nucleotide analogs [42]. In agreement with these previous data, we found a substantially weaker affinity with AMP ($K_d \sim 250\ \mu$M). These binding experiments were repeated at higher AMP concentrations; however, we did not observe significant changes in the pseudo-substrate affinity. Since the structure of the kinase in complex with AMP is not available, we speculate that the absence of the β and γ phosphates prevent the closure of the binding cleft, reducing the affinity for the substrate. The most interesting results were obtained for two non-hydrolysable nucleotides mimics that are commonly used for structural studies, namely, ATPγN and ATPγC. The presence of a nitrogen atom in place

of oxygen at the γ position of the ATP phosphoester (ATPγN) dramatically reduces the binding cooperativity (σ = 53). This phenomenon is accentuated for ATPγC, where a methylene group replaces the bridging oxygen. In this case, the binding cooperativity between the non-hydrolysable nucleotide and pseudo-substrate is completely abolished (σ = 1.0).

ATPγC prevents phospholamban binding. To further understand the role of the bridging oxygen of the β and γ phosphates on the binding cooperativity of more realistic substrates displaying much lower affinity than the pseudo-substrate, we utilized a 19 amino acid peptide corresponding to the cytoplasmic domain of phospholamban (PLN$_{1-19}$), a signaling target for PKA-C that regulates cardiac contractility [56, 127, 129]. Although phospholamban contains a transmembrane domain, the cytoplasmic domain alone is recognized and phosphorylated by PKA-C [129]. Remarkably, the binding titrations carried out in the presence of saturating concentration of ATPγC showed a dramatic reduction of the binding affinity. Previous binding studies show that the K_d for PLN$_{1-19}$ to the PKA-C/ATPγN complex is approximately 28 μM [517]. In stark contrast, PLN$_{1-19}$ binding affinity for the PKA-C/ATPγC complex is very weak (K_d > 1 mM) (**Figure 10.3A**). Accordingly, NMR titrations of the PLN$_{1-19}$ peptide on the PKA-C/ATPγC complex do not show any detectable chemical shift changes in both the amide and methyl group fingerprints (**Figure 10.3B**). Both ITC and NMR titrations indicate that the loss of binding affinity by ATPγC observed in the pseudo-substrate is not only confirmed using PLN$_{1-19}$, but is accentuated with substrates.

Linkage between structural transitions and binding cooperativity. To probe the conformational transitions of the enzyme with the different nucleotides, we mapped the enzyme's amide fingerprint using [^{1}H,^{15}N]-TROSY-HSQC experiments [176] as the

amide chemical shifts are a sensitive reporters of allosteric transitions [372, 410, 520].

Although previous crystallographic structures of these complexes were reported to be identical [2], small changes in chemical shifts have been demonstrated to report on subtle changes in conformation and allostery [373, 375, 521]. Resonance assignments for the different free and ligated states of the kinase were previously obtained using triple-resonance experiments [517] and transferred to the spectra of the kinase saturated with the different nucleotides, as well as in the ternary complexes. We found that the addition of the pseudo-substrate to nucleotide saturated PKA-C shifts the amide resonances of the enzyme along linear chemical shift trajectories (**Figure 10.4A**). This indicates that the enzyme predominately interconverts between a two state equilibrium and the binding of pseudo-substrate shifts the population of the enzyme toward the closed state with different extents. A succinct view of the process is offered by the analysis of the amide chemical shifts using CONCISE [410], a statistical approach that utilizes principal component analysis to quantify the global coordinated response of the amide chemical shifts upon ligand binding for linear chemical shift trajectories [410]. This method identifies the predominant linear trajectory of all the chemical shifts and the aggregate amide chemical shifts for each state is grouped together by their average position along the linear trajectory (PC score). These changes are displayed as probability density distributions defining a specific conformational state of the kinase along the conformational equilibrium [410]. Addition of PKI_{5-24} to all of the nucleotide-bound forms of the kinase shifts the conformation equilibrium toward the closed state (**Figures 10.4**), reflected in the higher PC score from CONCISE, but to different degrees. In particular, a gradual shift of the probability density distributions of the amide chemical shifts is apparent going from adenine, adenosine, ADP up to ATP, indicating that the presence of the ribose and the increased number of phosphates allows PKI_{5-24} to shift the conformational equilibrium further toward the closed state. To link the binding

thermodynamics of PKI$_{5-24}$ to the conformational transition, we first compared the free energy of binding for PKI$_{5-24}$ under nucleotide saturating conditions to the PC score of the nucleotides and did not find a firm correlation. However, a comparison between the free energy of binding for PKI$_{5-24}$ and the PC score of the enzyme's ternary complexes with PKI$_{5-24}$ (**Figure 10.4**) shows a linear correlation between the extent of the closed state and the free energy of binding ($|R| = 0.96$, **Figure 10.4C**), indicating that the degree of cooperativity of substrate binding strongly depends on the extent of the closed state.

The CONCISE analysis yields insights into the global opening and closing transitions following only those residues with linear trajectories. Therefore, we followed the chemical shift trajectories of the Ile, Val, and Leu methyl groups. Methyl group chemical shifts are sensitive reporters of allosteric networks in large proteins [339, 522, 523]. As for the backbone, upon ligand binding most of the methyl group chemical shifts follow predominately linear trajectories along the open to close conformational states, reporting on a two state equilibrium in the fast exchange regime (**Figure 10.5**). However, several methyl groups located near the binding site as well as in distal regions follow non-linear chemical shift trajectories in the PKA-C/ATPγC/PKI$_{5-24}$ complex, with many resonances exhibiting substantial line broadening at even at ligand saturation conditions. These features suggest that ATPγC with pseudo-substrate shifts the enzyme outside the reaction coordinates traceable with the other nucleotides into another conformational state that is unable to bind substrates at high affinity.

ATP-competitive inhibitors exhibit positive and negative cooperativity. The binding data using nucleotide analogues demonstrated that substrate binding cooperativity could be modulated by changing the chemical nature of the nucleotide. With an eye on the feasibility of this approach to drug design, we looked at whether current ATP-competitive

inhibitors of PKA-C could also alter binding cooperativity. To this end we measured the affinity of PKI$_{5-24}$ using ITC in the presence of two ATP-competitive inhibitors, H89 and balanol (**Table 2 and Figure 10.6**). H89 is an isoquiolinesulfonamide based inhibitor which was synthesized to have higher selectivity for PKA-C [524] and is commonly used to block PKA-C activity in cells. Balanol is a metabolite isolated from *Verticillium balanoides* and its kinase inhibition potency was first described on PKC [525], and later on PKA-C [526]. We found the K_d of PKI$_{5-24}$ decreases when PKA-C is saturated with balanol with a moderate positive cooperativity (σ = 7.0). For H89, on the other hand, we found a substantial loss of affinity for PKI$_{5-24}$, corresponding to negative binding cooperativity (σ = 0.55). These features show that ATP-competitive inhibitors can differentially alter kinases into either pseudo-kinases or into dead kinases based on differing binding cooperativity.

10.4: Discussion

The linear correlation described here between the conformational state of the ternary complex and the free energy of binding for the pseudo-substrate has many implications for kinase substrate recognition and function. The nucleotide emerges not only as carrier of the phosphate group for chemistry at the active site, but also having a structural role for mediating allosteric binding cooperativity. Importantly, high binding affinity of the substrate and pseudo-substrate can only be achieved when the appropriate nucleotide brings together the small and the large lobes, shifting the population of the enzyme toward the intermediate state [410], pre-organizing the active site such that it is complementary for substrate binding and enabling the ternary complex to reach a catalytically competent state [527, 528]. This conformational transition is most closely obtained with native substrates and ATP, leading to the most favorable free energy of binding. Removal of the β - and γ-phosphate, ribose, and adenine ring does

not significantly alter the nucleotide binding affinity, but results in an enzyme conformation progressively less complementary for substrate binding.

Interestingly, for both AMP and ATPγC we did not observe a linear relationship between free energy of pseudo-substrate binding and extent of the closed state, showing that these nucleotides do not exhibit positive K-type cooperativity (**Figures 10.2B and 10.4**). Not only AMP has a lower binding affinity, but it is also unable to drive the conformation of the glycine-rich loop in a competent state, abrogating binding cooperativity. Interestingly, the non-hydrolysable nucleotide mimic ATPγC has a similar effect (**Figure 10.2**). The recently determined crystal structures of the kinase (PDB entry 4IAC) in the presence of SP20 and ATPγC [65] with the PKA-C complexed with PKI_{5-24} and ATP (PDB entry 1ATP) are great complement to our data. Overall, the backbone structures of the two complexes are identical. However, in the 4IAC structure ATPγC does not interact with the backbone amide groups of Phe54 and Gly55, preventing the glycine-rich loop from closing and resulting in a more open conformation. Furthermore, in the presence of ATPγC the second Mg^{2+} ion adopts a bi-pyramidal coordination geometry rather than the octahedral geometry found with both ATP and ATPγN [65]. Therefore, the coordination of the metal ion plays a key role in positioning the γ-phosphate and the substrate for productive phosphoryl transfer. Accordingly, we found that the substitution of the oxygen in the phosphoester with a methylene group dramatically reduces the binding affinity and does not shift the population from the open to intermediate state as observed for ATPγN (**Figure 10.4**). Moreover, the chemical shifts of the methyl groups suggest that the ternary complex PKA-C/ATPγC/PKI_{5-24} occupies a different state in the conformational landscape of the enzyme, with a loss of binding cooperativity for the pseudosubstrate and complete obliteration of binding for phospholamban. Although all chemical moieties are important for binding cooperativity,

our data underscore the central role of the oxygen atom bridging the β and γ phosphate. Structurally, this atom provides the coordination geometry for the second Mg^{2+} ion, clamping down the glycine-rich loop and shifting the conformational equilibria for the formation of a productive ternary complex with substrates. In fact, the degree of cooperativity is significantly attenuated when nitrogen replaces the oxygen (ATPγN). The latter was also predicted but not proved in the published work by Walsh and coworkers [44]. If the degree of cooperativity is attenuated by the substitution of the oxygen with nitrogen (ATPγN), it is completely lost with ATPγC, a widely used non-hydrolysable ATP analog for both kinases and ATPases[529]. In the case of PKA-C, this compound appears to prevent the formation of a catalytically competent complex with endogenous substrates.

Based on the above considerations, we conclude that the oxygen bridging the β and γ phosphate is a *hot spot* for modulating binding cooperativity. By changing the chemistry around this hot spot, it is possible to convert a kinase into a completely dead kinase abrogating both its canonical and non-canonical functions. These results may have important implications in the design of new inhibitors of kinases. It is possible to anticipate that newly designed inhibitors may be directed to either the catalytic function (*i.e.*, phosphoryl transfer) or both catalytic and binding functions. In the former case, the kinase would still function as a pseudo-kinase preserving its signaling role as scaffolds, anchors, spatial modulators, traps, and ligand-driven regulators of canonical kinases [68, 113]. In fact this case has previously been observed with small molecular inhibitors of RAF kinase, activating kinase signaling pathways in a dose dependent manner [114, 115] or in the more recent finding that ATP-competitive inhibitors can block protein kinase recruitments to the Hsp90-Cdc37 system[530]. In the latter case, the kinase would be totally dead and removed from its signaling pathways (**Figure 10.7**). Mutations

have been reported to convert active kinases into pseudo-kinases, preserving their non-catalytic functions [449, 508]. In the case of PKA-C, residual catalytic activity enables yeast to survive[531]. On the other hand, a catalytically dead PKA-C fails to be autophosphorylated, but it can still bind ATP as well as the regulatory subunits and is recognized and phosphorylated by PDK-1 [508]. Another notable case is with a mutation that fuses the C-spine, blocks ATP binding and allows for dimerization of RAF kinase domains [113]. ATPγC renders the kinase dead, abolishing both catalysis and binding of substrates, despite assembly of the C-spine.

In fact, existing ATP-competitive inhibitors already inhibit catalysis or both catalytic and binding functions. By using balanol and H89 as representative small molecule inhibitors, existing compounds already exhibit differential activity with balanol rendering PKA-C as a pseudo-kinase and H89 into a dead kinase. The basis for this differentiation may lie within the chemistry of these groups. Although balanol is highly aromatic, there exist multiple polar groups that make hydrogen bonds with side-chain groups critical for substrate recognition and catalysis, including the conserved Lys72 and Glu91, in the active site [532]. H89 lacks these hydrophilic groups and the interaction within the binding site is almost exclusively through hydrophobic contacts. The stark differential chemistry and cooperative nature of these inhibitors suggest that chemical design of inhibitors can enable manipulation of binding cooperativity.

In a recent work on Src kinase, Foda *et al.* show a negative binding cooperativity between ATP and substrates[533]; while a positive cooperativity was measured for ADP and phosphorylated substrate. These authors found that the negative cooperativity is mediated by an allosteric network of contacts initiated by a protonation event occurring at the DFG loop [533]. This contrasts the positive *K*-type binding cooperativity found for PKA-C [12], where a high degree of cooperativity was observed for ATP with the

endogenous protein kinase inhibitor (PKI), regulatory subunits (R-subunits), [534] and substrates [517]. These findings suggest that the mechanism for cooperativity is not uniform throughout the kinome and that cooperativity hot spots may become a target for designing inhibitors able to fine-tune specific signaling pathways.

The other side of the coin is represented by the motions of these enzymes [56, 393, 517] as both structure and dynamics work together for kinase activity [24]. In fact, finely tuned productive motions in the nucleotide-bound state of the kinases are necessary for catalysis [55, 56]; and, importantly, changes in the motional regime causes a loss of cooperativity and/or catalytic efficiency [57]. The side-chain methyl spectrum shows that PKA-C with ATPγC does not engage in productive motions exhibited by other nucleotides with positive cooperativity. Although the control of motional properties of the kinases may represent another, more sophisticated level of control of kinase function [76], the current design of drug inhibitors has yet to include a control of conformational entropy.

In conclusion, this study identifies a hot spot for tuning binding cooperativity and decoupling canonical and non-canonical functions in kinases, introducing a higher level of control in the high affinity competitive inhibitors of these enzymes. Newly designed kinase inhibitors would then be able to convert a kinase into a pseudokinase, *i.e.*, creating a scaffold that it is still involved in signaling, or alternatively, subtract kinases from their signaling pathways altogether, impairing both enzymatic activity and substrate binding (dead kinases) [68, 507].

10.5: Footnotes

G.V., S.S.T. conceived, directed and analyzed all experimental research; G.V. prepared

the manuscript. J.K. prepared the samples, performed NMR spectroscopy experiments, processed and interpreted the data. All authors discussed the results and implications and commented on the manuscript at all stages.

Tables

Table 4.1: Validation of the statistics-based assignment of FLAMEnGO 2.0 with conventional through-bond experimental assignments. *Matched* indicate assignments that were verified using through-bond correlations. *Unassigned* indicates that peaks are present in the spectra but the through-bond correlations are absent. *Erroneous* indicates misassigned peaks in the FLAMEnGO 2.0 calculations.

		> 90% confidence			< 90% confidence		
	FLAMEnGO	*Matched*	*Unassigned in the through-bond correlation spectra*	*Erroneous Assignment in FLAMEnGO*	*Matched*	*Unassigned in the through-bond correlation spectra*	*Erroneous Assignment in FLAMEnGO*
ILE (21)	100%	90%	0%	10%	0%	0%	0%
LEU (64)	95%	44%	2%	6%	23%	12%	8%
VAL (40)	100%	68%	6%	9%	16%	1%	0%

TABLE 7.1: Summary of ^{15}N relaxation and ITC data for PKA-C^{WT} and PKA-C^{Y204A}.

	PKA-C^{WT}:ATPγN	*PKA-C^{Y204A}: ATPγN*
K_d for PKI$_{5-24}$ (μM)	0.12 ± 0005	14.6 ± 2.1
Average R_1 (s^{-1})	0.51 ± 0.08	0.51 ± 0.06
Average R_2 (s^{-1})	51 ± 5	46 ± 4
Average HX-NOE	0.79 ± 0.13	0.81 ± 0.12
k_{ex} from CPMG (s^{-1})	1020 ± 150	ND[a]
p_{closed} (%)[c]	93.5 ± 8.5	ND[a]

[a]Dynamics are no longer concerted; therefore overall parameters are not available.

TABLE 7.2: Thermodynamics of ligand binding to PKA-C^{WT} and PKA-C^{Y204A} determined by ITC. Binding of the ATP mimic, ATPγN, to Apo form of the enzyme (top) was measured as well as PKI$_{5-24}$ binding of the nucleotide bound form of the enzyme (bottom).

ATPγN	K_d (µM)	ΔH (kcal/mol)	TΔS (kcal/mol)
PKA-C^{WT}	58 ± 4	-2.7 ± 0.2	3.1 ± 0.2
PKA-C^{Y204A}	23.5 ± 0.85	-4.25 ± 0.05	2.11 ± 0.03

PKI$_{5-24}$ with 2mM ATPγN	K_d (µM)	ΔH (kcal/mol)	TΔS (kcal/mol)
PKA-C^{WT}	0.12 ± 0005	-18.1 ± 0.27	-8.64 ± 0.3
PKA-C^{Y204A}	14.6 ± 2.1	-8.57 ± 0.39	-1.92 ± 0.46

Table 8.1: Average φ values for the various structural motifs of PKA-C in the difference conformational states.

Motifs	$\langle\varphi\rangle$			$\langle\Delta\varphi\rangle$	
	apo	binary	ternary	$\varphi^{binary} - \varphi^{apo}$	$\varphi^{ternary} - \varphi^{binary}$
A-helix	1.30 ± 0.27	1.12 ± 0.34	0.98 ± 0.23	-0.16 ± 0.37	-0.08 ± 0.21
αA-β linker	1.52 ± 0.16	1.32 ± 0.39	1.26 ± 0.25	-0.23 ± 0.24	-0.13 ± 0.20
hinge (res 120-127)	1.03 ± 0.48	1.33 ± 0.65	1.23 ± 0.47	-0.03 ± 0.06	0.35 ± 0.30
E-helix	0.49 ± 0.13	0.41 ± 0.09	0.51 ± 0.57	-0.03 ± 0.07	-0.16 ± 0.23
F-helix	0.40 ± 0.12	0.56 ± 0.27	0.51 ± 0.33	0.12 ± 0.34	-0.19 ± 0.32
G-helix	1.39 ± 0.28	1.15 ± 0.46	1.31 ± 0.40	0.14 ± 0.002	-0.08 ± 0.84
H-helix	0.86 ± 0.60	1.36 ± 0.57	1.00 ± 0.88	0.06 ± 0.05	-0.10 ± 0.49
C-terminal tail					
Res 298-314	1.44 ± 0.63	1.10 ± 0.55	1.03 ± 0.59	-0.34 ± 0.22	-0.11 ± 0.33
Res 315-345	1.51 ± 0.39	1.65 ± 0.27	1.32 ± 0.37	0.28 ± 0.08	-0.25 ± 0.47
Res 346-350	1.18 ± 0.48	1.19 ± 0.18	1.07 ± 0.35	-0.18 ± 0.34	-0.13 ± 0.38

Table 10.1: The affinity, degree of cooperativity (σ), and thermodynamics of PKI_{5-24} binding with respect to the saturated nucleotide determined from ITC.

	K_d (μM)	σ	ΔG (kcal/mol)	ΔH (kcal/mol)	$T\Delta S$ (kcal/mol)
Apo	6.4 ± 0.56	1	-7.14 ± 0.05	-22.03 ± 0.63	-14.90 ± 0.68
ATPγC	6.1 ± 0.27	1.0	-7.17 ± 0.02	-13.61 ± 0.36	-6.43 ± 0.38
AMP	5.7 ± 0.18	1.1	-7.20 ± 0.02	-20.17 ± 0.07	-12.97 ± 0.08
Adenine	1.5 ± 0.03	4.3	-8.00 ± 0.01	-19.43 ± 0.16	-11.43 ± 0.18
Adenosine	0.53 ± 0.02	12	-8.63 ± 0.02	-21.32 ± 0.18	-12.69 ± 0.20
ADP	0.23 ± 0.0097	29	-9.13 ± 0.03	-17.67 ± 0.35	-8.54 ± 0.37
ATPγN	0.12 ± 0.0050	53	-9.49 ± 0.02	-18.12 ± 0.27	-8.64 ± 0.30
ATP	0.016 ± 0.0019	400	-10.72 ± 0.07	-11.90 ± 0.34	-1.17 ± 0.38

Table 10.2: The affinity, degree of cooperativity (σ), and thermodynamics of PKI$_{5-24}$ binding with respect to the saturated ATP-competitive inhibitor determined from ITC.

	K_d (μM)	σ	ΔG (kcal/mol)	ΔH (kcal/mol)	$T\Delta S$ (kcal/mol)
Balanol	0.92 ± 0.13	7.0	-8.30 ± 0.09	-16.14 ± 0.56	-7.83 ± 0.65
H89	11.2 ± 0.75	0.57	-6.81 ± 0.04	-18.46 ± 0.62	-11.65 ± 0.60

Figures
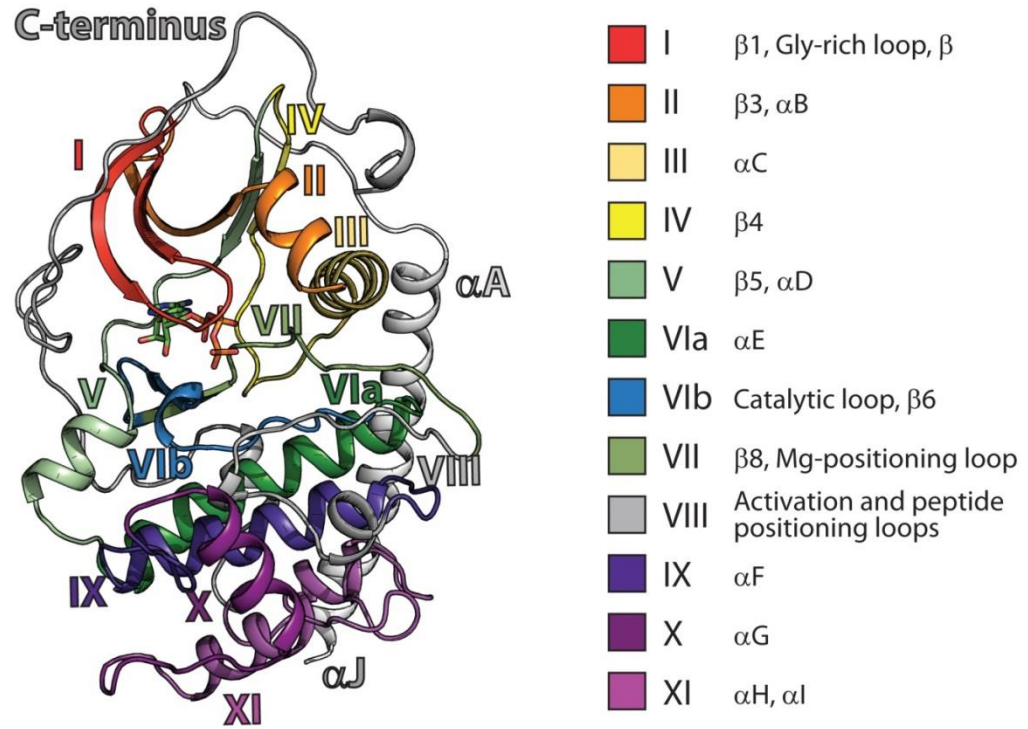
Figure 1.1: The subdomains of the kinase catalytic core mapped onto the structure of PKA-C.

A.

PLN$_{1-19}^{WT}$	M E K V Q Y L T R S	A I R R A S T I E ...
PLN$_{1-19}^{R14del}$	M E K V Q Y L T R	S A I R A S T I E ...
PKI$_{5-24}$	T T Y A D F I A S G R	T G R R N A I H D
PKS$_{5-24}$	T T Y A D F I A S G R	T G R R A S I H D
Kemptide		L R R A S L G

P-6   P-3 P-2 P-Site

B.
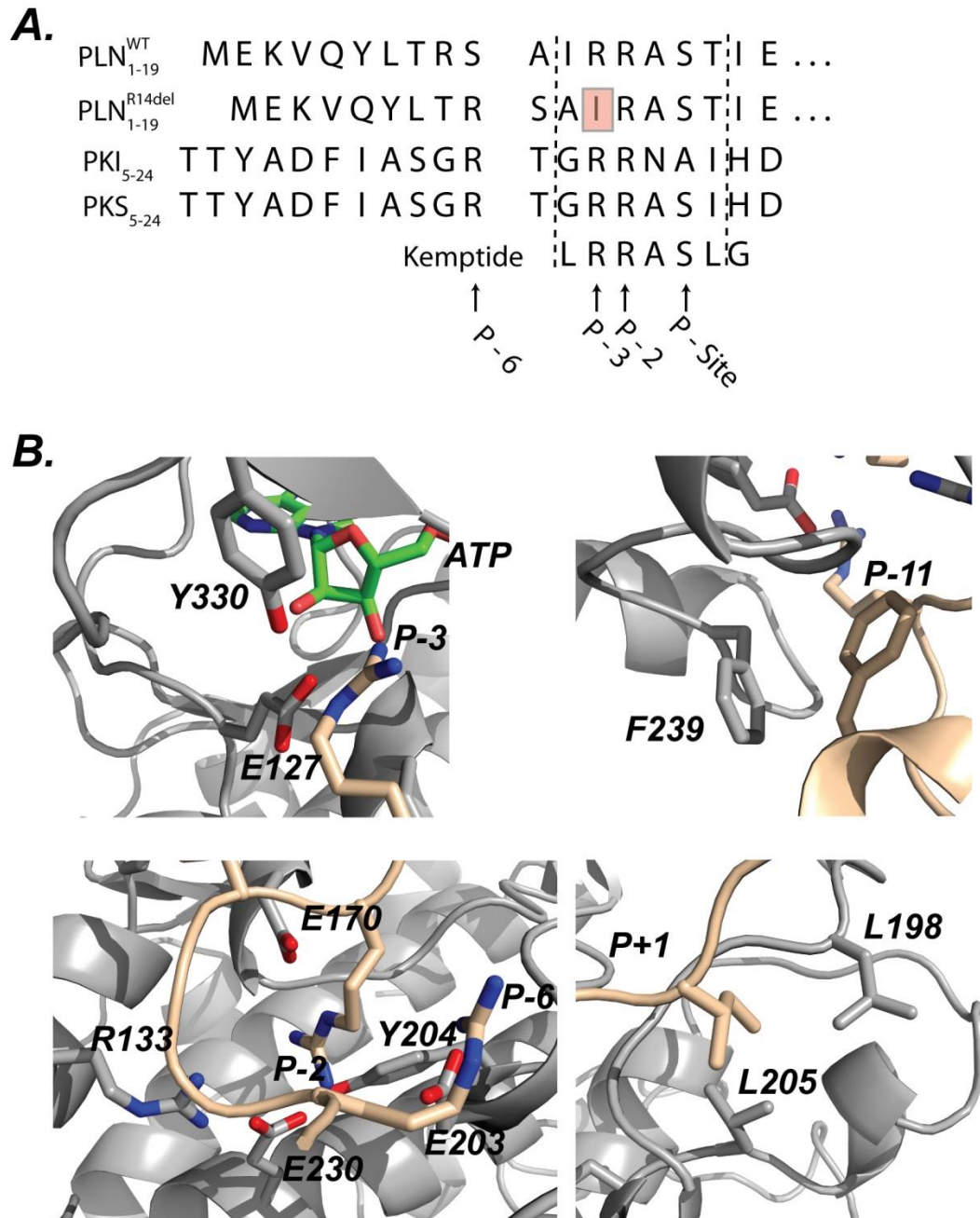
Figure 1.2: (A) Substrates and inhibitor peptide (PKI$_{5-24}$) of PKA-C described in this work. Note that substrates utilize an Arg group at the P-2 and P-3 position. (B) Structural interactions of the substrate with the kinase giving rise to the catalytic specificity of PKA-C

222
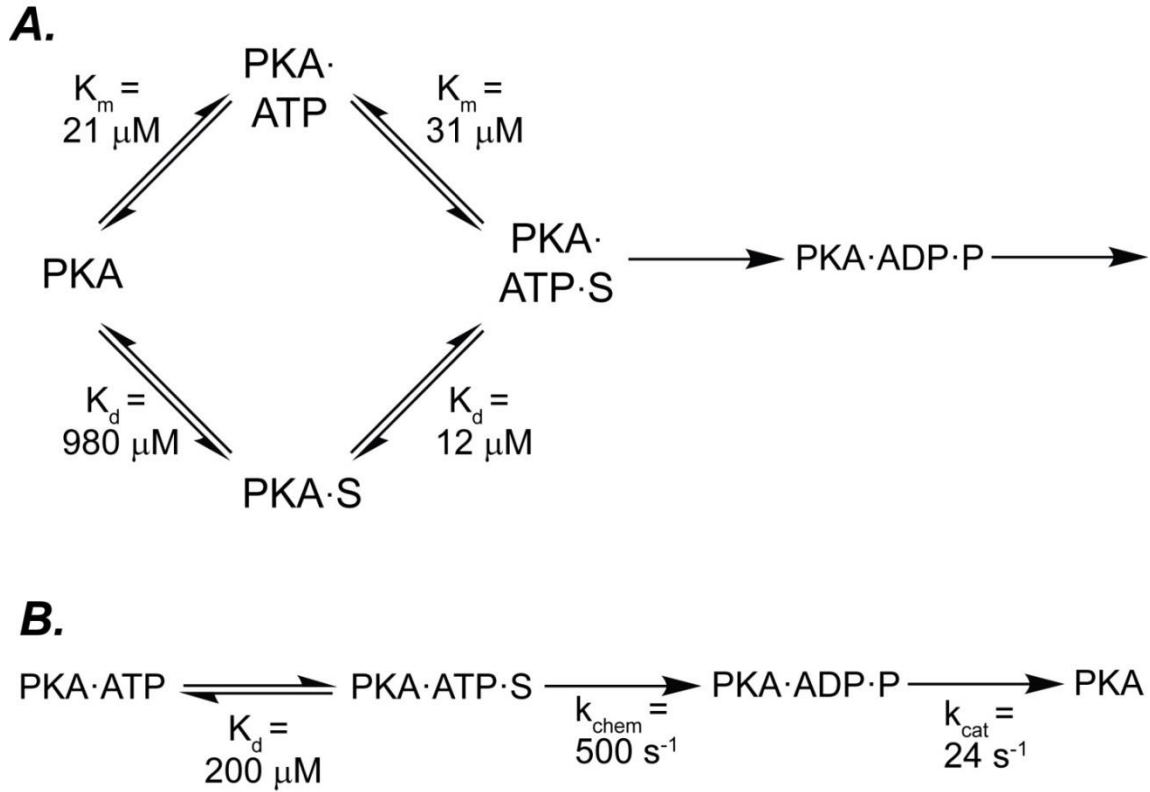
Figure 1.3: Catalytic mechanism of PKA-C. (A) K_m and K_d values for ATP and Kemptide (in place of S). The Km values were from Moore et. al. [9] and the K_d values were from Masterson et. al. [12]. (B) Canonical reaction rates for PKA-C under high Mg2+ concentrations (10 mM).
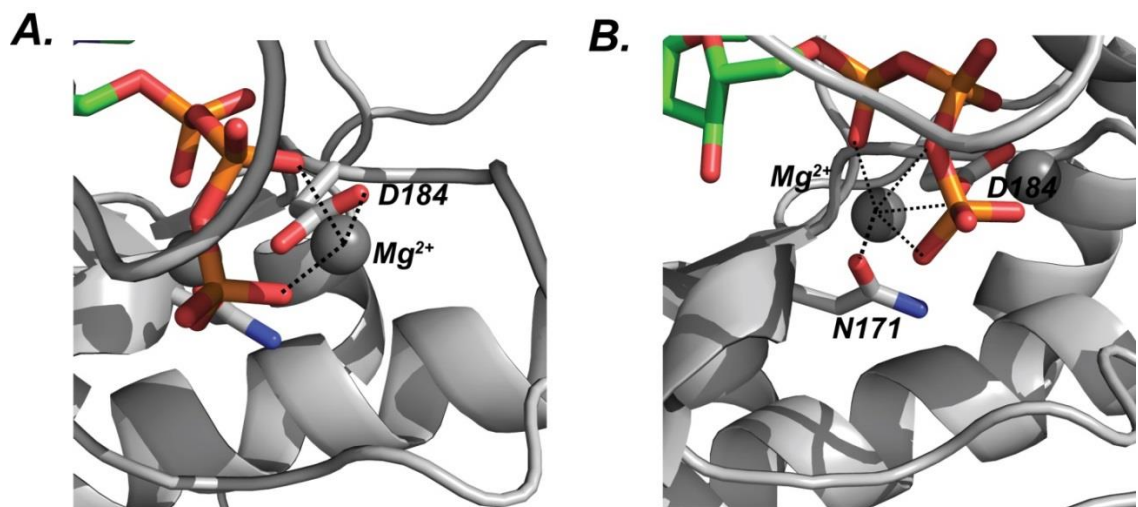
Figure 1.4: The Mg^{2+} binding sites in PKA-C (A) The site for the primary Mg2+ binding site, often dubbed as Mg1. (B) The site for the secondary Mg^{2+} binding site, often dubbed as Mg2. It is to be noted that high affinity binding of regulatory proteins, RI and PKI, requires both Mg^{2+} ions to be present [519].
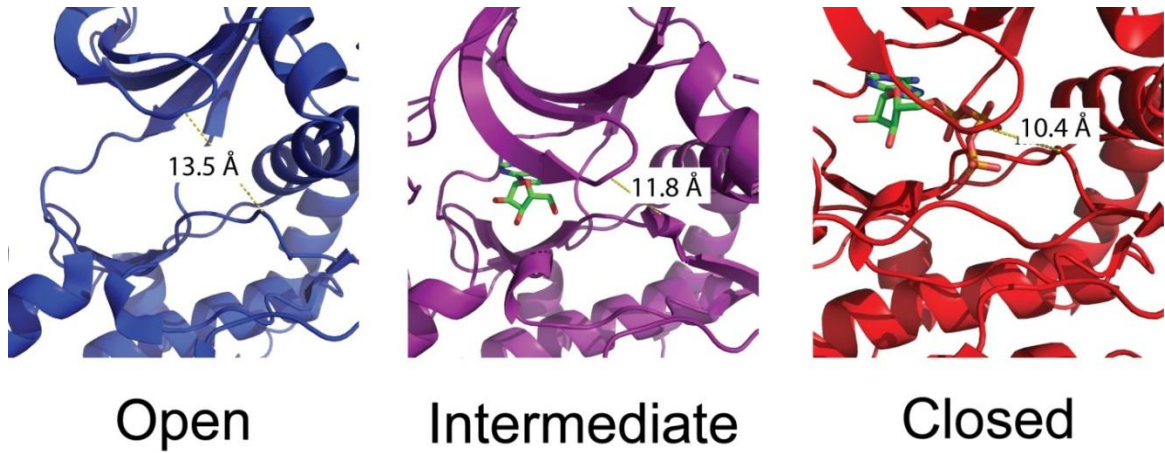
Figure 1.5: Conformational States of the open, intermediate (nucleotide bound) and closed state (Nucleotide with PKI_{5-24}). The states are defined by the distance between Ser53 of the Glycine Rich Loop and Gly186 of the DFG loop.
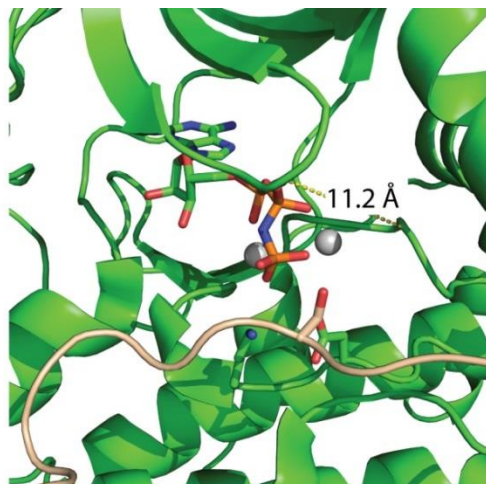
Micheals-Complex with PKS$_{5-24}$
PDB:4IA0
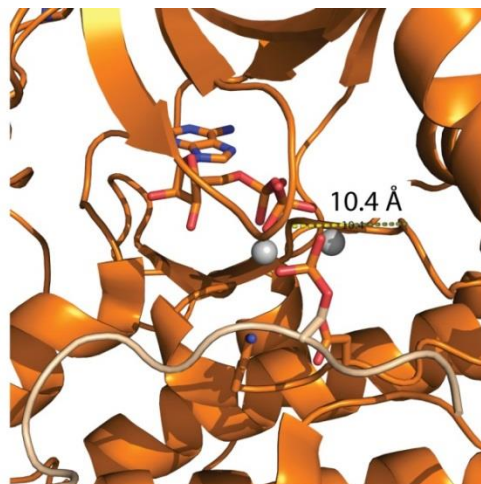
Product-Complex with PKS$_{5-24}$
PDB:4IAD

Figure 1.6: Comparison of the architecture of the active site immediately prior to phosphoryl transfer (left, with PDB: 4IA0) and immediately after phosphoryl transfer (right, PDB:4IAD)
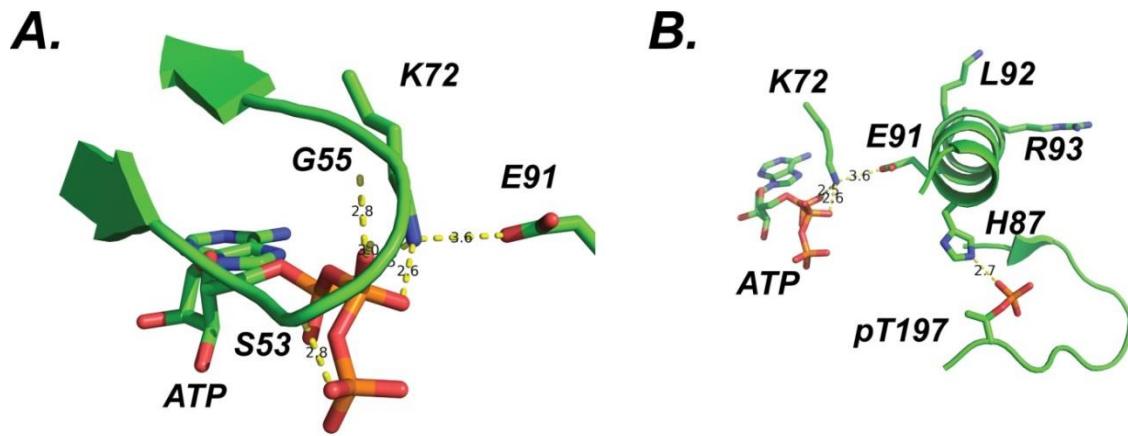
Figure 1.7: Highly conserved residues in the small lobe. (A) residues involved in positioining ATP for catalysis. S53 and G55 position the phosphates through the amide backbone group. (B) Connection of the αC as a central signalling hub between several different regions of the protein
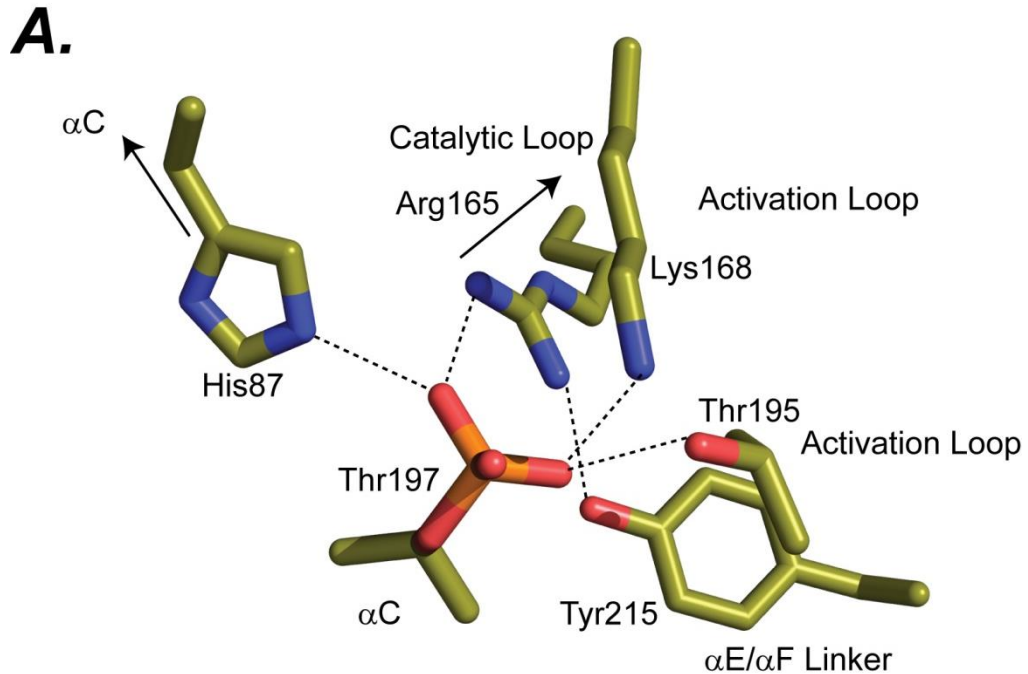
Figure 1.8: Interactions with activation loop phosphorylation. (A) Phosphorylation on T197 connections the aC, activation loop and the catalytic loop together. (B) The primary sequence of the peptide positioning loop and the hydrophobic motif for PKA-C and several other members of the AGC kinase family. Other kinases in the AGC family require phosphorylation on the residue immediately after the second Phe termed hydrophobic motif phosphorylation.
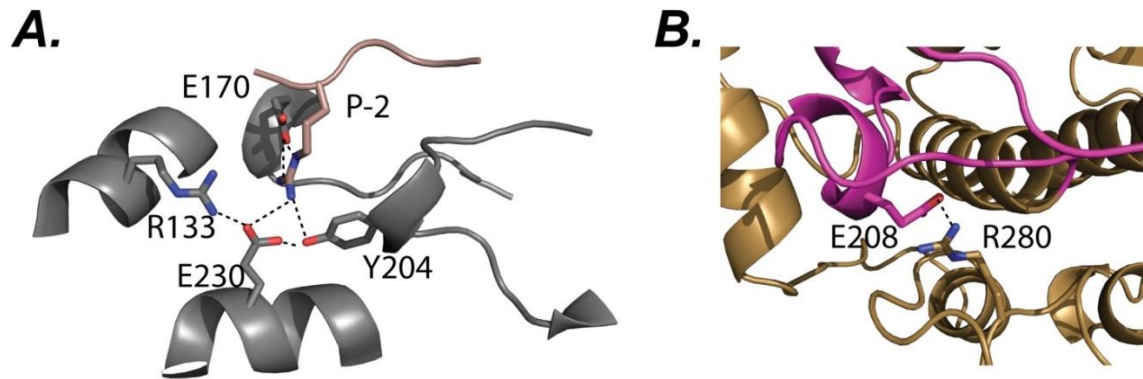
Figure 1.9: Critical interactions in the Large Lobe (A) The electrostatic lobe that Glu230 and Tyr204 are arranged in. This node networks together the peptide positioning loop, αF, catalytic loop and Arg P-2 of the substrate. (B) The conserved salt bridge between Glu208 and Arg280 linking the active site to the GHI subdomain.
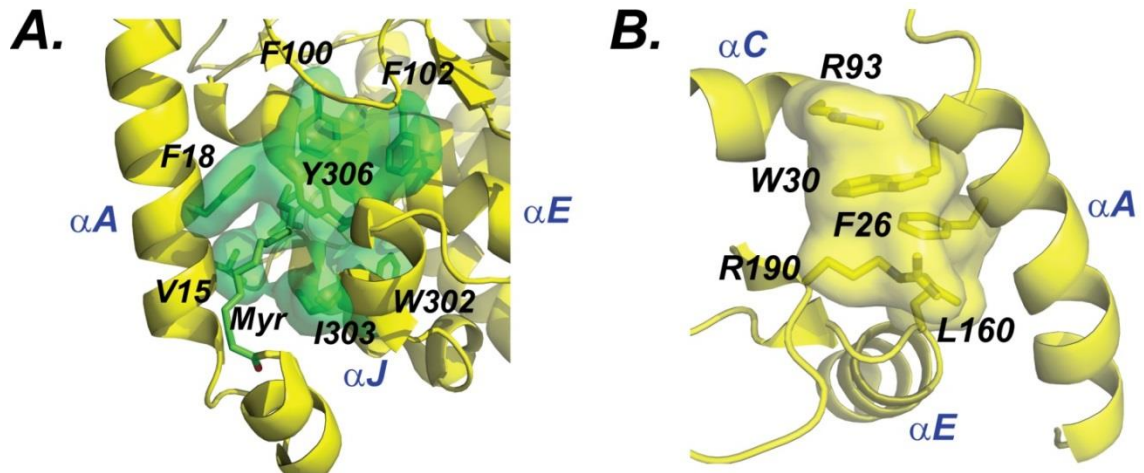
Figure 1.10: Interactions in the N-terminus of PKA-C (A) Hydrophobic pocket for the N-myristoyl group. The pocket is formed by Val15, Phe18, Phe100, Phe102, Trp302, Ile303, and Tyr306. (B) Trp30 makes π-cation interactions with Arg93 of αC, Arg190 of the activation loop linking the N-terminal aA to the active site.
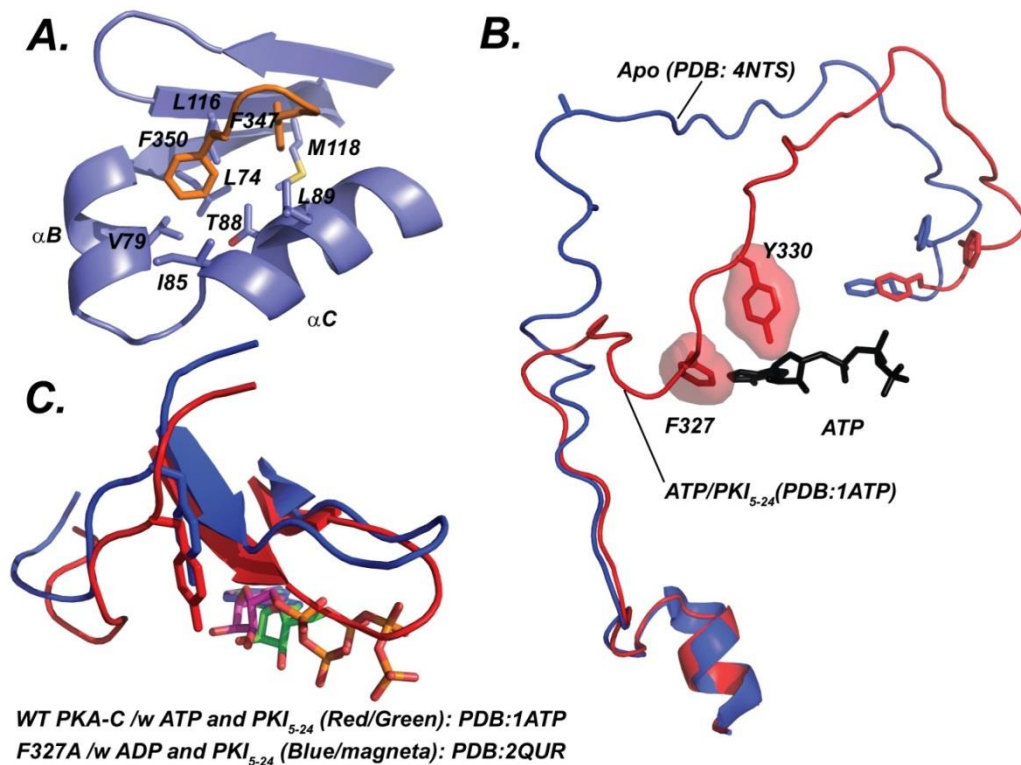
Figure 1.11: Critical interactions in the C-terminal Tail of PKA-C. (A) Phe350 and Phe347 of the hydrophobic motif of PKA-C placed between aC, aB β4 and β5 of the small lobe. (B) Overall conformational changes of the C-terminal tail between the open conformation (blue) and closed conformation (red). In the closed conformation the two critical residues, Phe327 and Tyr330 are aligned against the adenine moiety of ATP. (C) Positional change of the glycine rich loop and ATP upon Phe327Ala mutation.
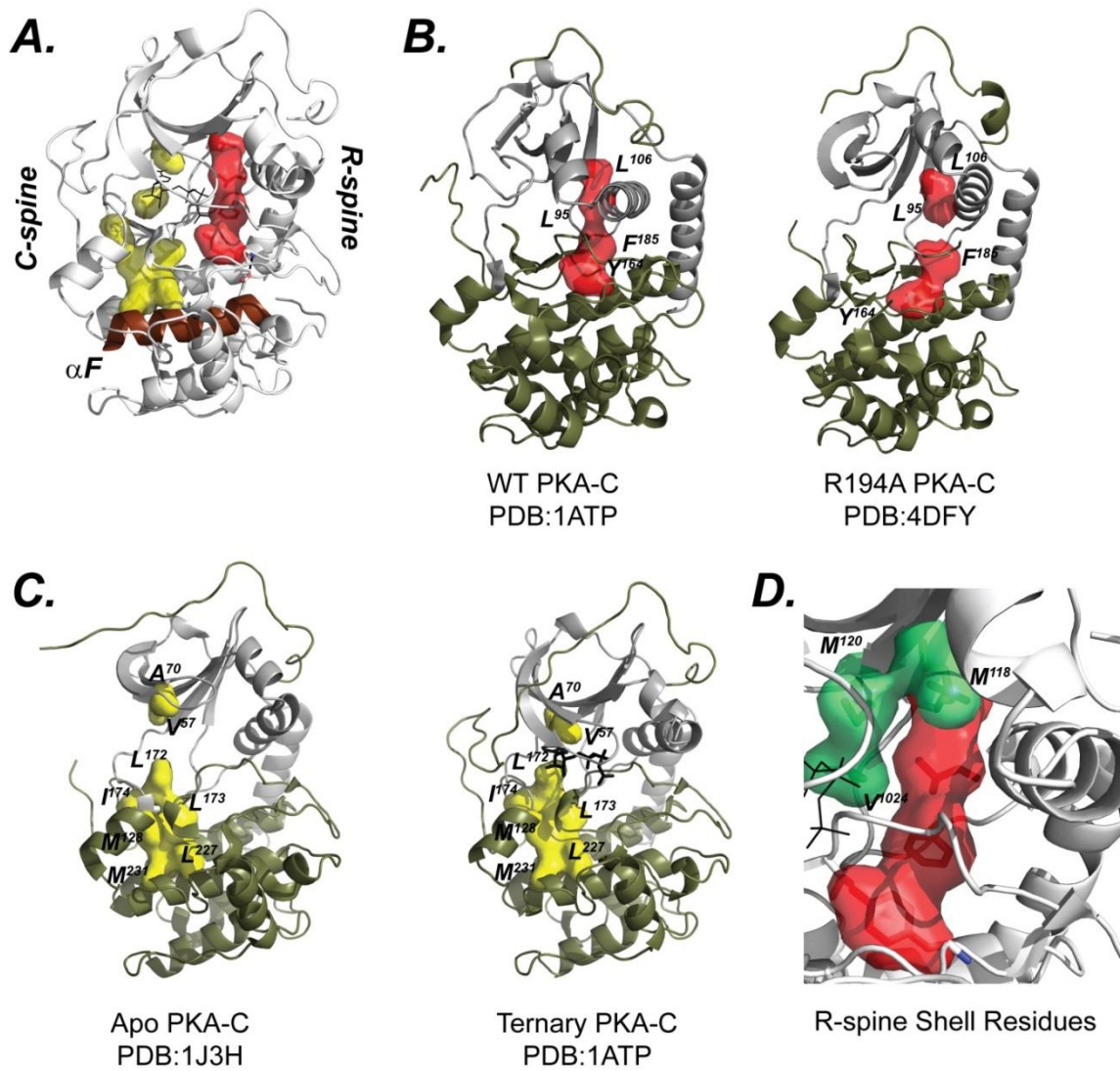
Figure 1.12: Architecture of the hydrophobic spin motifs. (A) General architecture of the spine motifs, C-spine (yellow) and R-spine (red) in PKA-C connected by αF (maroon). (B) Active and inactive conformation of the R-spine found by PKA-C and (C) the active and inactive conformation of the C-spine in PKA-C. (D) The R-spine shell residues (green) responding for coordinating the R-spine.
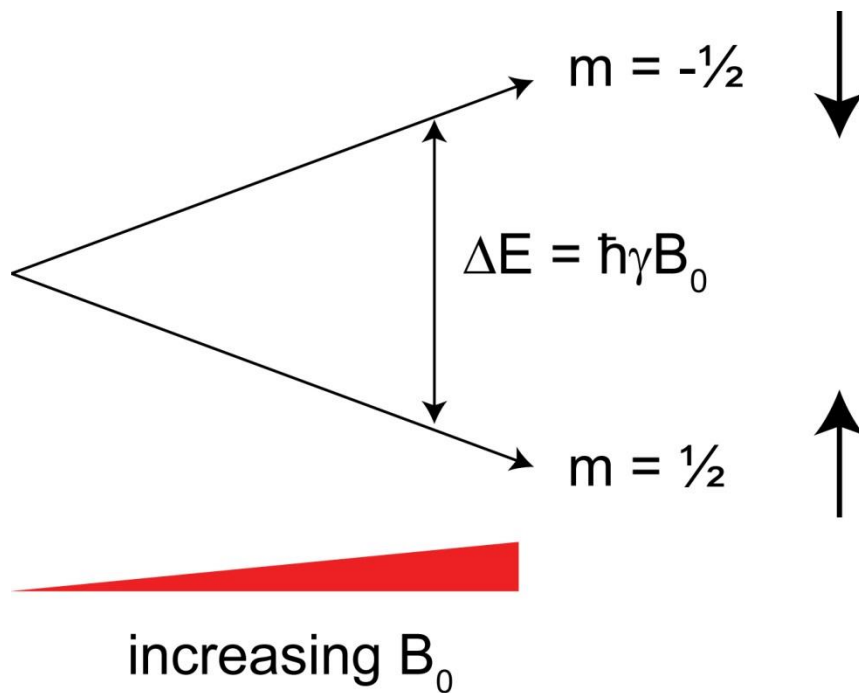
Figure 2.1: Energy level of a particle spin I = ½ in a magnetic field. Splitting of the spin up and spin down states of an I = ½ particle scaled linearly by the application of an external magnetic field.
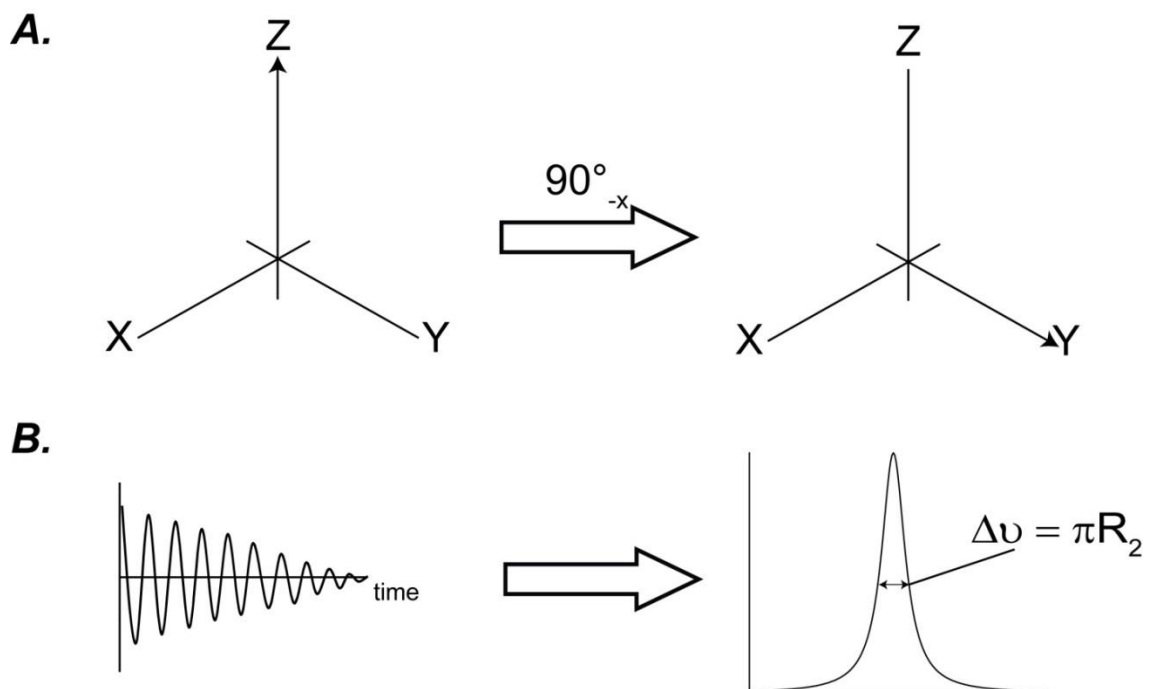
Figure 2.2: Schematic of a simple pulse-acquire NMR experiment A) Simple 90° pulse then acquire experiment on an uncoupled spin system. (B) The resultant NMR signal is a free induction decay, which is Fourier transformed to give the NMR spectrum. The NMR spectrum consists of a Lorentzian line-shape with a half-height linewidth of R_2.
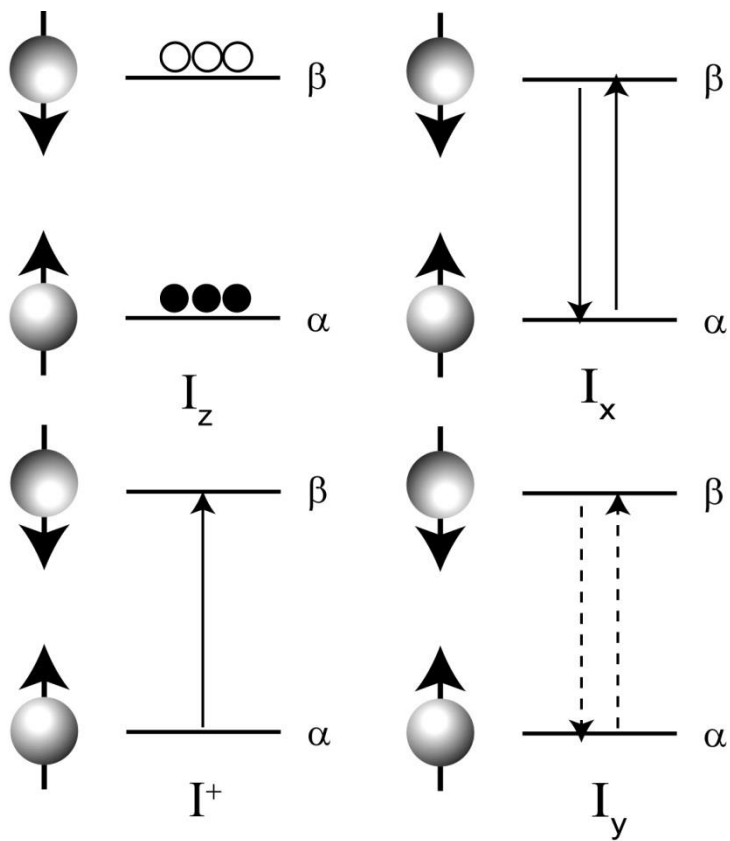
Figure 2.3: Pictorial representation of the quantum mechanical operators, I_z, I_x, I_y and I^+

for a single uncoupled spin.
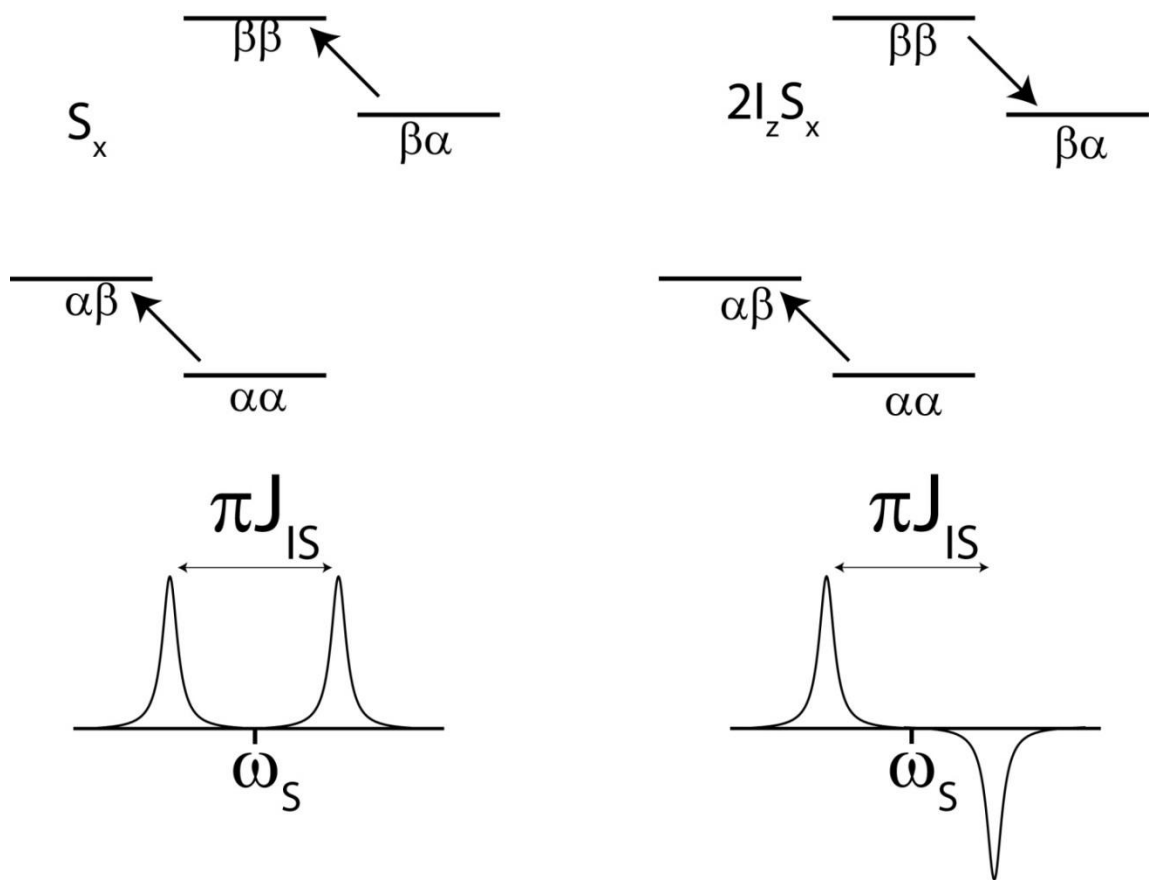
Figure 2.4: Spectroscopic definition of in-phase and anti-phase single quantum operators in a IS spin system and their corresponding quantum mechanical transitions.. For the in-phase operator the two transitions share the same sign while in the anti-phase operator they have the opposite sign.
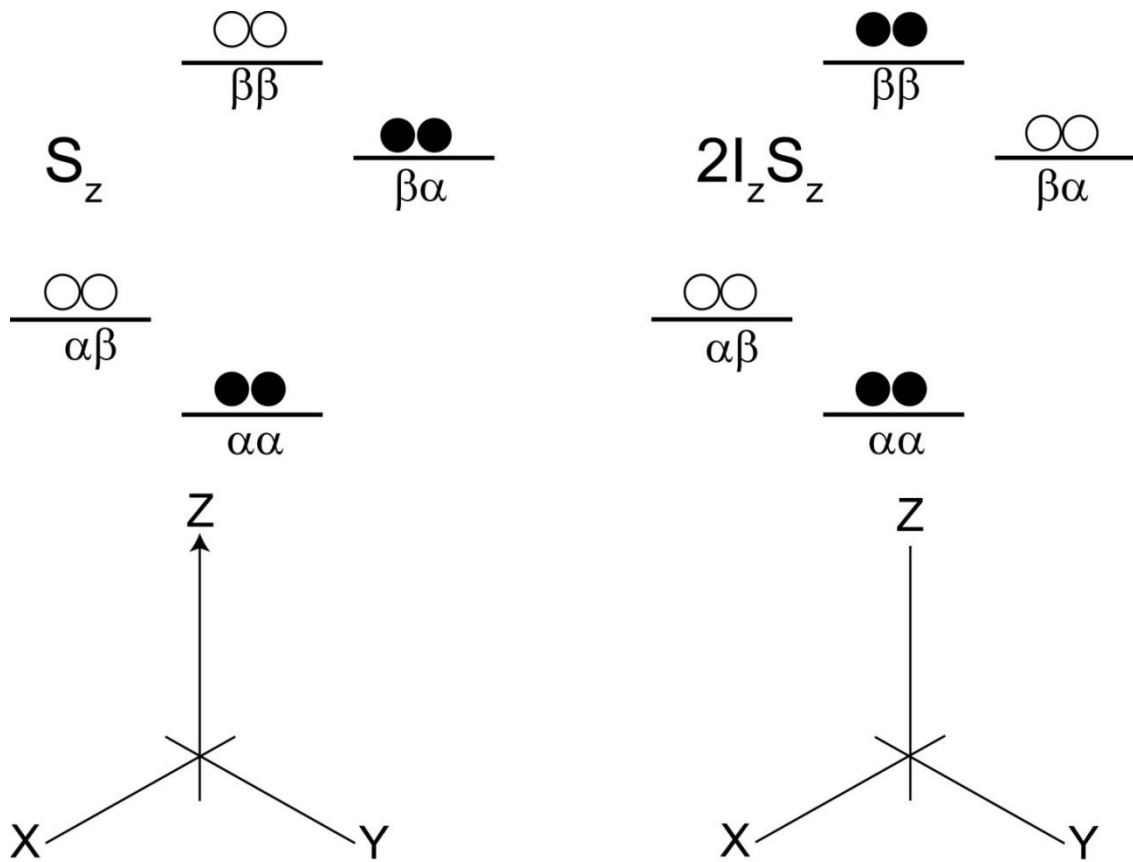
Figure 2.5: Population distribution represented by the S_z and $2I_zS_z$ operators. Below the spin system is the net longitudinal polarization from the operator. Note that there is no net polarization for the $2I_zS_z$ operator, but is in a non-equilibrium state.
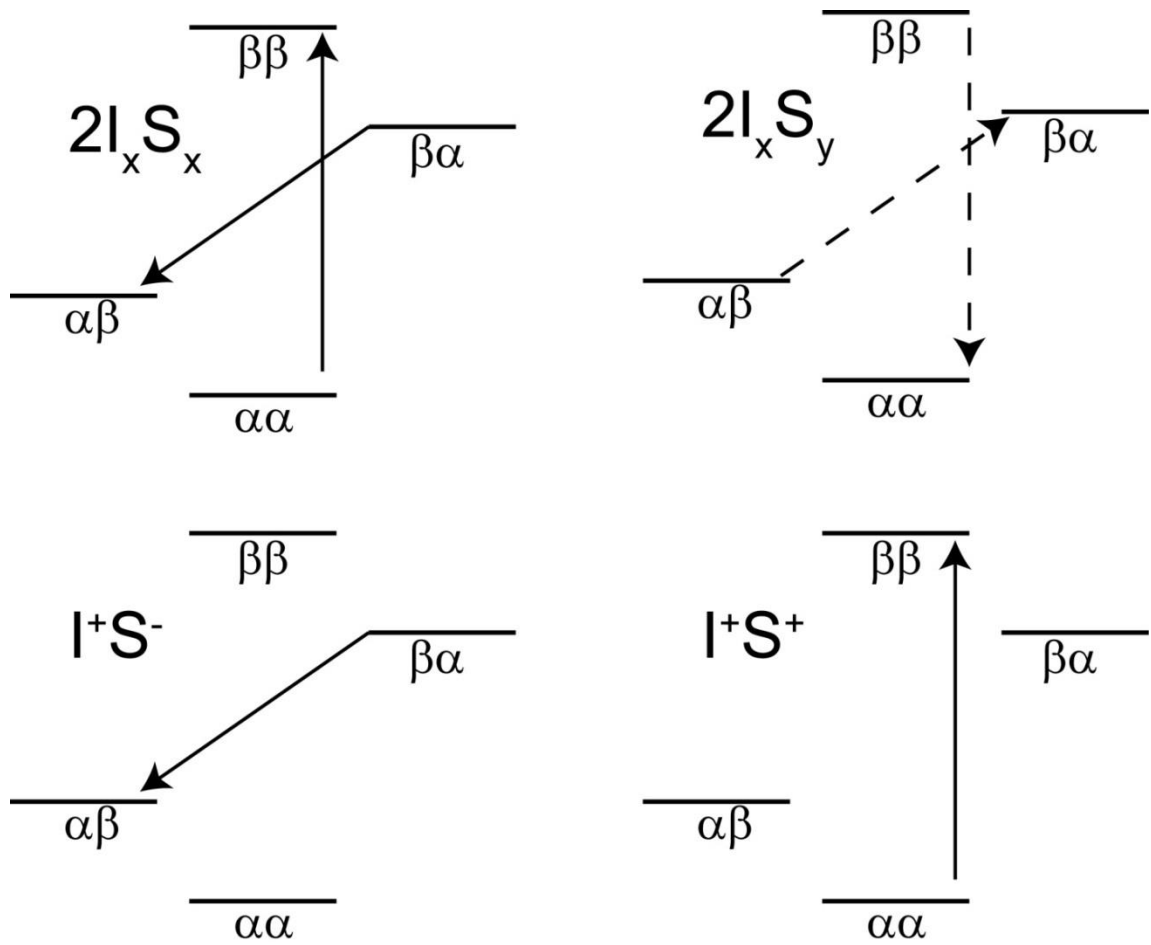
Figure 2.6: Multiple-quantum transitions and their respective operators for a two spin system.
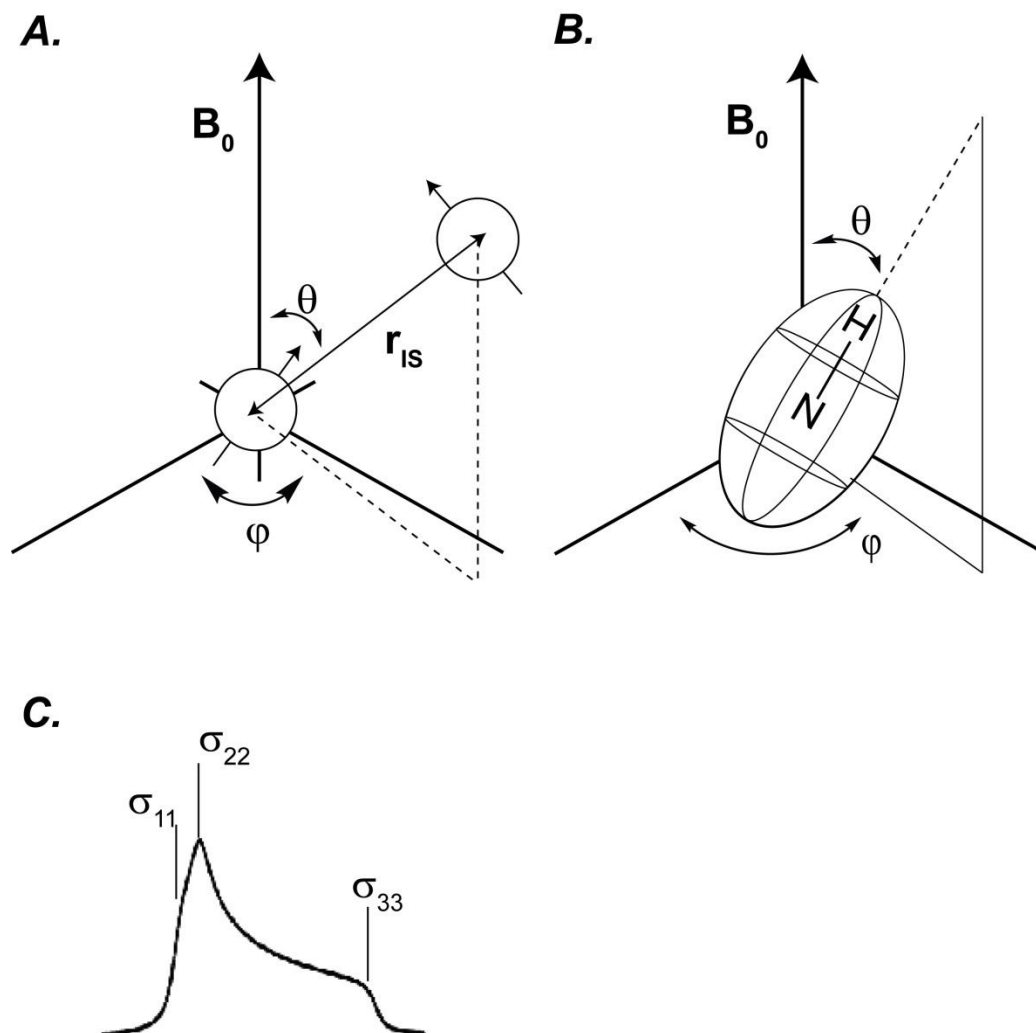
Figure 2.7: The dependence of dipolar coupling and chemical shift anisotropy to geometric constraints. These are described for (A) dipolar coupling and (B) Chemical shift Anisotropy. In a solid-state experiment the edges of the spectra defines the principle axis values.

$$[I_x, I_y] = iI_z$$
$$[I_x, 2I_yS_z] = i2I_zS_z$$
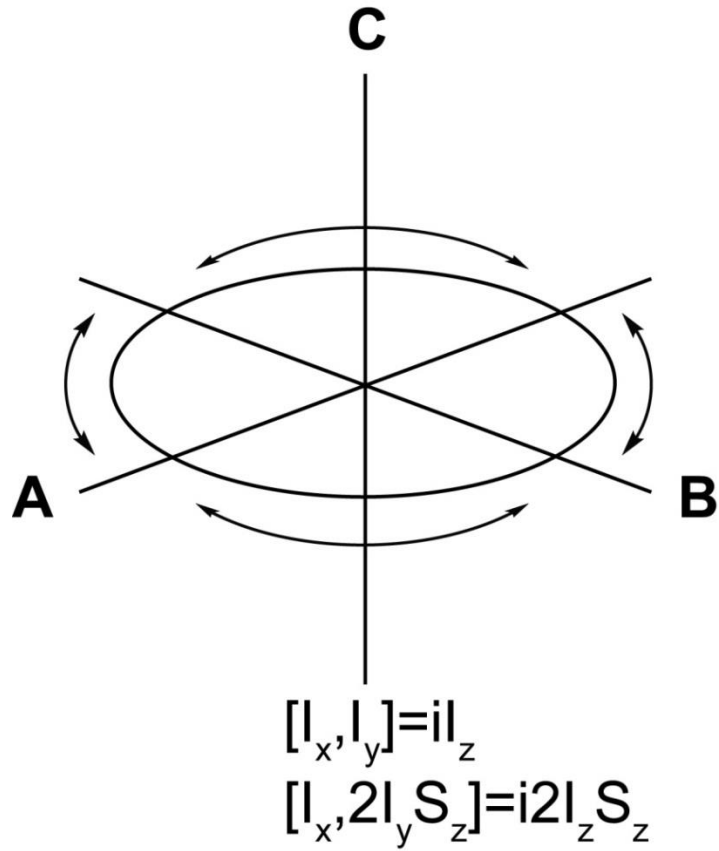
Figure 2.8: Geometric representation of evolution of operator A and B under the effect of operator C. The two operator relationships that define this are also provided.
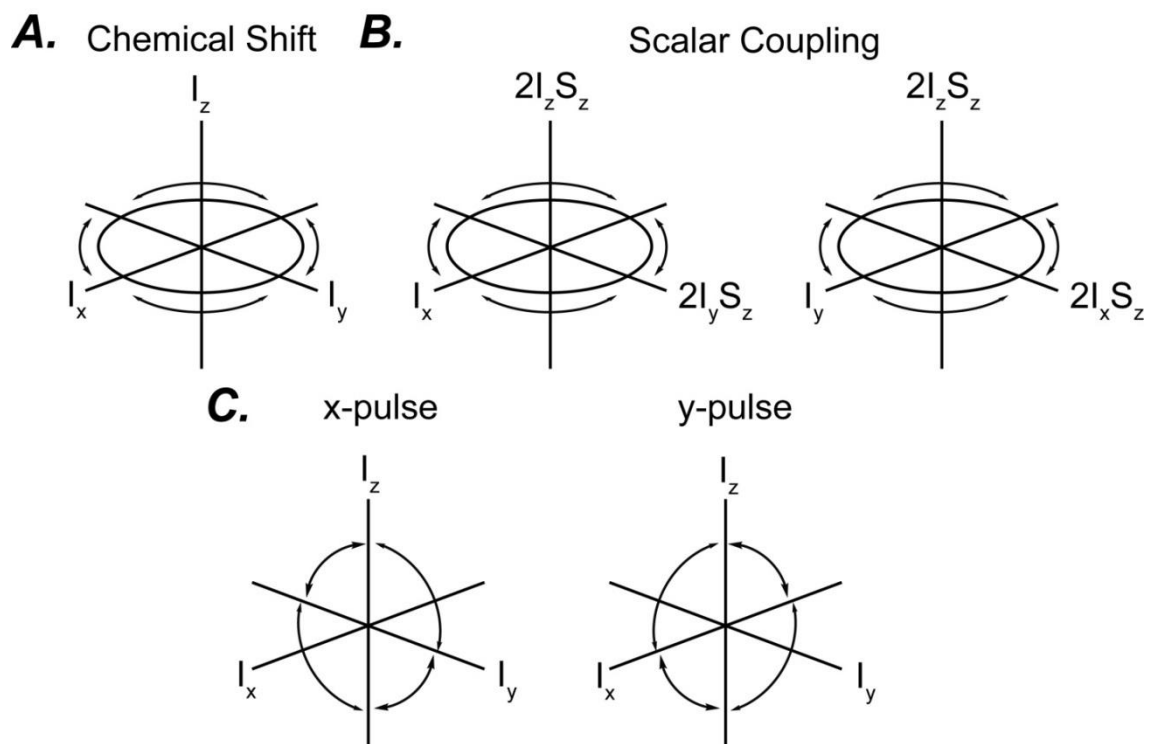
Figure 2.9: Geometric representation of the product operator approach. (A) The chemical shift rotates in a plane composed of operators I_x and I_y. (B) Scalar coupling Hamiltonian rotates the coherence in a plane composed of I_x and $2I_yS_z$ or I_y and $2I_xS_z$.(C) Rotation of the density matrix from rf pulses.
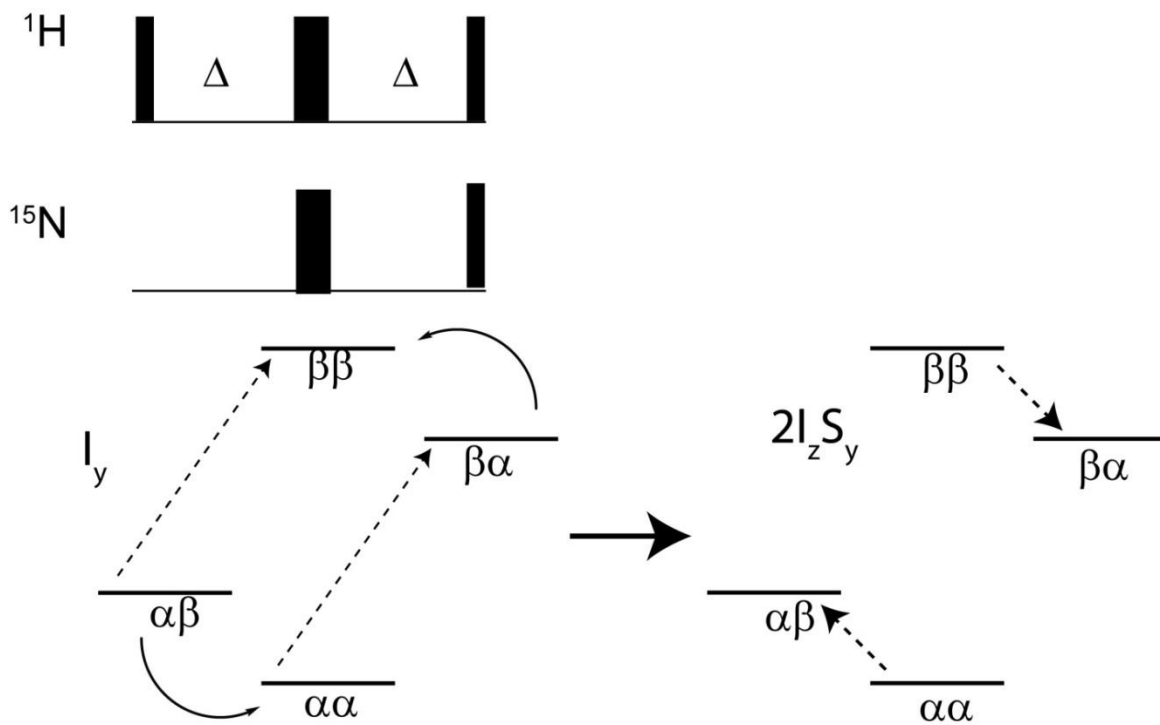
Figure 2.10: INEPT pulse sequence. The INEPT pulse sequence converts I_y to $2I_zS_y$. This effectively creates a state where the signal of the transverse magnetization of S is scaled by I_z.
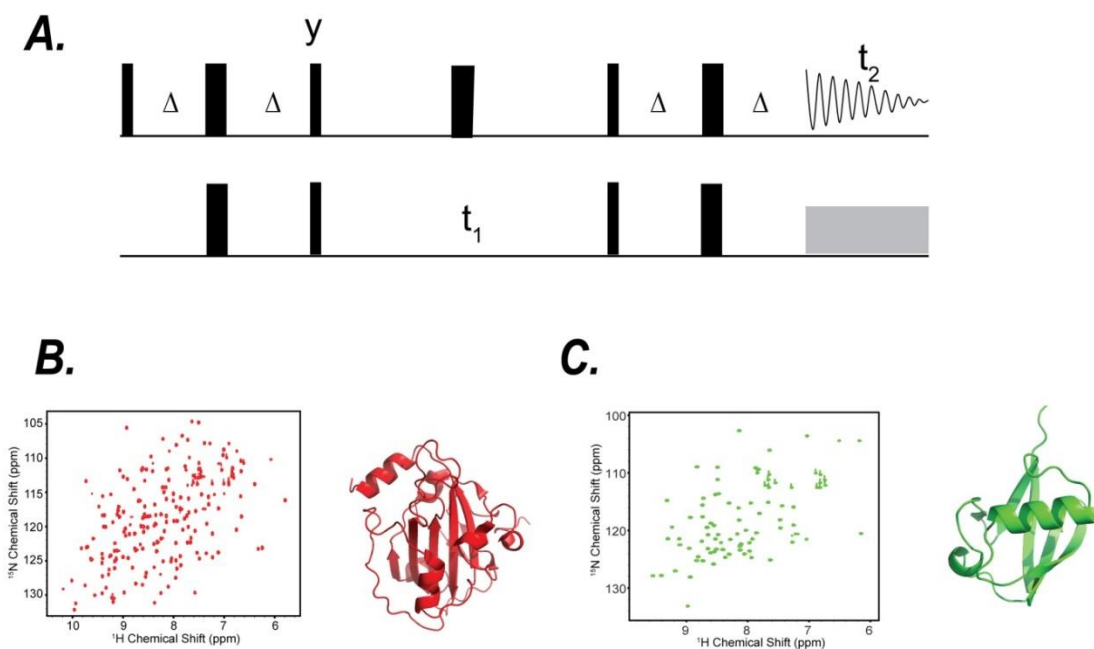
Figure 2.11: [^{1}H,^{15}N], HSQC pulse sequence and application to proteins. (A) Pulse sequence of a basic HSQC experiment. (B) [^{1}H-^{15}N], HSQC spectrum of a 21kDa phosphatidylethanolamine binding protein (red) and ubiquitin (green)
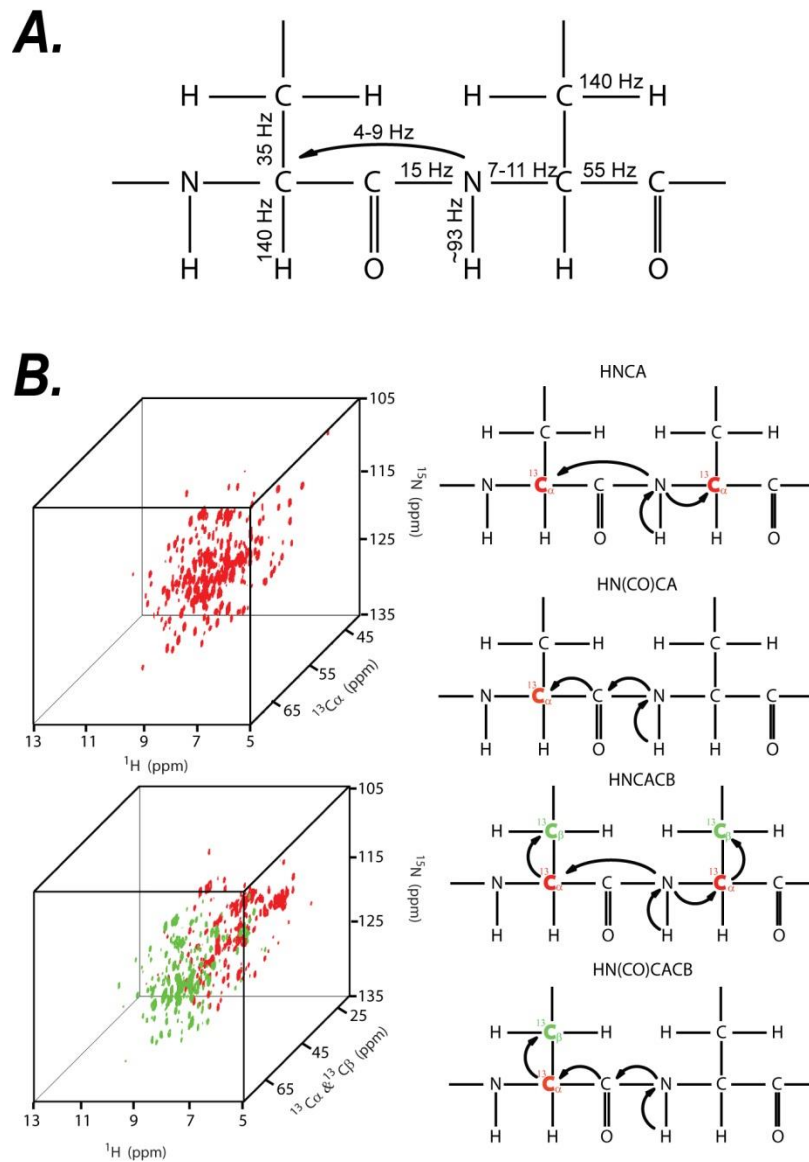
Figure 2.12: Extension of coherence transfer for triple resonance experiments. (A) The scalar coupling within a protein backbone is uniform for each bond coupling throughout the protein, enabling the spectroscopist to simultaneously excite and transfer coherence throughout the protein. (B) To assay the backbone amides two sets of experiments are typically performed. For measurement of the $^{13}C\alpha$ chemical shifts two experiments, HNCA (which measures the $^{13}C\alpha$ for the I and i-1 residue) and HN(CO)CA (measures the $^{13}C\alpha$ for the i-1 residue). The HNCACB and HN(CO)CACB experiments perform the same function but using the $^{13}C\beta$ chemical shifts.
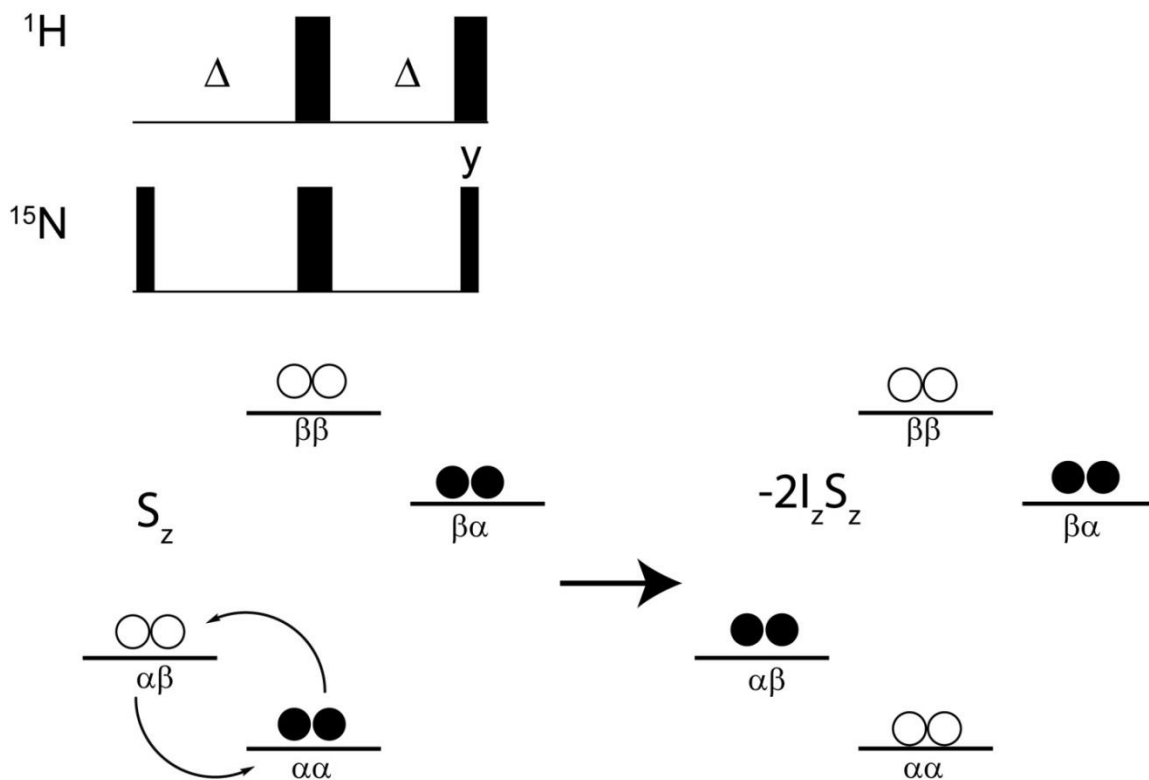
Figure 2.13: Spin-state-selective coherence transfer element (S^3CT). Pulse sequence element for S^3CT and the effective inversion of the only one of the S spins.

A.

$$B_{eff} = B_0 + B_{ex} \qquad B_{eff} = B_0 \qquad B_{eff} = B_0 - B_{ex}$$

B.
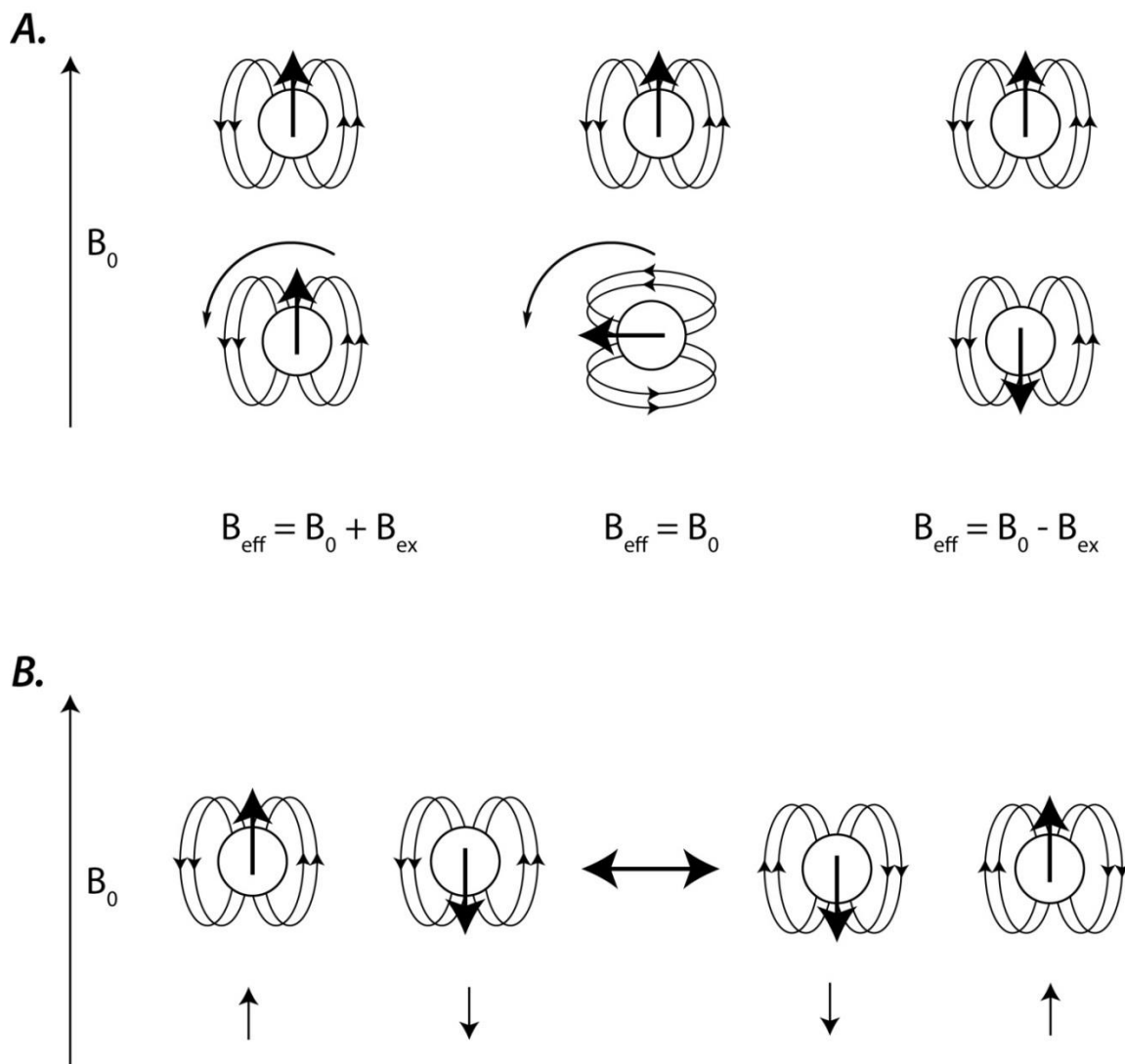
Figure 2.14: Relaxation mechanisms in NMR. (A) The first occurs when molecular tumbling alters the energy levels and this fluctuation is on the timescale of the transition (i.e. Larmor frequency). (B) The second mechanism occurs when a spin in the environment opposite in orientation (spin down) is in proximity of the excited nuclei (spin up). These two exchange energy and now the spin from the environment is excited.

Isotropic Rigid Rotor

$S^2=1$

"Model Free"
Diffusion in a Cone

$S^2=[\frac{1}{2}\cos\theta(1+\cos\theta)]^2$
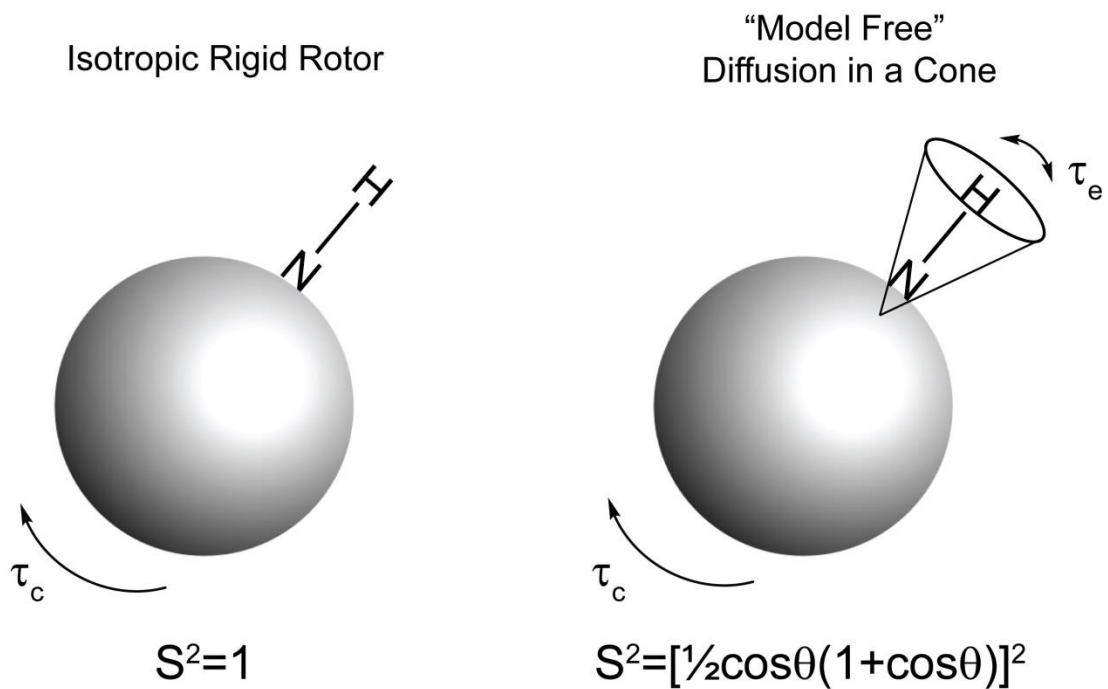
Figure 2.15: Physical models for the interpretation of spectral density functions (A) The simplest model, the isotropic rigid rotor, sees the overall protein as spherical with a rigid bond vector with the NMR signal. (B) The "model free" approach expands this by allowing the bond vector liberate in a timescale much faster than the overall molecular rotation.
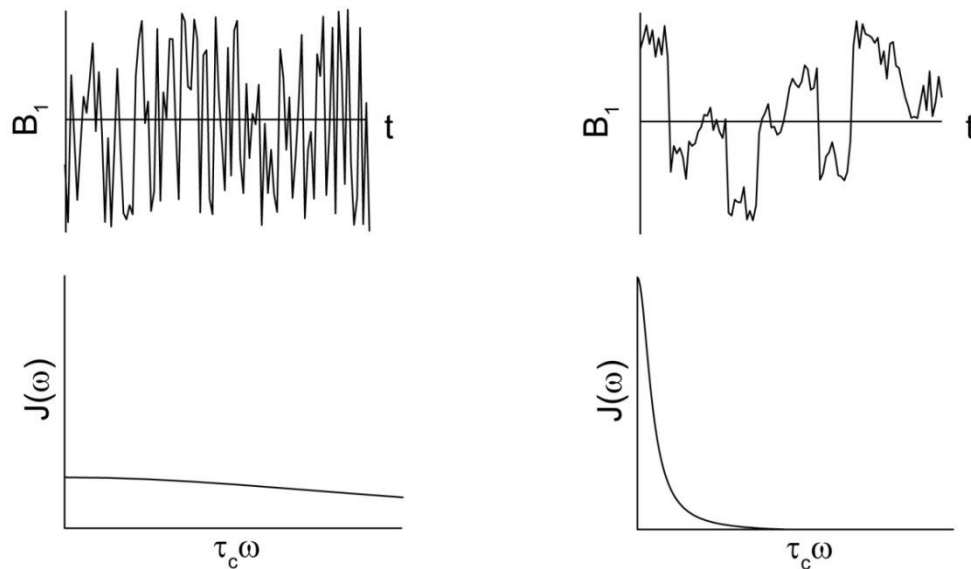
Figure 2.16: Magnetic fluctuations and spectral density function of two extreme of molecular motion. (A) For small molecules in the extreme narrowing limit the contribution is equal for all spectral density functions. (B) For macromolecules, such as proteins, in the spin diffusion limit only the zero frequency spectral density function contributes significantly.
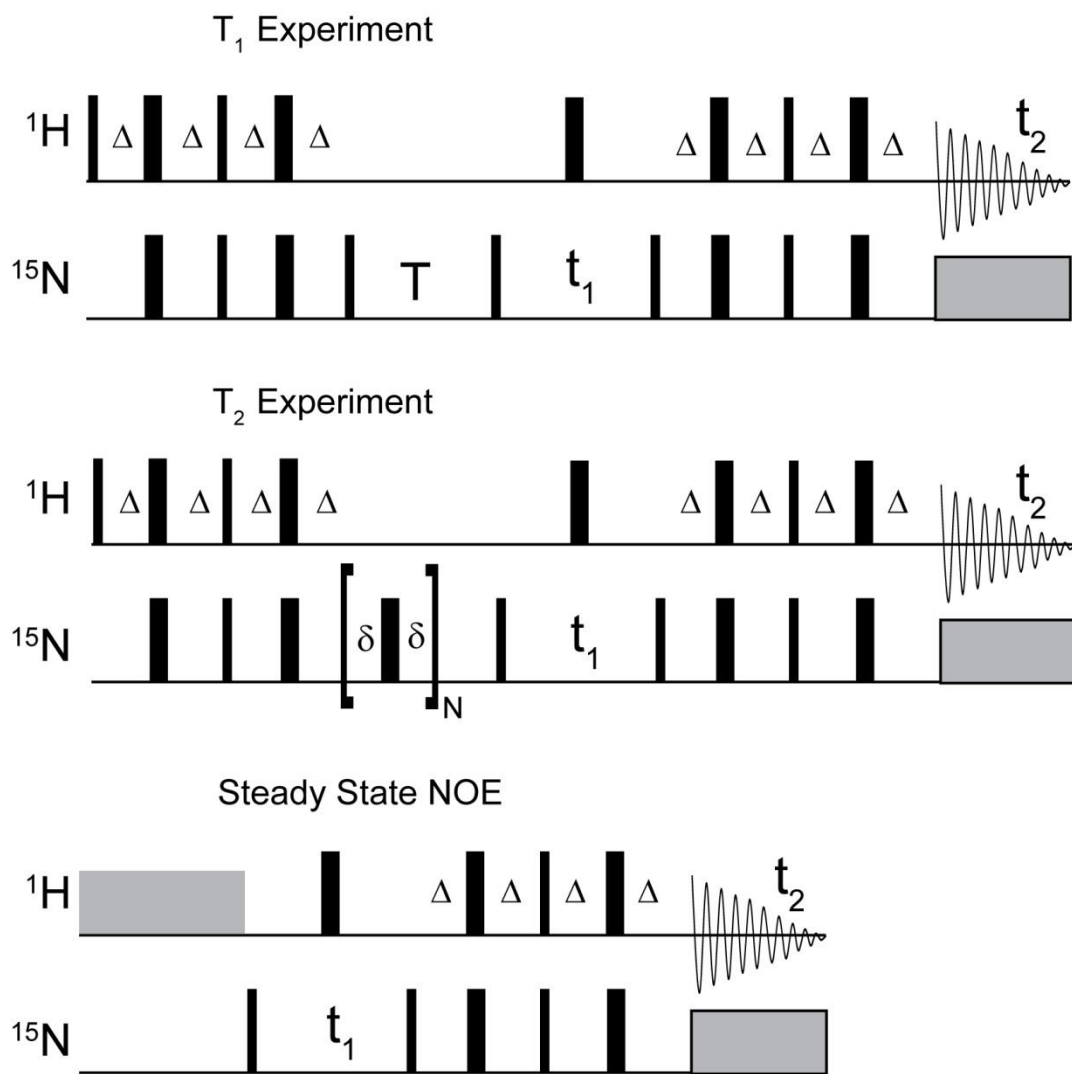
Figure 2.17: Standard pulse sequences for measuring relaxation in ^{1}H-^{15}N backbone amide groups. These include the T_1, T_2 and steady-state NOE experiment (from top to bottom). The delay, Δ, is the period $1/4J_{NH}$ and all experiments shown here use the sensitivity enhanced back transfer scheme [166].
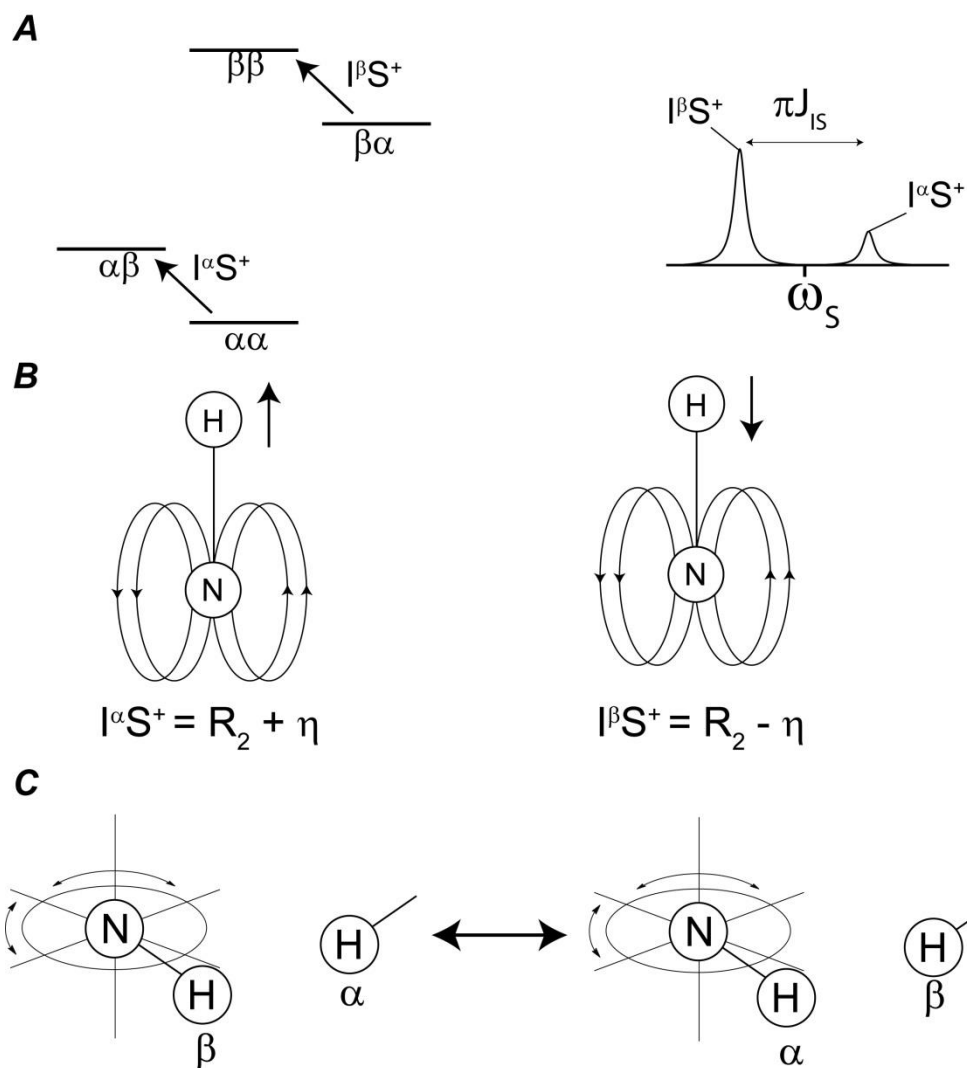
Figure 2.18: TROSY effect on a ^{1}H-^{15}N coupled spin system. (A) The doublet of a ^{15}N transition in a ^{1}H-^{15}N spin system experiences differential relaxation for each of the transitions. (B) Orientation of the passive spin for each of the transitions. When the orientation of 1H spin is opposite of that to ^{15}N the TROSY effect is active (C) Exchange with external protons transforms the TROSY transition to an anti-TROSY transition.
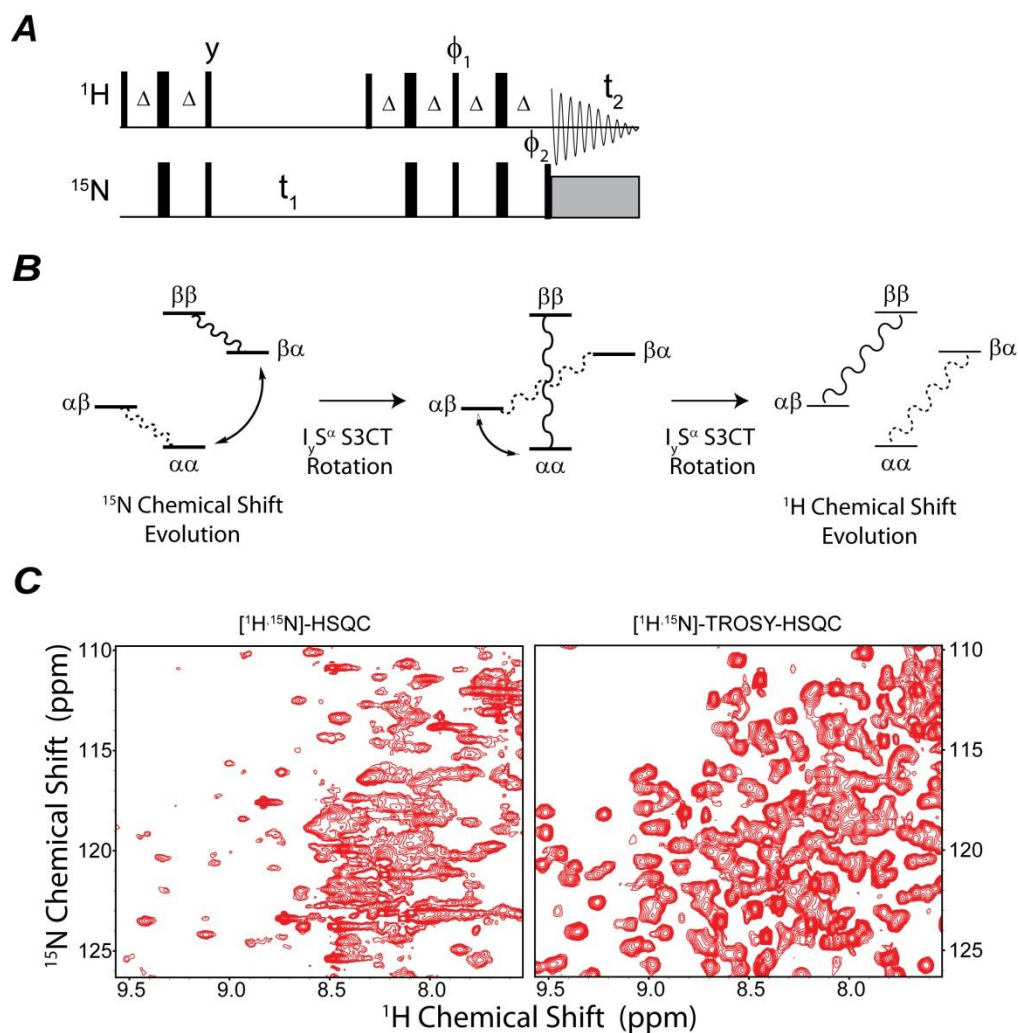
Figure 2.19: Experimental realization of the [^{1}H,^{15}N]-TROSY HSQC experiment. (A) Pulse sequence of the ^{1}H-^{15}N TROSY HSQC experiment. (B) Effect of two S^{3}CT elements that allows for the selective transfer of the ^{15}N single quantum TROSY transition to the 1H single quantum TROSY transition. (C) Application of the TROSY-HSQC pulse sequence on PKA-C.
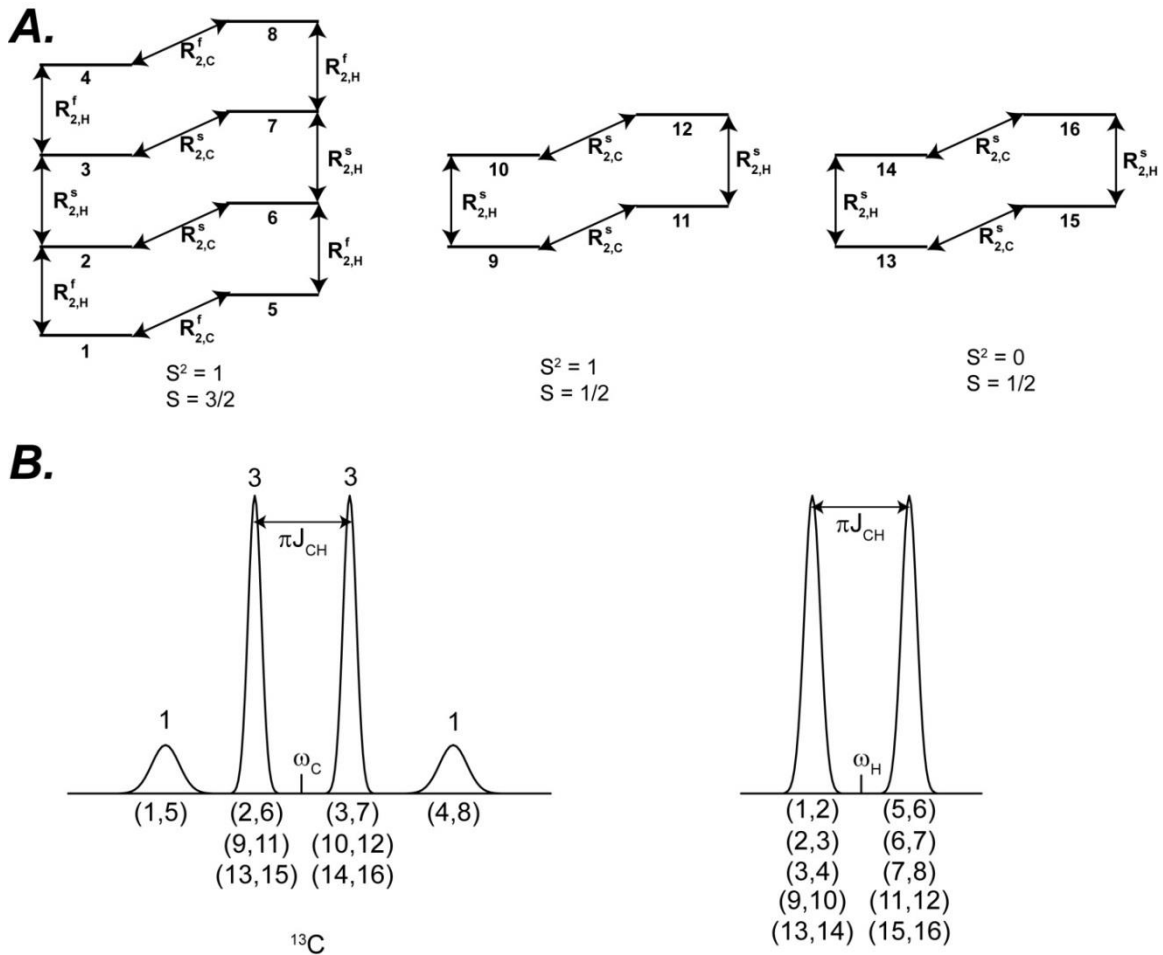
Figure 2.20: Energy levels of an isolated $^{13}CH_3$ labeled methyl group. (A) Description of the all the transitions and the relaxation rates of each of the transitions. S^2 denotes the total spin of the protons and S is the maximal z component of the magnetization from the protons. (B) Spectral description outcome of the ^{13}C transitions and the ^1H transitions. The carbon quartet has a characteristic 1:3:3:1 pattern and the protons are in a doublet. These multiplets are separated by πJ_{CH}.
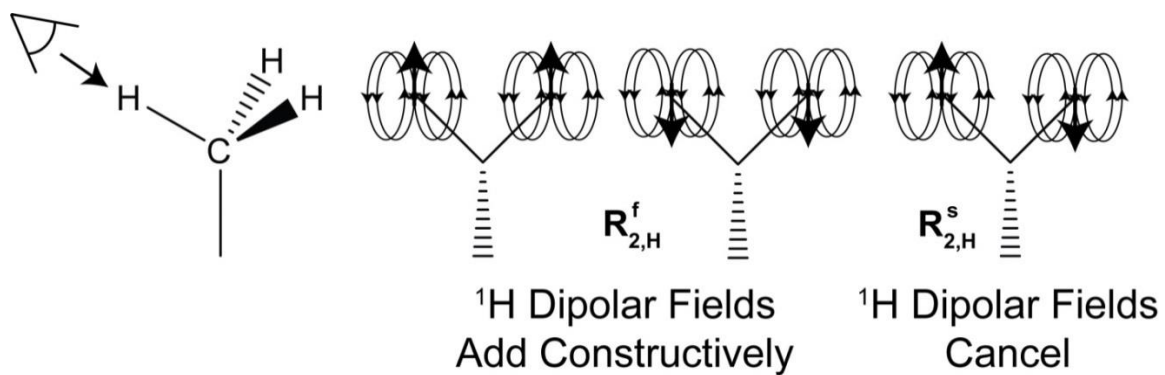
Figure 2.21: Dipolar fields in cross-correlation of relaxation rates. For the rapidly decaying ^1H transitions, $R^f_{2,H}$, the dipolar fields in the neighboring protons are parallel to each other. While for the slowly decaying transition, $R^s_{2,H}$, the spins are in opposite orientation and the dipolar fields cancel each other out.
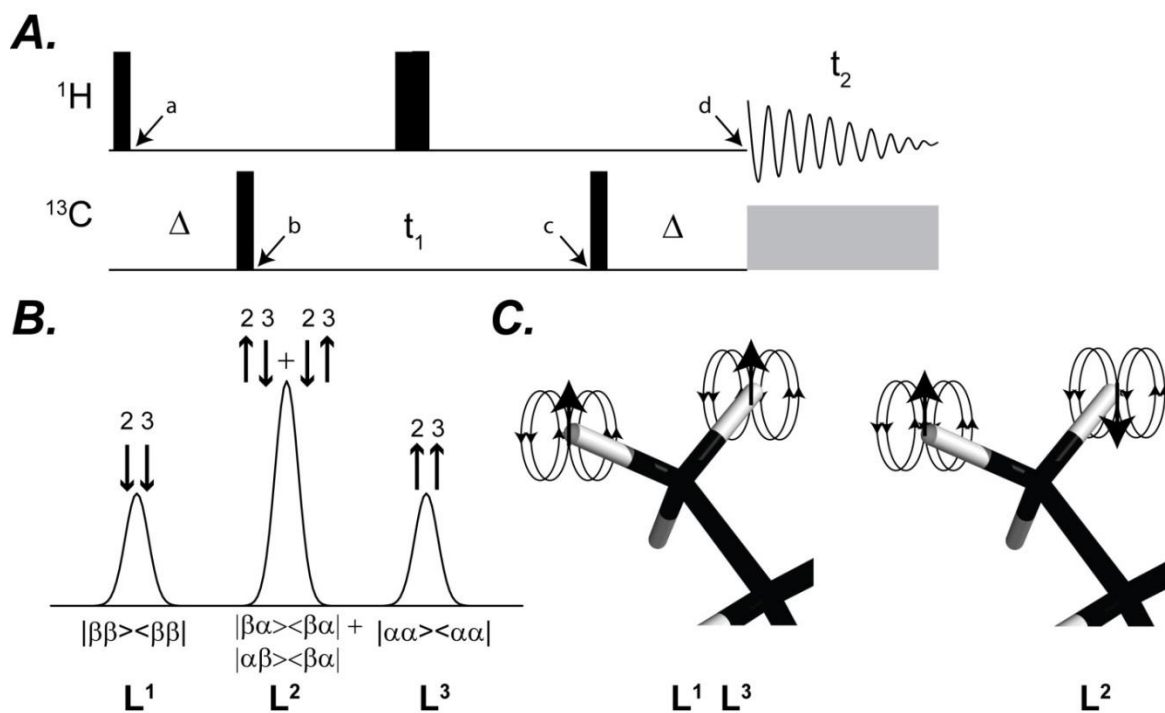
Figure 2.22: [^{1}H,^{13}C]-HMQC experiment and relaxation of multiple quantum coherences.
(A) Pulse sequence of the [^{1}H,^{13}C]-HMQC experiment. Δ = 1/2J_{CH} . (B) CH transitions during the multiple quantum t1 period of the HMQC experiment. (C) Dipolar fields from neighboring protons either add constructively (L_1 and L_3) or destructively (L_2) to create differential relaxation rates.
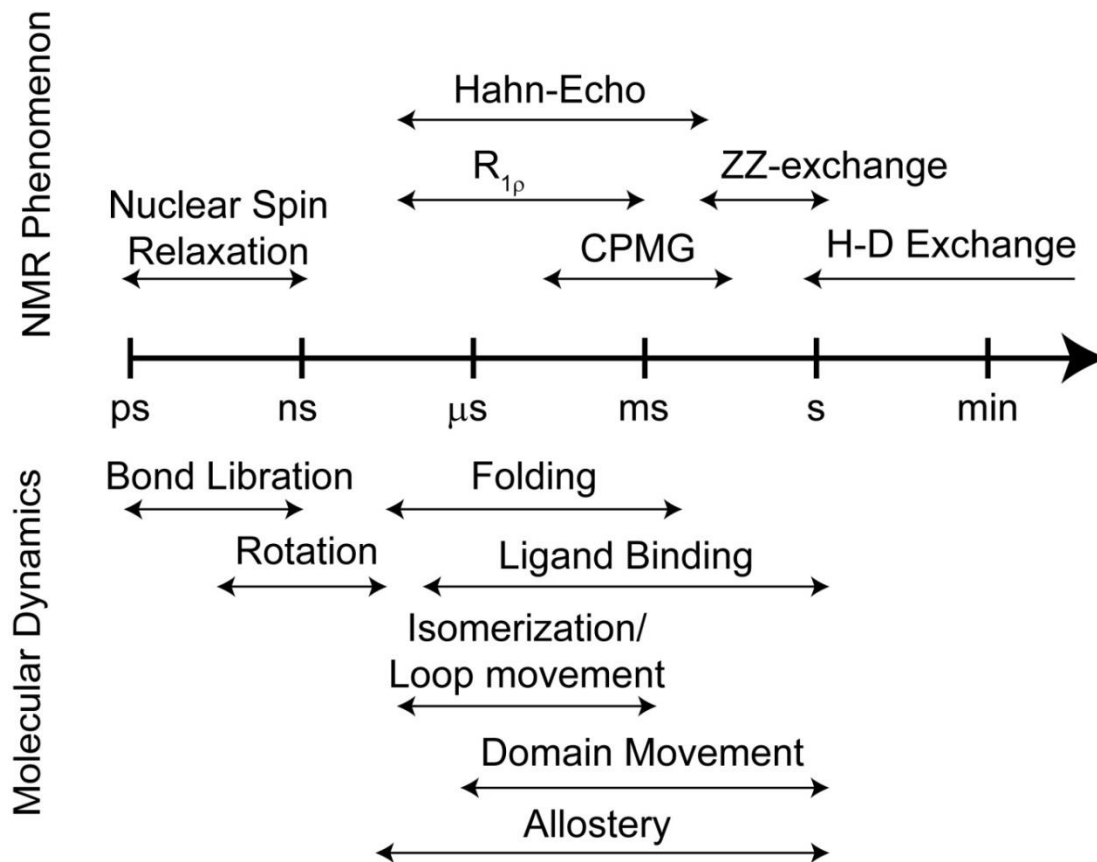
Figure 2.23: Range of motions that are probed using NMR relaxation measurements described. Figure is adapted from [535, 536]
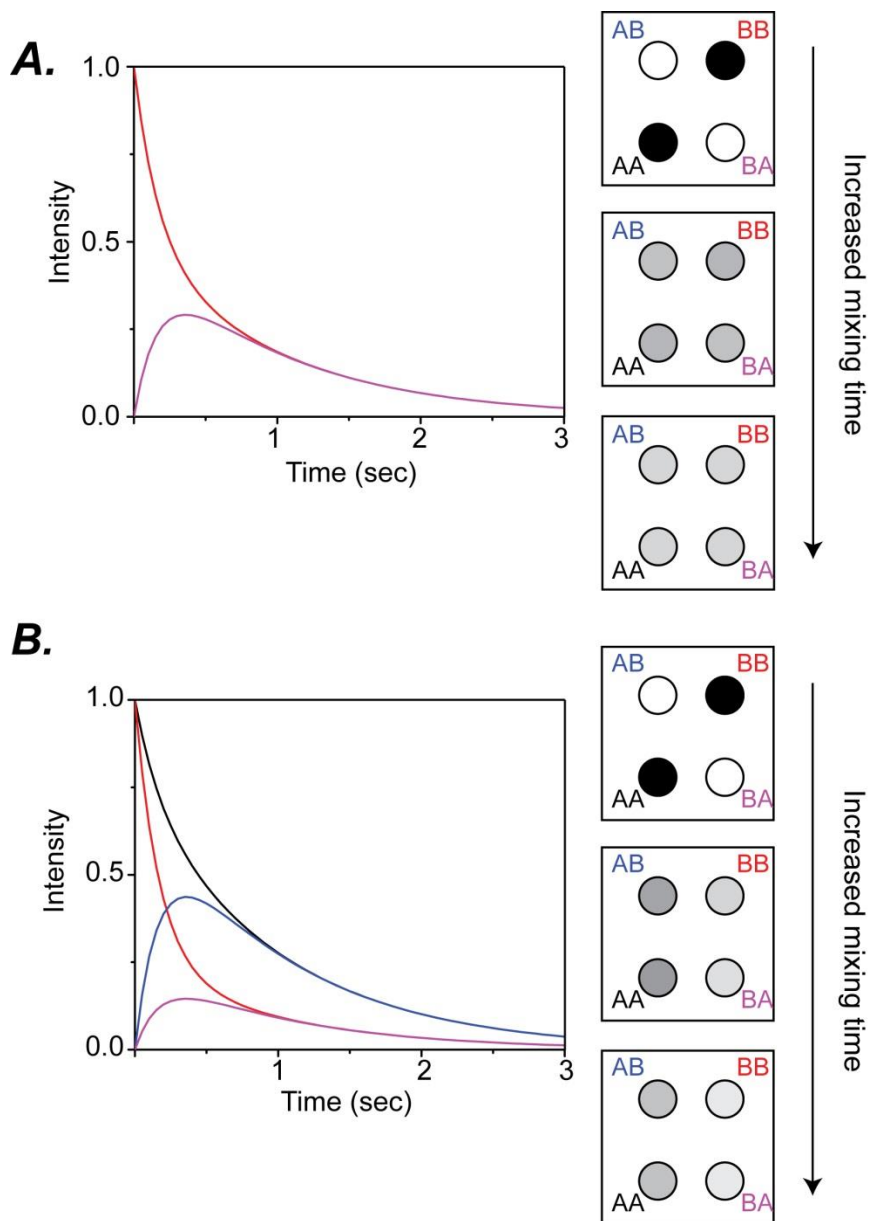
Figure 2.24: Profile of the intensity of chemical exchange on longitudinal magnetization. (A) In a case when exchange is occurring between two equal populations and (B) when p_A is three times larger than p_B. Note that the intensity in the plot if relative to their initial intensity.
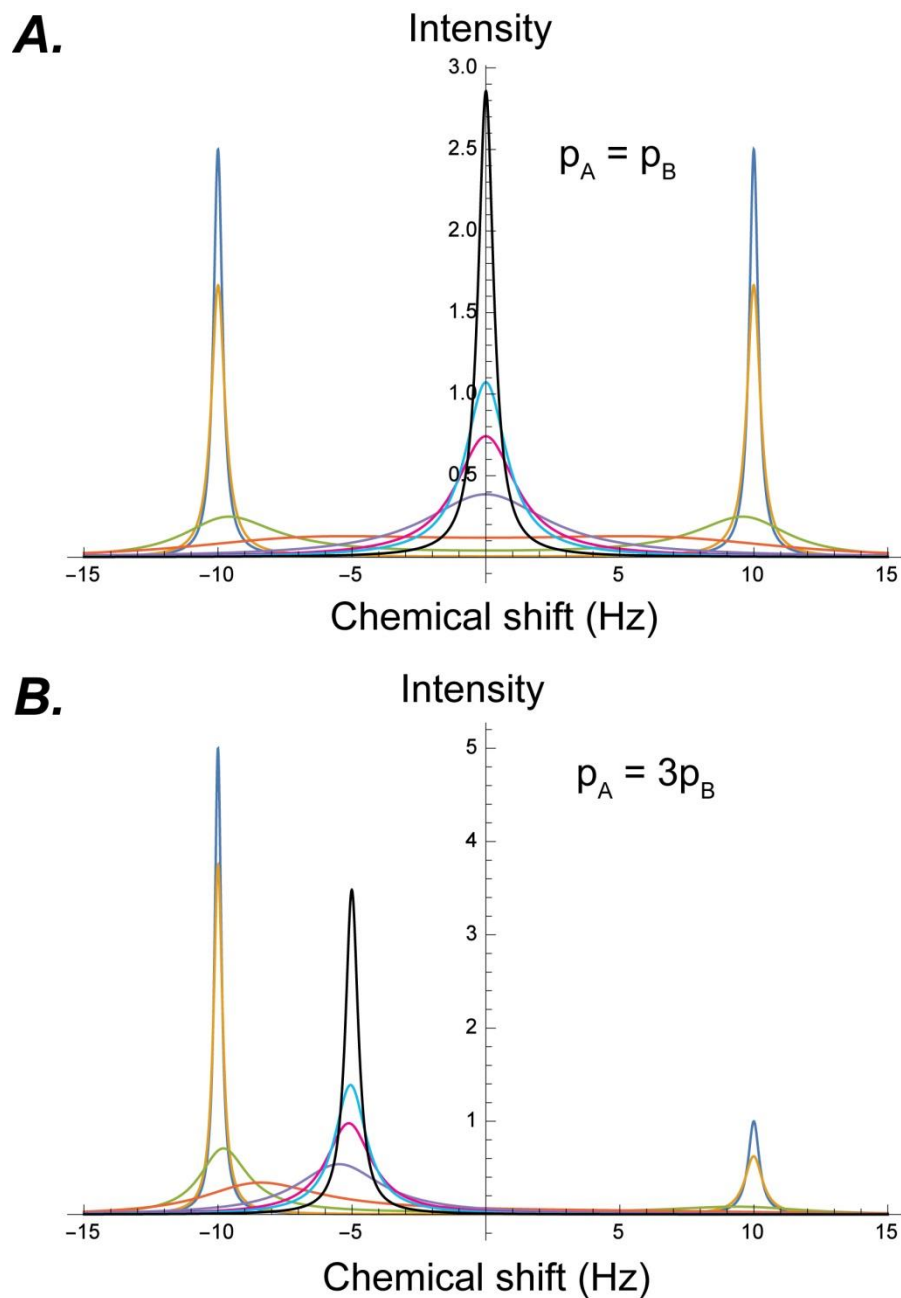
Figure 2.25: Two resonance undergoing chemical exchange in the fast, intermediate and slow timescale. The effect of chemical exchange was performed on two resonances $\Delta\delta$ = 20 Hz using a kex value of 0.2 (dark blue), 0.4 (yellow), 4 (green), 12 (orange), 40 (purple), 80 (magenta), 120 (cyan) and 400 s^{-1} (black). These have been performed using (A) two equally populated states and (B) when pA = 0.75., an asymmetric state
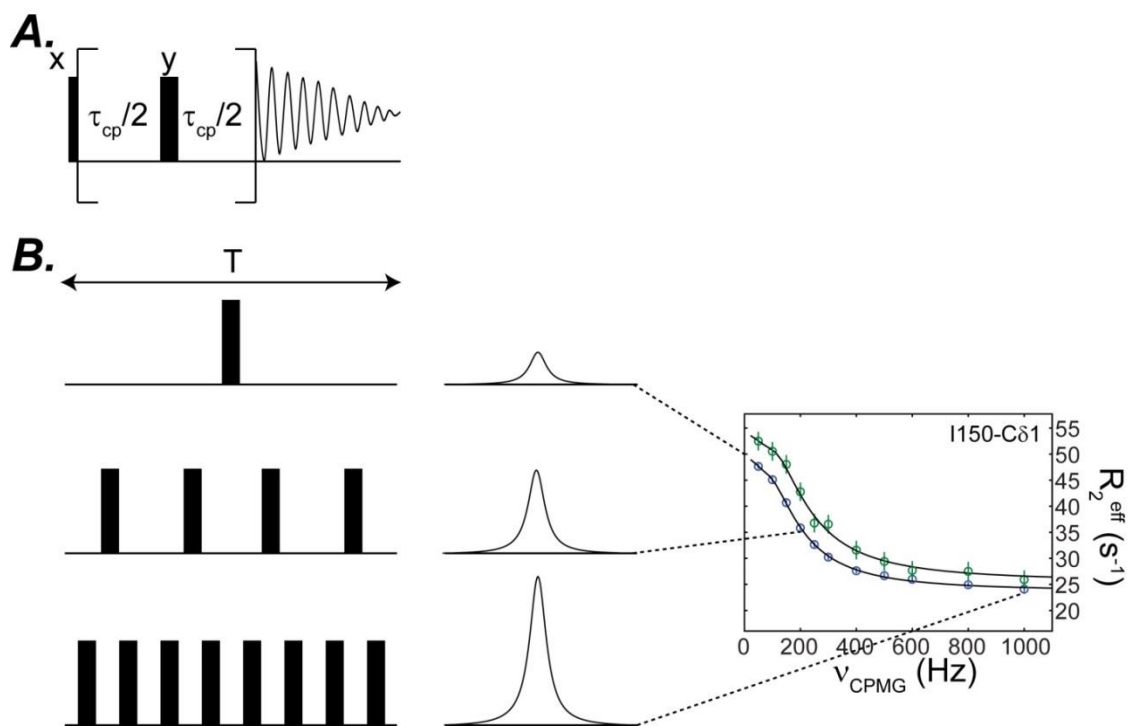
Figure 2.26: Effect of the CPMG pulse train on chemical exchange. (A) Basic schematic of the CPMG pulse train (B) Effect of CPMG on a resonance undergoing exchange. As the pulsing rate increases in a CPMG experiment, the relaxation contribution to the signal decreases. This can be plotted systematically with the Carver-Richards equation to extract quantitative protein dynamics.
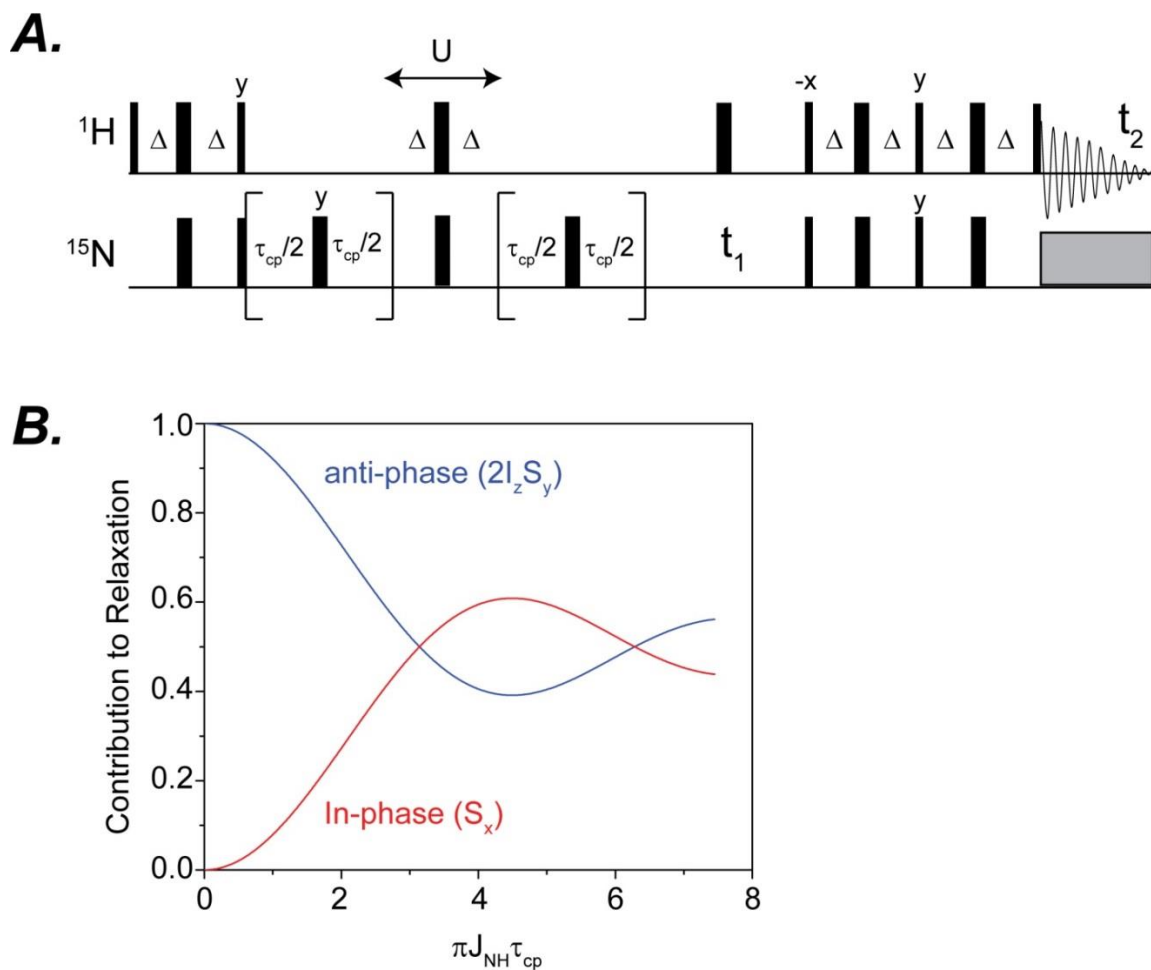
Figure 2.27: [^{1}H-^{15}N],-HSQC CPMG experiment. (A) Pulse sequence for the ^{15}N edited CPMG experiment for backbone amide groups. (B) Evolution of the anti-phase operator into the in-phase operator as a function of the pulsing frequency.
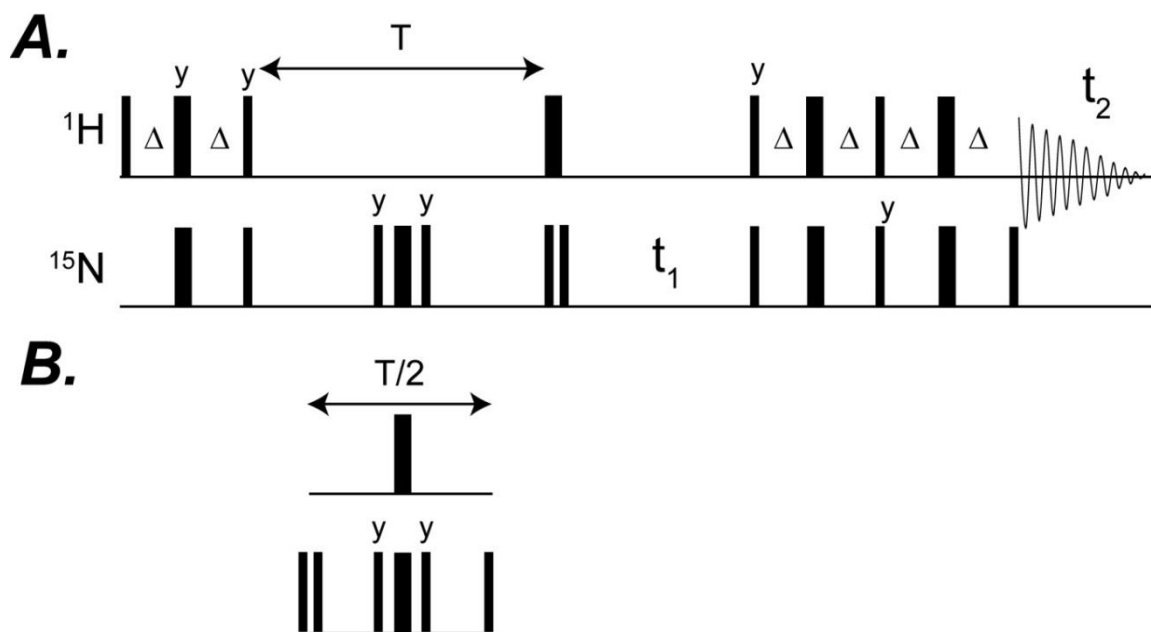
Figure 2.28: Pulse sequence of the TROSY Hahn-Echo experiment. (A) Pulse sequence for the measurement of the transverse relaxation of the TROSY and anti-TROSY transition for the determination of the cross-correlation rate. (B) Modification to the TROSY Hahn-echo sequence for the measurement of longitudinal double order magnetization.
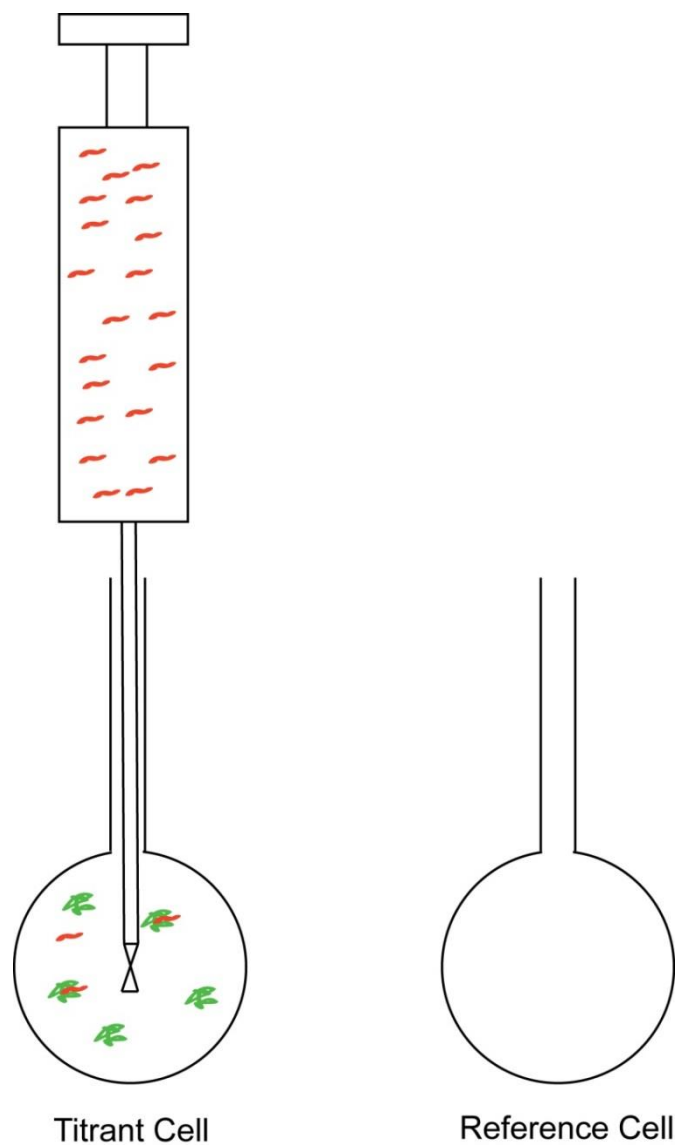
Figure 3.1: ITC schematic. An ITC experiment generally consists of two chambers, one filled with protein solution (Titrant cell) and another filled with buffer (reference cell). An automated syringe adds in ligand of a known concentration and amount into the titrant cell and records the heat required to maintain isothermal condition.
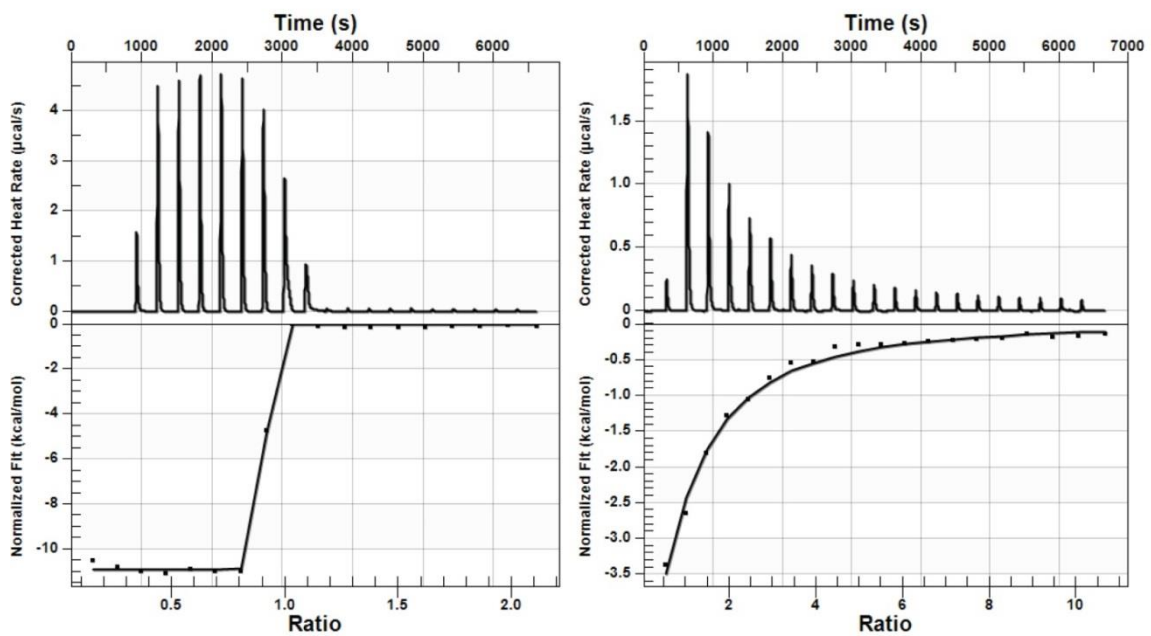
Figure 3.2: ITC isotherms of Ca^{2+} binding to EDTA (left) and Ba^{2+} binding to 18-crown-6 ether (right) Ca^{2+} binding is an example of tight binding by ITC while Ba^{2+} binding is an example of weaker binding that requires higher molar excess to extract an accurate K_d.
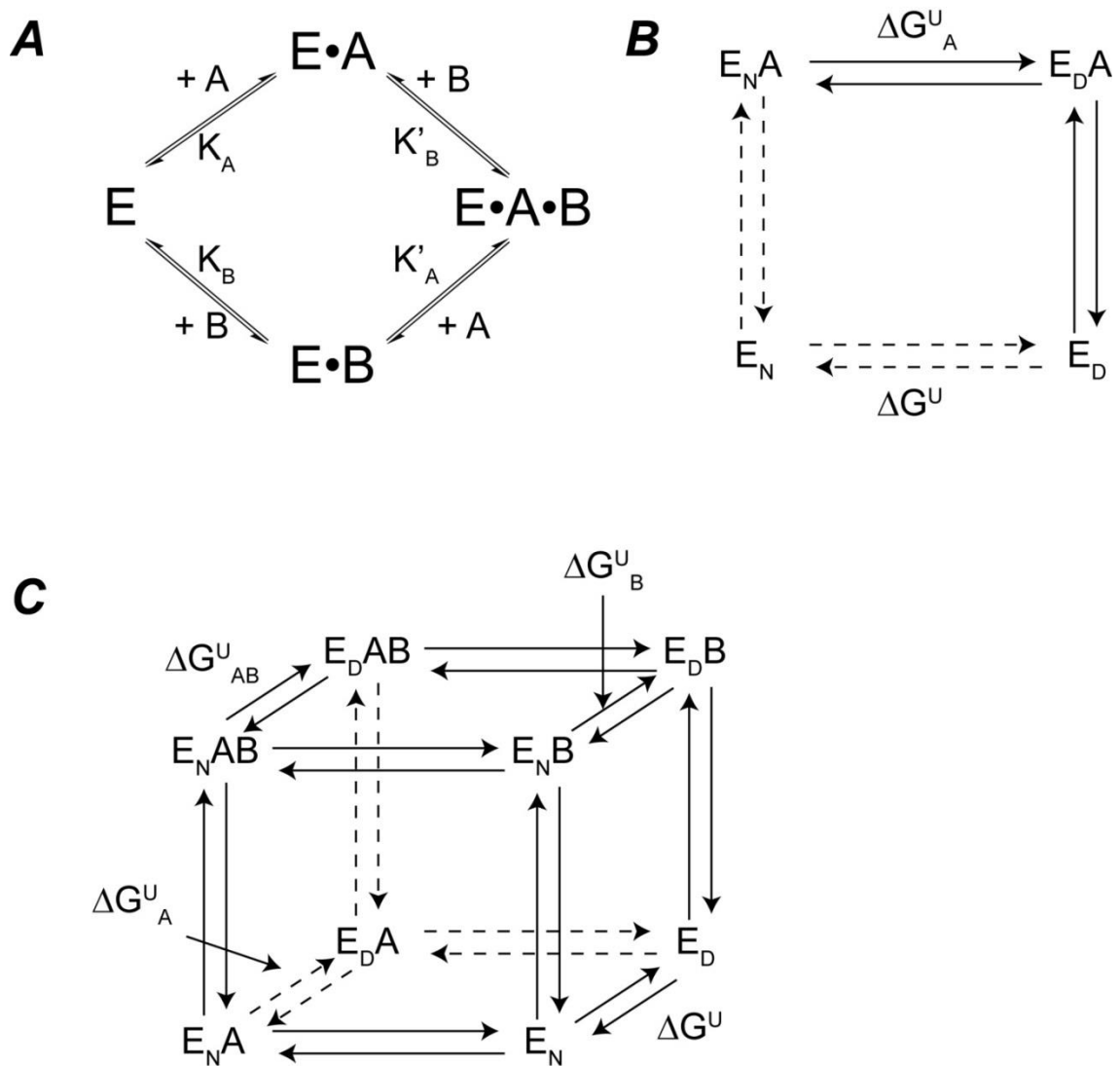
Figure 3.3: Thermodynamic cycles used for studying the effects of ligand binding and mutation. (A) A heterotropic linkage model between two ligands, A and B, binding to a protein. (B) A closed thermodynamic cycle showing the effect of a single mutation on the stability of a protein. (C) A double mutant requires a cube to define all the possible states that a protein can exist in.
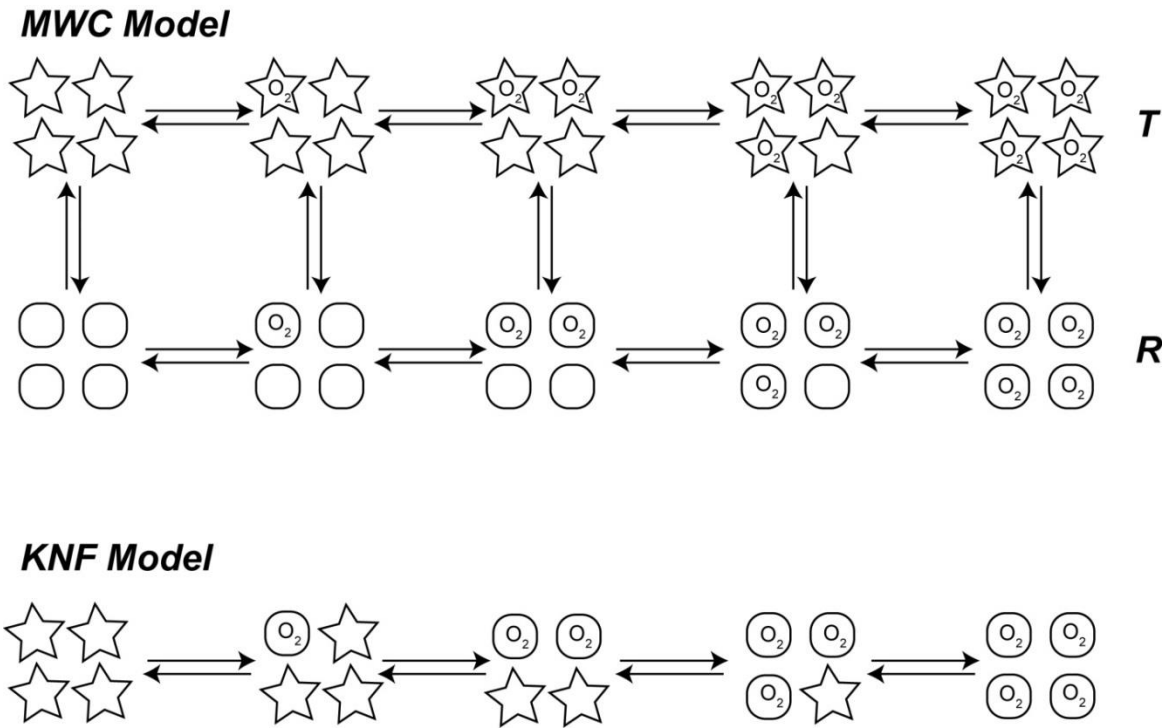
Figure 3.4: The two predominant models for cooperativity originally modeled to explain cooperative binding for hemoglobin. (A) The MWC model or "conformational selection" model in which two states are in equilibrium with and without ligand bound (B) The KNF model for sequentially tighter binding of O_2. The stars represent states with low binding affinity and circles represent states with higher affinity.
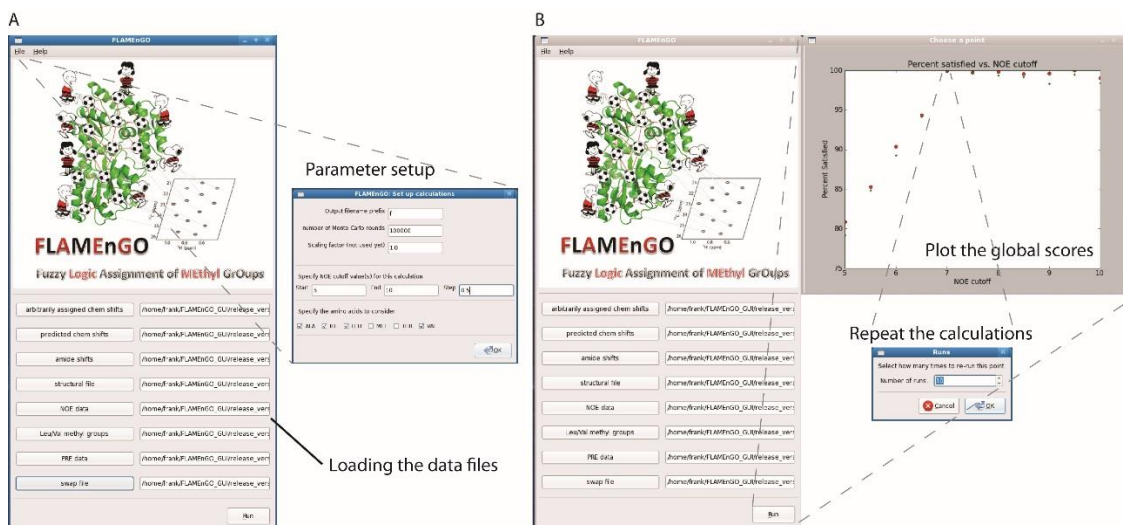
Figure 4.1: GUI interface of FLAMEnGO 2.0. (A) Main window of the GUI interface used to uppload various NMR restraints and the parameters for the calculations. (B) Output window, where the program plots the global score for each NOE distance cutoff. Note that multiple runs of calculations are necessary to optimize the assignments (see text). The optimal NOE distance cutoff can be chosen for multiple calculations, generating a probability-based assignment.
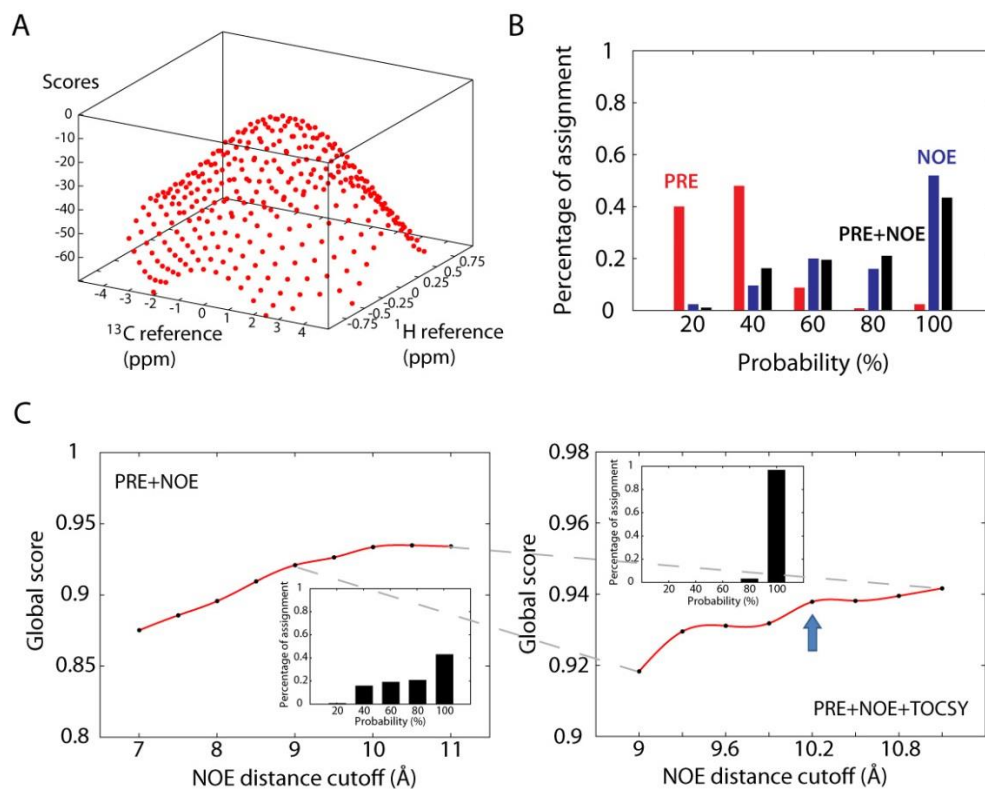
Figure 4.2: Application of FLAMEnGO 2.0 to PKA-C. (A) The surface of scores obtained by matching experimental chemical shifts with predicted chemical shifts at different references. (B) Percentage assignment versus probability using different combinations of experimental restraints (i.e., NOE, PRE or NOE+PRE). Each data set is used as an input for five independent calculations. In the histogram, the percent assignment from the PRE data is indicated in red, NOE data in blue, and PRE+NOE data in black. (C) Determination of the optimal NOE distance cutoff obtained by arraying different NOE distance cutoffs. Calculations of the global score using PRE and NOE data at coarse intervals of the NOE cutoffs (left). In this case, the optimal cutoff was found to be 10 Å with probability-based assignments reported in the inset. Global score calculations performed with PRE, NOE, and TOCSY data using finer intervals of NOE cutoffs (right). The optimal cutoff distance was found to be 10.2 Å, with assignment statistics shown in the insert.
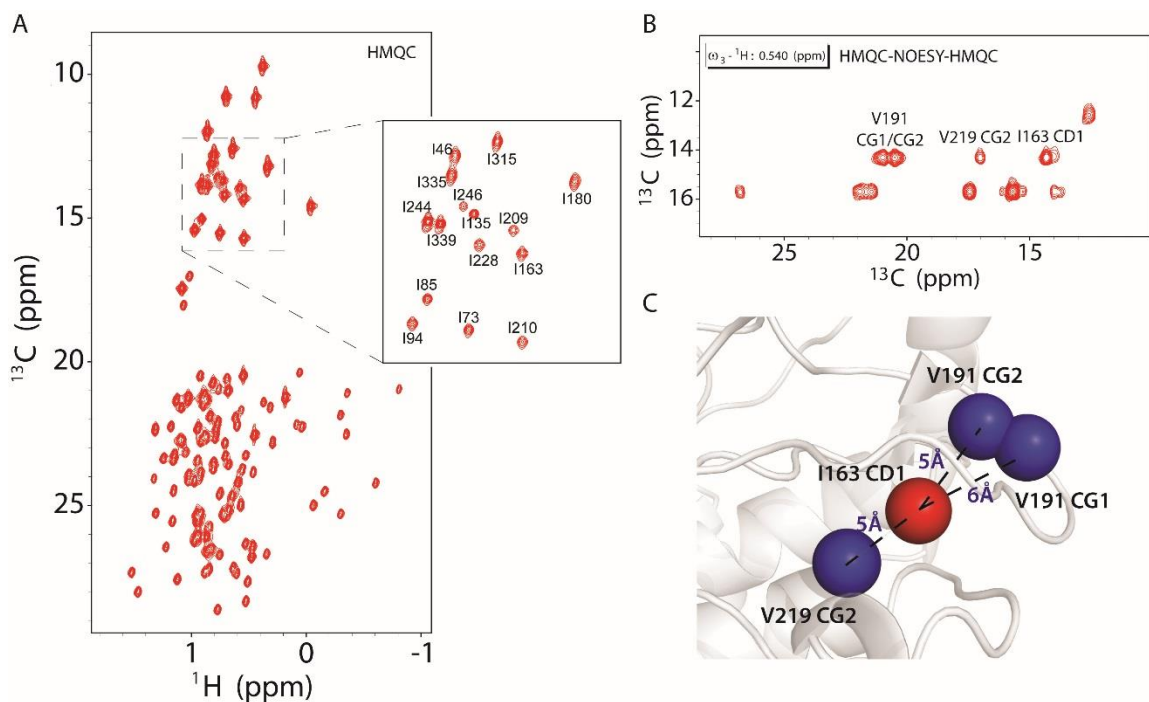
Figure 4.3: (A) The methyl-TROSY spectrum of PKA-C is shown with selected resonances labeled with highest global scores obtained from 100 independent calculations. (B) A 3D slice of the HMQC-NOESY-HMQC spectrum of PKA-C showing assigned cross peaks for I163 methyl group (δ1). (C) Example of NOE distance restraints obtained from the NOE cross peaks of the I163 methyl group (δ1) with the corresponding distances utilized in FLAMEnGO 2.0. The restraints are shown in the crystal structure (PDB: 1ATP).
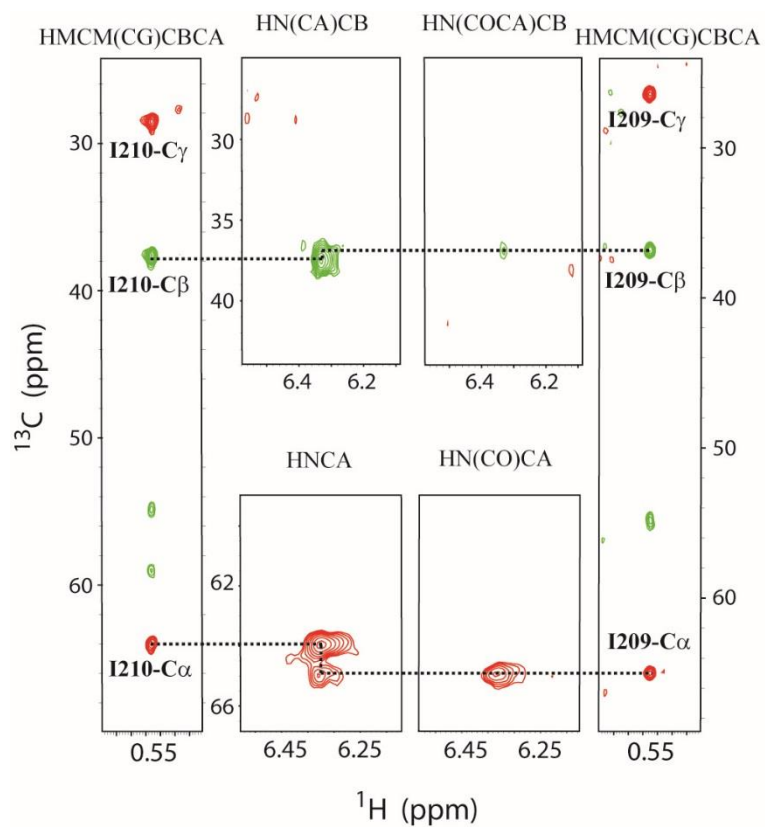
Figure 4.4:. Methyl assignments of I210 and I209 using FLAMEnGO 2.0 are confirmed

by sequential walks using triple-resonance and methyl out-and-back experiments.
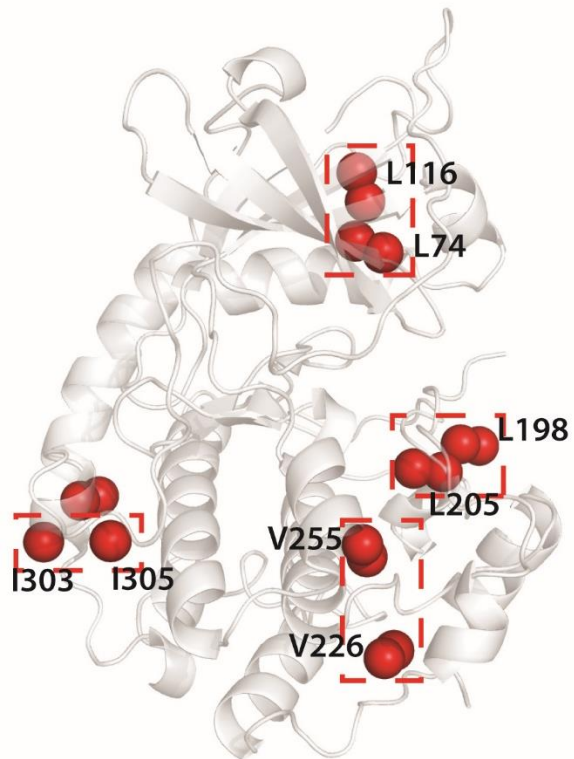
Figure 4.5: Distribution of mis-assigned methyl groups (red) resonances mapped on the crystal structure of PKA-C ternary complex with ATP and protein kinase inhibitor peptide (1ATP). The swapped assignments are indicated by red boxes.
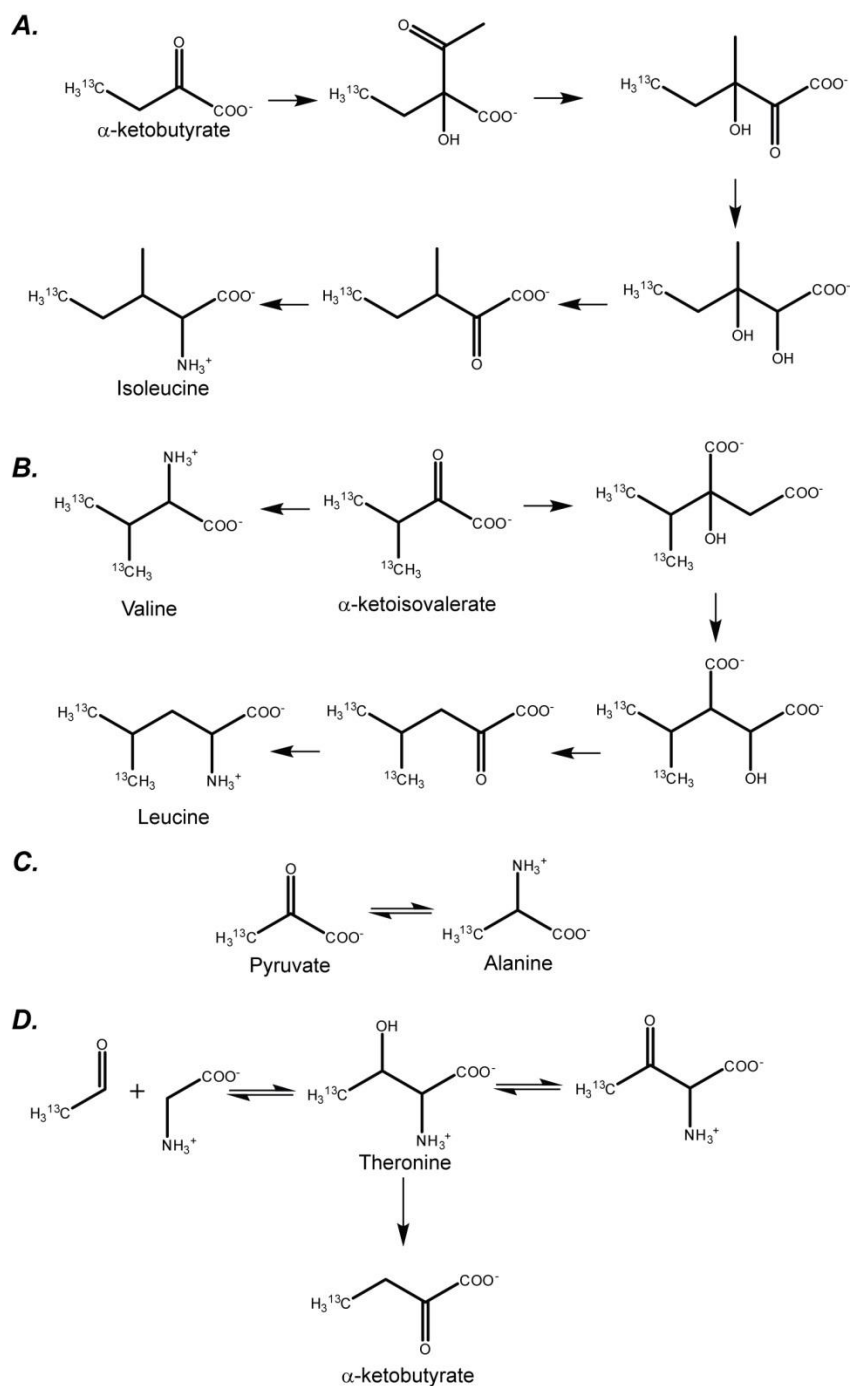
Figure 5.1: Biosynthetic pathways for the specific labeling of (A) isoleucine, (B) leucine and valine, (C) alanine, (D) methionine and (E) threonine. Note the off-pathway dilution of alanine and threonine amino acids.
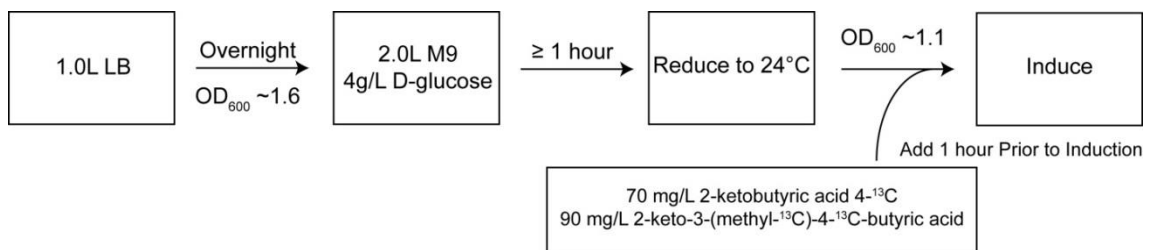
Figure 5.2: General growth scheme used to express ^{15}N ^{13}C-ILV labeled PKA-C. All cultures are grown in 32°C with induction occurring at 24°C. This is to prevent the formation of inclusion bodies during expression [344]. In M9 media, $^{15}NH_4Cl$ (1 g/L) and D-glucose (4 g/L) are used as the only nitrogen and carbon sources respectively.

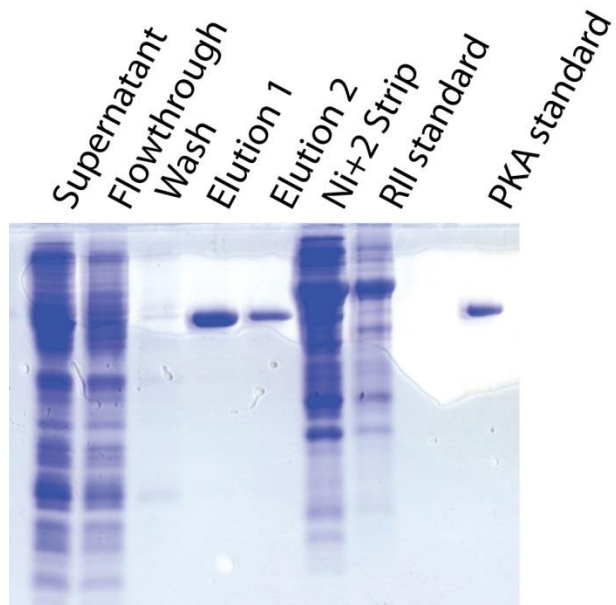**Figure 5.3**: SDS-PAGE of the purification of PKA-C using a His_6-RIIα immobilized construct.
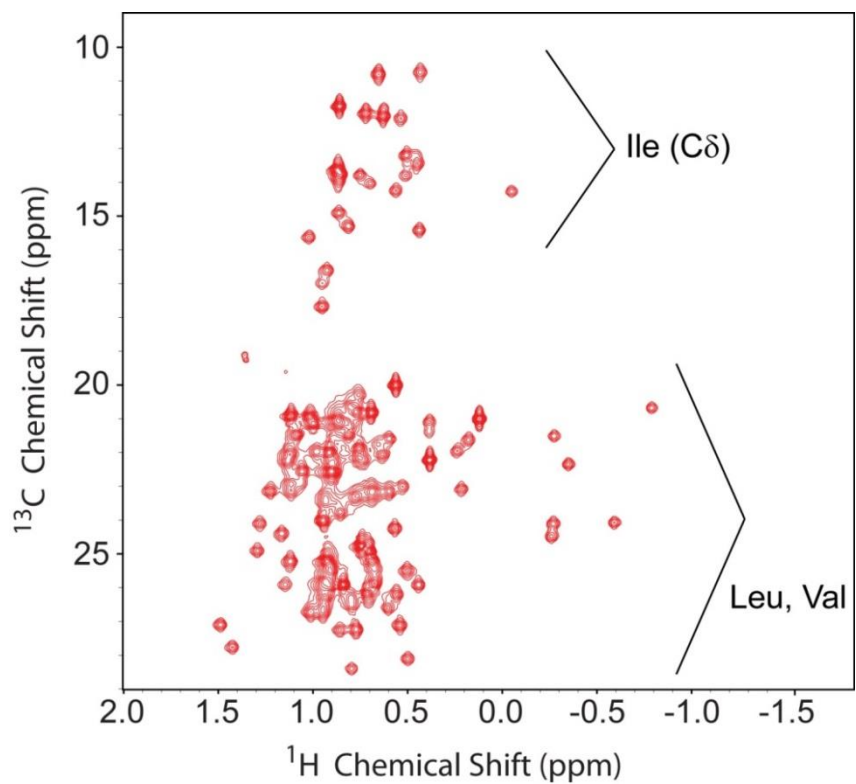
Figure 5.4: ^{13}C-HMQC of Apo PKA-C acquired with a 220 μM sample on an Avance III 900 MHz Bruker spectrometer. The spectrum was acquired with 2048 x 200 complex points and 16 transients at 27°C for a total acquisition time of approximately 1 ½ hours.
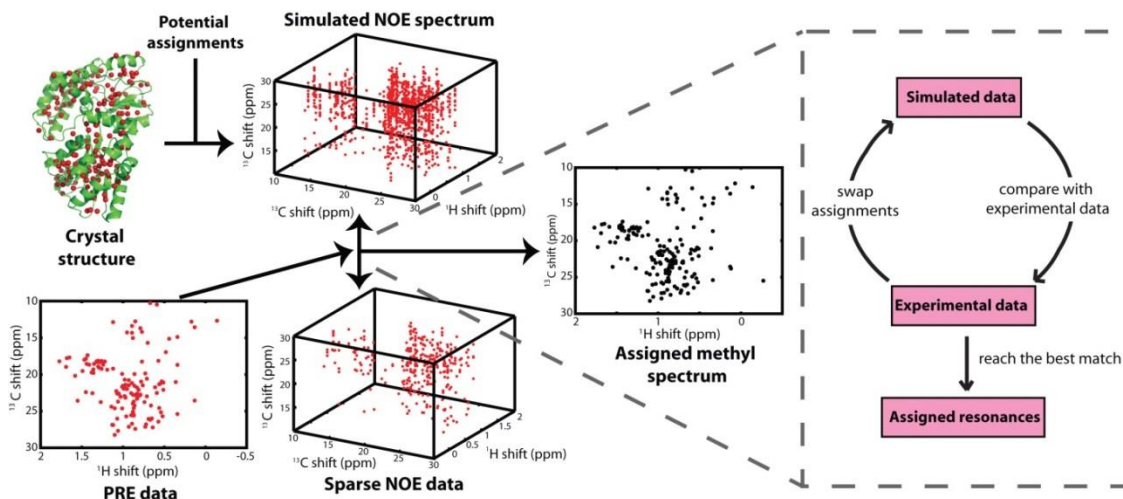
Figure 5.5: Overview of the FLAMEnGO algorithm. An input structure and the HMQC spectrum are used to simulate a NOE spectrum. This spectrum is compared with the experimental NOE data, the assignments swapped and the process is repeated until a best match is found. Other experimental restraints, such as PRE data, are used. Figure adapted from Chao, et al. [320]
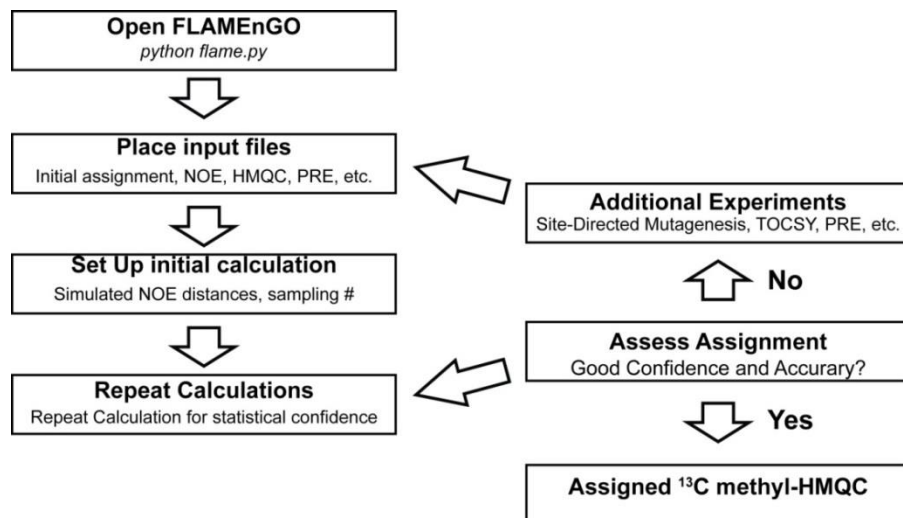
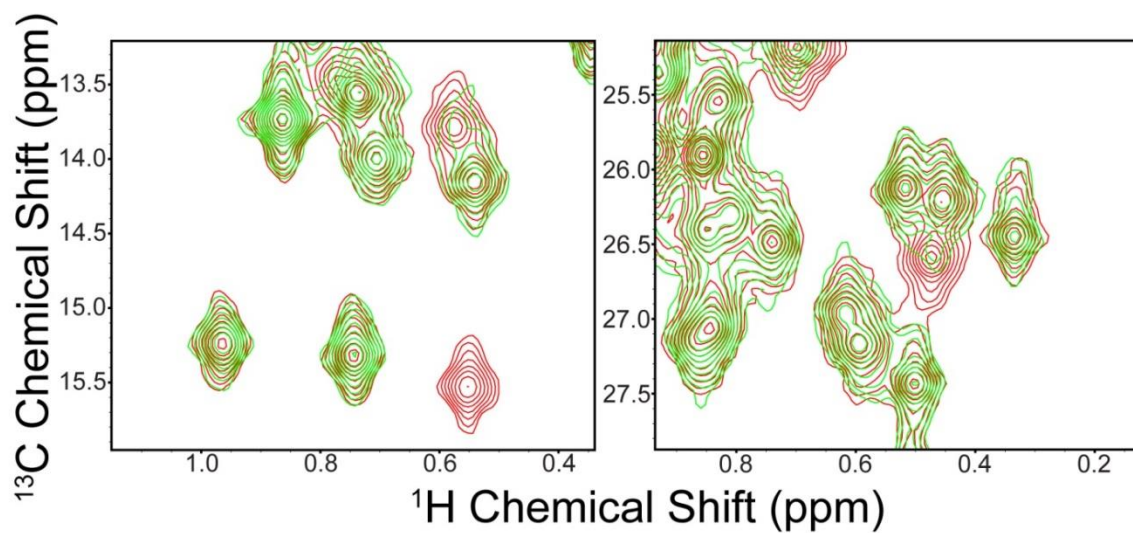**Figure 5.6**: Outline for running FLAMEnGO GUI.

Figure 5.7: Spectra of oxidized (green) and reduced (red) PKA-C with a spin label on residue 244. Note the spectrum should be nearly identical before and after the reduction of the spin label.
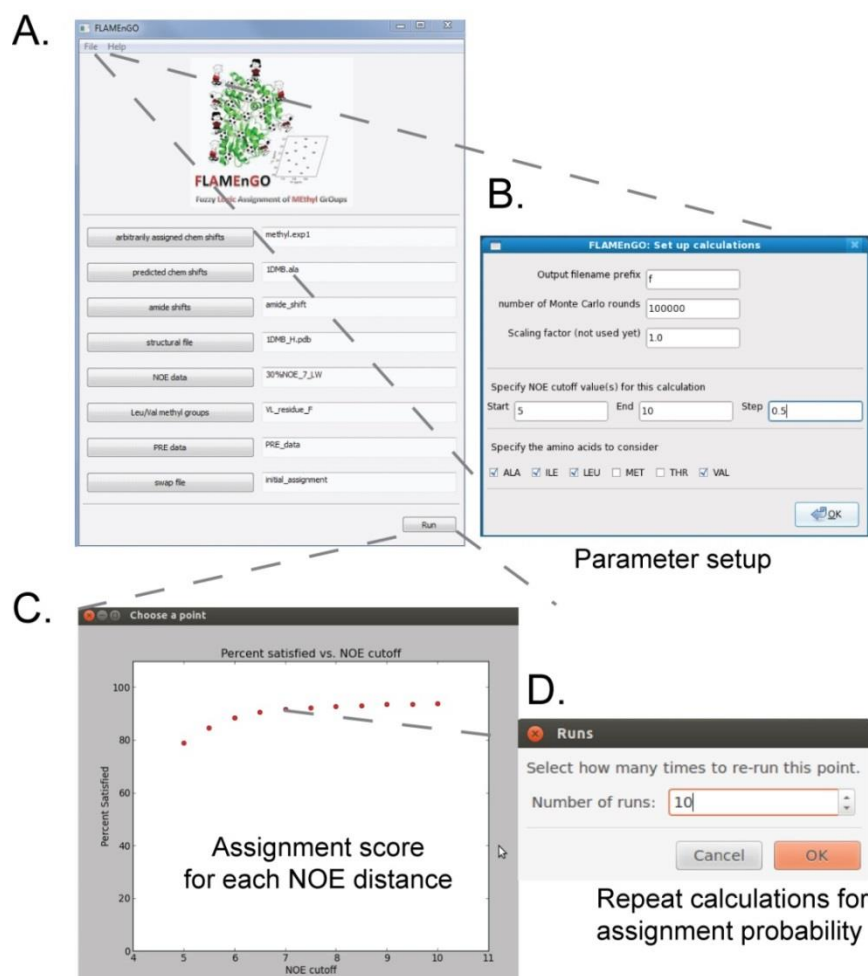
Figure 5.8: Graphical Interface for FLAMEnGO. (A) Main menu of FLAMEnGO. Input files are directly placed inside the selection. (B) Parameter set up for the NOE distances, amino acid types you wish to assign, and the number of Monte Carlo steps. (C) Output from the run. Note that the program performs the calculation at each NOE distance. (D) Once the score has plateaued from increasing the NOE distance, select the point and repeat the calculation at this distance to provide a statistical assignment of each residue. Figure adapted from [350]
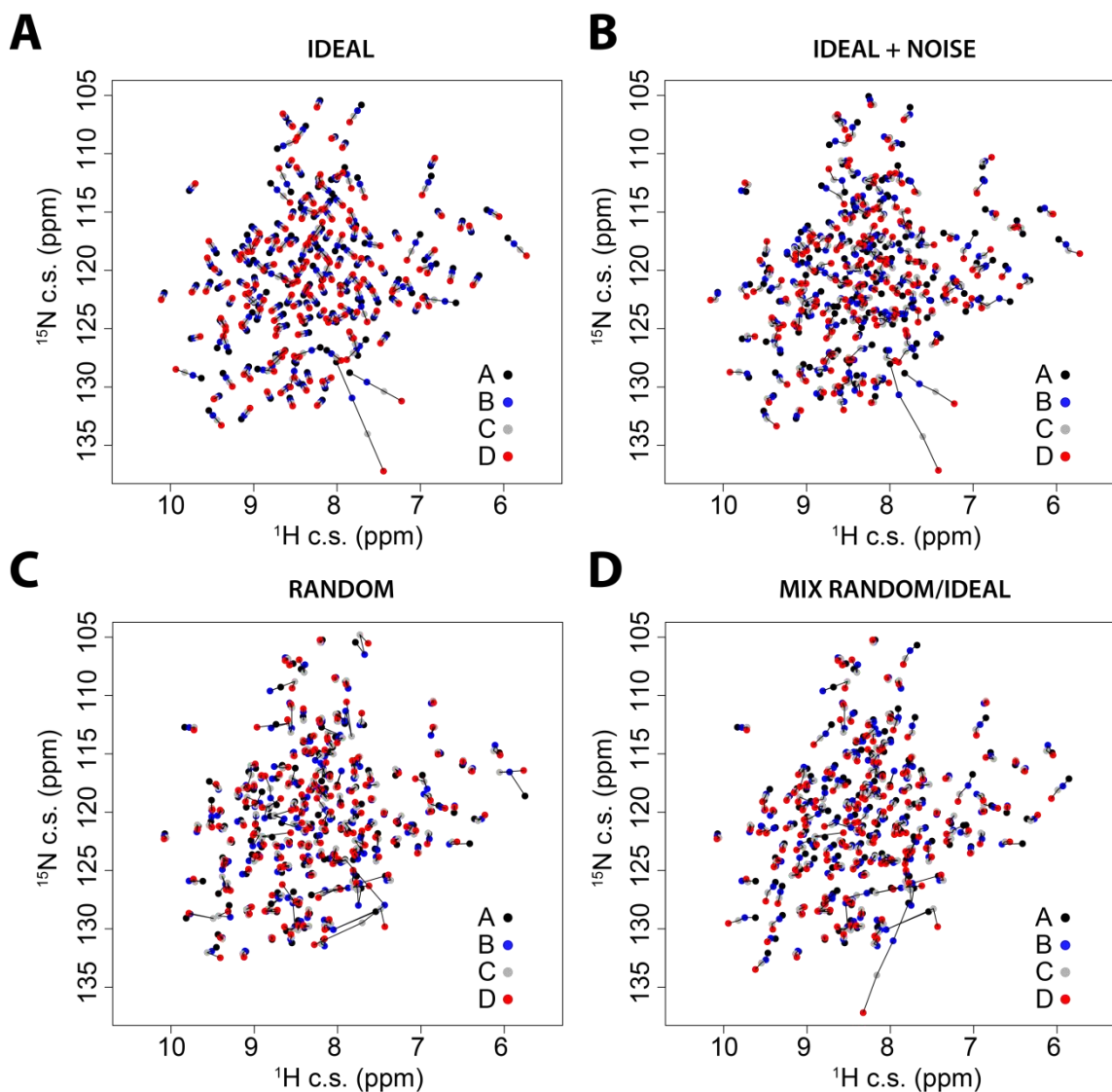
Figure 6.1: Synthetic [^{1}H,^{15}N]-HSQC spectra mimicking possible chemical shift perturbations upon ligand binding. (A) ideal case (perfect linear correlations); (B) ideal case with the addition random of noise; (C) completely random behavior of the chemical shifts; (D) mixed case, where half of the peaks follow random chemical shift trajectories and the other half follow linear behavior with noise added. For each spectrum, the trajectories of the chemical shifts for the four states (A, B, C, D) are connected with black lines.
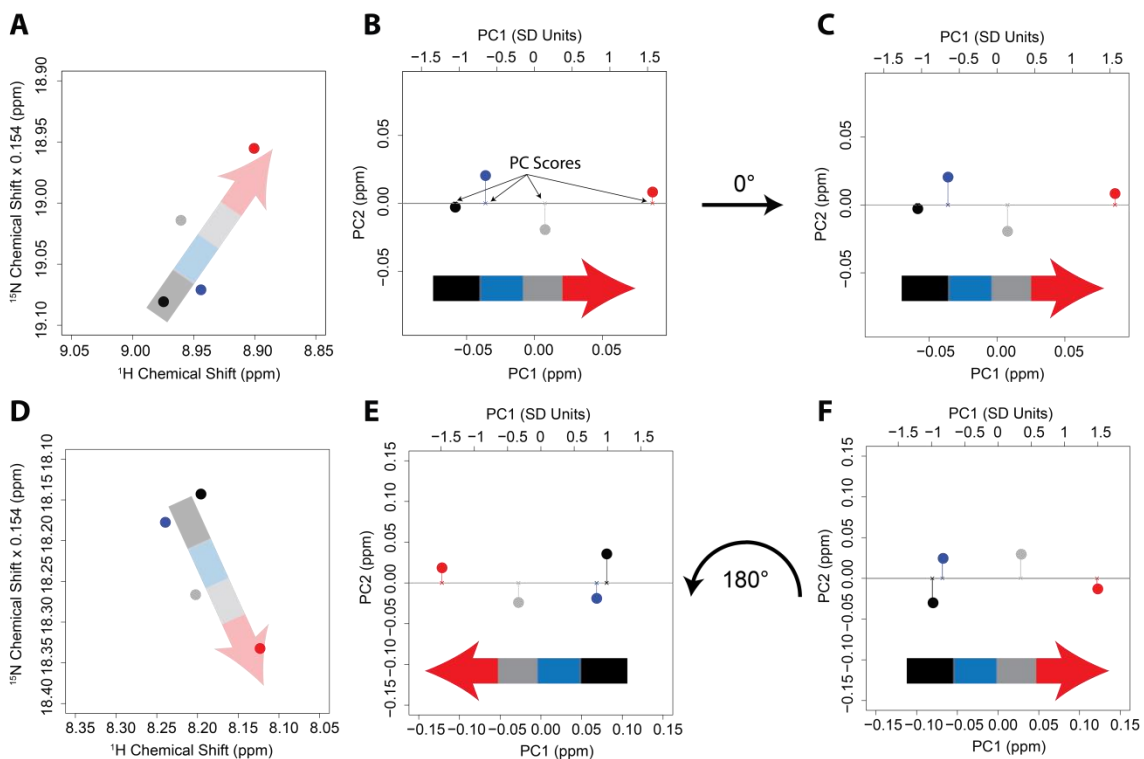
Figure 6.2: Graphical representation of the PCA of the linear chemical shift trajectories. PCA is applied to the chemical shifts of two residues for the *ideal+noise* case. Panels **A** and **D** show a close-up of the peaks positions in the synthetic [^{1}H,^{15}N]-HSQC spectra. The data projected along the two principal components are shown before (panels B and E) and after (panels C and F) orientation. For PC1, the top scale shows the projection normalized to one standard deviation.
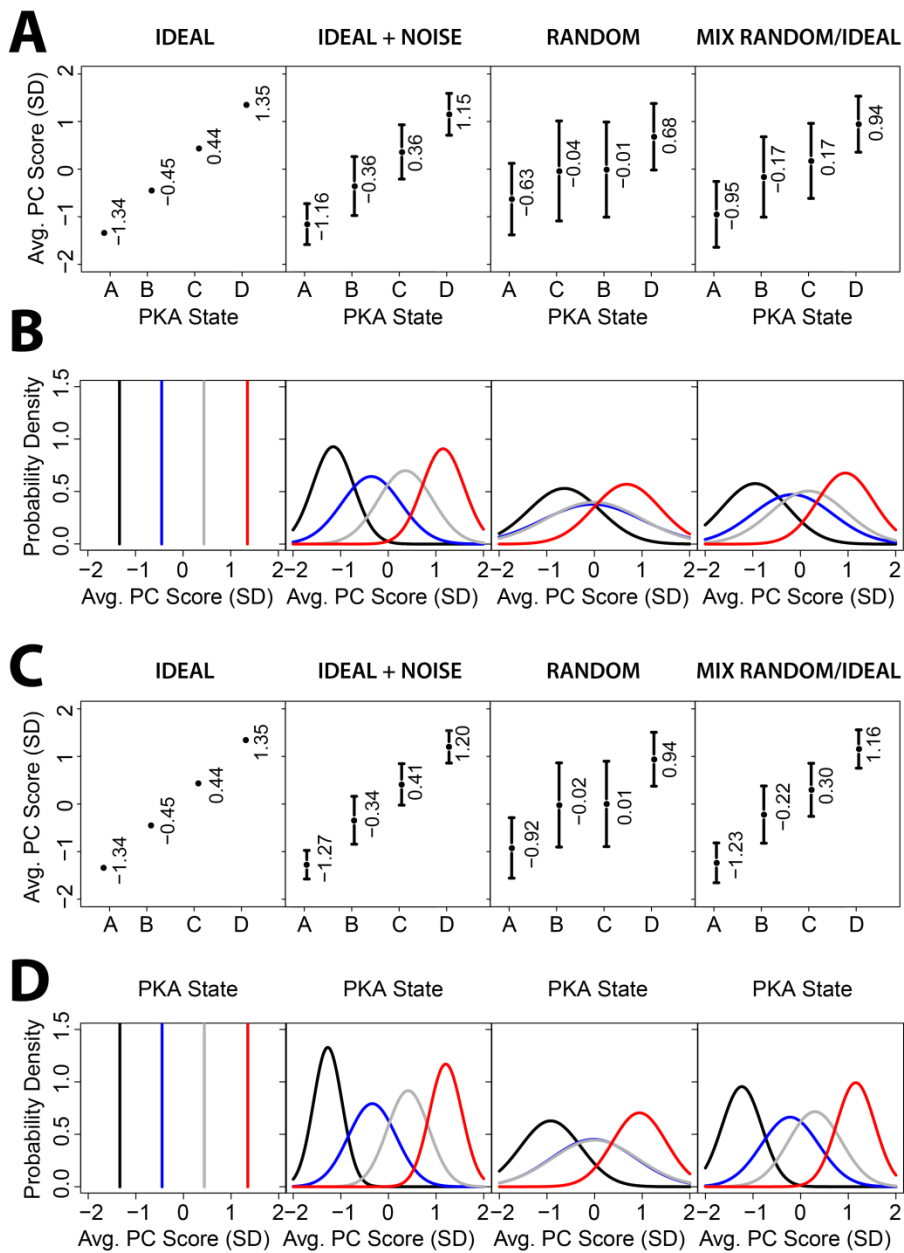
Figure 6.3: Application of the CONCISE method to four synthetic data sets represented in Fig. 1. (A) Average PC scores versus the different states (A, B, C, and D) for all residues. The mean equilibrium values (circles) and standard deviations (vertical bars). (B) Normal distributions for the residues around the mean values. (C) Average PC scores versus the different states plotted for the subset of residues showing linear trajectories. (D) Normal distributions for the case C for linear residues.
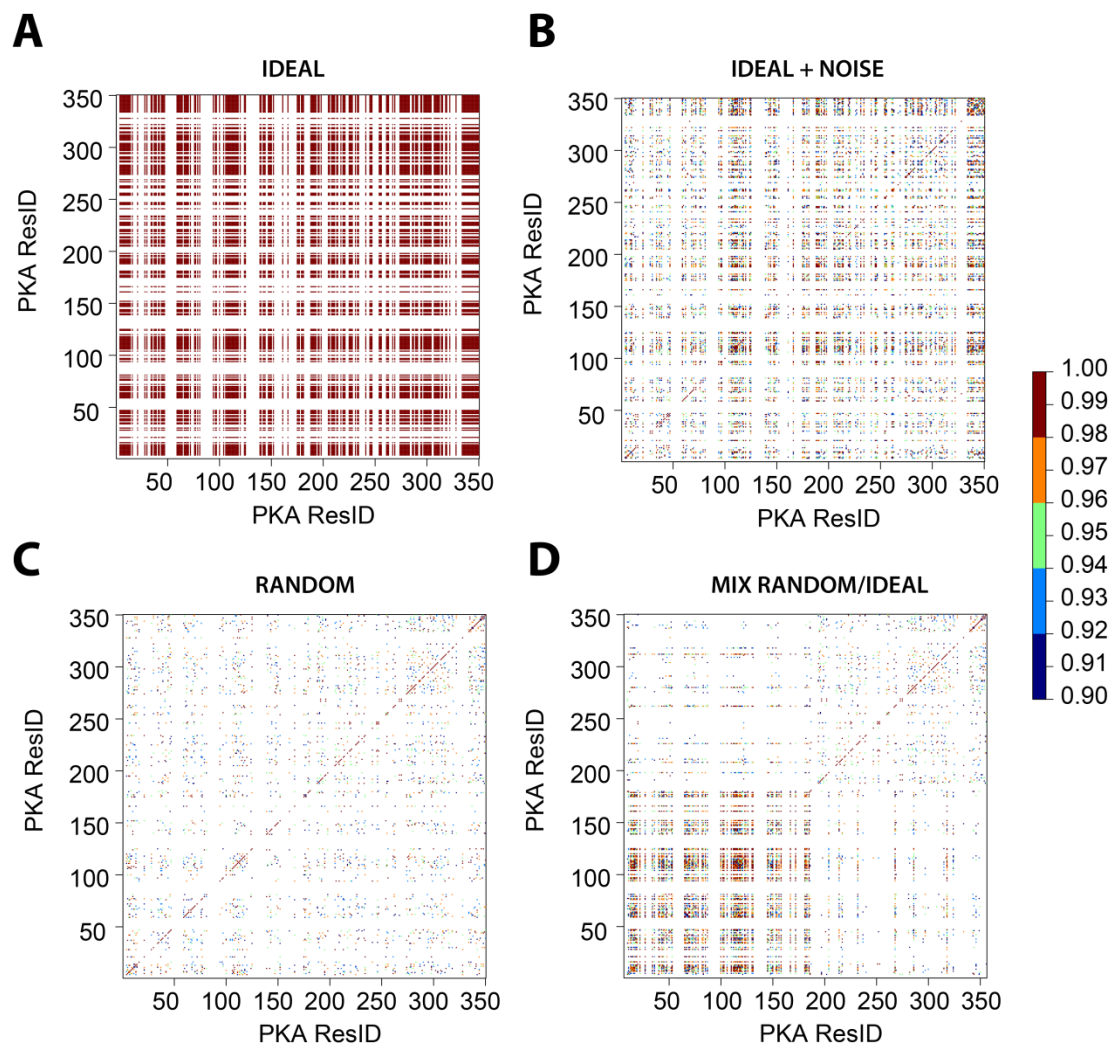
Figure 6.4: PCA correlations for the four synthetic states. The correlation coefficients between the PC1 scores for all residues are plotter using a scale showing only correlations higher than 0.9.
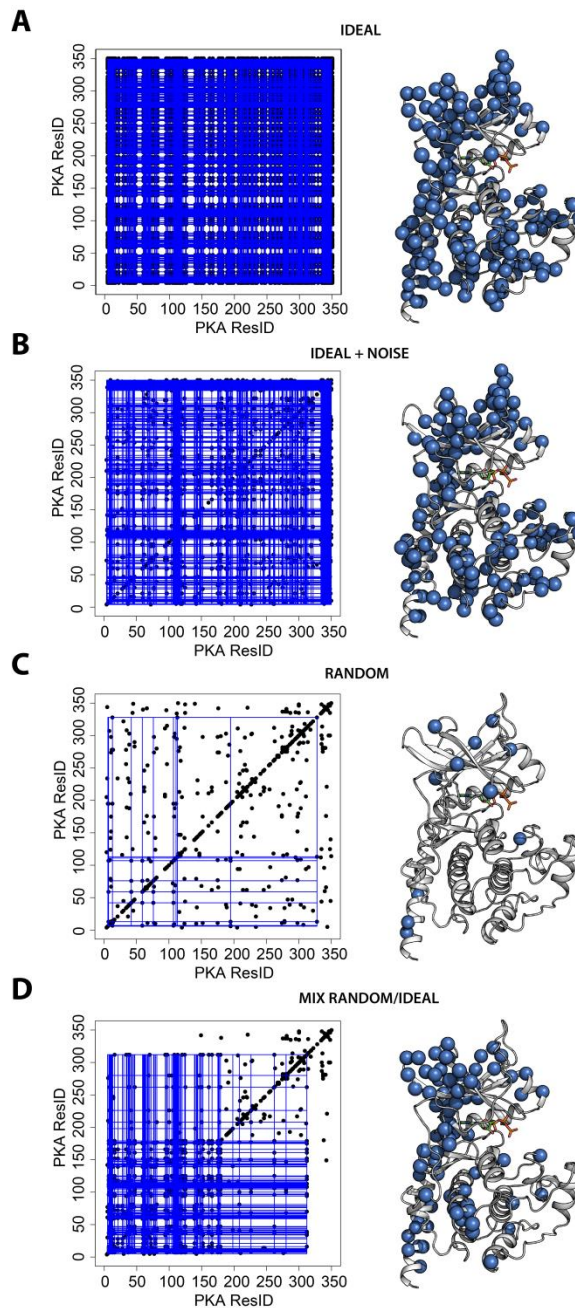
Figure 6.5: Correlation-Matrix as part of the CHESCA analysis for four synthetic states. On the matrix (left panel), the largest cluster resulting from hierarchical clustering (correlation cutoff of 0.99) is indicated with blue lines and mapped on the crystal structure of the kinase using blue spheres.
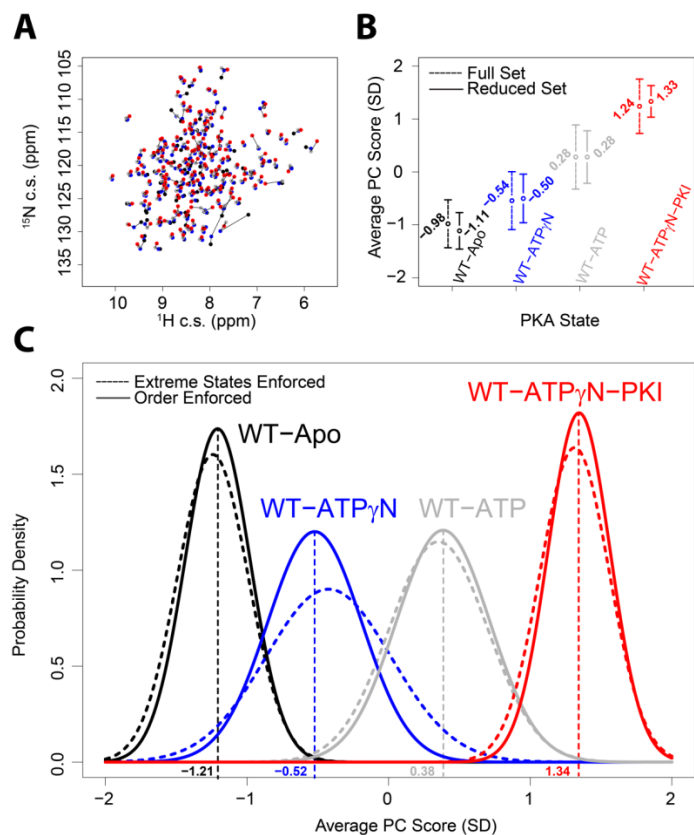
Figure 6.6: CONCISE analysis applied to the kinase experimental data. (A) Superposition of the kinase resonances of [^{1}H,^{15}N]-HSQC spectra for the four states with peak positions shown as dots of different colors connected by black lines. (B) The equilibrium position analysis for PKA-C four states is shown as circles and vertical bars, representing averages and standard deviations, respectively. Dotted lines show the results obtained using all available residues, and solid lines refer to the reduced set of residues. (C) The equilibrium positions for the reduced set of residues are plotted as normal distributions centered in the average and with width given by the standard deviation. Dotted lines display the results obtained by discarding all the residues for which the apo and closed states are not the two extremes; solid lines show the results obtained by discarding all residues in which the states are not in following the apo-ATPγN-ATP-closed order.
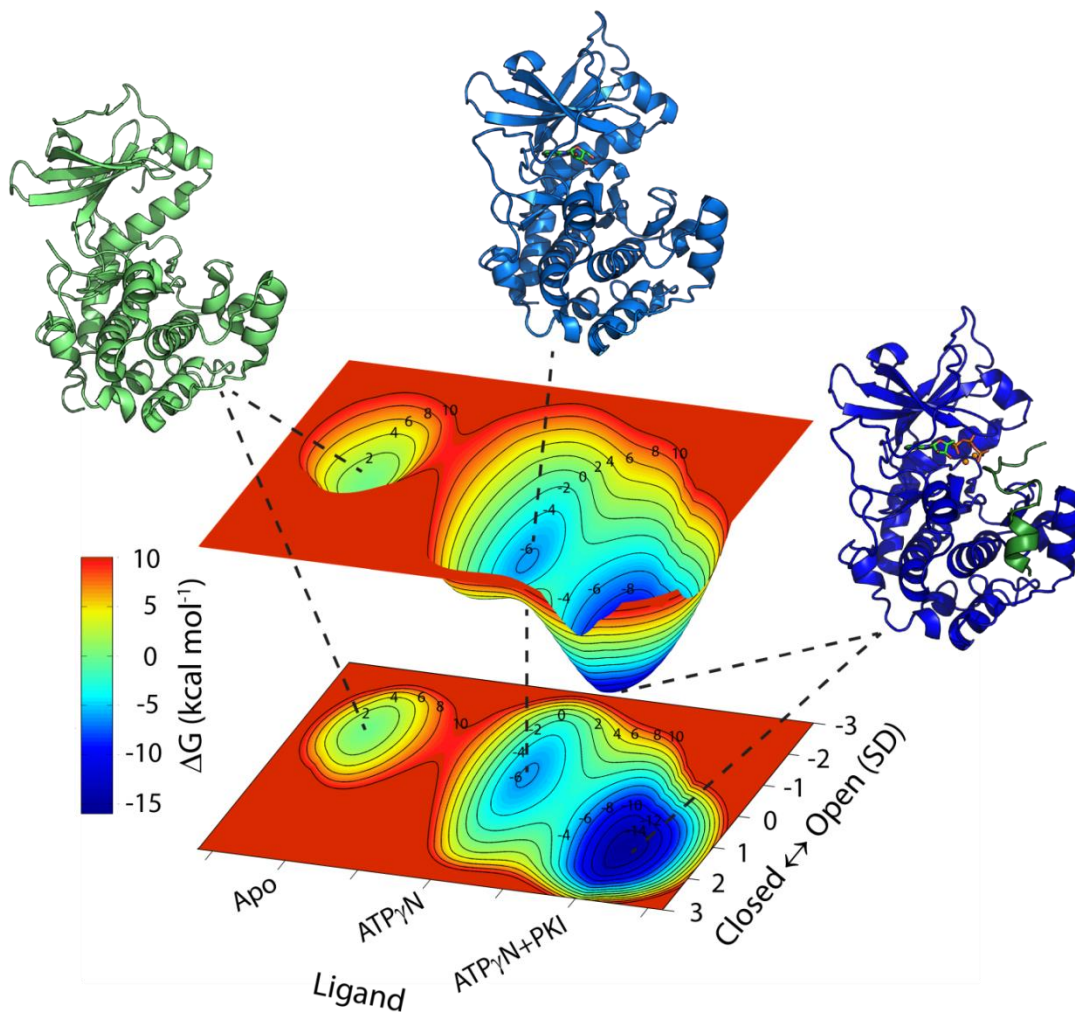
Figure 6.7: PKA-C free energy landscape. The PKA-C free energy profile is shown along the ligand binding and along the open/closed reaction coordinates. The Apo state is shown in green (pdb code 1J3H), the binary form in cyan (1BKX), and the ternary complex in blue (1ATP).
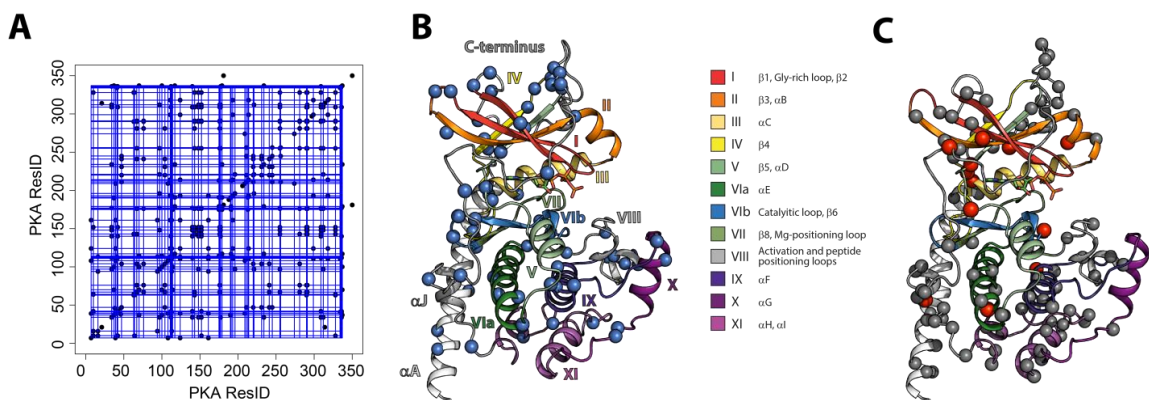
Figure 6.8: PKA-C Collective Behavior. (A) The largest cluster of correlated residues in the linear data set obtained with a cutoff of 0.99 is shown as blue lines on a matrix representation. (B) The largest correlated cluster is mapped onto the kinase structure as blue spheres. (C) The residues that do not follow linear paths are shown as grey spheres, and in red are highlighted those characterized by large chemical shifts perturbations.
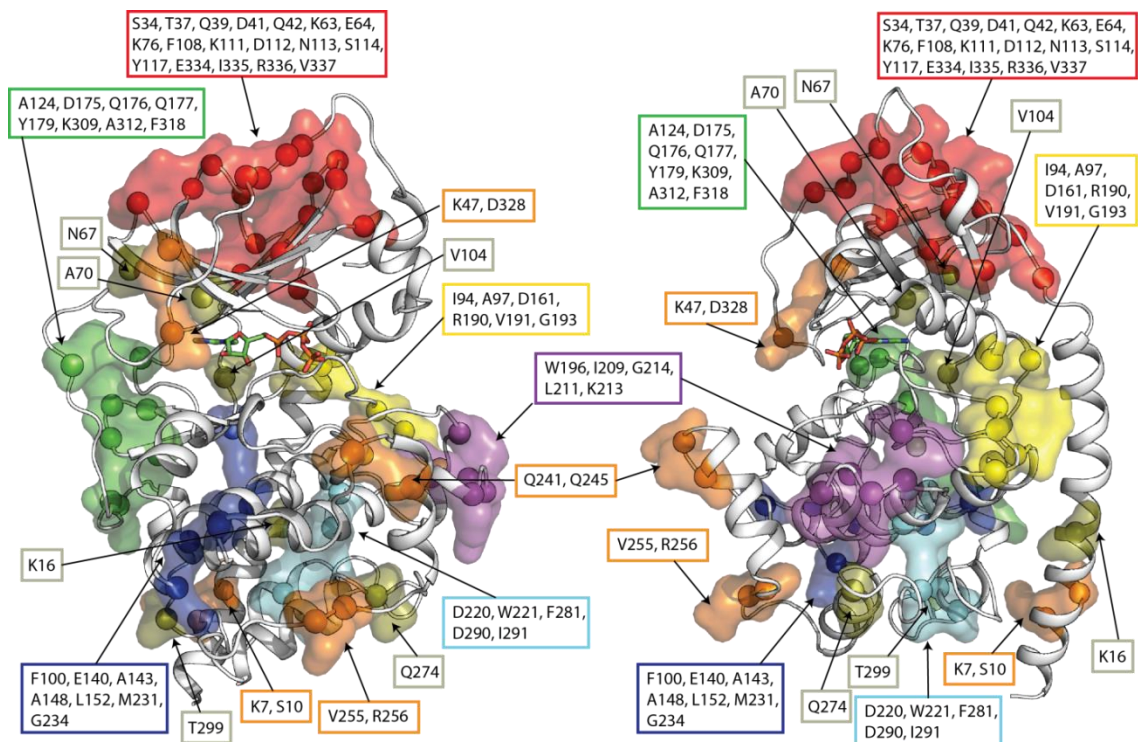
Figure 6.9: Contiguous and non-contiguous allosteric pathways. The groups of spatially connected residues within the largest correlated cluster are shown in colors (red, green, blue, yellow, magenta, and cyan). Pairs of spatially connected residues are shown in orange, while spatially isolated residues are shown in olive green.
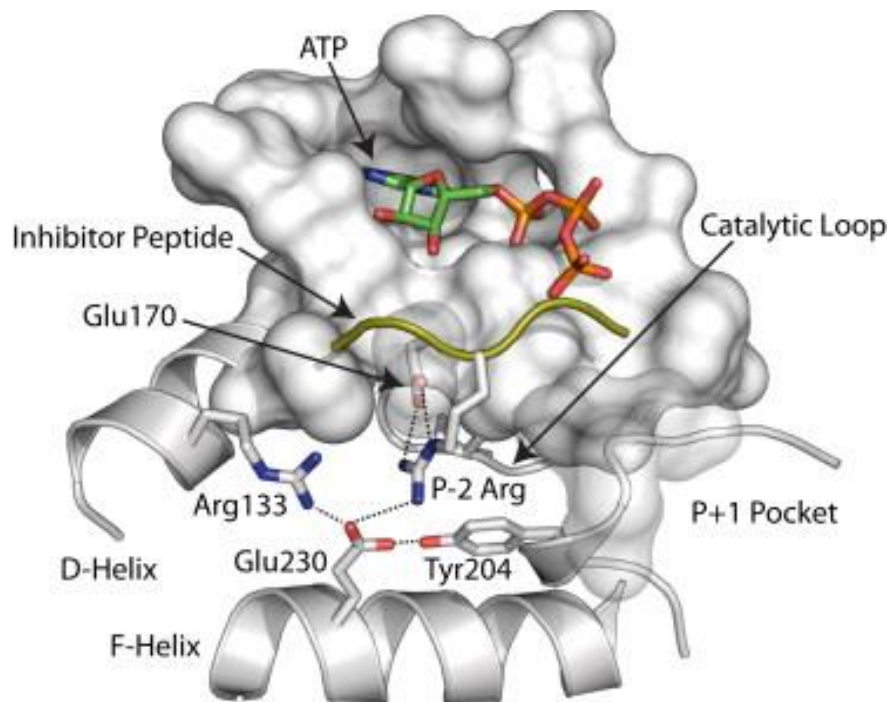
Figure 7.1: Electrostatic node Y204 mapped on the crystal structure (PDB: 1ATP). The mutation is located approximately at 15 Å from the active site and does not involve direct interactions with the substrate.
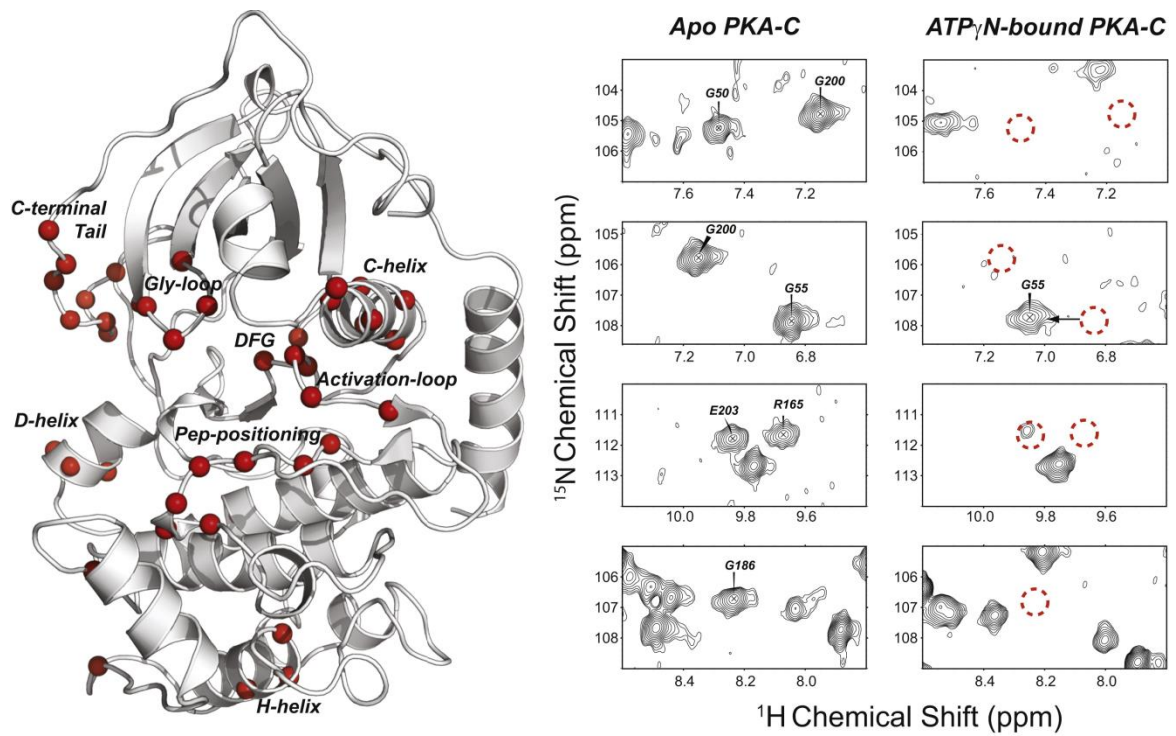
Figure 7.2: Residues broadened in PKA-C[WT] upon binding of ATPγN. Several broadened residues are located close to the active site (Gly-rich loop, DFG loop, C-helix, acidic residues in the C-terminal tail), others are distant (Peptide-positioning loop, activation loop, D and H helices).
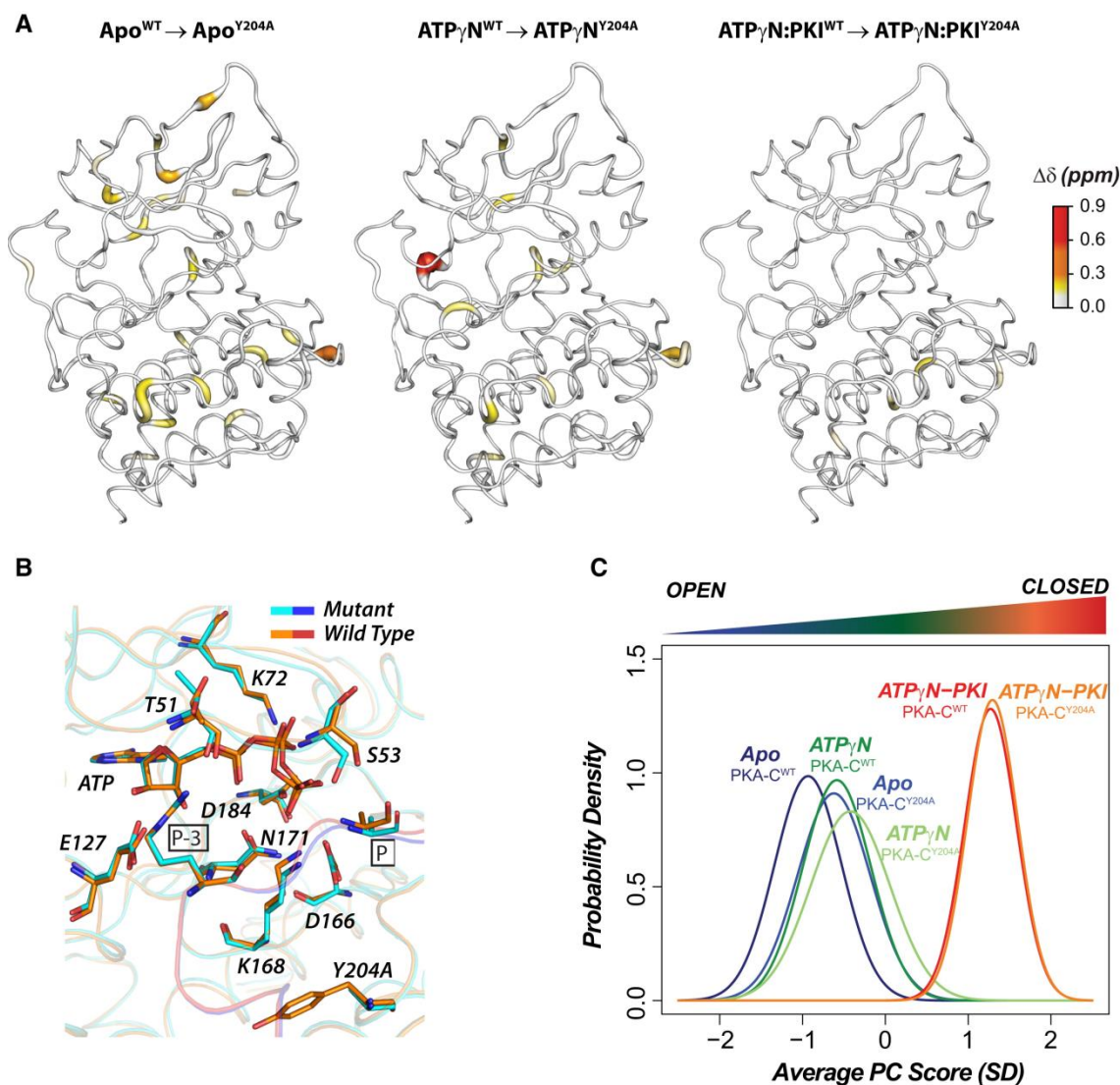
Figure 7.3: Chemical shift differences between PKA-C^{WT} and PKA-C^{Y204A} for Apo, ATPγN-bound and ternary (ATPγN and PKI$_{5-24}$-bound). (A) ^{1}H,^{15}N combined chemical shift differences mapped on the corresponding X-ray structures (B) Superposition of the active sites in the crystal structures of PKA-C^{WT} (orange/red) and PKA-C^{Y204A} (cyan/blue). C. CONCISE analysis of amide resonances.
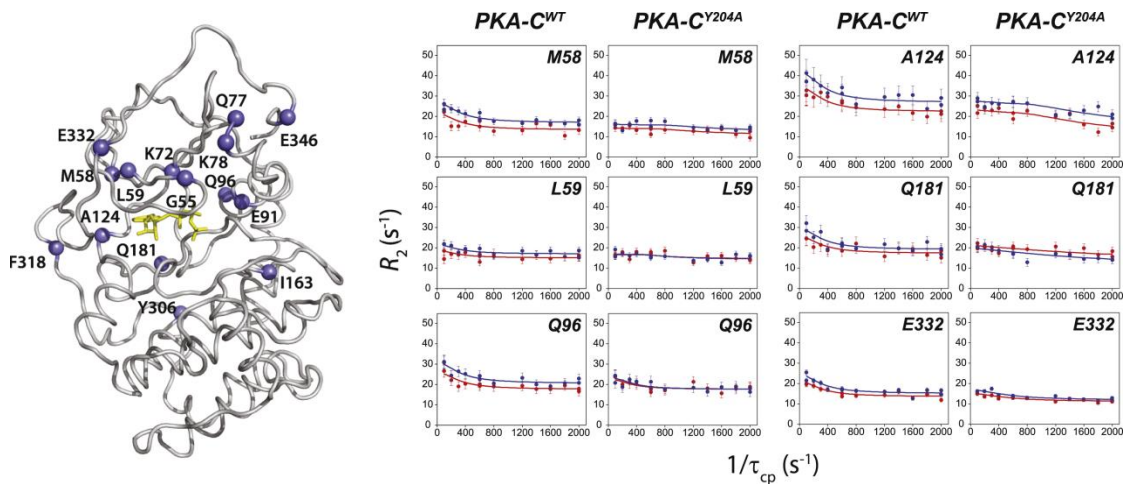
Figure 7.4: Conformational motions in the slow timescale probed by ^{15}N CPMG relaxation dispersion. Left: residues showing concerted motions in the wild-type enzyme are mapped on the structure. Right: ^{15}N CPMG dispersion curves for residues of PKA-C^{WT} and PKA-C^{Y204A} reveal a change in the nature of the dynamics upon Y204A mutation.
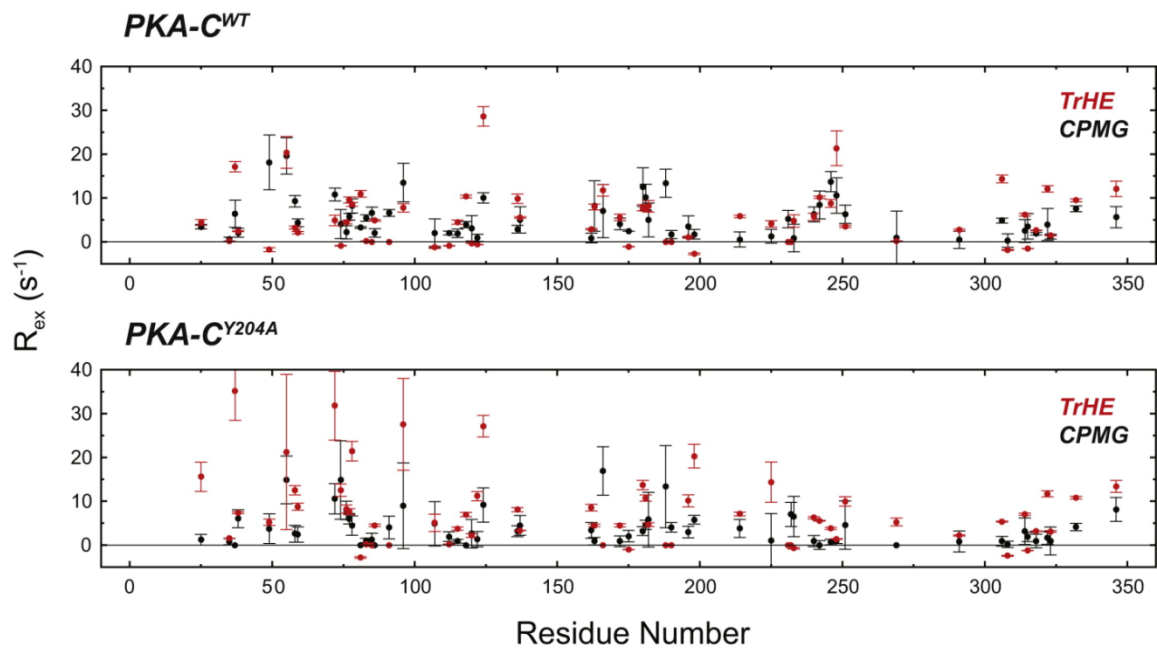
Figure 7.5: Comparison of the R_{ex} measured by CPMG relaxation dispersion and TrHE.

Only the residues with both CPMG and TrHE values are compared.
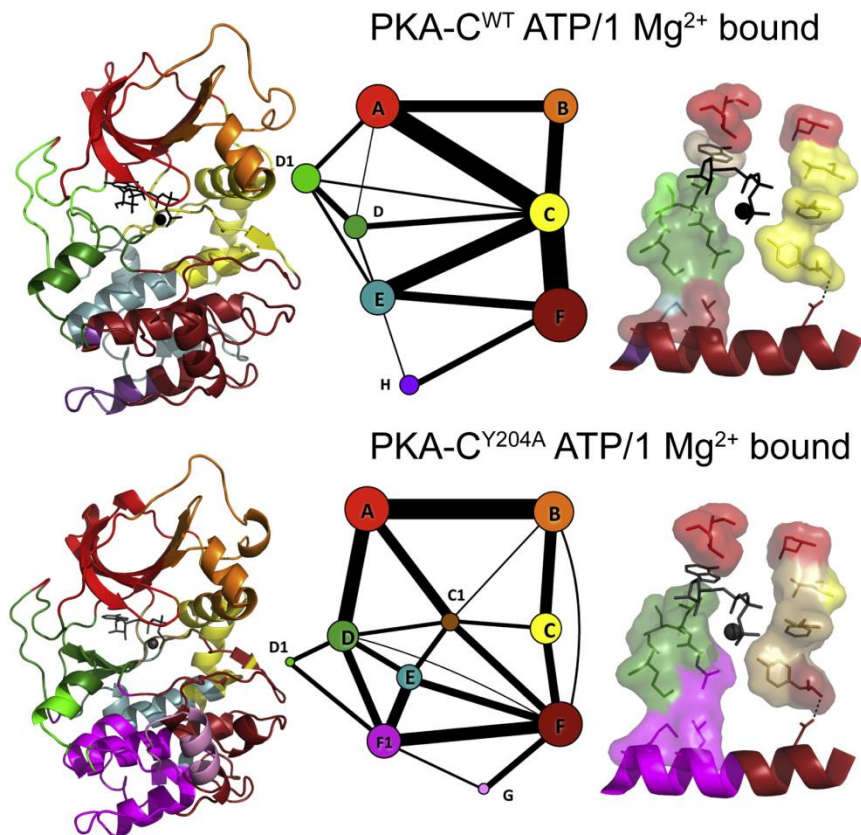
Figure 7.6: Molecular dynamics simulations (5-6 μs) community analysis of PKA-C^{WT} and PKA-C^{Y204A}. Left: The community map is colored on the structure. Middle: A graph representation of the community map where the thickness of the lines connecting the communities indicates the presence of correlation of the motions. Right: The C-spine and R-spine anchored to the F-helix. Y204A mutation disrupts semi-rigid communities and causes the dihedral populations to shift in a number of areas related to activation, ATP-binding, and substrate binding. Definition of the communities: ComA: ATP binding and substrate coordination; ComB: αC-helix adjusting; ComC: regulatory and assembly the R spine; ComD: ATP binding and catalytic site; ComE: C-spine supporting; ComF: Activation and substrate binding. ComF1 and ComG: substrate binding.
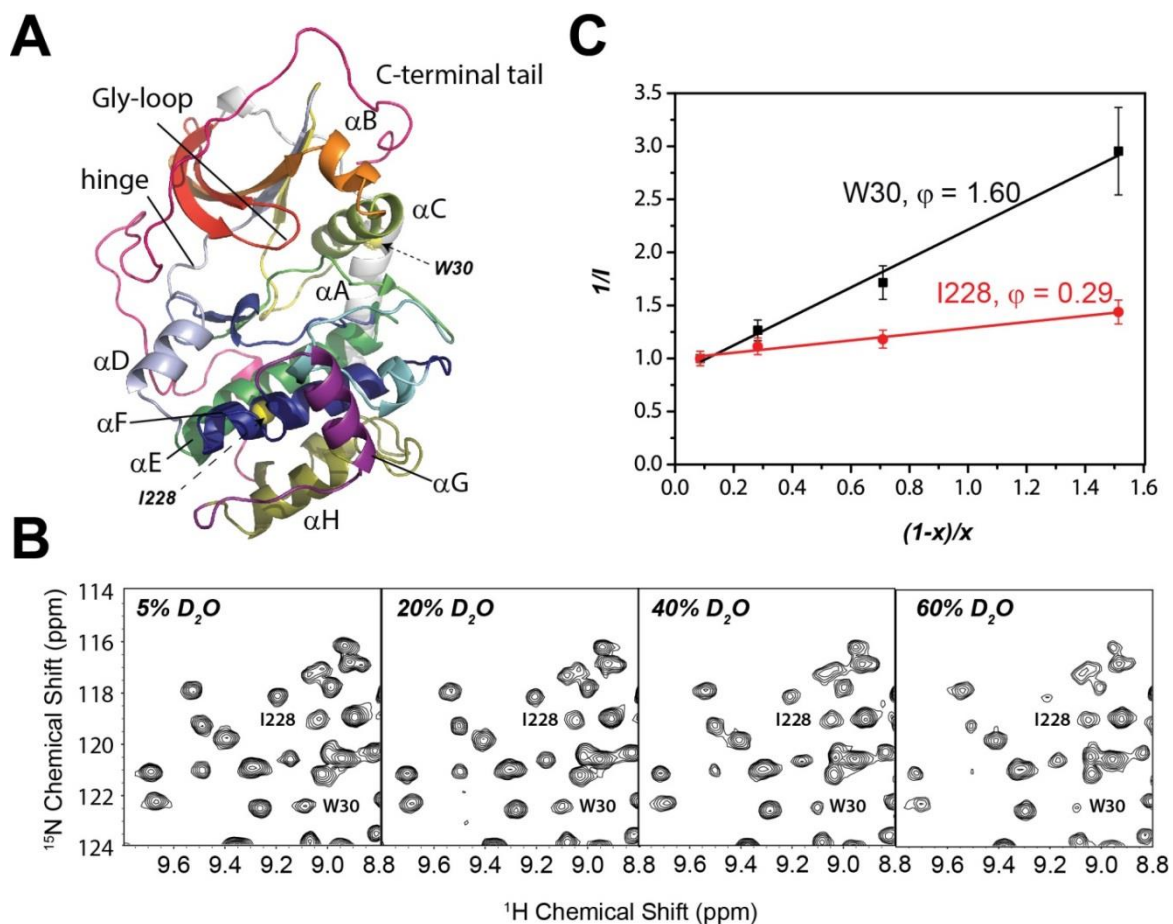
Figure 8.1: Determination of fractionation factors. (A) Structural motifs mapped onto the ternary complex of PKA-C (PDB ID: 1ATP). (B) Representative portions of the [^{1}H, ^{15}N]-TROSY-HSQC spectra for apo PKA-C at various concentrations of D_2O, highlighting W30 and I228 located in helical domains of the kinase. (C) Linear least-squares fit of the inverse of intensities for W30 and I228 versus (1-x)/x, where x is the mole fraction of H_2O.
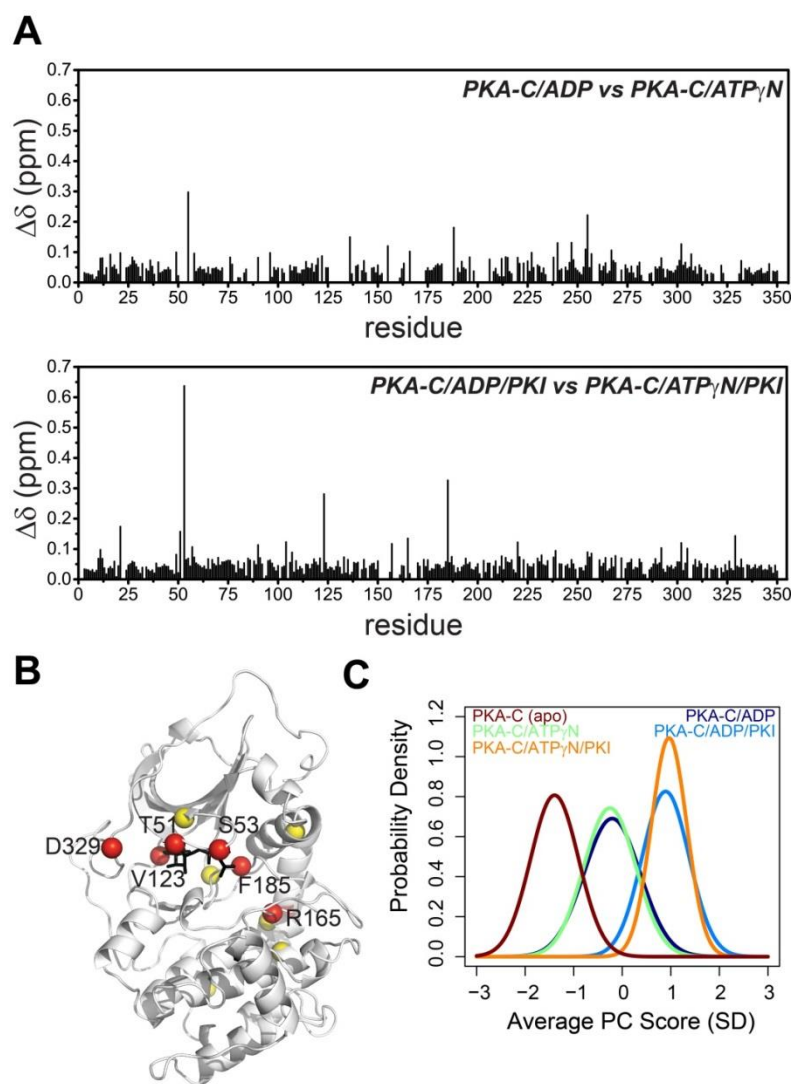
Figure 8.2. (A) Plots of the chemical shift changes upon addition of ADP and ATPγN (top) and. ADP/PKI$_{5-24}$ and ATPγN/PKI$_{5-24}$ (bottom). (B) Most significant chemical shift differences mapped onto the structure of PKA-C, PDB: 1ATP. Red spheres indicate residues with $\Delta\delta$ greater than one standard deviation from the mean (i.e. $\Delta\delta > 0.12$); yellow spheres are residues with $\Delta\delta > 0.10$. (C) CONCISE analysis[42] of the amide chemical shifts showing that the average conformations of the binary and ternary complexes using ADP as nucleotide are similar to their ATPγN counterparts.
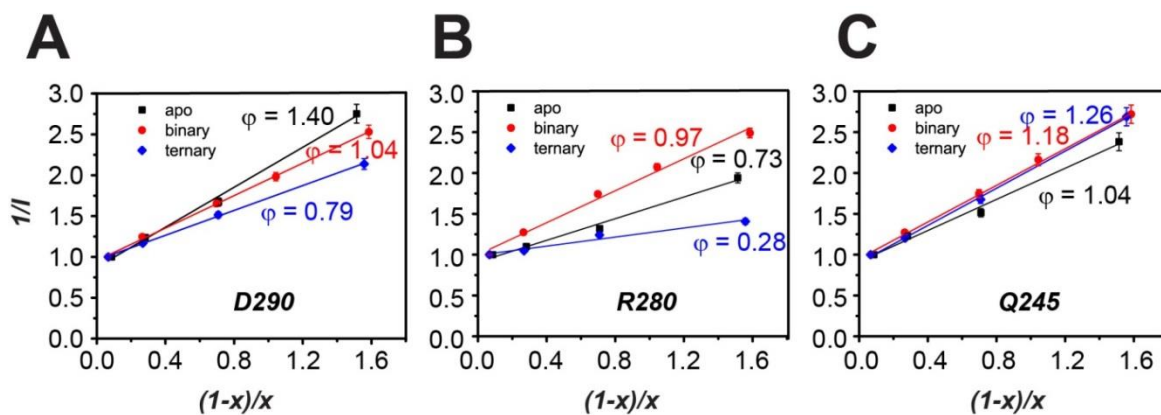
Figure 8.3: Representative least-squares fitting of residues showing different types of changes in hydrogen bond strengths upon binding nucleotide and pseudo-substrate.
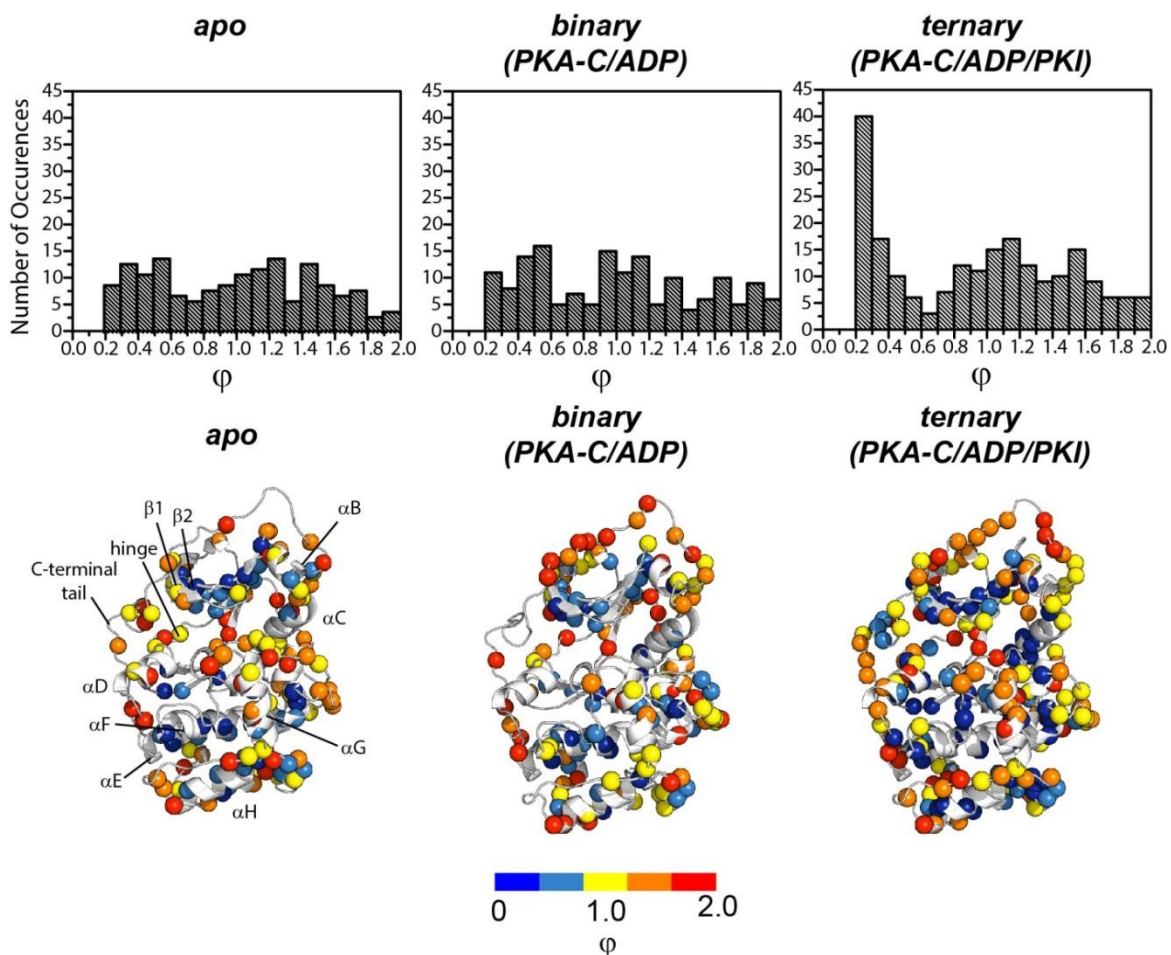
Figure 8.4: Distribution of the amide fractionation factors in three major states of PKA-C. Histogram of the occurrences vs fractionation factor values (top panel). Mapping of the fractionation factors on the PKA-C structure (lower panel, PDB ID: 1ATP). The amide groups are represented as spheres and color-coded according to the spectrum bar (Blue: strong hydrogen bonds, high φ values; Red: weak hydrogen bonds, low φ values).
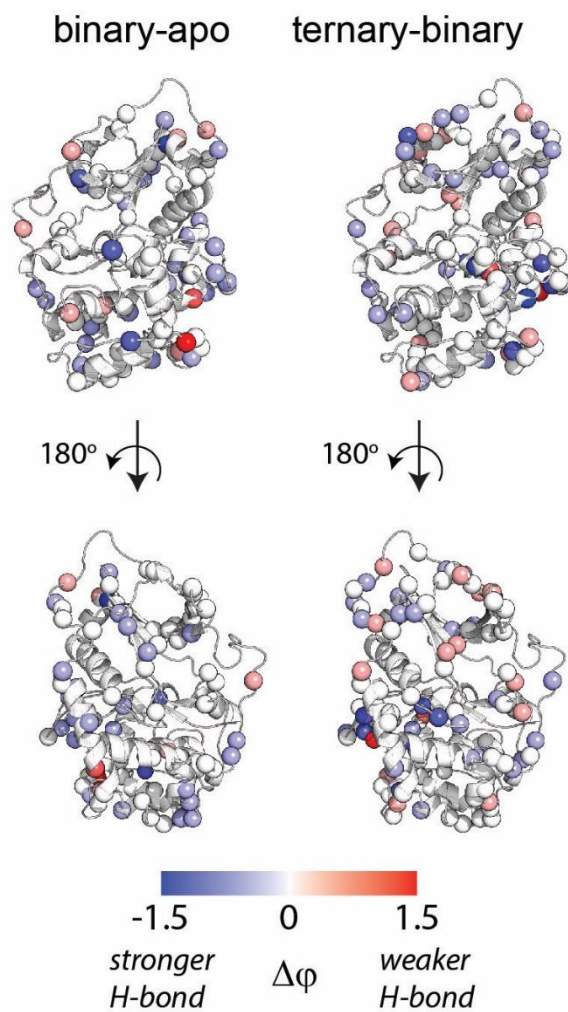
Figure 8.5: Differences in the fractionation factor between apo and binary (left), and binary and ternary complexes (right) of PKA-C mapped onto the PKA-C structure.
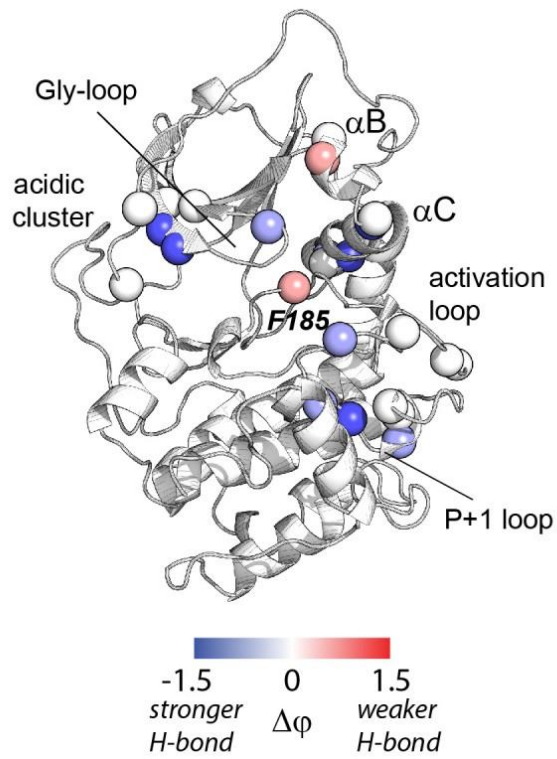
Figure 8.6: The difference in fractionation factor between apo and ternary complexes for the residues that were exchange-broadened upon ADP binding.

Figure 9.1: Molecular interactions between PKA-C and peptide substrates or inhibitors. (A) Primary sequence of the wild-type and R14del peptides corresponding to the cytoplasmic region of PLN and the high affinity peptide inhibitor, PKI_{5-24}. (B) X-ray structure of PKA-C (PDB:1ATP) with the architecture of the peptide binding site, with the electrostatic network of interactions between enzyme and substrate.

Figure 9.2: Thermodynamics and kinetics for PLN^{WT}_{1-19} and PLN^{R14del}_{1-19} **(A)** Thermodynamics of PLN^{WT}_{1-19} and PLN^{R14del}_{1-19} to PKA-C without (apo) or with nucleotide (ATPγN) present. (B) Steady-state phosphorylation kinetics of PLN^{WT}_{1-19} and PLN^{R14del}_{1-19} (C) Gel shift assays with the extent of phosphorylation for pentameric PLN^{WT} and PLN^{R14del}. Note that PLN^{WT} and PLN^{R14del} oligomerize into stable homo-pentamers and run on SDS-PAGE gels with an apparent molecular weight of ~36 kDa[537].
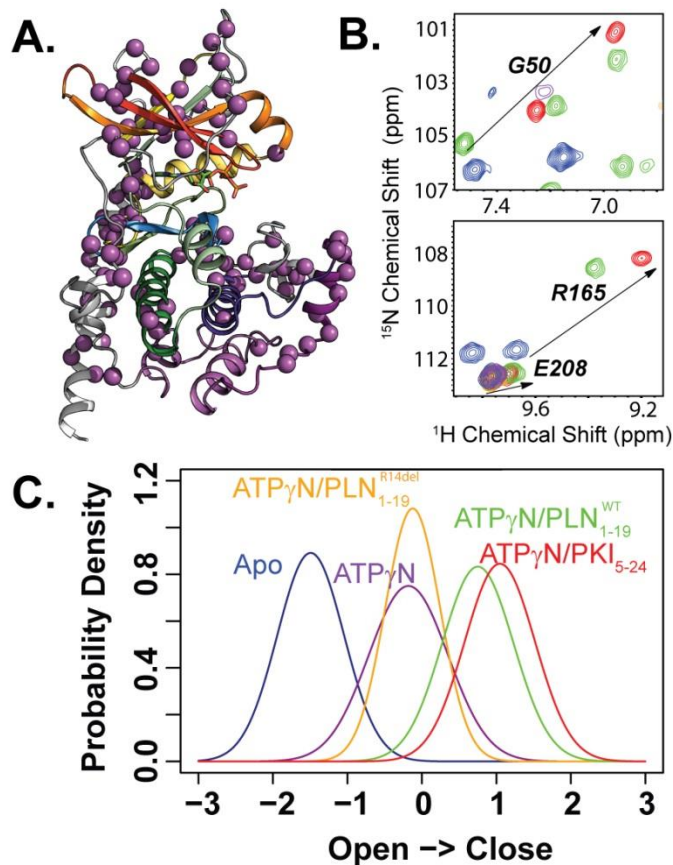
Figure 9.3: Shift in conformational equilibria by substrate binding (A) Colored (purple) residues which undergo concerted chemical shift changes upon ligand biding from the CONCISE and CHESCA analysis. (B) Ligand binding gives linear chemical shift changes from Apo (blue), Nucleotide bound (purple), substrate bound (green) to inhibiter bound (red). (C) Probability density plot of the different conformational states obtained using the CONCISE method. Ligand binding shifts the conformation equilibrium from open to closed states.
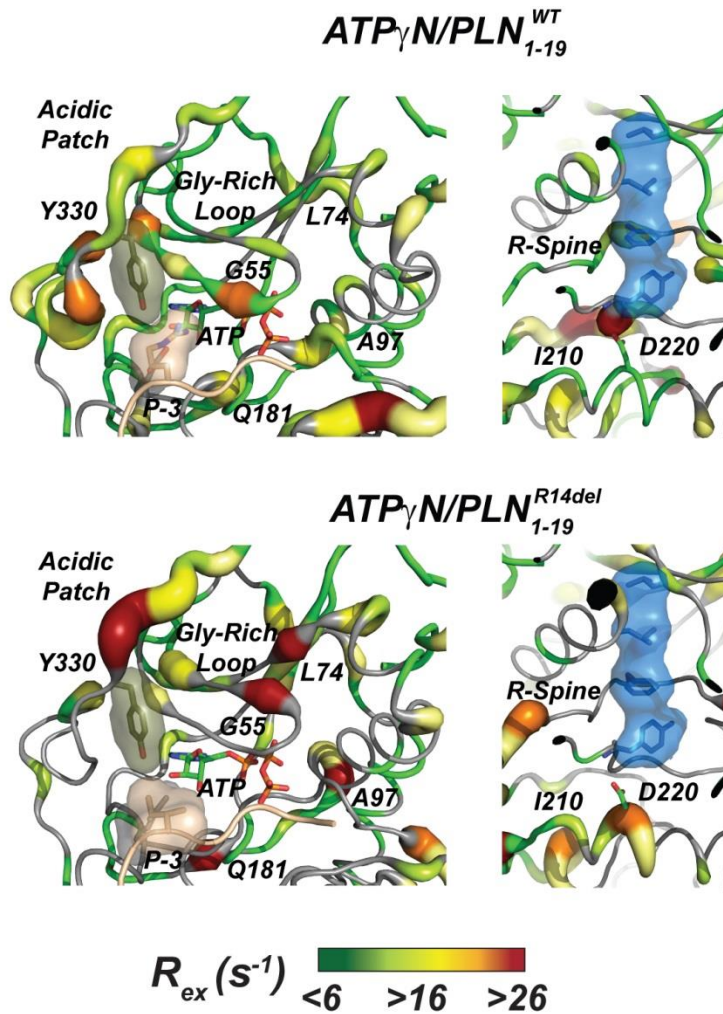
Figure 9.4: Allosteric changes in conformational dynamics upon substrate binding. Zoom in of the slow conformational dynamics plotted on the X-ray crystal structure. The PKAC/ATPγN/ PLN_{1-19}^{WT} complex (top) shows attenuated conformational dynamics with respect to the PKA-C/ATPγN/ $\mathrm{PLN}_{1-19}^{R14del}$ complex (bottom).
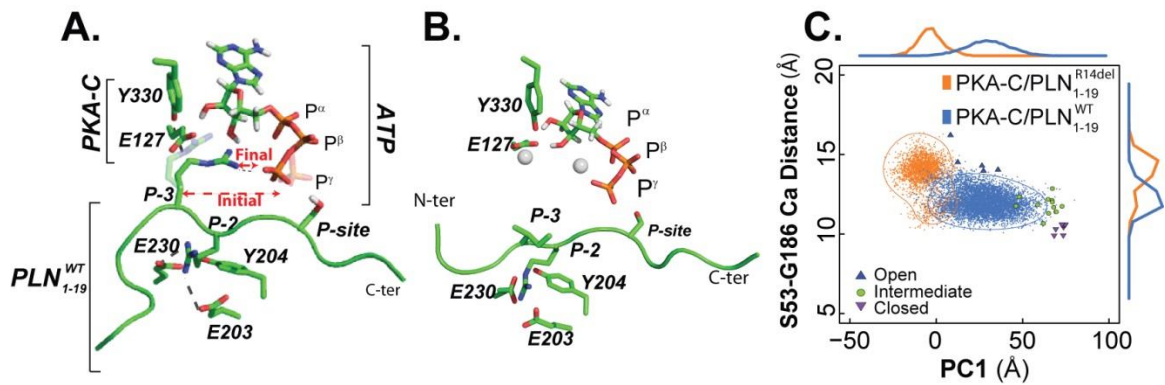
Figure 9.5: MD simulations of PKA-C in complex with PLN_{1-19}^{WT} and PLN_{1-19}^{R14del}. (A) Snapshot of MD simulations showing key interactions between R14 (P-2) and R13 (P-3) of PLN_{1-19} and the enzyme binding site. (B) Corresponding snapshot for the PKA-C/ PLN_{1-19}^{R14del} complex. C. Plot of the PC1 versus $d_{S53-G186}$ for the two complexes.

Intermediate state
(Committed conformational dynamics)

WT   *R14del*

Closed state
(Committed conformational dynamics)

Partially closed state
(Dysfunctional conformational dynamics)
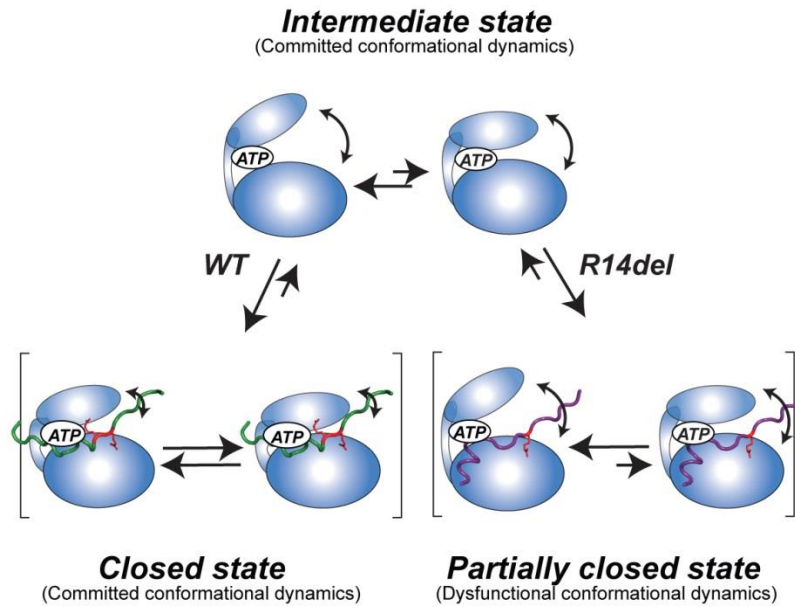
Figure 9.6: Recognition model of the kinase for PLN_{1-19}^{WT} and $\mathrm{PLN}_{1-19}^{R14del}$. Upon nucleotide binding, the enzyme's conformational ensemble shifts towards the intermediate conformation and with dynamics committed to catalysis. With PLN_{1-19}^{WT}, the two arginine residues of the PKA-C recognition sequence clamp together both lobes of the enzyme to produce a catalytically committed complex; while the PKA-C/ $\mathrm{PLN}_{1-19}^{R14del}$ complex adopts a partially closed conformation with dysfunctional dynamics.
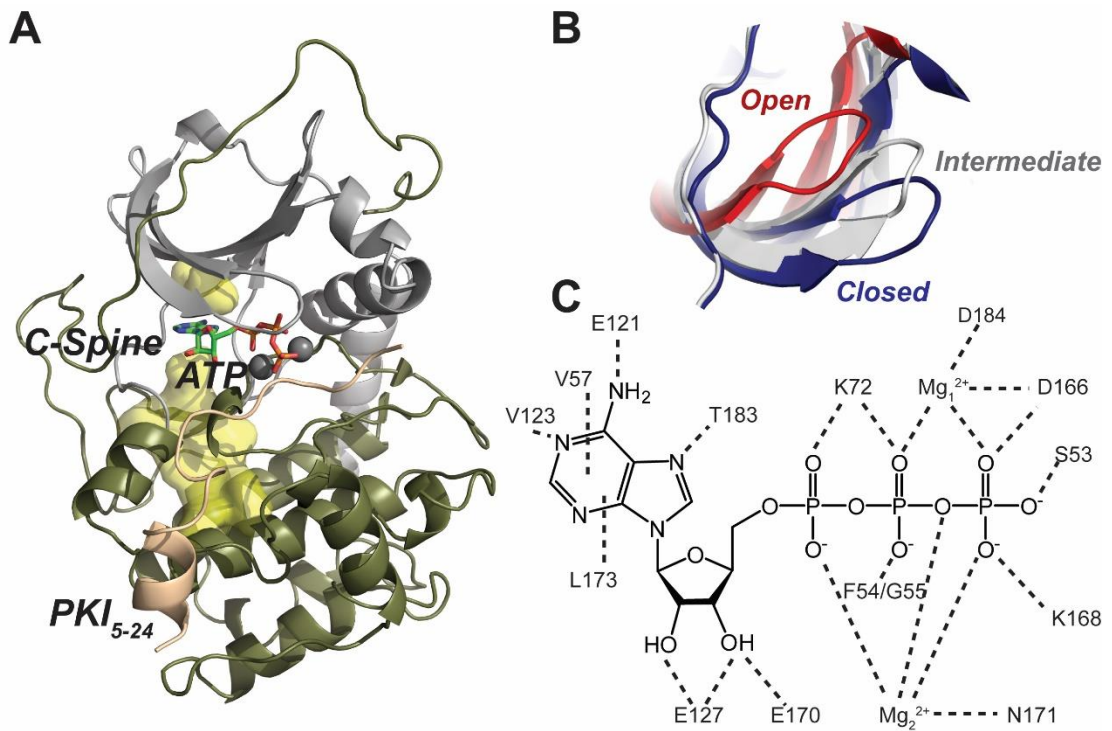
Figure 10.1: Three-dimensional fold and conformational states of PKA-C. (A) Ribbon diagram of the catalytic subunit of protein kinase A (PDB: 1ATP) shown with the C-spine scaffold (yellow surface), sandwiching the adenine moiety of ATP, and the peptide fragment of the heat stable protein kinase inhibitor (PKI$_{5-24}$). (B) Overlay of the glycine-rich loop of the open (PDB: 1J3H), intermediate (PDB:1BKX) and closed (PDB:1ATP) forms of PKA-C. (C). Electrostatic and hydrophobic contacts with ATP deduced from the 1ATP structure of PKA-C.
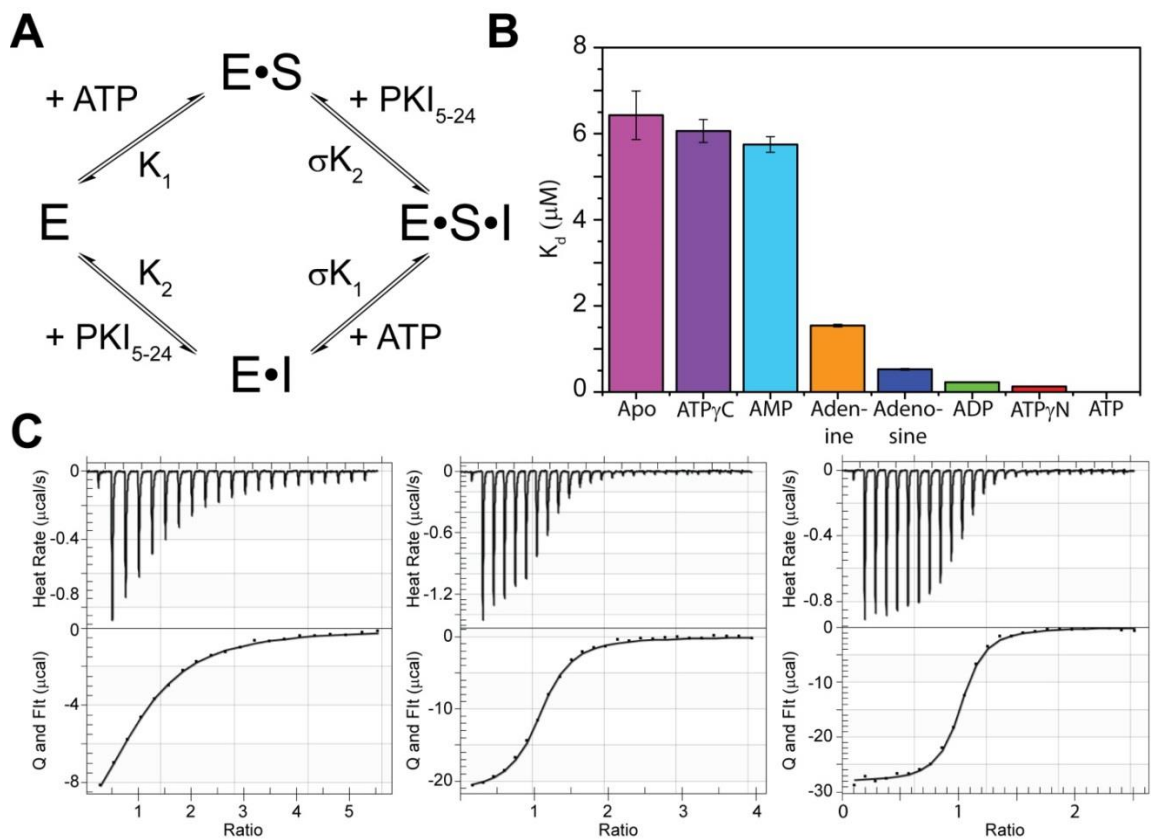
Figure 10.2: Binding cooperativity between nucleotide and pseudo-substrate. **(**A) Two-state heterotropic linkage model for nucleotide and pseudo-substrate binding. (B) Plot of the K_d of PKI$_{5-24}$ to PKA-C in the presence of various nucleotides. (C) Examples of ITC isotherms for PKI$_{5-24}$ binding to PKA-C saturated with ATPγC (left), adenosine (middle), and ADP (right).
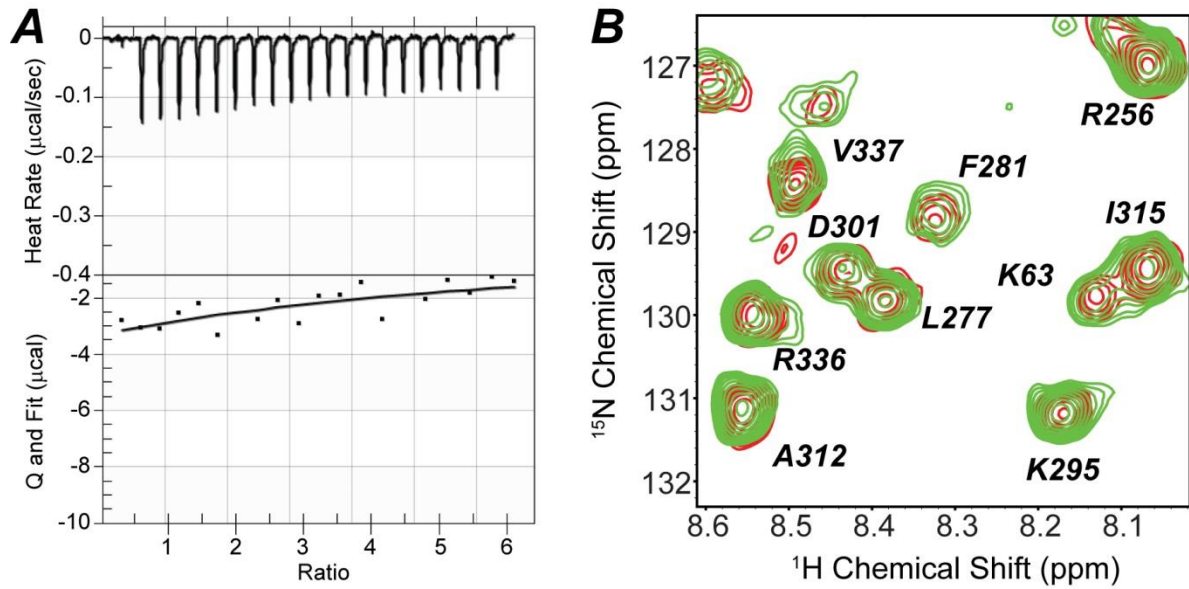
Figure 10.3: ATPγC abrogates native substrate binding. (A) ITC isotherm of PLN$_{1-19}$ binding to ATPγC saturated PKA-C. (B) Overlay of [^{1}H,^{15}N]-TROSY-HSQC spectra of the complexes PKA-C/ATPγC (green) and PKA-C/ATPγC/PLN$_{1-19}$ (red) showing no detectable chemical shift changes.
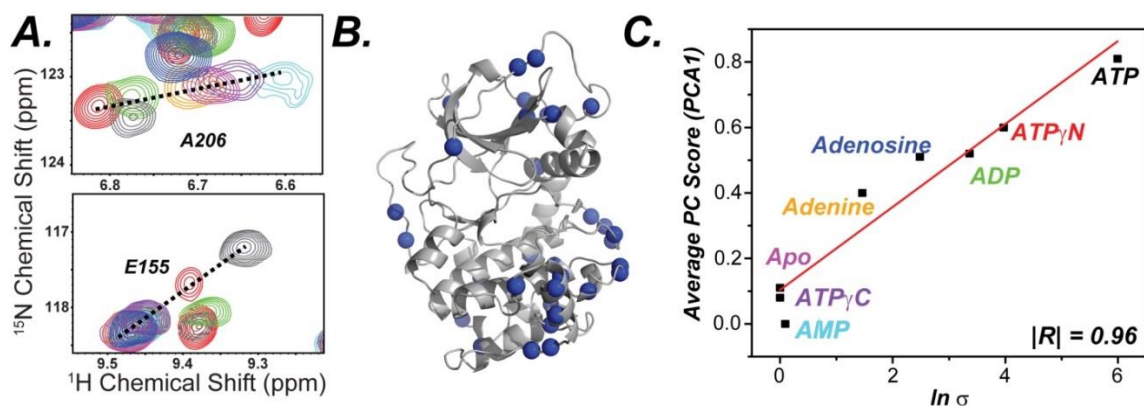
Figure 10.4: CONCISE analysis of the chemical shift changes. (A) [^{1}H,^{15}N]-TROSY-HSQC spectra showing the backbone amide chemical shift changes of PKA-C saturated with different nucleotides upon binding PKI$_{5-24}$ (B) Residues following linear trajectories (blue spheres) plotted on the cartoon representation of the PKA-C crystal structure (PDB: 1ATP). (C) Linear correlation between PC1 score and degree of cooperativity. Since the average PC score defines the extent of the closed state, the cooperativity increases with the population of the closed state.
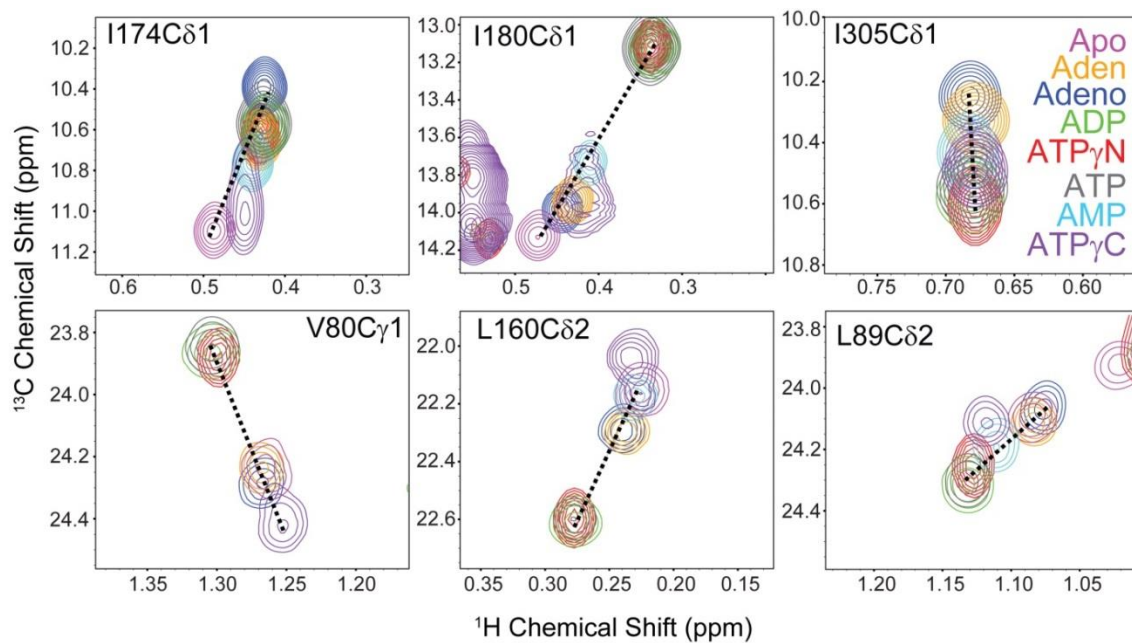
Figure 10.5: Effects of the ligand binding on the kinase side chains. Methyl-TROSY spectra of ^{13}C methyl-labeled PKA-C saturated with different nucleotides. Most of the resonances follow linear chemical shift trajectories. However, several resonances for ATPγC do not lay on the linear relationships.
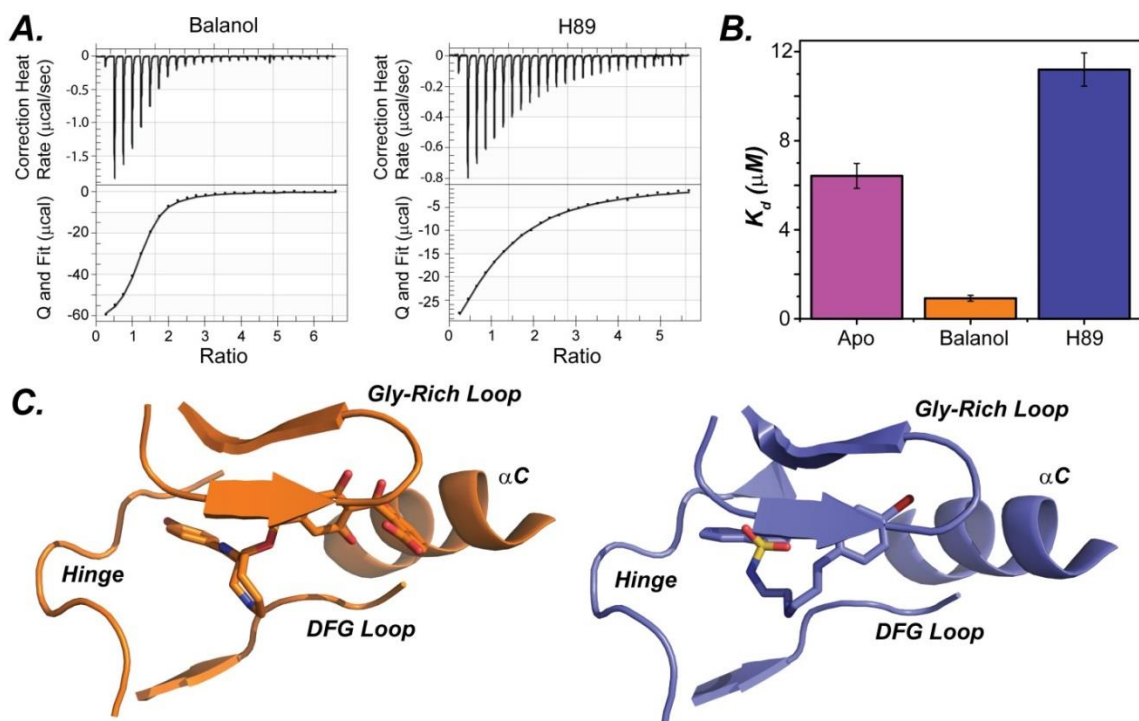
Figure 10.6: Binding cooperativity between ATP-competitive inhibitors and pseudo-substrate. (A) ITC isotherms for PKI_{5-24} binding to PKA-C saturated with Balanol (left), and H89 (right). (B) Plot of the K_d of PKI_{5-24} to PKA-C in the presence of ATP-competitive inhibitors. (C) structure of PKA-C with balanol (PDB:1BX6, orange) and H89 (PDB: 1YDT, blue)
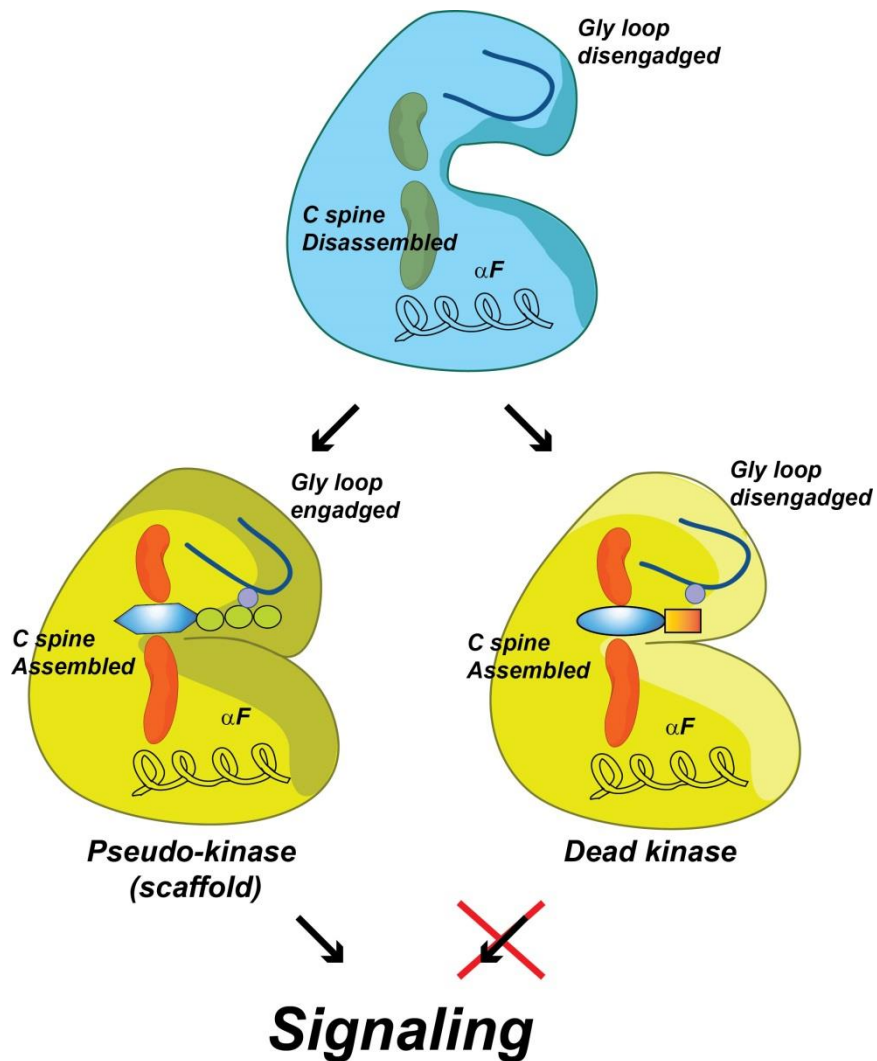
Figure 10.7: Uncoupling canonical and non-canonical function of kinases. The apo enzyme (blue) displays both disassembled C spine and disengaged Gly-loop. Binding of non-hydrolyzable ATP analogs or good ATP mimic drug inhibitors (i.e., able to engage Gly-rich loop via coordination of Mg^{2+} ion) produce a pseudokinase that is unable to carry out phosphoryl transfer but is able to bind substrates cooperatively (yellow). Binding of drug inhibitors that are unable to properly coordinate the Mg^{2+} ion to engage the Gly-loop (i.e., ATPγC, H89) obliterates both catalytic and scaffolding function (dead kinase).

References

1. Manning, G., et al., *The Protein Kinase Complement of the Human Genome.* Science, 2002. **298**(5600): p. 1912-1934.
2. Johnson, D.A., et al., *Dynamics of cAMP-dependent protein kinase.* Chem Rev, 2001. **101**(8): p. 2243-70.
3. Taylor, S.S., et al., *PKA: lessons learned after twenty years.* Biochim Biophys Acta, 2013. **1834**(7): p. 1271-8.
4. Masterson, L.R., et al., *Allostery and binding cooperativity of the catalytic subunit of protein kinase A by NMR spectroscopy and molecular dynamics simulations.* Adv Protein Chem Struct Biol, 2012. **87**: p. 363-89.
5. Walsh, D.A., J.P. Perkins, and E.G. Krebs, *An adenosine 3',5'-monophosphate-dependant protein kinase from rabbit skeletal muscle.* J Biol Chem, 1968. **243**(13): p. 3763-5.
6. Slice, L.W. and S.S. Taylor, *Expression of the catalytic subunit of cAMP-dependent protein kinase in Escherichia coli.* J Biol Chem, 1989. **264**(35): p. 20940-6.
7. Adams, J.A., *Kinetic and catalytic mechanisms of protein kinases.* Chemical reviews, 2001. **101**(8): p. 2271-2290.
8. Moore, M.J., et al., *Phosphorylation of the catalytic subunit of protein kinase A. Autophosphorylation versus phosphorylation by phosphoinositide-dependent kinase-1.* J Biol Chem, 2002. **277**(49): p. 47878-84.
9. Moore, M.J., J.A. Adams, and S.S. Taylor, *Structural basis for peptide binding in protein kinase A. Role of glutamic acid 203 and tyrosine 204 in the peptide-positioning loop.* J Biol Chem, 2003. **278**(12): p. 10613-8.
10. Yang, J., et al., *Crystal Structure of a cAMP-dependent Protein Kinase Mutant at 1.26Å: New Insights into the Catalytic Mechanism.* Journal of Molecular Biology, 2004. **336**(2): p. 473-487.
11. Endicott, J.A., M.E. Noble, and L.N. Johnson, *The structural basis for control of eukaryotic protein kinases.* Annu Rev Biochem, 2012. **81**(1): p. 587-613.
12. Masterson, L.R., et al., *Allosteric cooperativity in protein kinase A.* Proc Natl Acad Sci U S A, 2008. **105**(2): p. 506-11.
13. Kornev, A.P., S.S. Taylor, and L.F. Ten Eyck, *A helix scaffold for the assembly of active protein kinases.* Proc Natl Acad Sci U S A, 2008. **105**(38): p. 14377-82.
14. Hammes, G.G., S.J. Benkovic, and S. Hammes-Schiffer, *Flexibility, diversity, and cooperativity: pillars of enzyme catalysis.* Biochemistry, 2011. **50**(48): p. 10422-30.
15. Bhabha, G., et al., *A dynamic knockout reveals that conformational fluctuations influence the chemical step of enzyme catalysis.* Science, 2011. **332**(6026): p. 234-8.
16. Whittier, S.K., A.C. Hengge, and J.P. Loria, *Conformational motions regulate phosphoryl transfer in related protein tyrosine phosphatases.* Science, 2013. **341**(6148): p. 899-903.
17. Henzler-Wildman, K.A., et al., *A hierarchy of timescales in protein dynamics is linked to enzyme catalysis.* Nature, 2007. **450**(7171): p. 913-U27.
18. Pisliakov, A.V., et al., *Enzyme millisecond conformational dynamics do not catalyze the chemical step.* Proc Natl Acad Sci U S A, 2009. **106**(41): p. 17359-64.
19. Hammes-Schiffer, S. and S.J. Benkovic, *Relating protein motion to catalysis.* Annu Rev Biochem, 2006. **75**(1): p. 519-41.
20. Hanks, S.K., A.M. Quinn, and T. Hunter, *The protein kinase family: conserved features and deduced phylogeny of the catalytic domains.* Science, 1988. **241**(4861): p. 42-52.

21.   Zheng, J., et al., *Crystal structure of the catalytic subunit of cAMP-dependent protein kinase complexed with magnesium-ATP and peptide inhibitor.* Biochemistry, 1993. **32**(9): p. 2154-2161.

22.   Zheng, J., et al., *Crystal structures of the myristylated catalytic subunit of cAMP-dependent protein kinase reveal open and closed conformations.* Protein Sci, 1993. **2**(10): p. 1559-73.

23.   Schindler, T., et al., *Structural mechanism for STI-571 inhibition of abelson tyrosine kinase.* Science, 2000. **289**(5486): p. 1938-42.

24.   Huse, M. and J. Kuriyan, *The conformational plasticity of protein kinases.* Cell, 2002. **109**(3): p. 275-82.

25.   McClendon, C.L., et al., *Dynamic architecture of a protein kinase.* Proc Natl Acad Sci U S A, 2014. **111**(43): p. E4623-31.

26.   Kannan, N., et al., *The hallmark of AGC kinase functional divergence is its C-terminal tail, a cis-acting regulatory module (vol 104, pg 1272, 2007).* Proceedings of the National Academy of Sciences of the United States of America, 2008. **105**(26): p. 9130-9130.

27.   Pearce, L.R., D. Komander, and D.R. Alessi, *The nuts and bolts of AGC protein kinases.* Nat Rev Mol Cell Biol, 2010. **11**(1): p. 9-22.

28.   Bylund, D.B. and E.G. Krebs, *Effect of denaturation on the susceptibility of proteins to enzymic phosphorylation.* J Biol Chem, 1975. **250**(16): p. 6355-61.

29.   Shabb, J.B., *Physiological substrates of cAMP-dependent protein kinase.* Chemical reviews, 2001. **101**(8): p. 2381-2411.

30.   Wegener, A.D., et al., *Phospholamban phosphorylation in intact ventricles. Phosphorylation of serine 16 and threonine 17 in response to beta-adrenergic stimulation.* J Biol Chem, 1989. **264**(19): p. 11468-74.

31.   Kemp, B.E., et al., *Substrate specificity of the cyclic AMP-dependent protein kinase.* Proc Natl Acad Sci U S A, 1975. **72**(9): p. 3448-52.

32.   Kemp, B.E., E. Benjamini, and E.G. Krebs, *Synthetic hexapeptide substrates and inhibitors of 3':5'-cyclic AMP-dependent protein kinase.* Proc Natl Acad Sci U S A, 1976. **73**(4): p. 1038-42.

33.   Kemp, B.E., et al., *Role of multiple basic residues in determining the substrate specificity of cyclic AMP-dependent protein kinase.* J Biol Chem, 1977. **252**(14): p. 4888-94.

34.   Walsh, D.A., et al., *Krebs EG: Purification and characterization of a protein inhibitor of adenosine 3',5'-monophosphate-dependent protein kinases.* J Biol Chem, 1971. **246**(7): p. 1977-85.

35.   Demaille, J.G., K.A. Peters, and E.H. Fischer, *Isolation and properties of the rabbit skeletal muscle protein inhibitor of adenosine 3',5'-monophosphate dependent protein kinases.* Biochemistry, 1977. **16**(14): p. 3080-6.

36.   Cheng, H.C., et al., *An active twenty-amino-acid-residue peptide derived from the inhibitor protein of the cyclic AMP-dependent protein kinase.* Biochem J, 1985. **231**(3): p. 655-61.

37.   Scott, J.D., et al., *Identification of an inhibitory region of the heat-stable protein inhibitor of the cAMP-dependent protein kinase.* Proc Natl Acad Sci U S A, 1985. **82**(13): p. 4379-83.

38.   Cheng, H.C., et al., *A potent synthetic peptide inhibitor of the cAMP-dependent protein kinase.* J Biol Chem, 1986. **261**(3): p. 989-92.

39.   Glass, D.B., et al., *Primary structural determinants essential for potent inhibition of cAMP-dependent protein kinase by inhibitory peptides corresponding to the active portion of the heat-stable inhibitor protein.* J Biol Chem, 1989. **264**(15): p. 8802-10.

40.   Glass, D.B., et al., *Protein kinase inhibitor-(6-22)-amide peptide analogs with standard and nonstandard amino acid substitutions for phenylalanine 10. Inhibition of cAMP-dependent protein kinase.* J Biol Chem, 1989. **264**(24): p. 14579-84.

41.   Cook, P.F., et al., *Adenosine cyclic 3',5'-monophosphate dependent protein kinase: kinetic mechanism for the bovine skeletal muscle catalytic subunit.* Biochemistry, 1982. **21**(23): p. 5794-9.

42.   Bhatnagar, D., et al., *Adenosine cyclic 3',5'-monophosphate dependent protein kinase: a new fluorescence displacement titration technique for characterizing the nucleotide binding site on the catalytic subunit.* Biochemistry, 1983. **22**(26): p. 6310-7.

43.   Whitehouse, S., et al., *Studies on the kinetic mechanism of the catalytic subunit of the cAMP-dependent protein kinase.* J Biol Chem, 1983. **258**(6): p. 3693-701.

44.   Whitehouse, S. and D.A. Walsh, *Mg X ATP2-dependent interaction of the inhibitor protein of the cAMP-dependent protein kinase with the catalytic subunit.* Journal of Biological Chemistry, 1983. **258**(6): p. 3682-3692.

45.   Kong, C.T. and P.F. Cook, *Isotope partitioning in the adenosine 3',5'-monophosphate dependent protein kinase reaction indicates a steady-state random kinetic mechanism.* Biochemistry, 1988. **27**(13): p. 4795-9.

46.   Adams, J.A. and S.S. Taylor, *Divalent metal ions influence catalysis and active-site accessibility in the cAMP-dependent protein kinase.* Protein Sci, 1993. **2**(12): p. 2177-86.

47.   Bastidas, A.C., et al., *Phosphoryl transfer by protein kinase A is captured in a crystal lattice.* J Am Chem Soc, 2013. **135**(12): p. 4788-98.

48.   Khavrutskii, I.V., et al., *A transition path ensemble study reveals a linchpin role for Mg(2+) during rate-limiting ADP release from protein kinase A.* Biochemistry, 2009. **48**(48): p. 11532-45.

49.   Valiev, M., et al., *Phosphorylation reaction in cAPK protein kinase-free energy quantum mechanical/molecular mechanics simulations.* J Phys Chem B, 2007. **111**(47): p. 13455-64.

50.   Adams, J.A. and S.S. Taylor, *Energetic Limits of Phosphotransfer in the Catalytic Subunit of Camp-Dependent Protein-Kinase as Measured by Viscosity Experiments.* Biochemistry, 1992. **31**(36): p. 8516-8522.

51.   Grant, B.D. and J.A. Adams, *Pre-steady-state kinetic analysis of cAMP-dependent protein kinase using rapid quench flow techniques.* Biochemistry, 1996. **35**(6): p. 2022-2029.

52.   Zhou, J. and J.A. Adams, *Participation of ADP dissociation in the rate-determining step in cAMP-dependent protein kinase.* Biochemistry, 1997. **36**(50): p. 15733-15738.

53.   Shaffer, J. and J.A. Adams, *An ATP-Linked Structural Change in Protein Kinase A Precedes Phosphoryl Transfer under Physiological Magnesium Concentrations†.* Biochemistry, 1999. **38**(17): p. 5572-5581.

54.   Shaffer, J. and J.A. Adams, *Detection of Conformational Changes along the Kinetic Pathway of Protein Kinase A Using a Catalytic Trapping Technique†.* Biochemistry, 1999. **38**(37): p. 12072-12079.

55.   Masterson, L.R., et al., *Dynamically committed, uncommitted, and quenched states encoded in protein kinase A revealed by NMR spectroscopy.* Proc Natl Acad Sci U S A, 2011. **108**(17): p. 6969-74.

56.   Masterson, L.R., et al., *Dynamics connect substrate recognition to catalysis in protein kinase A.* Nat Chem Biol, 2010. **6**(11): p. 821-8.

57.   Srivastava, A.K., et al., *Synchronous Opening and Closing Motions Are Essential for cAMP-Dependent Protein Kinase A Signaling.* Structure, 2014. **22**(12): p. 1735-43.

58.   Taylor, S.S., et al., *PKA: a portrait of protein kinase dynamics.* Biochim Biophys Acta, 2004. **1697**(1-2): p. 259-69.

59.   Akamine, P., et al., *Dynamic Features of cAMP-dependent Protein Kinase Revealed by Apoenzyme Crystal Structure.* Journal of Molecular Biology, 2003. **327**(1): p. 159-171.

60.   Narayana, N., et al., *A binary complex of the catalytic subunit of cAMP-dependent protein kinase and adenosine further defines conformational flexibility.* Structure, 1997. **5**(7): p. 921-935.

61.   Taylor, S.S., et al., *Assembly of allosteric macromolecular switches: lessons from PKA.* Nat Rev Mol Cell Biol, 2012. **13**(10): p. 646-58.

62.   Madhusudan, et al., *Crystal structure of a transition state mimic of the catalytic subunit of cAMP-dependent protein kinase.* Nat Struct Mol Biol, 2002. **9**(4): p. 273-277.

63.   Madhusudan, et al., *cAMP-dependent protein kinase: crystallographic insights into substrate recognition and phosphotransfer.* Protein science : a publication of the Protein Society, 1994. **3**(2): p. 176-187.

64.   Mitchell, R.D., et al., *Heat-stable inhibitor protein derived peptide substrate analogs: phosphorylation by cAMP-dependent and cGMP-dependent protein kinases.* Biochemistry, 1995. **34**(2): p. 528-34.

65.   Gerlits, O., et al., *Insights into the phosphoryl transfer catalyzed by cAMP-dependent protein kinase: an X-ray crystallographic study of complexes with various metals and peptide substrate SP20.* Biochemistry, 2013. **52**(21): p. 3721-7.

66.   Hanks, S.K. and T. Hunter, *Protein kinases 6. The eukaryotic protein kinase superfamily: kinase (catalytic) domain structure and classification.* FASEB J, 1995. **9**(8): p. 576-96.

67.   Grant, B.D., et al., *Kinetic analyses of mutations in the glycine-rich loop of cAMP-dependent protein kinase.* Biochemistry, 1998. **37**(21): p. 7708-15.

68.   Reiterer, V., P.A. Eyers, and H. Farhan, *Day of the dead: pseudokinases and pseudophosphatases in physiology and disease.* Trends Cell Biol, 2014. **24**(9): p. 489-505.

69.   Boudeau, J., et al., *Emerging roles of pseudokinases.* Trends Cell Biol, 2006. **16**(9): p. 443-52.

70.   Herberg, F.W., S.M. Bell, and S.S. Taylor, *Expression of the catalytic subunit of cAMP-dependent protein kinase in Escherichia coli: multiple isozymes reflect different phosphorylation states.* Protein Eng, 1993. **6**(7): p. 771-7.

71.   Cheng, X., et al., *Phosphorylation and activation of cAMP-dependent protein kinase by phosphoinositide-dependent protein kinase.* Proc Natl Acad Sci U S A, 1998. **95**(17): p. 9849-54.

72.   Gao, X. and T.K. Harris, *Steady-state kinetic mechanism of PDK1.* J Biol Chem, 2006. **281**(31): p. 21670-81.

73.   Biondi, R.M., et al., *Identification of a pocket in the PDK1 kinase domain that interacts with PIF and the C-terminal residues of PKA.* The EMBO Journal, 2000. **19**(5): p. 979-988.

74.   Steichen, J.M., et al., *Global consequences of activation loop phosphorylation on protein kinase A.* J Biol Chem, 2010. **285**(6): p. 3825-32.

75.   Steichen, J.M., et al., *Structural basis for the regulation of protein kinase A by activation loop phosphorylation.* J Biol Chem, 2012. **287**(18): p. 14672-80.

76.   Tong, M. and M.A. Seeliger, *Targeting conformational plasticity of protein kinases.* ACS Chem Biol, 2015. **10**(1): p. 190-200.

77.   Beuschlein, F., et al., *Constitutive activation of PKA catalytic subunit in adrenal Cushing's syndrome.* N Engl J Med, 2014. **370**(11): p. 1019-28.

78. Di Dalmazi, G., et al., *Novel somatic mutations in the catalytic subunit of the protein kinase A as a cause of adrenal Cushing's syndrome: a European multicentric study.* J Clin Endocrinol Metab, 2014. **99**(10): p. E2093-100.

79. Wu, J., et al., *Crystal structure of the E230Q mutant of cAMP-dependent protein kinase reveals an unexpected apoenzyme conformation and an extended N-terminal A helix.* Protein Sci, 2005. **14**(11): p. 2871-9.

80. Yang, J., et al., *Allosteric network of cAMP-dependent protein kinase revealed by mutation of Tyr204 in the P+1 loop.* J Mol Biol, 2005. **346**(1): p. 191-201.

81. Taylor, S.S. and A.P. Kornev, *Protein kinases: evolution of dynamic regulatory proteins.* Trends in biochemical sciences, 2011. **36**(2): p. 65-77.

82. Yang, J., et al., *A conserved Glu-Arg salt bridge connects coevolved motifs that define the eukaryotic protein kinase fold.* J Mol Biol, 2012. **415**(4): p. 666-79.

83. Duronio, R.J., et al., *Protein N-myristoylation in Escherichia coli: reconstitution of a eukaryotic protein modification in bacteria.* Proc Natl Acad Sci U S A, 1990. **87**(4): p. 1506-10.

84. Bastidas, A.C., et al., *Role of N-terminal myristylation in the structure and regulation of cAMP-dependent protein kinase.* J Mol Biol, 2012. **422**(2): p. 215-29.

85. Zozulya, S. and L. Stryer, *Calcium-myristoyl protein switch.* Proc Natl Acad Sci U S A, 1992. **89**(23): p. 11569-73.

86. Patwardhan, P. and M.D. Resh, *Myristoylation and membrane binding regulate c-Src stability and kinase activity.* Molecular and cellular biology, 2010. **30**(17): p. 4094-4107.

87. Saad, J.S., et al., *Structural basis for targeting HIV-1 Gag proteins to the plasma membrane for virus assembly.* Proc Natl Acad Sci U S A, 2006. **103**(30): p. 11364-9.

88. Struppe, J., et al., *2H NMR studies of a myristoylated peptide in neutral and acidic phospholipid bicelles.* Biochemistry, 1998. **37**(44): p. 15523-15527.

89. Gaffarogullari, E.C., et al., *A myristoyl/phosphoserine switch controls cAMP-dependent protein kinase association to membranes.* J Mol Biol, 2011. **411**(4): p. 823-36.

90. Cembran, A., et al., *Conformational equilibrium of N-myristoylated cAMP-dependent protein kinase A by molecular dynamics simulations.* Biochemistry, 2012. **51**(51): p. 10186-96.

91. Herberg, F.W., et al., *Importance of the A-helix of the catalytic subunit of cAMP-dependent protein kinase for stability and for orienting subdomains at the cleft interface.* Protein Sci, 1997. **6**(3): p. 569-79.

92. Sastri, M., et al., *A-kinase-interacting protein localizes protein kinase A in the nucleus.* Proc Natl Acad Sci U S A, 2005. **102**(2): p. 349-54.

93. Gao, N., et al., *AKIP1 enhances NF-kappaB-dependent gene expression by promoting the nuclear retention and phosphorylation of p65.* J Biol Chem, 2008. **283**(12): p. 7834-43.

94. King, C.C., et al., *The rate of NF-kappaB nuclear translocation is regulated by PKA and A kinase interacting protein 1.* PLoS One, 2011. **6**(4): p. e18713.

95. Sastri, M., et al., *A kinase interacting protein (AKIP1) is a key regulator of cardiac stress.* Proc Natl Acad Sci U S A, 2013. **110**(5): p. E387-96.

96. Keshwani, M.M., et al., *Hydrophobic Motif Phosphorylation Is Not Required for Activation Loop Phosphorylation of p70 Ribosomal Protein S6 Kinase 1 (S6K1).* Journal of Biological Chemistry, 2011. **286**(26): p. 23552-23558.

97. Sadowsky, J.D., et al., *Turning a protein kinase on or off from a single allosteric site via disulfide trapping.* Proc Natl Acad Sci U S A, 2011. **108**(15): p. 6056-61.

98.   Stockman, B.J., et al., *Identification of allosteric PIF-pocket ligands for PDK1 using NMR-based fragment screening and 1H-15N TROSY experiments.* Chem Biol Drug Des, 2009. **73**(2): p. 179-88.

99.   Batkin, M., I. Schvartz, and S. Shaltiel, *Snapping of the Carboxyl Terminal Tail of the Catalytic Subunit of PKA onto Its Core: Characterization of the Sites by Mutagenesis†.* Biochemistry, 2000. **39**(18): p. 5366-5373.

100.   Chestukhin, A., et al., *Functional malleability of the carboxyl-terminal tail in protein kinase A.* J Biol Chem, 1996. **271**(17): p. 10175-82.

101.   Yang, J., et al., *Contribution of non-catalytic core residues to activity and regulation in protein kinase A.* J Biol Chem, 2009. **284**(10): p. 6241-8.

102.   Keshwani, M.M., et al., *Cotranslational cis-phosphorylation of the COOH-terminal tail is a key priming step in the maturation of cAMP-dependent protein kinase.* Proc Natl Acad Sci U S A, 2012. **109**(20): p. E1221-9.

103.   Yonemoto, W., et al., *Identification of phosphorylation sites in the recombinant catalytic subunit of cAMP-dependent protein kinase.* J Biol Chem, 1993. **268**(25): p. 18626-32.

104.   Gao, T.Y. and A.C. Newton, *The turn motif is a phosphorylation switch that regulates the binding of Hsp70 to protein kinase C.* Journal of Biological Chemistry, 2002. **277**(35): p. 31585-31592.

105.   Gao, T. and A.C. Newton, *Invariant Leu preceding turn motif phosphorylation site controls the interaction of protein kinase C with Hsp70.* J Biol Chem, 2006. **281**(43): p. 32461-8.

106.   Hubbard, S.R., et al., *Crystal structure of the tyrosine kinase domain of the human insulin receptor.* Nature, 1994. **372**(6508): p. 746-54.

107.   Hubbard, S.R., *Crystal structure of the activated insulin receptor tyrosine kinase in complex with peptide substrate and ATP analog.* EMBO J, 1997. **16**(18): p. 5572-81.

108.   De Bondt, H.L., et al., *Crystal structure of cyclin-dependent kinase 2.* Nature, 1993. **363**(6430): p. 595-602.

109.   Jeffrey, P.D., et al., *Mechanism of CDK activation revealed by the structure of a cyclinA-CDK2 complex.* Nature, 1995. **376**(6538): p. 313-20.

110.   Kornev, A.P., et al., *Surface comparison of active and inactive protein kinases identifies a conserved activation mechanism.* Proc Natl Acad Sci U S A, 2006. **103**(47): p. 17783-8.

111.   Meharena, H.S., et al., *Deciphering the structural basis of eukaryotic protein kinase regulation.* PLoS Biol, 2013. **11**(10): p. e1001680.

112.   Azam, M., et al., *Activation of tyrosine kinases by mutation of the gatekeeper threonine.* Nat Struct Mol Biol, 2008. **15**(10): p. 1109-18.

113.   Hu, J., et al., *Mutation that blocks ATP binding creates a pseudokinase stabilizing the scaffolding function of kinase suppressor of Ras, CRAF and BRAF.* Proc Natl Acad Sci U S A, 2011. **108**(15): p. 6067-72.

114.   Poulikakos, P.I., et al., *RAF inhibitors transactivate RAF dimers and ERK signalling in cells with wild-type BRAF.* Nature, 2010. **464**(7287): p. 427-30.

115.   Hatzivassiliou, G., et al., *RAF inhibitors prime wild-type RAF to activate the MAPK pathway and enhance growth.* Nature, 2010. **464**(7287): p. 431-5.

116.   Gregory, R.B. and R. Lumry, *Hydrogen-exchange evidence for distinct structural classes in globular proteins.* Biopolymers, 1985. **24**(2): p. 301-26.

117.   Eisenmesser, E.Z., et al., *Intrinsic dynamics of an enzyme underlies catalysis.* Nature, 2005. **438**(7064): p. 117-21.

118.   Boehr, D.D., et al., *The dynamic energy landscape of dihydrofolate reductase catalysis.* Science, 2006. **313**(5793): p. 1638-42.

119.   Xiao, Y., et al., *Phosphorylation releases constraints to domain motion in ERK2.* Proc Natl Acad Sci U S A, 2014. **111**(7): p. 2506-11.

120.   Vogtherr, M., et al., *NMR characterization of kinase p38 dynamics in free and ligand-bound forms.* Angew Chem Int Ed Engl, 2006. **45**(6): p. 993-7.

121.   Vajpai, N., et al., *Solution conformations and dynamics of ABL kinase-inhibitor complexes determined by NMR substantiate the different binding modes of imatinib/nilotinib and dasatinib.* J Biol Chem, 2008. **283**(26): p. 18292-302.

122.   Skora, L., et al., *NMR reveals the allosteric opening and closing of Abelson tyrosine kinase by ATP-site and myristoyl pocket inhibitors.* Proc Natl Acad Sci U S A, 2013. **110**(47): p. E4437-45.

123.   Wang, C., M. Rance, and A.G. Palmer, 3rd, *Mapping chemical exchange in proteins with MW > 50 kD.* J Am Chem Soc, 2003. **125**(30): p. 8968-9.

124.   Zamoon, J., et al., *NMR solution structure and topological orientation of monomeric phospholamban in dodecylphosphocholine micelles.* Biophys J, 2003. **85**(4): p. 2589-98.

125.   Brittsan, A.G. and E.G. Kranias, *Phospholamban and cardiac contractile function.* J Mol Cell Cardiol, 2000. **32**(12): p. 2131-9.

126.   Traaseth, N.J., et al., *Structural and dynamic basis of phospholamban and sarcolipin inhibition of Ca(2+)-ATPase.* Biochemistry, 2008. **47**(1): p. 3-13.

127.   Metcalfe, E.E., N.J. Traaseth, and G. Veglia, *Serine 16 phosphorylation induces an order-to-disorder transition in monomeric phospholamban.* Biochemistry, 2005. **44**(11): p. 4386-96.

128.   Gustavsson, M., N.J. Traaseth, and G. Veglia, *Probing ground and excited states of phospholamban in model and native lipid membranes by magic angle spinning NMR spectroscopy.* Biochim Biophys Acta, 2012. **1818**(2): p. 146-53.

129.   Masterson, L.R., et al., *cAMP-dependent protein kinase A selects the excited state of the membrane substrate phospholamban.* J Mol Biol, 2011. **412**(2): p. 155-64.

130.   Jencks, W.P., *Binding Energy, Specificity, and Enzymic Catalysis: The Circe Effect*, in *Advances in Enzymology and Related Areas of Molecular Biology*. 1975, John Wiley & Sons, Inc. p. 219-410.

131.   Young, M.A., et al., *Dynamic coupling between the SH2 and SH3 domains of c-Src and hck underlies their inactivation by C-terminal tyrosine phosphorylation.* Cell, 2001. **105**(1): p. 115-126.

132.   Shaw, D.E., et al., *Anton, a special-purpose machine for molecular dynamics simulation*, in *Proceedings of the 34th annual international symposium on Computer architecture*. 2007, ACM: San Diego, California, USA. p. 1-12.

133.   Weinert, F., *Wrong theory—Right experiment: The significance of the Stern-Gerlach experiments.* Studies in History and Philosophy of Science Part B: Studies in History and Philosophy of Modern Physics, 1995. **26**(1): p. 75-86.

134.   Bloch, F., *Nuclear Induction.* Physical Review, 1946. **70**(7-8): p. 460-474.

135.   Palmer, A.G., 3rd, C.D. Kroenke, and J.P. Loria, *Nuclear magnetic resonance methods for quantifying microsecond-to-millisecond motions in biological macromolecules.* Methods in enzymology, 2001. **339**: p. 204-238.

136.   Fano, U., *Description of States in Quantum Mechanics by Density Matrix and Operator Techniques.* Reviews of Modern Physics, 1957. **29**(1): p. 74-93.

137.   Hansen, D.F., et al., *An exchange-free measure of 15N transverse relaxation: an NMR spectroscopy application to the study of a folding intermediate with pervasive chemical exchange.* J Am Chem Soc, 2007. **129**(37): p. 11468-79.

138. Jaccard, G., S. Wimperis, and G. Bodenhausen, *Observation of 2izsz Order in Nmr Relaxation Studies for Measuring Cross-Correlation of Chemical-Shift Anisotropy and Dipolar Interactions.* Chemical Physics Letters, 1987. **138**(6): p. 601-606.

139. Kroenke, C.D., et al., *Longitudinal and Transverse1H–15N Dipolar/15N Chemical Shift Anisotropy Relaxation Interference: Unambiguous Determination of Rotational Diffusion Tensors and Chemical Exchange Effects in Biological Macromolecules.* Journal of the American Chemical Society, 1998. **120**(31): p. 7905-7915.

140. John, B.K., D. Plant, and R.E. Hurd, *Improved Proton-Detected Heteronuclear Correlation Using Gradient-Enhanced Z and Zz Filters.* Journal of Magnetic Resonance Series A, 1993. **101**(1): p. 113-117.

141. Bax, A., R. Freeman, and S.P. Kempsell, *Natural abundance carbon-13-carbon-13 coupling observed via double-quantum coherence.* Journal of the American Chemical Society, 1980. **102**(14): p. 4849-4851.

142. Braunschweiler, L., G. Bodenhausen, and R.R. Ernst, *Analysis of networks of coupled spins by multiple quantum N.M.R.* Molecular Physics, 2006. **48**(3): p. 535-560.

143. Williamson, M.P., *Using chemical shift perturbation to characterise ligand binding.* Prog Nucl Magn Reson Spectrosc, 2013. **73**: p. 1-16.

144. Wishart, D.S., B.D. Sykes, and F.M. Richards, *Relationship between Nuclear-Magnetic-Resonance Chemical-Shift and Protein Secondary Structure.* Journal of Molecular Biology, 1991. **222**(2): p. 311-333.

145. Wishart, D.S., B.D. Sykes, and F.M. Richards, *The Chemical-Shift Index - a Fast and Simple Method for the Assignment of Protein Secondary Structure through Nmr-Spectroscopy.* Biochemistry, 1992. **31**(6): p. 1647-1651.

146. Wishart, D. and B. Sykes, *The 13C Chemical-Shift Index: A simple method for the identification of protein secondary structure using 13C chemical-shift data.* Journal of Biomolecular NMR, 1994. **4**(2): p. 171-180.

147. Schwarzinger, S., et al., *Sequence-dependent correction of random coil NMR chemical shifts.* J Am Chem Soc, 2001. **123**(13): p. 2970-8.

148. Cornilescu, G., F. Delaglio, and A. Bax, *Protein backbone angle restraints from searching a database for chemical shift and sequence homology.* J Biomol NMR, 1999. **13**(3): p. 289-302.

149. Shen, Y., et al., *TALOS+: a hybrid method for predicting protein backbone torsion angles from NMR chemical shifts.* J Biomol NMR, 2009. **44**(4): p. 213-23.

150. Shen, Y. and A. Bax, *Protein backbone and sidechain torsion angles predicted from NMR chemical shifts using artificial neural networks.* J Biomol NMR, 2013. **56**(3): p. 227-41.

151. Robustelli, P., et al., *Using NMR Chemical Shifts as Structural Restraints in Molecular Dynamics Simulations of Proteins.* Structure, 2010. **18**(8): p. 923-933.

152. Robustelli, P., K.A. Stafford, and A.G. Palmer, 3rd, *Interpreting protein structural dynamics from NMR chemical shifts.* J Am Chem Soc, 2012. **134**(14): p. 6365-74.

153. Lange, O.F., et al., *Determination of solution structures of proteins up to 40 kDa using CS-Rosetta with sparse NMR data from deuterated samples.* Proc Natl Acad Sci U S A, 2012. **109**(27): p. 10873-8.

154. Gutowsky, H.S., D.W. McCall, and C.P. Slichter, *Nuclear Magnetic Resonance Multiplets in Liquids.* The Journal of Chemical Physics, 1953. **21**(2): p. 279.

155. Prestegard, J.H., C.M. Bougault, and A.I. Kishore, *Residual dipolar couplings in structure determination of biomolecules.* Chemical reviews, 2004. **104**(8): p. 3519-3540.

156. Tolman, J.R. and K. Ruan, *NMR Residual Dipolar Couplings as Probes of Biomolecular Dynamics.* Chemical Reviews, 2006. **106**(5): p. 1720-1736.

157. Mehring, M., *Principles of High Resolution Nmr in Solids*. Vol. 2nd. 1983: Springer-Verlag.

158. Gopinath, T., K.R. Mote, and G. Veglia, *Sensitivity and resolution enhancement of oriented solid-state NMR: application to membrane proteins.* Prog Nucl Magn Reson Spectrosc, 2013. **75**: p. 50-68.

159. Saito, H., I. Ando, and A. Ramamoorthy, *Chemical shift tensor - the heart of NMR: Insights into biological aspects of proteins.* Prog Nucl Magn Reson Spectrosc, 2010. **57**(2): p. 181-228.

160. Vostrikov, V.V., et al., *Charged or aromatic anchor residue dependence of transmembrane peptide tilt.* J Biol Chem, 2010. **285**(41): p. 31723-30.

161. Vostrikov, V.V. and R.E. Koeppe, 2nd, *Response of GWALP transmembrane peptides to changes in the tryptophan anchor positions.* Biochemistry, 2011. **50**(35): p. 7522-35.

162. Sørensen, O.W., et al., *Product operator formalism for the description of NMR pulse experiments.* Progress in Nuclear Magnetic Resonance Spectroscopy, 1984. **16**(0): p. 163-192.

163. Morris, G.A. and R. Freeman, *Enhancement of Nuclear Magnetic-Resonance Signals by Polarization Transfer.* Journal of the American Chemical Society, 1979. **101**(3): p. 760-762.

164. Burum, D.P. and R.R. Ernst, *Net Polarization Transfer Via a J-Ordered State for Signal Enhancement of Low-Sensitivity Nuclei.* Journal of Magnetic Resonance, 1980. **39**(1): p. 163-168.

165. Bodenhausen, G. and D.J. Ruben, *Natural abundance nitrogen-15 NMR by enhanced heteronuclear spectroscopy.* Chemical Physics Letters, 1980. **69**(1): p. 185-189.

166. Cavanagh, J., et al., *Sensitivity improvement in proton-detected two-dimensional heteronuclear relay spectroscopy.* Journal of Magnetic Resonance (1969), 1991. **91**(2): p. 429-436.

167. Kay, L.E., P. Keifer, and T. Saarinen, *Pure Absorption Gradient Enhanced Heteronuclear Single Quantum Correlation Spectroscopy with Improved Sensitivity.* Journal of the American Chemical Society, 1992. **114**(26): p. 10663-10665.

168. Dominguez, C., R. Boelens, and A.M. Bonvin, *HADDOCK: a protein-protein docking approach based on biochemical or biophysical information.* J Am Chem Soc, 2003. **125**(7): p. 1731-7.

169. Ikura, M., L.E. Kay, and A. Bax, *A novel approach for sequential assignment of proton, carbon-13, and nitrogen-15 spectra of larger proteins: heteronuclear triple-resonance three-dimensional NMR spectroscopy. Application to calmodulin.* Biochemistry, 1990. **29**(19): p. 4659-4667.

170. Kay, L.E., et al., *Three-dimensional triple-resonance NMR spectroscopy of isotopically enriched proteins.* Journal of Magnetic Resonance (1969), 1990. **89**(3): p. 496-514.

171. Yang, D.W. and L.E. Kay, *TROSY triple-resonance four-dimensional NMR spectroscopy of a 46 ns tumbling protein.* Journal of the American Chemical Society, 1999. **121**(11): p. 2571-2575.

172. Tugarinov, V., et al., *Four-dimensional NMR spectroscopy of a 723-residue protein: chemical shift assignments and secondary structure of malate synthase g.* J Am Chem Soc, 2002. **124**(34): p. 10025-35.

173. Atreya, H.S., A. Eletsky, and T. Szyperski, *Resonance assignment of proteins with high shift degeneracy based on 5D spectral information encoded in G2FT NMR experiments.* J Am Chem Soc, 2005. **127**(13): p. 4554-5.

174. Meissner, A., J.ø. Duus, and O.W. Sørensen, *Spin-State-Selective Excitation. Application for E.COSY-Type Measurement ofJHHCoupling Constants.* Journal of Magnetic Resonance, 1997. **128**(1): p. 92-97.

175. Sørensen, M.D., A. Meissner, and O.W. Sørensen, *Spin-state-selective coherence transfer via intermediate states of two-spin coherence in IS spin systems: Application to E.COSY-type measurement of J coupling constants.* Journal of Biomolecular NMR, 1997. **10**(2): p. 181-186.

176. Pervushin, K., et al., *Attenuated T2 relaxation by mutual cancellation of dipole–dipole coupling and chemical shift anisotropy indicates an avenue to NMR structures of very large biological macromolecules in solution.* Proceedings of the National Academy of Sciences, 1997. **94**(23): p. 12366-12371.

177. Meissner, A., et al., *Double spin-state-selective coherence transfer. Application for two-dimensional selection of multiplet components with long transverse relaxation times.* Molecular Physics, 1998. **95**(6): p. 1137-1142.

178. Salzmann, M., et al., *TROSY in triple-resonance experiments: new perspectives for sequential NMR assignment of large proteins.* Proc Natl Acad Sci U S A, 1998. **95**(23): p. 13585-90.

179. Salzmann, M., et al., *TROSY-type triple-resonance experiments for sequential NMR assignments of large proteins.* Journal of the American Chemical Society, 1999. **121**(4): p. 844-848.

180. Loria, J.P., M. Rance, and A.G. Palmer, 3rd, *A TROSY CPMG sequence for characterizing chemical exchange in large proteins.* J Biomol NMR, 1999. **15**(2): p. 151-5.

181. Igumenova, T.I. and A.G. Palmer, *Off-Resonance TROSY-Selected R1ρ Experiment with Improved Sensitivity for Medium- and High-Molecular-Weight Proteins.* Journal of the American Chemical Society, 2006. **128**(25): p. 8110-8111.

182. Li, Y. and A.G. Palmer, 3rd, *TROSY-selected ZZ-exchange experiment for characterizing slow chemical exchange in large proteins.* J Biomol NMR, 2009. **45**(4): p. 357-60.

183. J.J., S., *Modern Quantum Mechanics.* 1994.

184. Abragam, A., *Principles of Nuclear Magnetism.* 1961.

185. Ernst, R.R., Bodenhausen, G., Wokaun, A., *Principles of Nuclear Magnetic Resonance in One and Two Dimensions.* 1987.

186. Jarymowycz, V.A. and M.J. Stone, *Fast time scale dynamics of protein backbones: NMR relaxation methods, applications, and functional consequences.* Chem Rev, 2006. **106**(5): p. 1624-71.

187. Macura, S. and R.R. Ernst, *Elucidation of cross relaxation in liquids by two-dimensional N.M.R. spectroscopy.* Molecular Physics, 1980. **41**(1): p. 95-117.

188. Woessner, D.E., *Spin Relaxation Processes in a Two-Proton System Undergoing Anisotropic Reorientation.* The Journal of Chemical Physics, 1962. **36**(1): p. 1.

189. Brainard, J.R. and A. Szabo, *Theory for nuclear magnetic relaxation of probes in anisotropic systems: application of cholesterol in phospholipid vesicles.* Biochemistry, 1981. **20**(16): p. 4618-28.

190. Lipari, G. and A. Szabo, *Model-Free Approach to the Interpretation of Nuclear Magnetic-Resonance Relaxation in Macromolecules .1. Theory and Range of Validity.* Journal of the American Chemical Society, 1982. **104**(17): p. 4546-4559.

191. Lipari, G. and A. Szabo, *Model-Free Approach to the Interpretation of Nuclear Magnetic-Resonance Relaxation in Macromolecules .2. Analysis of Experimental Results.* Journal of the American Chemical Society, 1982. **104**(17): p. 4559-4570.

192. Lee, A.L., P.F. Flynn, and A.J. Wand, *Comparison of 2H and 13C NMR Relaxation Techniques for the Study of Protein Methyl Group Dynamics in Solution.* Journal of the American Chemical Society, 1999. **121**(12): p. 2891-2902.

193. Ishima, R., et al., *Comparison of Methyl Rotation Axis Order Parameters Derived from Model-Free Analyses of2H and13C Longitudinal and Transverse Relaxation Rates Measured in the Same Protein Sample.* Journal of the American Chemical Society, 2001. **123**(25): p. 6164-6171.

194. Farrow, N.A., et al., *Backbone dynamics of a free and phosphopeptide-complexed Src homology 2 domain studied by 15N NMR relaxation.* Biochemistry, 1994. **33**(19): p. 5984-6003.

195. Kay, L.E., D.A. Torchia, and A. Bax, *Backbone dynamics of proteins as studied by nitrogen-15 inverse detected heteronuclear NMR spectroscopy: application to staphylococcal nuclease.* Biochemistry, 1989. **28**(23): p. 8972-8979.

196. Palmer, A.G., 3rd, *Nmr probes of molecular dynamics: overview and comparison with other techniques.* Annu Rev Biophys Biomol Struct, 2001. **30**: p. 129-55.

197. Yao, L., et al., *NMR determination of amide N-H equilibrium bond length from concerted dipolar coupling measurements.* J Am Chem Soc, 2008. **130**(49): p. 16518-20.

198. Oas, T.G., et al., *The amide nitrogen-15 chemical shift tensors of four peptides determined from carbon-13 dipole-coupled chemical shift powder patterns.* Journal of the American Chemical Society, 1987. **109**(20): p. 5962-5966.

199. Tjandra, N., A. Szabo, and A. Bax, *Protein Backbone Dynamics and 15N Chemical Shift Anisotropy from Quantitative Measurement of Relaxation Interference Effects.* Journal of the American Chemical Society, 1996. **118**(29): p. 6986-6991.

200. Carr, H. and E. Purcell, *Effects of Diffusion on Free Precession in Nuclear Magnetic Resonance Experiments.* Physical Review, 1954. **94**(3): p. 630-638.

201. Meiboom, S. and D. Gill, *Modified Spin-Echo Method for Measuring Nuclear Relaxation Times.* Review of Scientific Instruments, 1958. **29**(8): p. 688.

202. Solomon, I., *Relaxation Processes in a System of Two Spins.* Physical Review, 1955. **99**(2): p. 559-565.

203. Ha, K.N., et al., *Controlling the inhibition of the sarcoplasmic Ca2+-ATPase by tuning phospholamban structural dynamics.* J Biol Chem, 2007. **282**(51): p. 37205-14.

204. Jensen, M.R., et al., *Exploring free-energy landscapes of intrinsically disordered proteins at atomic resolution using NMR spectroscopy.* Chem Rev, 2014. **114**(13): p. 6632-60.

205. Kragelj, J., et al., *Structure and dynamics of the MKK7-JNK signaling complex.* Proc Natl Acad Sci U S A, 2015. **112**(11): p. 3409-14.

206. Tugarinov, V. and L.E. Kay, *Relaxation Rates of Degenerate 1H Transitions in Methyl Groups of Proteins as Reporters of Side-Chain Dynamics.* Journal of the American Chemical Society, 2006. **128**(22): p. 7299-7308.

207. Tugarinov, V., R. Sprangers, and L.E. Kay, *Probing side-chain dynamics in the proteasome by relaxation violated coherence transfer NMR spectroscopy.* J Am Chem Soc, 2007. **129**(6): p. 1743-50.

208. Sun, H., L.E. Kay, and V. Tugarinov, *An optimized relaxation-based coherence transfer NMR experiment for the measurement of side-chain order in methyl-protonated, highly deuterated proteins.* J Phys Chem B, 2011. **115**(49): p. 14878-84.

209. Igumenova, T.I., K.K. Frederick, and A.J. Wand, *Characterization of the fast dynamics of protein amino acid side chains using NMR relaxation in solution.* Chem Rev, 2006. **106**(5): p. 1672-99.

210. Tugarinov, V., J.E. Ollerenshaw, and L.E. Kay, *Probing side-chain dynamics in high molecular weight proteins by deuterium NMR spin relaxation: an application to an 82-kDa enzyme.* J Am Chem Soc, 2005. **127**(22): p. 8214-25.

211. Millet, O., et al., *Deuterium Spin Probes of Side-Chain Dynamics in Proteins. 1. Measurement of Five Relaxation Rates per Deuteron in13C-Labeled and Fractionally2H-Enriched Proteins in Solution.* Journal of the American Chemical Society, 2002. **124**(22): p. 6439-6448.

212. Skrynnikov, N.R., O. Millet, and L.E. Kay, *Deuterium spin probes of side-chain dynamics in proteins. 2. Spectral density mapping and identification of nanosecond time-scale side-chain motions.* J Am Chem Soc, 2002. **124**(22): p. 6449-60.

213. Mittermaier, A. and L.E. Kay, *Measurement of Methyl2H Quadrupolar Couplings in Oriented Proteins. How Uniform Is the Quadrupolar Coupling Constant?* Journal of the American Chemical Society, 1999. **121**(45): p. 10608-10613.

214. Tugarinov, V. and L.E. Kay, *A 2H NMR Relaxation Experiment for the Measurement of the Time Scale of Methyl Side-Chain Dynamics in Large Proteins.* Journal of the American Chemical Society, 2006. **128**(38): p. 12484-12489.

215. Gueron, M., J.L. Leroy, and R.H. Griffey, *Proton nuclear magnetic relaxation of nitrogen-15-labeled nucleic acids via dipolar coupling and chemical shift anisotropy.* Journal of the American Chemical Society, 1983. **105**(25): p. 7262-7266.

216. Goldman, M., *Interference effects in the relaxation of a pair of unlike nuclei.* Journal of Magnetic Resonance (1969), 1984. **60**(3): p. 437-452.

217. Cornilescu, G. and A. Bax, *Measurement of proton, nitrogen, and carbonyl chemical shielding anisotropies in a protein dissolved in a dilute liquid crystalline phase.* Journal of the American Chemical Society, 2000. **122**(41): p. 10143-10154.

218. Dalvit, C. and G. Bodenhausen, *Proton Chemical-Shift Anisotropy - Detection of Cross-Correlation with Dipole-Dipole Interactions by Double-Quantum Filtered Two-Dimensional Nmr Exchange Spectroscopy.* Chemical Physics Letters, 1989. **161**(6): p. 554-560.

219. Pervushin, K., *Impact of Transverse Relaxation Optimized Spectroscopy (TROSY) on NMR as a technique in structural biology.* Quarterly Reviews of Biophysics, 2000. **33**(2): p. 161-197.

220. Kay, L.E., et al., *Pulse sequences for removal of the effects of cross correlation between dipolar and chemical-shift anisotropy relaxation mechanisms on the measurement of heteronuclear T1 and T2 values in proteins.* Journal of Magnetic Resonance (1969), 1992. **97**(2): p. 359-375.

221. Palmer, A.G., et al., *Suppression of the Effects of Cross-Correlation between Dipolar and Anisotropic Chemical-Shift Relaxation Mechanisms in the Measurement of Spin Spin Relaxation Rates.* Molecular Physics, 1992. **75**(3): p. 699-711.

222. Dalvit, C., *1H to 15N polarization transfer via 1H chemical-shift anisotropy — 1H-15N dipole-dipole cross correlation.* Journal of Magnetic Resonance (1969), 1992. **97**(3): p. 645-650.

223. Pervushin, K.V., G. Wider, and K. Wuthrich, *Single Transition-to-single Transition Polarization Transfer (ST2-PT) in [15N,1H]-TROSY.* J Biomol NMR, 1998. **12**(2): p. 345-8.

224. Yang, D. and L.E. Kay, *Improved 1HN-detected triple resonance TROSY-based experiments.* J Biomol NMR, 1999. **13**(1): p. 3-10.

225. Schulte-Herbrüggen, T. and O.W. Sørensen, *Clean TROSY: Compensation for Relaxation-Induced Artifacts.* Journal of Magnetic Resonance, 2000. **144**(1): p. 123-128.

226. Nietlispach, D., *Suppression of anti-TROSY lines in a sensitivity enhanced gradient selection TROSY scheme.* J Biomol NMR, 2005. **31**(2): p. 161-6.

227. Riek, R., K. Pervushin, and K. Wuthrich, *TROSY and CRINEPT: NMR with large molecular and supramolecular structures in solution.* Trends Biochem Sci, 2000. **25**(10): p. 462-8.

228. Riek, R., et al., *Polarization transfer by cross-correlated relaxation in solution NMR with very large molecules.* Proceedings of the National Academy of Sciences of the United States of America, 1999. **96**(9): p. 4918-4923.

229. Fiaux, J., et al., *NMR analysis of a 900K GroEL GroES complex.* Nature, 2002. **418**(6894): p. 207-11.

230. Rosenzweig, R. and L.E. Kay, *Bringing dynamic molecular machines into focus by methyl-TROSY NMR.* Annu Rev Biochem, 2014. **83**(1): p. 291-315.

231. Gardner, K.H. and L.E. Kay, *Production and Incorporation of15N,13C,2H (1H-δ1 Methyl) Isoleucine into Proteins for Multidimensional NMR Studies.* Journal of the American Chemical Society, 1997. **119**(32): p. 7599-7600.

232. Goto, N.K., et al., *A robust and cost-effective method for the production of Val, Leu, Ile (delta 1) methyl-protonated 15N-, 13C-, 2H-labeled proteins.* J Biomol NMR, 1999. **13**(4): p. 369-74.

233. Ruschak, A.M., A. Velyvis, and L.E. Kay, *A simple strategy for (1)(3)C, (1)H labeling at the Ile-gamma2 methyl position in highly deuterated proteins.* J Biomol NMR, 2010. **48**(3): p. 129-35.

234. Zecevic, A., et al., *Dephasing of electron spin echoes for nitroxyl radicals in glassy solvents by non-methyl and methyl protons.* Molecular Physics, 1998. **95**(6): p. 1255-1263.

235. Jeschke, G. and Y. Polyhach, *Distance measurements on spin-labelled biomacromolecules by pulsed electron paramagnetic resonance.* Phys Chem Chem Phys, 2007. **9**(16): p. 1895-910.

236. Tugarinov, V. and L. Kay, *1H,13C-1H,1H Dipolar Cross-correlated Spin Relaxation in Methyl Groups.* Journal of Biomolecular NMR, 2004. **29**(3): p. 369-376.

237. Kay, L.E. and J.H. Prestegard, *Methyl-Group Dynamics from Relaxation of Double Quantum Filtered Nmr Signals - Application to Deoxycholate.* Journal of the American Chemical Society, 1987. **109**(13): p. 3829-3835.

238. Kay, L.E. and T.E. Bull, *Heteronuclear transverse relaxation in AMX, AX2, and AX3 spin systems.* Journal of Magnetic Resonance (1969), 1992. **99**(3): p. 615-622.

239. Kay, L.E., et al., *The Measurement of Heteronuclear Transverse Relaxation-Times in Ax3 Spin Systems Via Polarization-Transfer Techniques.* Journal of Magnetic Resonance, 1992. **100**(3): p. 538-558.

240. Müller, N., G. Bodenhausen, and R.R. Ernst, *Relaxation-induced violations of coherence transfer selection rules in nuclear magnetic resonance.* Journal of Magnetic Resonance (1969), 1987. **75**(2): p. 297-334.

241. Werbelow, L.G. and D.M. Grant, *Intramolecular Dipolar Relaxation in Multispin Systems*, in *Advances in Magnetic and Optical Resonance*, W. John S, Editor. 1977, Academic Press. p. 189-299.

242. Ollerenshaw, J.E., V. Tugarinov, and L.E. Kay, *Methyl TROSY: explanation and experimental verification.* Magnetic Resonance in Chemistry, 2003. **41**(10): p. 843-852.

243. Tugarinov, V., et al., *Cross-correlated relaxation enhanced 1H[bond]13C NMR spectroscopy of methyl groups in very high molecular weight proteins and protein complexes.* J Am Chem Soc, 2003. **125**(34): p. 10420-8.

244. Kay, L.E., *NMR studies of protein structure and dynamics.* J Magn Reson, 2005. **173**(2): p. 193-207.

245. Sheppard, D., R. Sprangers, and V. Tugarinov, *Experimental approaches for NMR studies of side-chain dynamics in high-molecular-weight proteins.* Prog Nucl Magn Reson Spectrosc, 2010. **56**(1): p. 1-45.

246. Prestegard, J.H. and D.M. Grant, *Characterization of Anisotropic Motion in Fatty-Acid Micelles by Analysis of Transverse Relaxation in an Ax2 Nuclear-Spin System.* Journal of the American Chemical Society, 1978. **100**(15): p. 4664-4668.

247. Meier, B.H. and R.R. Ernst, *Elucidation of chemical exchange networks by two-dimensional NMR spectroscopy: the heptamethylbenzenonium ion.* Journal of the American Chemical Society, 1979. **101**(21): p. 6441-6442.

248. McConnell, H.M., *Reaction Rates by Nuclear Magnetic Resonance.* The Journal of Chemical Physics, 1958. **28**(3): p. 430.

249. Wennerström, H., *Nuclear magnetic relaxation induced by chemical exchange.* Molecular Physics, 1972. **24**(1): p. 69-80.

250. Davis, D.G., Perlman M. E., London, R. E., *Direct Measurement of the Dissociation -Rate Constant for Inhibitor-Enzyme Complexes via the T1rho and T2 (CPMG) Methods.* J Magn Reson B, 1994. **104**: p. 266-275.

251. Montelione, G.T. and G. Wagner, *2d Chemical-Exchange Nmr-Spectroscopy by Proton-Detected Heteronuclear Correlation.* Journal of the American Chemical Society, 1989. **111**(8): p. 3096-3098.

252. Farrow, N.A., et al., *A heteronuclear correlation experiment for simultaneous determination of 15N longitudinal decay and chemical exchange rates of systems in slow equilibrium.* J Biomol NMR, 1994. **4**(5): p. 727-34.

253. Leigh, J.S., *Relaxation times in systems with chemical exchange: Some exact solutions.* Journal of Magnetic Resonance (1969), 1971. **4**(3): p. 308-311.

254. Baldwin, A.J. and L.E. Kay, *NMR spectroscopy brings invisible protein states into focus.* Nat Chem Biol, 2009. **5**(11): p. 808-14.

255. Spiess, H.W., *Molecular motion studied by NMR powder spectra. I. Lineshape calculation for axially symmetric sheilding tensors.* Chemical Physics, 1974. **6**(2): p. 217-225.

256. Ishima, R. and D.A. Torchia, *Estimating the time scale of chemical exchange of proteins from measurements of transverse relaxation rates in solution.* J Biomol NMR, 1999. **14**(4): p. 369-72.

257. Millet, O., et al., *The static magnetic field dependence of chemical exchange linebroadening defines the NMR chemical shift time scale.* Journal of the American Chemical Society, 2000. **122**(12): p. 2867-2877.

258. Akke, M. and A.G. Palmer, *Monitoring Macromolecular Motions on Microsecond to Millisecond Time Scales by R1ρ−R1 Constant Relaxation Time NMR Spectroscopy.* Journal of the American Chemical Society, 1996. **118**(4): p. 911-912.

259. Deverell, C., R.E. Morgan, and J.H. Strange, *Studies of chemical exchange by nuclear magnetic relaxation in the rotating frame.* Molecular Physics, 1970. **18**(4): p. 553-559.

260. Korzhnev, D.M., V.Y. Orekhov, and L.E. Kay, *Off-resonance R(1rho) NMR studies of exchange dynamics in proteins with low spin-lock fields: an application to a Fyn SH3 domain.* J Am Chem Soc, 2005. **127**(2): p. 713-21.

261. Palmer, A.G. and F. Massi, *Characterization of the Dynamics of Biomacromolecules Using Rotating-Frame Spin Relaxation NMR Spectroscopy.* Chemical Reviews, 2006. **106**(5): p. 1700-1719.

262.   Mangia, S., et al., *Probing slow protein dynamics by adiabatic R(1rho) and R(2rho) NMR experiments.* J Am Chem Soc, 2010. **132**(29): p. 9979-81.

263.   Traaseth, N.J., et al., *Heteronuclear Adiabatic Relaxation Dispersion (HARD) for quantitative analysis of conformational dynamics in proteins.* J Magn Reson, 2012. **219**(0): p. 75-82.

264.   Allerhand, A. and H.S. Gutowsky, *Spin—Echo NMR Studies of Chemical Exchange. I. Some General Aspects.* The Journal of Chemical Physics, 1964. **41**(7): p. 2115.

265.   Allerhand, A. and H.S. Gutowsky, *Spin-Echo Studies of Chemical Exchange. Ii. Closed Formulas for Two Sites.* J Chem Phys, 1965. **42**(5): p. 1587-99.

266.   Carver, J.P. and R.E. Richards, *A general two-site solution for the chemical exchange produced dependence of T2 upon the carr-Purcell pulse separation.* Journal of Magnetic Resonance (1969), 1972. **6**(1): p. 89-105.

267.   Ishima, R. and D.A. Torchia, *Accuracy of optimized chemical-exchange parameters derived by fitting CPMG R2 dispersion profiles when R2(0a) not = R2(0b).* J Biomol NMR, 2006. **34**(4): p. 209-19.

268.   Kovrigin, E.L., et al., *Faithful estimation of dynamics parameters from CPMG relaxation dispersion measurements.* J Magn Reson, 2006. **180**(1): p. 93-104.

269.   Vold, R.R. and R.L. Vold, *Transverse Relaxation in Heteronuclear Coupled Spin Systems - Ax, Ax2, Ax3, and Axy.* Journal of Chemical Physics, 1976. **64**(1): p. 320-332.

270.   Loria, J.P., M. Rance, and A.G. Palmer, *A Relaxation-Compensated Carr–Purcell–Meiboom–Gill Sequence for Characterizing Chemical Exchange by NMR Spectroscopy.* Journal of the American Chemical Society, 1999. **121**(10): p. 2331-2332.

271.   Skrynnikov, N.R., et al., *Probing slow time scale dynamics at methyl-containing side chains in proteins by relaxation dispersion NMR measurements: Application to methionine residues in a cavity mutant of T4 lysozyme.* Journal of the American Chemical Society, 2001. **123**(19): p. 4556-4566.

272.   Mulder, F.A.A., et al., *Measurement of Slow (µs–ms) Time Scale Dynamics in Protein Side Chains by15N Relaxation Dispersion NMR Spectroscopy: Application to Asn and Gln Residues in a Cavity Mutant of T4 Lysozyme.* Journal of the American Chemical Society, 2001. **123**(5): p. 967-975.

273.   Tollinger, M., et al., *Slow dynamics in folded and unfolded states of an SH3 domain.* Journal of the American Chemical Society, 2001. **123**(46): p. 11341-11352.

274.   Boehr, D.D., et al., *Millisecond timescale fluctuations in dihydrofolate reductase are exquisitely sensitive to the bound ligands.* Proc Natl Acad Sci U S A, 2010. **107**(4): p. 1373-8.

275.   Religa, T.L., R. Sprangers, and L.E. Kay, *Dynamic regulation of archaeal proteasome gate opening as studied by TROSY NMR.* Science, 2010. **328**(5974): p. 98-102.

276.   Fushman, D., N. Tjandra, and D. Cowburn, *Direct Measurement of15N Chemical Shift Anisotropy in Solution.* Journal of the American Chemical Society, 1998. **120**(42): p. 10947-10952.

277.   Kroenke, C.D., M. Rance, and A.G. Palmer, *Variability of the15N Chemical Shift Anisotropy inEscherichia coliRibonuclease H in Solution.* Journal of the American Chemical Society, 1999. **121**(43): p. 10119-10125.

278.   Fenwick, M.K. and R.E. Oswald, *NMR spectroscopy of the ligand-binding core of ionotropic glutamate receptor 2 bound to 5-substituted willardiine partial agonists.* J Mol Biol, 2008. **378**(3): p. 673-85.

279.   Leavitt, S. and E. Freire, *Direct measurement of protein binding energetics by isothermal titration calorimetry.* Curr Opin Struct Biol, 2001. **11**(5): p. 560-6.

280.   Wiseman, T., et al., *Rapid Measurement of Binding Constants and Heats of Binding Using a New Titration Calorimeter.* Analytical Biochemistry, 1989. **179**(1): p. 131-137.

281.   Freire, E., A. Schön, and A. Velazquez-Campoy, *Chapter 5 Isothermal Titration Calorimetry.* 2009. **455**: p. 127-155.

282.   Herrera, I. and M.A. Winnik, *Differential binding models for isothermal titration calorimetry: moving beyond the Wiseman isotherm.* J Phys Chem B, 2013. **117**(29): p. 8659-72.

283.   Sigurskjold, B.W., *Exact analysis of competition ligand binding by displacement isothermal titration calorimetry.* Anal Biochem, 2000. **277**(2): p. 260-6.

284.   Turnbull, W.B. and A.H. Daranas, *On the value of c: can low affinity systems be studied by isothermal titration calorimetry?* J Am Chem Soc, 2003. **125**(48): p. 14859-66.

285.   Tellinghuisen, J., *Optimizing Experimental Parameters in Isothermal Titration Calorimetry.* The Journal of Physical Chemistry B, 2005. **109**(42): p. 20027-20035.

286.   Tellinghuisen, J., *Optimizing Experimental Parameters in Isothermal Titration Calorimetry: Variable Volume Procedures.* The Journal of Physical Chemistry B, 2007. **111**(39): p. 11531-11537.

287.   Whitty, A., *Cooperativity and biological complexity.* Nat Chem Biol, 2008. **4**(8): p. 435-9.

288.   Shuker, S.B., et al., *Discovering high-affinity ligands for proteins: SAR by NMR.* Science, 1996. **274**(5292): p. 1531-4.

289.   Jencks, W.P., *On the attribution and additivity of binding energies.* Proc Natl Acad Sci U S A, 1981. **78**(7): p. 4046-50.

290.   Frederick, K.K., et al., *Conformational entropy in molecular recognition by proteins.* Nature, 2007. **448**(7151): p. 325-329.

291.   Marlow, M.S., et al., *The role of conformational entropy in molecular recognition by calmodulin.* Nat Chem Biol, 2010. **6**(5): p. 352-8.

292.   Grunberg, R., M. Nilges, and J. Leckner, *Flexibility and conformational entropy in protein-protein binding.* Structure, 2006. **14**(4): p. 683-93.

293.   Polyansky, A., R. Zubac, and B. Zagrovic, *Estimation of Conformational Entropy in Protein–Ligand Interactions: A Computational Perspective*, in *Computational Drug Discovery and Design*, R. Baron, Editor. 2012, Springer New York. p. 327-353.

294.   Karplus, M. and J.A. McCammon, *Molecular dynamics simulations of biomolecules.* Nat Struct Mol Biol, 2002. **9**(9): p. 646-652.

295.   Griko, Y.V., *Energetics of Ca2+–EDTA interactions: calorimetric study.* Biophysical Chemistry, 1999. **79**(2): p. 117-127.

296.   Wyman, J., *The Binding Potential, a Neglected Linkage Concept.* J Mol Biol, 1965. **11**(3): p. 631-44.

297.   Fersht, A.R., A. Matouschek, and L. Serrano, *The folding of an enzyme. I. Theory of protein engineering analysis of stability and pathway of protein folding.* J Mol Biol, 1992. **224**(3): p. 771-82.

298.   Horovitz, A. and A.R. Fersht, *Co-operative interactions during protein folding.* J Mol Biol, 1992. **224**(3): p. 733-40.

299.   Horovitz, A., *Double-mutant cycles: a powerful tool for analyzing protein structure and function.* Folding and Design, 1996. **1**(6): p. R121-R126.

300.   Serrano, L., M. Bycroft, and A.R. Fersht, *Aromatic-aromatic interactions and protein stability. Investigation by double-mutant cycles.* J Mol Biol, 1991. **218**(2): p. 465-75.

301.   McLaughlin Jr, R.N., et al., *The spatial architecture of protein function and adaptation.* Nature, 2012. **491**(7422): p. 138-142.

302. Sadovsky, E. and O. Yifrach, *Principles underlying energetic coupling along an allosteric communication trajectory of a voltage-activated K+ channel.* Proc Natl Acad Sci U S A, 2007. **104**(50): p. 19813-8.

303. Monod, J., J. Wyman, and J.P. Changeux, *On the Nature of Allosteric Transitions: A Plausible Model.* J Mol Biol, 1965. **12**(1): p. 88-118.

304. Koshland, D.E., Jr., G. Nemethy, and D. Filmer, *Comparison of experimental binding data and theoretical models in proteins containing subunits.* Biochemistry, 1966. **5**(1): p. 365-85.

305. Garcia, H.G., et al., *Chapter Two - Thermodynamics of Biological Processes*, in *Methods in Enzymology*, J.M.H. Michael L. Johnson and K.A. Gary, Editors. 2011, Academic Press. p. 27-59.

306. Hilser, V.J., et al., *A statistical thermodynamic model of the protein ensemble.* Chem Rev, 2006. **106**(5): p. 1545-58.

307. Hilser, V.J. and E.B. Thompson, *Intrinsic disorder as a mechanism to optimize allosteric coupling in proteins.* Proc Natl Acad Sci U S A, 2007. **104**(20): p. 8311-5.

308. Neudecker, P., et al., *Structure of an intermediate state in protein folding and aggregation.* Science, 2012. **336**(6079): p. 362-6.

309. Tzeng, S.R. and C.G. Kalodimos, *Allosteric inhibition through suppression of transient conformational states.* Nat Chem Biol, 2013. **9**(7): p. 462-5.

310. Sprangers, R. and L.E. Kay, *Quantitative dynamics and binding studies of the 20S proteasome by NMR.* Nature, 2007. **445**(7128): p. 618-22.

311. Tugarinov, V. and L.E. Kay, *Methyl groups as probes of structure and dynamics in NMR studies of high-molecular-weight proteins.* Chembiochem : a European journal of chemical biology, 2005. **6**(9): p. 1567-1577.

312. Tugarinov, V. and L.E. Kay, *Ile, Leu, and Val methyl assignments of the 723-residue malate synthase G using a new labeling strategy and novel NMR methods.* J Am Chem Soc, 2003. **125**(45): p. 13868-78.

313. Yang, D., et al., *Sequence-specific assignments of methyl groups in high-molecular weight proteins.* J Am Chem Soc, 2004. **126**(12): p. 3710-1.

314. Tugarinov, V., V. Venditti, and G. Marius Clore, *A NMR experiment for simultaneous correlations of valine and leucine/isoleucine methyls with carbonyl chemical shifts in proteins.* J Biomol NMR, 2014. **58**(1): p. 1-8.

315. Amero, C., et al., *A systematic mutagenesis-driven strategy for site-resolved NMR studies of supramolecular assemblies.* J Biomol NMR, 2011. **50**(3): p. 229-36.

316. Kato, H., et al., *Architecture of the high mobility group nucleosomal protein 2-nucleosome complex as revealed by methyl-based NMR.* Proc Natl Acad Sci U S A, 2011. **108**(30): p. 12283-8.

317. Velyvis, A., H.K. Schachman, and L.E. Kay, *Assignment of Ile, Leu, and Val methyl correlations in supra-molecular systems: an application to aspartate transcarbamoylase.* J Am Chem Soc, 2009. **131**(45): p. 16534-43.

318. Xu, Y., et al., *Automated assignment in selectively methyl-labeled proteins.* J Am Chem Soc, 2009. **131**(27): p. 9480-1.

319. Xu, Y. and S. Matthews, *MAP-XSII: an improved program for the automatic assignment of methyl resonances in large proteins.* J Biomol NMR, 2013. **55**(2): p. 179-87.

320. Chao, F.A., et al., *FLAMEnGO: a fuzzy logic approach for methyl group assignment using NOESY and paramagnetic relaxation enhancement data.* J Magn Reson, 2012. **214**(1): p. 103-10.

321. Hemmer, W., M. McGlone, and S.S. Taylor, *Recombinant strategies for rapid purification of catalytic subunits of cAMP-dependent protein kinase.* Anal Biochem, 1997. **245**(2): p. 115-22.

322. Brooks, B.R., et al., *Charmm - a Program for Macromolecular Energy, Minimization, and Dynamics Calculations.* Journal of Computational Chemistry, 1983. **4**(2): p. 187-217.

323. Sahakyan, A.B., et al., *Structure-based prediction of methyl chemical shifts in proteins.* J Biomol NMR, 2011. **50**(4): p. 331-46.

324. Schwieters, C.D., et al., *The Xplor-NIH NMR molecular structure determination package.* Journal of magnetic resonance (San Diego, Calif.: 1997), 2003. **160**(1): p. 65-73.

325. Venditti, V., N.L. Fawzi, and G.M. Clore, *Automated sequence- and stereo-specific assignment of methyl-labeled proteins by paramagnetic relaxation and methyl-methyl nuclear Overhauser enhancement spectroscopy.* J Biomol NMR, 2011. **51**(3): p. 319-28.

326. Crespi, H.L. and J.J. Katz, *High resolution proton magnetic resonance studies of fully deuterated and isotope hybrid proteins.* Nature, 1969. **224**(5219): p. 560-2.

327. Crespi, H.L., Rosenberg, R.M. Katzz, J.J., *proton magnetic resonance of proteins fully deuterated except for 1H-leucine side chains.* Science, 1968. **161**: p. 795-796.

328. Markley, J.L., I. Putter, and O. Jardetzky, *High-resolution nuclear magnetic resonance spectra of selectively deuterated staphylococcal nuclease.* Science, 1968. **161**(3847): p. 1249-51.

329. Putter, I., et al., *Nuclear magnetic resonance studies of the structure and binding sites of enzymes. X. Preparation of selectively deuterated analogs of staphylococcal nuclease.* Proc Natl Acad Sci U S A, 1969. **64**(4): p. 1396-403.

330. Meissner, A. and O.W. Sorensen, *Optimization of three-dimensional TROSY-type HCCH NMR correlation of aromatic (1)H-(13)C groups in proteins.* J Magn Reson, 1999. **139**(2): p. 447-50.

331. Kainosho, M., et al., *Optimal isotope labelling for NMR protein structure determinations.* Nature, 2006. **440**(7080): p. 52-7.

332. Kasinath, V., K.G. Valentine, and A.J. Wand, *A 13C labeling strategy reveals a range of aromatic side chain motion in calmodulin.* J Am Chem Soc, 2013. **135**(26): p. 9560-3.

333. Venters, R.A., et al., *High-level 2H/13C/15N labeling of proteins for NMR studies.* J Biomol NMR, 1995. **5**(4): p. 339-44.

334. Nietlispach, D., et al., *An Approach to the Structure Determination of Larger Proteins Using Triple Resonance NMR Experiments in Conjunction with Random Fractional Deuteration.* Journal of the American Chemical Society, 1996. **118**(2): p. 407-415.

335. Gelis, I., et al., *Structural basis for signal-sequence recognition by the translocase motor SecA as determined by NMR.* Cell, 2007. **131**(4): p. 756-69.

336. Velyvis, A., A.M. Ruschak, and L.E. Kay, *An economical method for production of (2)H, (13)CH3-threonine for solution NMR studies of large protein complexes: application to the 670 kDa proteasome.* PLoS One, 2012. **7**(9): p. e43725.

337. Ayala, I., et al., *An efficient protocol for the complete incorporation of methyl-protonated alanine in perdeuterated protein.* J Biomol NMR, 2009. **43**(2): p. 111-9.

338. Ruschak, A.M., et al., *The proteasome antechamber maintains substrates in an unfolded state.* Nature, 2010. **467**(7317): p. 868-71.

339. Shi, L. and L.E. Kay, *Tracing an allosteric pathway regulating the activity of the HslV protease.* Proc Natl Acad Sci U S A, 2014. **111**(6): p. 2140-5.

340. Saio, T., et al., *Structural basis for protein antiaggregation activity of the trigger factor chaperone.* Science, 2014. **344**(6184): p. 1250494.

341. Tzeng, S.R. and C.G. Kalodimos, *Protein activity regulation by conformational entropy.* Nature, 2012. **488**(7410): p. 236-40.

342. Religa, T.L., et al., *Site-directed methyl group labeling as an NMR probe of structure and dynamics in supramolecular protein systems: applications to the proteasome and to the ClpP protease.* J Am Chem Soc, 2011. **133**(23): p. 9063-8.

343. Narayana, N., et al., *Crystal structure of a polyhistidine-tagged recombinant catalytic subunit of cAMP-dependent protein kinase complexed with the peptide inhibitor PKI(5-24) and adenosine.* Biochemistry, 1997. **36**(15): p. 4438-48.

344. Yonemoto, W.M., et al., *Prokaryotic expression of catalytic subunit of adenosine cyclic monophosphate-dependent protein kinase.* Methods Enzymol, 1991. **200**: p. 581-96.

345. Gardner, K.H., et al., *Solution NMR Studies of a 42 KDaEscherichiaColiMaltose Binding Protein/β-Cyclodextrin Complex: Chemical Shift Assignments and Analysis.* Journal of the American Chemical Society, 1998. **120**(45): p. 11738-11748.

346. Studier, F.W., *Protein production by auto-induction in high density shaking cultures.* Protein Expr Purif, 2005. **41**(1): p. 207-34.

347. Sattler, M., J. Schleucher, and C. Griesinger, *Heteronuclear multidimensional NMR experiments for the structure determination of proteins in solutions employing pulsed field gradients.* Prog. Nucl. Magn. Reson. Spectrosc., 1999. **34**: p. 93-158.

348. Tugarinov, V. and L.E. Kay, *Side chain assignments of Ile delta 1 methyl groups in high molecular weight proteins: an application to a 46 ns tumbling molecule.* J Am Chem Soc, 2003. **125**(19): p. 5701-6.

349. Sheppard, D., C. Guo, and V. Tugarinov, *Methyl-detected 'out-and-back' NMR experiments for simultaneous assignments of Alabeta and Ilegamma2 methyl groups in large proteins.* J Biomol NMR, 2009. **43**(4): p. 229-38.

350. Chao, F.A., et al., *FLAMEnGO 2.0: An enhanced fuzzy logic algorithm for structure-based assignment of methyl group resonances.* J Magn Reson, 2014. **245**: p. 17-23.

351. Battiste, J.L. and G. Wagner, *Utilization of site-directed spin labeling and high-resolution heteronuclear nuclear magnetic resonance for global fold determination of large proteins with limited nuclear overhauser effect data.* Biochemistry, 2000. **39**(18): p. 5355-5365.

352. Han, B., et al., *SHIFTX2: significantly improved protein chemical shift prediction.* J Biomol NMR, 2011. **50**(1): p. 43-57.

353. Li, D.W. and R. Bruschweiler, *PPM: a side-chain and backbone chemical shift predictor for the assessment of protein conformational ensembles.* J Biomol NMR, 2012. **54**(3): p. 257-65.

354. Bryngelson, J.D., et al., *Funnels, pathways, and the energy landscape of protein folding: a synthesis.* Proteins, 1995. **21**(3): p. 167-95.

355. Oliveberg, M. and P.G. Wolynes, *The experimental survey of protein-folding energy landscapes.* Q Rev Biophys, 2005. **38**(3): p. 245-88.

356. Tsai, C.J., et al., *Folding funnels, binding funnels, and protein function.* Protein Science, 1999. **8**(6): p. 1181-1190.

357. Kumar, S., et al., *Folding and binding cascades: Dynamic landscapes and population shifts.* Protein Science, 2000. **9**(1): p. 10-19.

358. Csermely, P., R. Palotai, and R. Nussinov, *Induced fit, conformational selection and independent dynamic segments: an extended view of binding events.* Trends in Biochemical Sciences, 2010. **35**(10): p. 539-546.

359. Monod, J., J. Wyman, and J.P. Changeux, *ON THE NATURE OF ALLOSTERIC TRANSITIONS: A PLAUSIBLE MODEL.* Journal of molecular biology, 1965. **12**: p. 88-118.

360. Kay, L.E., *NMR studies of protein structure and dynamics.* Journal of Magnetic Resonance, 2005. **173**(2): p. 193-207.

361. Tugarinov, V., P.M. Hwang, and L.E. Kay, *Nuclear magnetic resonance spectroscopy of high-molecular-weight proteins.* Annual Review of Biochemistry, 2004. **73**: p. 107-146.

362. Tzeng, S.R., M.T. Pai, and C.G. Kalodimos, *NMR studies of large protein systems.* Methods Mol Biol, 2012. **831**: p. 133-40.

363. Bodenhausen, G. and D.J. Ruben, *Natural abundance nitrogen-15 NMR by enhanced heteronuclear spectroscopy.* Chem Phys Letters, 1980. **69**(1): p. 185-189.

364. Zhuravleva, A. and L.M. Gierasch, *Allosteric signal transmission in the nucleotide-binding domain of 70-kDa heat shock protein (Hsp70) molecular chaperones.* Proceedings of the National Academy of Sciences of the United States of America, 2011. **108**(17): p. 6987-6992.

365. Revington, M., et al., *NMR investigations of allosteric processes in a two-domain Thermus thermophilus Hsp70 molecular chaperone.* Journal of Molecular Biology, 2005. **349**(1): p. 163-183.

366. Shen, Y., et al., *Consistent blind protein structure generation from NMR chemical shift data.* Proc Natl Acad Sci U S A, 2008. **105**(12): p. 4685-90.

367. Cavalli, A., et al., *Protein structure determination from NMR chemical shifts.* Proceedings of the National Academy of Sciences of the United States of America, 2007. **104**(23): p. 9615-9620.

368. Li, P., et al., *Internal dynamics control activation and activity of the autoinhibited Vav DH domain.* Nature Structural & Molecular Biology, 2008. **15**(6): p. 613-618.

369. Strickland, D., et al., *Rationally improving LOV domain-based photoswitches.* Nature Methods, 2010. **7**(8): p. 623-U18.

370. Das, R. and G. Melacini, *A model for agonism and antagonism in an ancient and ubiquitous cAMP-binding domain.* The Journal of biological chemistry, 2007. **282**(1).

371. Sakurai, K. and Y. Goto, *Principal component analysis of the pH-dependent conformational transitions of bovine beta-lactoglobulin monitored by heteronuclear NMR.* Proc Natl Acad Sci U S A, 2007. **104**(39): p. 15346-51.

372. Selvaratnam, R., et al., *Mapping allostery through the covariance analysis of NMR chemical shifts.* Proc Natl Acad Sci U S A, 2011. **108**(15): p. 6133-8.

373. Selvaratnam, R., et al., *The projection analysis of NMR chemical shifts reveals extended EPAC autoinhibition determinants.* Biophys J, 2012. **102**(3): p. 630-9.

374. Akimoto, M., et al., *Signaling through dynamic linkers as revealed by PKA.* Proc Natl Acad Sci U S A, 2013. **110**(35): p. 14231-6.

375. Selvaratnam, R., et al., *The Auto-Inhibitory Role of the EPAC Hinge Helix as Mapped by NMR.* PLoS ONE, 2012. **7**(11): p. e48707.

376. Dawson, J.E., P.J. Farber, and J.D. Forman-Kay, *Allosteric Coupling between the Intracellular Coupling Helix 4 and Regulatory Sites of the First Nucleotide-binding Domain of CFTR.* PLoS One, 2013. **8**(9): p. e74347.

377. Stollar, E.J., et al., *Differential dynamic engagement within 24 SH3 domain: peptide complexes revealed by co-linear chemical shift perturbation analysis.* PLoS One, 2012. **7**(12): p. e51282.

378. Arai, M., J.C. Ferreon, and P.E. Wright, *Quantitative analysis of multisite protein-ligand interactions by NMR: binding of intrinsically disordered p53 transactivation subdomains with the TAZ2 domain of CBP.* J Am Chem Soc, 2012. **134**(8): p. 3792-803.

379. Knighton, D.R., et al., *Structure of a peptide inhibitor bound to the catalytic subunit of cyclic adenosine monophosphate-dependent protein kinase.* Science, 1991. **253**(5018): p. 414-20.

380. Johnson, D.A., et al., *Dynamics of cAMP-dependent protein kinase.* Chemical Reviews, 2001. **101**(8): p. 2243-2270.

381. Konuma, T., et al., *Principal component analysis of chemical shift perturbation data of a multiple-ligand-binding system for elucidation of respective binding mechanism.* Proteins, 2013. **81**(1): p. 107-18.

382. Kornev, A.P. and S.S. Taylor, *Defining the conserved internal architecture of a protein kinase.* Biochim Biophys Acta, 2010. **1804**(3): p. 440-4.

383. Hilser, V.J., J.O. Wrabl, and H.N. Motlagh, *Structural and energetic basis of allostery.* Annu Rev Biophys, 2012. **41**: p. 585-609.

384. Fischer, E., *Einfluss der Configuration auf die Wirkung der Enzyme.* Berichte der deutschen chemischen Gesellschaft, 1894. **27**(3): p. 2985-2993.

385. Koshland, D.E., *Application of a Theory of Enzyme Specificity to Protein Synthesis.* Proceedings of the National Academy of Sciences, 1958. **44**(2): p. 98-104.

386. Pellicena, P. and J. Kuriyan, *Protein-protein interactions in the allosteric regulation of protein kinases.* Current Opinion in Structural Biology, 2006. **16**(6): p. 702-709.

387. Ma, B., et al., *Folding funnels and binding mechanisms.* Protein Eng, 1999. **12**(9): p. 713-20.

388. Tsai, C.J., et al., *Structured disorder and conformational selection.* Proteins-Structure Function and Genetics, 2001. **44**(4): p. 418-427.

389. Cui, Q. and M. Karplus, *Allostery and cooperativity revisited.* Protein Science, 2008. **17**(8): p. 1295-1307.

390. Kuzu, G., et al., *Expanding the conformational selection paradigm in protein-ligand docking.* Methods Mol Biol, 2012. **819**: p. 59-74.

391. Nussinov, R. and B. Ma, *Protein dynamics and conformational selection in bidirectional signal transduction.* BMC Biol, 2012. **10**: p. 2.

392. Nussinov, R., B. Ma, and C.J. Tsai, *Multiple conformational selection and induced fit events take place in allosteric propagation.* Biophys Chem, 2013.

393. Veglia, G. and A. Cembran, *Role of conformational entropy in the activity and regulation of the catalytic subunit of protein kinase A.* FEBS J, 2013. **280**(22): p. 5608-15.

394. Lockless, S.W. and R. Ranganathan, *Evolutionarily conserved pathways of energetic connectivity in protein families.* Science, 1999. **286**(5438): p. 295-299.

395. Suel, G.M., et al., *Evolutionarily conserved networks of residues mediate allosteric communication in proteins.* Nature Structural Biology, 2003. **10**(1): p. 59-69.

396. Krebs, E.G., D.J. Graves, and E.H. Fischer, *Factors affecting the activity of muscle phosphorylase b kinase.* J Biol Chem, 1959. **234**: p. 2867-73.

397. Scott, J.D. and T. Pawson, *Cell Signaling in Space and Time: Where Proteins Come Together and When They're Apart.* Science, 2009. **326**(5957): p. 1220-1224.

398. Zhang, P., et al., *Structure and allostery of the PKA RIIbeta tetrameric holoenzyme.* Science, 2012. **335**(6069): p. 712-6.

399. Lew, J., S.S. Taylor, and J.A. Adams, *Identification of a partially rate-determining step in the catalytic mechanism of cAMP-dependent protein kinase: a transient kinetic study using stopped-flow fluorescence spectroscopy.* Biochemistry, 1997. **36**(22).

400. Yang, J., et al., *Allosteric network of cAMP-dependent protein kinase revealed by mutation of Tyr204 in the P+1 loop.* Journal of Molecular Biology, 2005. **346**(1): p. 191-201.

401.   Iyer, G.H., M.J. Moore, and S.S. Taylor, *Consequences of lysine 72 mutation on the phosphorylation and activation state of cAMP-dependent kinase.* Journal of Biological Chemistry, 2005. **280**(10): p. 8800-8807.

402.   Iyer, G.H., et al., *Catalytic independent functions of a protein kinase as revealed by a kinase-dead mutant: Study of the Lys72His mutant of cAMP-dependent kinase.* Journal of Molecular Biology, 2005. **351**(5): p. 1110-1122.

403.   Yang, J., et al., *Crystal structure of a cAMP-dependent protein kinase mutant at 1.26A: new insights into the catalytic mechanism.* Journal of molecular biology, 2004. **336**(2).

404.   Moore, M.J., J.A. Adams, and S.S. Taylor, *Structural basis for peptide binding in protein kinase A. Role of glutamic acid 203 and tyrosine 204 in the peptide-positioning loop.* The Journal of biological chemistry, 2003. **278**(12).

405.   Aimes, R.T., W. Hemmer, and S.S. Taylor, *Serine-53 at the tip of the glycine-rich loop of cAMP-dependent protein kinase: Role in catalysis, P-site specificity, and interaction with inhibitors.* Biochemistry, 2000. **39**(28): p. 8325-8332.

406.   Adams, J.A., *Kinetic and catalytic mechanisms of protein kinases.* Chemical reviews, 2001. **101**(8).

407.   Palmer, A.G., *NMR characterization of the dynamics of biomacromolecules.* Chemical Reviews, 2004. **104**(8): p. 3623-3640.

408.   Boehr, D.D., H.J. Dyson, and P.E. Wright, *An NMR perspective on enzyme dynamics.* Chemical Reviews, 2006. **106**(8): p. 3055-3079.

409.   Mittermaier, A. and L.E. Kay, *New tools provide new insights in NMR studies of protein dynamics.* Science, 2006. **312**(5771): p. 224-8.

410.   Cembran, A., et al., *NMR mapping of protein conformational landscapes using coordinated behavior of chemical shifts upon ligand binding.* Phys Chem Chem Phys, 2014. **16**(14): p. 6508-18.

411.   Gotz, A.W., et al., *Routine Microsecond Molecular Dynamics Simulations with AMBER on GPUs. 1. Generalized Born.* Journal of Chemical Theory and Computation, 2012. **8**(5): p. 1542-1555.

412.   Le Grand, S., A.W. Gotz, and R.C. Walker, *SPFP: Speed without compromise-A mixed precision model for GPU accelerated molecular dynamics simulations.* Computer Physics Communications, 2013. **184**(2): p. 374-380.

413.   Morcos, F., et al., *Modeling conformational ensembles of slow functional motions in Pin1-WW.* PLoS Comput Biol, 2010. **6**(12): p. e1001015.

414.   Morcos, F., et al., *Modeling conformational ensembles of slow functional motions in Pin1-WW.* PLoS Computational Biology, 2010. **in press**.

415.   McClendon, C.L., et al., *Quantifying Correlations Between Allosteric Sites in Thermodynamic Ensembles.* Journal of Chemical Theory and Computation, 2009. **5**(9): p. 2486-2502.

416.   Wan, X., et al., *Ab initio modeling and experimental assessment of Janus Kinase 2 (JAK2) kinase-pseudokinase complex structure.* PLoS Computational Biology, 2013. **9**(4): p. e1003022.

417.   McClendon, C.L., et al., *Comparing Conformational Ensembles Using the Kullback-Leibler Divergence Expansion.* Journal of Chemical Theory and Computation, 2012. **8**(6): p. 2115-2126.

418.   Herberg, F.W., et al., *Dissection of the nucleotide and metal-phosphate binding sites in cAMP-dependent protein kinase.* Biochemistry, 1999. **38**(19).

419.   Wang, C.Y., M.J. Grey, and A.G. Palmer, *CPMG sequences with enhanced sensitivity to chemical exchange.* Journal of Biomolecular Nmr, 2001. **21**(4): p. 361-366.

420.   Wang, C.Y., M. Rance, and A.G. Palmer, *Mapping chemical exchange in proteins with MW > 50 kD.* Journal of the American Chemical Society, 2003. **125**(30): p. 8968-8969.

421.   Palmer, A.G., 3rd, C.D. Kroenke, and J.P. Loria, *Nuclear magnetic resonance methods for quantifying microsecond-to-millisecond motions in biological macromolecules.* Methods Enzymol, 2001. **339**: p. 204-38.

422.   Wang, C.Y. and A.G. Palmer, *Solution NMR methods for quantitative identification of chemical exchange in N-15-labeled proteins.* Magnetic Resonance in Chemistry, 2003. **41**(10): p. 866-876.

423.   Sethi, A., et al., *Dynamical networks in tRNA:protein complexes.* Proceedings of the National Academy of Sciences of the United States of America, 2009. **106**(16): p. 6620-5.

424.   Newman, M.E.J., *Analysis of weighted networks.* Physical Review E, 2004. **70**(5).

425.   Kappel, K., et al., *The binding mechanism, multiple binding modes, and allosteric regulation of Staphylococcus aureus Sortase A probed by molecular dynamics simulations.* Protein science : a publication of the Protein Society, 2012. **21**(12): p. 1858-71.

426.   Pisliakov, A.V., et al., *Enzyme millisecond conformational dynamics do not catalyze the chemical step.* Proceedings of the National Academy of Sciences of the United States of America, 2009. **106**(41): p. 17359-17364.

427.   Garcia-Viloca, M., et al., *How enzymes work: Analysis by modern rate theory and computer simulations.* Science, 2004. **303**(5655): p. 186-195.

428.   Schwartz, S.D. and V.L. Schramm, *Enzymatic transition states and dynamic motion in barrier crossing.* Nat Chem Biol, 2009. **5**(8): p. 551-8.

429.   Hammes-Schiffer, S., *Impact of enzyme motion on activity.* Biochemistry, 2002. **41**(45): p. 13335-13343.

430.   Hammes-Schiffer, S. and S.J. Benkovic, *Relating protein motion to catalysis*, in *Annual Review of Biochemistry*. 2006. p. 519-541.

431.   Bhabha, G., et al., *A Dynamic Knockout Reveals That Conformational Fluctuations Influence the Chemical Step of Enzyme Catalysis.* Science, 2011. **332**(6026): p. 234-238.

432.   Boehr, D.D., et al., *The dynamic energy landscape of dihydrofolate reductase catalysis.* Science, 2006. **313**(5793): p. 1638-1642.

433.   Lipchock, J.M. and J.P. Loria, *Nanometer propagation of millisecond motions in V-type allostery.* Structure, 2010. **18**(12): p. 1596-607.

434.   Tzeng, S.-R. and C.G. Kalodimos, *Dynamic activation of an allosteric regulatory protein.* Nature, 2009. **462**(7271): p. 368-U139.

435.   Popovych, N., et al., *Dynamically driven protein allostery.* Nature Structural & Molecular Biology, 2006. **13**(9): p. 831-838.

436.   Henzler-Wildman, K.A., et al., *Intrinsic motions along an enzymatic reaction trajectory.* Nature, 2007. **450**(7171): p. 838-U13.

437.   Mauldin, R.V., M.J. Carroll, and A.L. Lee, *Dynamic dysfunction in dihydrofolate reductase results from antifolate drug binding: modulation of dynamics within a structural state.* Structure, 2009. **17**(3): p. 386-94.

438.   Chao, F.-A., et al., *Structure and dynamics of a primordial catalytic fold generated by in vitro evolution.* Nat Chem Biol, 2012. **advance online publication**.

439.   Bhabha, G., et al., *Divergent evolution of protein conformational dynamics in dihydrofolate reductase.* Nat Struct Mol Biol, 2013. **20**(11): p. 1243-9.

440.   Wolf-Watz, M., et al., *Linkage between dynamics and catalysis in a thermophilic-mesophilic enzyme pair.* Nat Struct Mol Biol, 2004. **11**(10): p. 945-9.

441.   Jackson, C.J., et al., *Conformational sampling, catalysis, and evolution of the bacterial phosphotriesterase.* Proceedings of the National Academy of Sciences of the United States of America, 2009. **106**(51): p. 21631-21636.

442.   Honndorf, V.S., et al., *Dynamics in the p38alpha MAP kinase-SB203580 complex observed by liquid-state NMR spectroscopy.* Angew Chem Int Ed Engl, 2008. **47**(19): p. 3548-51.

443.   Wang, X., et al., *The linker between the dimerization and catalytic domains of the CheA histidine kinase propagates changes in structure and dynamics that are important for enzymatic activity.* Biochemistry, 2014. **53**(5): p. 855-61.

444.   Taylor, S.S., et al., *Dynamics of signaling by PKA.* Biochimica et biophysica acta, 2005. **1754**(1-2).

445.   Lu, B.Z., C.F. Wong, and J.A. McCammon, *Release of ADP from the catalytic subunit of protein kinase A: A molecular dynamics simulation study.* Protein Science, 2005. **14**(1): p. 159-168.

446.   Li, F., et al., *Evidence for an internal entropy contribution to phosphoryl transfer: a study of domain closure, backbone flexibility, and the catalytic cycle of cAMP-dependent protein kinase.* Journal of Molecular Biology, 2002. **315**(3): p. 459-469.

447.   Daily, M.D., G.N. Phillips, Jr., and Q. Cui, *Many local motions cooperate to produce the adenylate kinase conformational transition.* J Mol Biol, 2010. **400**(3): p. 618-31.

448.   Knighton, D.R., et al., *Crystal structure of the catalytic subunit of cyclic adenosine monophosphate-dependent protein kinase.* Science, 1991. **253**(5018): p. 407-14.

449.   Hu, J., et al., *Allosteric activation of functionally asymmetric RAF kinase dimers.* Cell, 2013. **154**(5): p. 1036-46.

450.   Mirsky, A.E. and L. Pauling, *On the Structure of Native, Denatured, and Coagulated Proteins.* Proc Natl Acad Sci U S A, 1936. **22**(7): p. 439-47.

451.   Loh, S.N. and J.L. Markley. *Measurement of amide hydrogen deuterium/hydrogen fractionation factors in proteins by NMR spectroscopy*. 1993. Academic.

452.   Schowen, K.B. and R.L. Schowen, *Solvent isotope effects of enzyme systems.* Methods Enzymol, 1982. **87**: p. 551-606.

453.   Kreevoy, M.M., T. Liang, and K.C. Chang, *Structures and Isotopic Fractionation Factors of Complexes Aha-.* Journal of the American Chemical Society, 1977. **99**(15): p. 5207-5209.

454.   Cleland, W.W., P.A. Frey, and J.A. Gerlt, *The low barrier hydrogen bond in enzymatic catalysis.* J Biol Chem, 1998. **273**(40): p. 25529-32.

455.   Loh, S.N. and J.L. Markley, *Hydrogen bonding in proteins as studied by amide hydrogen D/H fractionation factors: application to staphylococcal nuclease.* Biochemistry, 1994. **33**(4): p. 1029-36.

456.   Harris, T.K., C. Abeygunawardana, and A.S. Mildvan, *NMR studies of the role of hydrogen bonding in the mechanism of triosephosphate isomerase.* Biochemistry, 1997. **36**(48): p. 14661-75.

457.   Cao, Z. and J.U. Bowie, *An energetic scale for equilibrium H/D fractionation factors illuminates hydrogen bond free energies in proteins.* Protein Sci, 2014. **23**(5): p. 566-75.

458.   Englander, S.W. and M.M. Krishna, *Hydrogen exchange.* Nat Struct Biol, 2001. **8**(9): p. 741-2.

459.   Skinner, J.J., et al., *Protein dynamics viewed by hydrogen exchange.* Protein Sci, 2012. **21**(7): p. 996-1005.

460.   Korzhnev, D.M., et al., *A transient and low-populated protein-folding intermediate at atomic resolution.* Science, 2010. **329**(5997): p. 1312-6.

461. Li, Y., et al., *Mechanism of E-cadherin dimerization probed by NMR relaxation dispersion.* Proc Natl Acad Sci U S A, 2013. **110**(41): p. 16462-7.
462. Nietlispach, D., *Suppression of anti-TROSY lines in a sensitivity enhanced gradient selection TROSY scheme.* Journal of Biomolecular NMR, 2005. **31**(2): p. 161-166.
463. Delaglio, F., et al., *NMRPipe: a multidimensional spectral processing system based on UNIX pipes.* J Biomol NMR, 1995. **6**(3): p. 277-93.
464. Goddard, T.D.K., D.G. *SPARKY 3*. 1999.
465. Kim, J., et al., *Dysfunctional conformational dynamics of protein kinase A induced by a lethal mutant of phospholamban hinder phosphorylation.* Proc Natl Acad Sci U S A, 2015. **112**(12): p. 3716-21.
466. Yang, J., et al., *Allosteric Network of cAMP-dependent Protein Kinase Revealed by Mutation of Tyr204 in the P+1 Loop.* Journal of Molecular Biology, 2005. **346**(1): p. 191-201.
467. LiWang, A.C. and A. Bax, *Equilibrium protium/deuterium fractionation of backbone amides in U-C-13/N-15 labeled human ubiquitin by triple resonance NMR.* Journal of the American Chemical Society, 1996. **118**(50): p. 12864-12865.
468. Khare, D., P. Alexander, and J. Orban, *Hydrogen Bonding and Equilibrium Protium−Deuterium Fractionation Factors in the Immunoglobulin G Binding Domain of Protein G.* Biochemistry, 1999. **38**(13): p. 3918-3925.
469. Bowers, P.M. and R.E. Klevit, *Hydrogen bonding and equilibrium isotope enrichment in histidine-containing proteins.* Nat Struct Biol, 1996. **3**(6): p. 522-31.
470. Bastidas, A.C., J. Wu, and S.S. Taylor, *Molecular features of product release for the PKA catalytic cycle.* Biochemistry, 2015. **54**(1): p. 2-10.
471. Nick Pace, C., J.M. Scholtz, and G.R. Grimsley, *Forces stabilizing proteins.* FEBS Lett, 2014. **588**(14): p. 2177-84.
472. Perutz, M.F., *Mechanisms of cooperativity and allosteric regulation in proteins.* Q Rev Biophys, 1989. **22**(2): p. 139-237.
473. Gardino, A.K., et al., *Transient non-native hydrogen bonds promote activation of a signaling protein.* Cell, 2009. **139**(6): p. 1109-18.
474. Levinson, N.M. and S.G. Boxer, *A conserved water-mediated hydrogen bond network defines bosutinib's kinase selectivity.* Nat Chem Biol, 2014. **10**(2): p. 127-132.
475. Andersen, M.D., et al., *Structural characterization of protein kinase A as a function of nucleotide binding. Hydrogen-deuterium exchange studies using matrix-assisted laser desorption ionization-time of flight mass spectrometry detection.* J Biol Chem, 2001. **276**(17): p. 14204-11.
476. Das, R., M. Abu-Abed, and G. Melacini, *Mapping allostery through equilibrium perturbation NMR spectroscopy.* Journal of the American Chemical Society, 2006. **128**(26): p. 8406-8407.
477. Mazhab-Jafari, M.T., et al., *Understanding cAMP-dependent allostery by NMR spectroscopy: comparative analysis of the EPAC1 cAMP-binding domain in its apo and cAMP-bound states.* J Am Chem Soc, 2007. **129**(46): p. 14482-92.
478. Das, R., et al., *Dynamically driven ligand selectivity in cyclic nucleotide binding domains.* J Biol Chem, 2009. **284**(35): p. 23682-96.
479. Lin, J., et al., *Fractionation factors and activation energies for exchange of the low barrier hydrogen bonding proton in peptidyl trifluoromethyl ketone complexes of chymotrypsin.* Proc Natl Acad Sci U S A, 1998. **95**(25): p. 14664-8.

480. Gangal, M., et al., *Backbone Flexibility of Five Sites on the Catalytic Subunit of cAMP-Dependent Protein Kinase in the Open and Closed Conformations.* Biochemistry, 1998. **37**(39): p. 13728-13735.

481. Li, F., et al., *Evidence for an internal entropy contribution to phosphoryl transfer: a study of domain closure, backbone flexibility, and the catalytic cycle of cAMP-dependent protein kinase.* J Mol Biol, 2002. **315**(3): p. 459-69.

482. Herberg, F.W., et al., *Dissection of the nucleotide and metal-phosphate binding sites in cAMP-dependent protein kinase.* Biochemistry, 1999. **38**(19): p. 6352-60.

483. Bers, D.M., *Calcium cycling and signaling in cardiac myocytes.* Annu Rev Physiol, 2008. **70**: p. 23-49.

484. Lompre, A.M., et al., *Ca2+ cycling and new therapeutic approaches for heart failure.* Circulation, 2010. **121**(6): p. 822-830.

485. Vandecaetsbeek, I., et al., *Factors controlling the activity of the SERCA2a pump in the normal and failing heart.* Biofactors, 2009. **35**(6): p. 484-99.

486. Frank, K.F., et al., *Modulation of SERCA: implications for the failing human heart.* Basic Res Cardiol, 2002. **97 Suppl 1**: p. I72-8.

487. MacLennan, D.H. and E.G. Kranias, *Phospholamban: a crucial regulator of cardiac contractility.* Nat Rev Mol Cell Biol, 2003. **4**(7): p. 566-77.

488. MacLennan, D.H., *Ca2+ signalling and muscle disease.* Eur J Biochem, 2000. **267**(17): p. 5291-7.

489. Dellefave, L. and E.M. McNally, *The genetics of dilated cardiomyopathy.* Curr Opin Cardiol, 2010. **25**(3): p. 198-204.

490. Movsesian, M.A., *Altered cAMP-mediated signalling and its role in the pathogenesis of dilated cardiomyopathy.* Cardiovasc Res, 2004. **62**(3): p. 450-9.

491. Haghighi, K., et al., *A mutation in the human phospholamban gene, deleting arginine 14, results in lethal, hereditary cardiomyopathy.* Proc Natl Acad Sci U S A, 2006. **103**(5): p. 1388-93.

492. Posch, M.G., et al., *Genetic deletion of arginine 14 in phospholamban causes dilated cardiomyopathy with attenuated electrocardiographic R amplitudes.* Heart Rhythm, 2009. **6**(4): p. 480-6.

493. van der Zwaag, P.A., et al., *Phospholamban R14del mutation in patients diagnosed with dilated cardiomyopathy or arrhythmogenic right ventricular cardiomyopathy: evidence supporting the concept of arrhythmogenic cardiomyopathy.* Eur J Heart Fail, 2012. **14**(11): p. 1199-207.

494. Haghighi, K., et al., *The human phospholamban Arg14-deletion mutant localizes to plasma membrane and interacts with the Na/K-ATPase.* J Mol Cell Cardiol, 2012. **52**(3): p. 773-82.

495. Delaglio, F., et al., *NMRPipe: A multidimensional spectral processing system based on UNIX pipes.* Journal of Biomolecular NMR, 1995. **6**(3): p. 277-293.

496. Adams, J.A. and S.S. Taylor, *Phosphorylation of peptide substrates for the catalytic subunit of cAMP-dependent protein kinase.* J Biol Chem, 1993. **268**(11): p. 7747-52.

497. Ceholski, D.K., et al., *Lethal, hereditary mutants of phospholamban elude phosphorylation by protein kinase A.* J Biol Chem, 2012. **287**(32): p. 26596-605.

498. Hughes, E. and D.A. Middleton, *Comparison of the structure and function of phospholamban and the arginine-14 deficient mutant associated with dilated cardiomyopathy.* PLoS One, 2014. **9**(9): p. e106746.

499. Srivastava A.K., M.L., Cembran A., Kim J., Masterson L.R., and Veglia G., *Synchronous Opening and Closing Motions are Essential for cAMP-Dependent Protein Kinase A Signaling.* Structure, 2014: p. In Press.

500. Fan, Y., et al., *Connecting Protein Conformational Dynamics with Catalytic Function As Illustrated in Dihydrofolate Reductase.* Biochemistry, 2013. **52**(12): p. 2036-2049.

501. Ha, K.N., et al., *Lethal Arg9Cys phospholamban mutation hinders Ca2+-ATPase regulation and phosphorylation by protein kinase A.* Proc Natl Acad Sci U S A, 2011. **108**(7): p. 2735-40.

502. Vostrikov, V.V., et al., *Effects of naturally occurring arginine 14 deletion on phospholamban conformational dynamics and membrane interactions.* Biochim Biophys Acta, 2015. **1848**(1 Pt B): p. 315-22.

503. Fischer, E.H. and E.G. Krebs, *Conversion of phosphorylase b to phosphorylase a in muscle extracts.* J Biol Chem, 1955. **216**(1): p. 121-32.

504. Manning, G., et al., *Evolution of protein kinase signaling from yeast to man.* Trends Biochem Sci, 2002. **27**(10): p. 514-20.

505. Johnson, L.N. and R.J. Lewis, *Structural basis for control by phosphorylation.* Chem Rev, 2001. **101**(8): p. 2209-42.

506. Endicott, J.A., M.E. Noble, and L.N. Johnson, *The structural basis for control of eukaryotic protein kinases.* Annu Rev Biochem, 2012. **81**: p. 587-613.

507. Shaw, A.S., et al., *Kinases and pseudokinases: lessons from RAF.* Mol Cell Biol, 2014. **34**(9): p. 1538-46.

508. Iyer, G.H., M.J. Moore, and S.S. Taylor, *Consequences of lysine 72 mutation on the phosphorylation and activation state of cAMP-dependent kinase.* J Biol Chem, 2005. **280**(10): p. 8800-7.

509. Dar, A.C. and K.M. Shokat, *The evolution of protein kinase inhibitors from antagonists to agonists of cellular signaling.* Annu Rev Biochem, 2011. **80**: p. 769-95.

510. Cowan-Jacob, S.W., W. Jahnke, and S. Knapp, *Novel approaches for targeting kinases: allosteric inhibition, allosteric activation and pseudokinases.* Future Med Chem, 2014. **6**(5): p. 541-61.

511. Fang, Z., C. Grutter, and D. Rauh, *Strategies for the selective regulation of kinases with allosteric modulators: exploiting exclusive structural features.* ACS Chem Biol, 2013. **8**(1): p. 58-70.

512. Arencibia, J.M., et al., *AGC protein kinases: from structural mechanism of regulation to allosteric drug development for the treatment of human diseases.* Biochim Biophys Acta, 2013. **1834**(7): p. 1302-21.

513. Wu, P., T.E. Nielsen, and M.H. Clausen, *FDA-approved small-molecule kinase inhibitors.* Trends Pharmacol Sci, 2015.

514. Taylor, S.S., et al., *Dynamics of signaling by PKA.* Biochim Biophys Acta, 2005. **1754**(1-2): p. 25-37.

515. Sims, P.C., et al., *Electronic measurements of single-molecule catalysis by cAMP-dependent protein kinase A.* J Am Chem Soc, 2013. **135**(21): p. 7861-8.

516. Adams, J.A., *Kinetic and catalytic mechanisms of protein kinases.* Chem Rev, 2001. **101**(8): p. 2271-90.

517. Kim, J., et al., *Dysfunctional conformational dynamics of protein kinase A induced by a lethal mutant of phospholamban hinder phosphorylation.* Proc Natl Acad Sci U S A, 2015: p. 201502299.

518. Ni, D.Q., J. Shaffer, and J.A. Adams, *Insights into nucleotide binding in protein kinase A using fluorescent adenosine derivatives.* Protein Science, 2000. **9**(9): p. 1818-1827.

519. Zimmermann, B., et al., *Effect of metal ions on high-affinity binding of pseudosubstrate inhibitors to PKA.* Biochem J, 2008. **413**(1): p. 93-101.

520. Axe, J.M., et al., *Amino Acid Networks in a (β/α)8 Barrel Enzyme Change during Catalytic Turnover.* Journal of the American Chemical Society, 2014. **136**(19): p. 6818-6821.

521. Boulton, S., et al., *A Tool Set to Map Allosteric Networks through the NMR Chemical Shift Covariance Analysis.* Scientific Reports, 2014. **4**.

522. Ruschak, A.M. and L.E. Kay, *Proteasome allostery as a population shift between interchanging conformers.* Proc Natl Acad Sci U S A, 2012. **109**(50): p. E3454-62.

523. Velyvis, A. and L.E. Kay, *Measurement of active site ionization equilibria in the 670 kDa proteasome core particle using methyl-TROSY NMR.* J Am Chem Soc, 2013. **135**(25): p. 9259-62.

524. Chijiwa, T., et al., *Inhibition of forskolin-induced neurite outgrowth and protein phosphorylation by a newly synthesized selective inhibitor of cyclic AMP-dependent protein kinase, N-[2-(p-bromocinnamylamino)ethyl]-5-isoquinolinesulfonamide (H-89), of PC12D pheochromocytoma cells.* J Biol Chem, 1990. **265**(9): p. 5267-72.

525. Kulanthaivel, P., et al., *Balanol: a novel and potent inhibitor of protein kinase C from the fungus Verticillium balanoides.* Journal of the American Chemical Society, 1993. **115**(14): p. 6452-6453.

526. Koide, K., et al., *Molecular design and biological activity of potent and selective protein kinase inhibitors related to balanol.* Chem Biol, 1995. **2**(9): p. 601-8.

527. Fersht, A.R., *Catalysis, binding and enzyme-substrate complementarity.* Proc R Soc Lond B Biol Sci, 1974. **187**(1089): p. 397-407.

528. Schramm, V.L., *Enzymatic transition states, transition-state analogs, dynamics, thermodynamics, and lifetimes.* Annu Rev Biochem, 2011. **80**(1): p. 703-32.

529. Toyoshima, C. and T. Mizutani, *Crystal structure of the calcium pump with a bound ATP analogue.* Nature, 2004. **430**(6999): p. 529-35.

530. Polier, S., et al., *ATP-competitive inhibitors block protein kinase recruitment to the Hsp90-Cdc37 system.* Nat Chem Biol, 2013. **9**(5): p. 307-12.

531. Gibbs, C.S. and M.J. Zoller, *Rational scanning mutagenesis of a protein kinase identifies functional regions involved in catalysis and substrate interactions.* J Biol Chem, 1991. **266**(14): p. 8923-31.

532. Narayana, N., et al., *Crystal structure of the potent natural product inhibitor balanol in complex with the catalytic subunit of cAMP-dependent protein kinase.* Biochemistry, 1999. **38**(8): p. 2367-76.

533. Foda, Z.H., et al., *A dynamically coupled allosteric network underlies binding cooperativity in Src kinase.* Nat Commun, 2015. **6**: p. 5939.

534. Herberg, F.W. and S.S. Taylor, *Physiological inhibitors of the catalytic subunit of cAMP-dependent protein kinase: effect of magnesium-ATP on protein-protein interactions.* Biochemistry, 1993. **32**(50): p. 14015-14022.

535. Kleckner, I.R. and M.P. Foster, *An introduction to NMR-based approaches for measuring protein dynamics.* Biochim Biophys Acta, 2011. **1814**(8): p. 942-68.

536. Boehr, D.D., H.J. Dyson, and P.E. Wright, *An NMR perspective on enzyme dynamics.* Chem Rev, 2006. **106**(8): p. 3055-79.

537. Verardi, R., et al., *Structural topology of phospholamban pentamer in lipid bilayers by a hybrid solution and solid-state NMR method.* Proc Natl Acad Sci U S A, 2011. **108**(22): p. 9101-6.